

EFFECT OF INJECTION STRATEGIES ON PARTICULATE MATTER EMISSIONS FROM HPDI NATURAL-GAS ENGINES

by

EHSAN FAGHANI

B.Sc., The University of Tehran, 2005

M.Sc., Sharif University of Technology, 2008

A THESIS SUBMITTED IN PARTIAL FULFILLMENT OF
THE REQUIREMENTS FOR THE DEGREE OF

DOCTOR OF PHILOSOPHY

in

THE FACULTY OF GRADUATE AND POSTDOCTORAL STUDIES

(Mechanical Engineering)

THE UNIVERSITY OF BRITISH COLUMBIA

(Vancouver)

November 2015

© Ehsan Faghani, 2015

ABSTRACT

Internal combustion engines produce emissions of NOx and particulate matter (PM). Westport Innovations Inc. has developed the pilot-ignited high-pressure direct-injection (HPDI) natural gas (NG) engine system. To ignite the natural gas, HPDI uses a small diesel pilot injection (~5% of total fuel energy), which is normally injected before the NG. Although HPDI engines produce less PM than diesel engines, further reductions of engine-out PM emissions are desired in order to meet future regulations. The goal of this project is to reduce PM from HPDI engines and study the drawbacks of the injection strategies in terms of engine performance or other emissions. This thesis proposes mechanisms for two injection strategies useful in PM reduction: Late Post Injection (LPI) and Slightly Premixed Combustion (SPC).

Tests on LPI and SPC were performed in the UBC Single Cylinder Research Engine (SCRE). In LPI, a second natural gas injection (10-25% of total fuel mass) is injected into the cylinder later in the cycle. In SPC, more premixing of NG is achieved by injecting NG before the diesel injection and engine operating parameters are adjusted to minimize the effect on other emissions. Both of the injection strategies show significant PM reduction (over 75% on the SCRE) with small effects on other emissions and engine performance.

Westport's computational fluid dynamics package, "GOLD", was used to help to understand the mechanisms of the new injection strategies. The PM reductions from LPI and SPC were captured by GOLD.

A phenomenological model (Transient Slice Model, TSM) has been developed in this study to provide better insight into the PM reduction process, using the Hiroyasu model with a transport equation for soot. TSM results show good agreement in the prediction of pressure trace and heat release rates in most cases. Engine-out PM trends with changing engine parameters are well-captured in the TSM for exhaust gas recirculation (EGR), equivalence ratio (EQR), load and natural gas (NG) flow. TSM cannot predict the effect of NG injection pressure. For the new injection strategies, TSM can predict the PM trends for LPI, relative gas-diesel timing and the SPC injection strategy.

PREFACE

The doctoral candidate identified and/or developed the injection strategies, designed test matrix, performed the experiments, performed data analysis and presented of the results. All test matrix designs were reviewed by the thesis committee and engineers at Westport Innovations Inc. (Drs. McTaggart-Cowan and Wu, and Mr. Bronson Patychuk).

The doctoral candidate is the primary and corresponding author of the technical papers which were published as part of this thesis. The technical papers are referred to in the bibliography [1], [2]. Figure 2-5 and Figure 4-1, from momentum measurement study [2], are included in this thesis with permission from SAE International. The co-authors of the published technical papers made contributions as a supervisory committee or expert in a specific area of the current work. The supervisory committee provided direction and support. The technical papers have been reviewed by the co-authors prior to submission by providing critical evaluation of the publication; however, the candidate was responsible for the writing and the final content of these manuscripts. Pooyan Kheirkhah performed the CFD simulations using the Westport CFD package (GOLD), the results are discussed in sections 4.3.4 and 5.3.5. Post processing of CFD results, evaluating the concept and comparing the experiments with CFD results was jointly performed by Pooyan Kheirkhah and the PhD candidate. Christopher Mabson performed the TEM image analysis (sections 4.1.3 and 5.3.4) with support from Ramin Dastanpour.

TABLE OF CONTENTS

ABSTRACT	ii
PREFACE.....	iii
TABLE OF CONTENTS	iv
LIST OF FIGURES.....	xii
NOMENCLATURE.....	xvii
ACKNOWLEDGEMENTS	xx
1 INTRODUCTION	1
1.1 HPDI Introduction	1
1.2 Motivation for PM Reduction.....	3
1.3 Combustion and PM Formation in Direct-Injection Engines.....	7
1.4 Injection Strategies in DI Engines	11
1.4.1 Late Post Injection (LPI) in Diesel Engines.....	13
1.4.2 Partially Premixed Combustion	15
1.5 Phenomenological Modeling for DI Engines	21
1.6 Thesis Objectives	25
1.7 Thesis Structure	27
2 EXPERIMENTAL METHODS	29
2.1 Single Cylinder Research Engine.....	29
2.1.1 Operating Modes	39
2.1.2 Measurement Variability in SCRE Experiments	40
2.2 Momentum Measurement Method.....	44
3 MODELLING METHODS	47
3.1 Overview of Transient Slice Model (TSM)	47
3.2 The Jet Model.....	51

3.2.1	Injection Specifications.....	53
3.2.2	Transport of Scalars.....	55
3.2.3	Radial Distribution of Velocity.....	56
3.2.4	Radial Distribution of Mixture Fraction.....	57
3.2.5	Mixture Fraction Maps.....	57
3.2.6	Ignition and Flame Propagation.....	61
3.2.7	Jet Integral Calculations	64
3.3	Cylinder Thermodynamics Model.....	65
3.3.1	Initial Conditions at SOS.....	65
3.3.2	Cylinder Volume.....	66
3.3.3	Cylinder Mass Balance	66
3.3.4	Cylinder Energy Balance	66
3.3.5	Cylinder Wall Heat Transfer.....	67
3.3.6	Motored Pressure and Temperature.....	68
3.4	Soot Model.....	68
3.5	Summary of Adjustable Parameters in TSM	69
3.6	CFD Modeling (GOLD).....	70
3.7	φ -T Map.....	72
4	RESULTS FOR LATE POST INJECTION	74
4.1	Experimental Design	75
4.1.1	Momentum Measurement.....	75
4.1.2	Engine Experiments.....	76
4.1.3	Mode B75 Tests: GSEP and SI Sweeps	77
4.1.4	Multi-Mode Tests	78
4.1.5	Pulse Isolation Tests.....	79

4.2	Computational Model.....	83
4.3	Results and Discussion.....	83
4.3.1	SCRE Experimental Results for Mode B75- GSEP and SI Sweeps.....	83
4.3.2	SCRE Experimental Results for LPI Multi-Mode Tests	92
4.3.3	SCRE Experimental Results for Pulse Isolation Tests.....	94
4.3.4	CFD Results and Discussion of LPI Mechanism.....	97
4.3.5	LPI Multi-Injector Tests.....	102
4.3.6	Comparison of the Effect of LPI in Diesel and HPDI Engines.....	106
4.4	Conclusions for Late Post Injection	109
5	RESULTS FOR SLIGHTLY PREMIXED COMBUSTION.....	112
5.1	Experimental Design	112
5.2	Computational Model.....	114
5.3	Results and Discussion	115
5.3.1	Effect of Delaying Pilot Injection for Normal EGR and EQR Conditions	115
5.3.2	PSEP Sweeps at different EGR and EQR	119
5.3.3	SCRE Experimental Results for Effect of Pilot Quantity on SPC.....	127
5.3.4	Optimized Slightly Premixed Combustion and PM Characterization from the SCRE Experiments.....	128
5.3.5	CFD Results and Discussion of SPC Mechanism.....	131
5.3.6	SPC Multi-injector tests	137
5.4	Conclusions for Slightly Premixed Combustion	139
6	RESULTS FOR TRANSIENT SLICE MODEL.....	142
6.1	Experimental Points to be Modeled by TSM	142
6.2	Results and Discussion.....	144
6.2.1	B75 Pressure and Heat Release Rate	144

6.2.2	EGR Sweep.....	145
6.2.3	NG Flow Sweep	148
6.2.4	EQR Sweep.....	150
6.2.5	Timing (CA50) Sweep	152
6.2.6	Gas Rail Pressure (GRP) Sweep.....	154
6.2.7	Mode Sweep.....	156
6.2.8	LPI-GSEP Sweep	158
6.2.9	PSEP Sweep.....	161
6.2.10	SPC-PSEP Sweep.....	163
6.3	Conclusions for the Transient Slice Model	165
7	CONCLUSIONS	167
7.1	Late Post Injection.....	167
7.2	Slightly Premixed Combustion	170
7.3	Transient Slice Model (TSM).....	174
7.4	Conclusions Drawn from all Chapters	177
8	RECOMMENDATIONS FOR FUTURE WORK	181
8.1	Recommendations for Engine Testing and CFD Methodology	181
8.2	Recommendations for Areas for Future Engine Testing.....	182
8.3	Recommendations for Phenomenological Model Development.....	184
8.4	Recommendations for Product Development.....	185
BIBLIOGRAPHY.....	187	
APPENDICES	197	
Appendix A: Non-Reacting TSM and Validation	197	
Impingement Model (included for possible future development of TSM)	197	
Model Validation.....	199	

Steady Methane-Air Jets, Mass Fraction Comparison	200
Steady Methane-Hot Air Jet, Mixing Temperature Comparison	202
Steady N ₂ -CO ₂ -H ₂ Jets, Entrainment Comparison for Different Density Ratios	202
Transient N ₂ -CO ₂ -H ₂ Jets, Penetration Comparison for Different Density Ratios.....	203
Decelerating Air-Air Jet, Entrainment Comparison after EOI	204
Steady Impinging Air-Air Jet, Velocity Comparison.....	205
Transient Impinging C ₂ H ₂ -Air Jet, Jet Penetration Comparison.....	206
Pulsed Air-Air Jet, Fuel Rate Shape Effect on Penetration Rate	207
Cold Injection in Variable Environment, Penetration and Mixing Rate Comparison ...	209
Appendix B: Mesh Sensitivity, Computational Time, and Parametric Tuning of TSM.....	211
TSM Mesh Sensitivity.....	211
TSM Computational Time.....	213
TSM Soot tuning.....	213
Appendix C: A Physical Ignition Model (for future TSM development)	217
Pilot Ignition Delay (PID)	217
Gas Ignition Delay (GID)	218
Appendix D: Sample Calculation for In-Cylinder Integrals.....	221
Appendix E: Different Methods of Setting the Point for PPW Sweep	222
Appendix F: AHRR of the Normal PSEP Sweep Cases.....	223
Appendix G: Electronic Archives and Data Processing	224
Electronic Archives.....	224
Data Processing.....	224
Appendix H: Balances for Engine Simulation	226
Appendix I: Engine-out PM and Peak AHRR Location vs. RIT for all SPC Experiments ...	229
Appendix J: Particulate Matter Sampling System.....	230

Appendix K: AHRR of Post Injections.....	232
Appendix L: Air Handling Systems of SCRE.....	234
Exhaust and EGR System.....	234
Air Intake System	235
Appendix M: HPDI-Fuel Conditioning	238
Appendix N: Emissions Bench	243
Appendix O: Injector-Injector Variations.....	246
Injectors	246
Heat Release rate comparison of LPI points (from first test block)	246
Test Matrix of the second test block	248
Apparent Heat Release graphs.....	250
LPI Multi-injector tests.....	251
SPC Multi-injector tests.....	254
Appendix P: TSM Simulation of the Effect of Ramp-up/down of the Injection on Engine-out PM	256
Appendix Q: Injection Timings for LPI Experiments	257
Appendix R: Injection-Injection Variability of LPI Momentum Measurement Tests	261

LIST OF TABLES

Table 1-1- European emission regulations [20], [21].....	5
Table 2-1 SCRE engine, injector and fuel specifications	33
Table 2-2 Mode B75 and permitted range for set parameters.....	40
Table 2-3 Mode B75 variations for April-December 2014	42
Table 2-4 Range of parameters selected for the experiments.....	46
Table 3-1 TSM model parameters	70
Table 4-1 Summary of the mode B75 GSEP and SI sweep tests	78
Table 4-2 Summary of the multi-mode tests for single injection and LPI	79
Table 4-3 Summary of the pulse isolation tests	80
Table 4-4 Summary of the CFD tests	83
Table 4-5 Comparing optimized LPI point with the baseline	90
Table 4-6 Summary of the results from SMPS and TEM sampling for LPI and baseline points at B75.....	91
Table 4-7 Summary of the multi-mode results.....	93
Table 4-8 Summary of the results from CFD compared to the experiments (SI=15%, GSEP=2.0 ms).	98
Table 4-9 Emission and injector performance of baseline B75 and LPI point for different injectors.....	106
Table 5-1 Summary of SPC engine experiments. Gas-diesel separation (PSEP) sweeps are combined with other conditions.....	114
Table 5-2 Summary of CFD tests*	115
Table 5-3 Comparing optimized SPC point with the baseline	129
Table 5-4 Summary of the results from SMPS and TEM sampling for SPC and baseline points	130
Table 5-5 Emission and injector performance of baseline B75 and SPC point for different injectors.....	139
Table 6-1 TSM cases used for validation.....	143
Table 6-2 Normalized PM for different modes	157

Table 7-1 Baseline B75 values and LPI and SPC measurements normalized by corresponding baseline values	178
--	-----

LIST OF FIGURES

Figure 1-1 HPDI injector and inner structure, show flow passages for gas (green) and pilot fuel (red).....	3
Figure 1-2 Representative engine-out particle from HPDI engine (mode B75 baseline); TEM image.....	7
Figure 1-3 Schematic diagram of soot formation process (adapted from [33])	8
Figure 1-4 Dec's model of combustion and soot formation in diesel jets [42]. Reprinted with permission from SAE paper 970873 Copyright © 1997 SAE International. Further use, copying, sharing or distribution is not permitted without prior written permission from SAE.....	10
Figure 1-5 Conceptual PM reduction model by premixing (adapted from Ref. [82])	19
Figure 2-1 Single Cylinder Research Engine (SCRE) gas flow system.....	32
Figure 2-2 Phasing of the injection events. Green is NG commanded signal and red is Pilot commanded signal.....	34
Figure 2-3 PM ratio between TEOM and DRX for all the points in the current study for baseline injector.....	38
Figure 2-4 AHRR graphs of the mode B75 points (a) Variations over-time; each grey line is the average of 45 cycles of each points and the black line is the average of all B75 points (total 52 points) (b) Cycle-cycle variations; grey curves show individual cycles and the black curve is the average of 45 cycles.....	43
Figure 2-5 Momentum measurement system.....	44
Figure 3-1 Schematic of TSM.....	49
Figure 3-2 Flowchart of the TSM	51
Figure 3-3 Schematic of the jet model	52
Figure 3-4 mixture fraction maps for ambient conditions approximating (a) SOS: $P_a=5$ bar, $T_a=400$ K and (b) TDC: $P_a=100$ bar, $T_a=1000$ K	60
Figure 3-5 Ignition and flame propagation (a) Schematic of the ignition model (b) a sample of temperature distribution.....	63
Figure 3-6 Impact of effective flame speed on modelled AHRR	64

Figure 3-7 φ -T map generated for Natural Gas (96% Methane) at a pressure of 140bar and a residence time of 2 ms. The numbers in the map are the concentration of each species.....	73
Figure 4-1 Experimental measurement of momentum rate for split injection cases.....	76
Figure 4-2 Command signals for diesel (red) and gas (green) injections in pulse isolation tests	82
Figure 4-3 B75 heat release rate for (a) GSEP and (b) SI sweeps from SCRE experiments..	85
Figure 4-4 B75 gaseous emission and engine performance graphs for GSEP sweep, SI=15% from SCRE experiments.....	87
Figure 4-5 Gaseous emission and engine performance graphs for SI sweeps, GSEP=2.0 ms from SCRE experiments.....	88
Figure 4-6 In-cylinder pressures subtracted from baseline in-cylinder pressure for post injection (blue lines) and “only first pulse” case (85% of NG flow of the baseline, dashed line).....	89
Figure 4-7 PM Size Distributions for baseline and LPI points from SCRE experiments. The open/ closed symbols are two repeats of Baseline or LPI point. The curves are the moving average of each data set.....	92
Figure 4-8 AHRR and IHR of different modes, dashed line is the LPI with GSEP=2 ms and SI=15%.....	94
Figure 4-9 Variation of engine-out PM with NG for single and double injections from pulse-isolation SCRE experiments.....	95
Figure 4-10 AHRR for baseline and LPI from CFD simulation compared with the experiments. The narrow lines show the fuel rate shape from CFD.....	98
Figure 4-11 Evaluation of PM in the cylinder for baseline and LPI point from CFD simulation.....	99
Figure 4-12 In-cylinder PM formation and movement for GSEP=1.0 ms. Soot regions from first and second injections are outlined by red and black contours, respectively. The timing of the presented contour is shown by a red dashed line in the AHRR graph and fuel rate shape graph.....	101
Figure 4-13 In-cylinder PM formation and movement for GSEP=2.0 ms. Soot regions from first and second injections are outlined by red and black contours, respectively. The timing	

of the presented contour is shown by a red dashed line in the AHRR graph and fuel rate shape graph.....	102
Figure 4-14 PM comparison for all the injectors in LPI multi-injector tests. GSEP is 2 ms for all the tests.....	104
Figure 4-15 Comparison of PM reduction and SFC penalty between diesel experiments [59] and current HPDI engines based on same start of AHRR for second pulse (SOH2). Blue symbols are PM reduction; black symbols are fuel consumption penalty.	108
Figure 5-1 Apparent heat release rate (from SCRE experiments) and injection timing for different PSEPs, including gas injection profile (green line, simplified version from momentum measurement tests), diesel ignition (red star) and gas ignition (green star) both from the SCRE experiments.....	116
Figure 5-2 Timing of ignition and peak AHRR relative to EOI from the SCRE experiments.	
.....	117
Figure 5-3 Emission and engine performance by changing pilot separation (PSEP), for mode B75 from the SCRE experiments.	119
Figure 5-4 Apparent heat release rate for PSEP=-0.9ms and different EGR and EQR levels, CA50=11 ° ATDC for all the cases from the SCRE experiments.	120
Figure 5-5 Ignition dwell, and peak AHRR timing and magnitude for different PSEPs from the SCRE experiments.....	122
Figure 5-6 Engine-out emission as a function of separation of gas and diesel injections (PSEP) for different engine environment from the SCRE experiments.	124
Figure 5-7 Engine-out methane versus ignition dwell from the SCRE experiments.	125
Figure 5-8 Engine performance for different engine environment from the SCRE experiments.	127
Figure 5-9 Engine-out PM for different PPW-PSEP sweep from the SCRE experiments....	128
Figure 5-10 PM Size Distributions for baseline and SPC points. The open/ closed symbols are two repeats of Baseline or SPC points from the SCRE experiments. The curves are the moving average of each data set.	130
Figure 5-11 Predicted (CFD) apparent heat release rate of baseline and SPC case compared with the experiments. The green dashed line is the NG fuel rate shape and the red dashed line is the pilot fuel rate shape.....	132

Figure 5-12 PM as a function of crank angle for different mixing controlled and SPC cases from the CFD simulations.....	133
Figure 5-13 Development of rich zone and lean zone in the cycle for baseline and SPC case from the CFD simulations. The stars are the NG ignition points.....	134
Figure 5-14 EQR distribution of baseline and SPC case at the ignition time from the CFD simulations.....	135
Figure 5-15 φ -T map computed for 2 ms residence time at 140 bar. The fuel temperature is 370 K and ambient temperature is 1000K. The simulation is based on GRI3.0 mechanism. The contour numbers show the concentration of each species based on a PSR simulation. The blue combustion path line is the conceptual baseline combustion while the orange line is the SPC conceptual combustion line.....	137
Figure 6-1 Pressure and AHRR of mode B75 compared to the TSM results. The star means the NG ignition point from the SCRE experiment. The green dashed line in the TSM fuel rate shape.....	145
Figure 6-2 Effect of EGR on pressure (a,b) and heat release rate (c,d) for EGR=0-24% at mode B75.....	146
Figure 6-3 Effect of EGR on predicted PM emissions at mode B75. The PM-CAD graph is for EGR=0-80%.....	148
Figure 6-4 Effect of NG flow on pressure (a,b) and heat release rate (c,d) for NG flow=25-115% of the baseline mode B75.....	149
Figure 6-5 Effect of NG flow on predicted PM emissions for NG flow=25-115% of the baseline mode B75.....	150
Figure 6-6 Effect of EQR on pressure (a,b) and heat release rate (c,d) for EQR=0.5-0.7 at mode B75.....	151
Figure 6-7 Effect of EQR on predicted PM emissions for EQR=0.5-0.7 at mode B75.....	152
Figure 6-8 Effect of timing on pressure (a,b) and heat release rate (c,d) for CA50=7-15° ATDC at mode B75.....	153
Figure 6-9 Effect of combustion timing (CA50) on predicted PM emissions for CA50=7-15° ATDC at mode B75.....	154
Figure 6-10 Effect of GRP on pressure (a,b) and heat release rate (c,d) for GRP=22-29 MPa at mode B75.....	155

Figure 6-11 Effect of GRP on predicted PM emissions for GRP=22-29 MPa at mode B75..156	
Figure 6-12 Effect of load and speed on pressure (a,b) and heat release rate (c,d) for different modes.....	157
Figure 6-13 Effect of load and speed on PM-CAD graph.....	158
Figure 6-14 Effect of GSEP on pressure (a,b) and heat release rate (c,d) of LPI points for GSEP=1-3 ms at mode B75.....	159
Figure 6-15 Effect of GSEP on predicted PM emissions for GSEP=1-3 ms at mode B75.....	160
Figure 6-16 Effect of PSEP on pressure (a,b) and heat release rate (c,d) for PSEP=-2.1-0.9 ms at mode B75 ..	161
Figure 6-17 Effect of PSEP on predicted PM emissions for PSEP=-2.1-0.9 ms(EGR=18%, EQR=0.6) at mode B75.....	162
Figure 6-18 Effect of PSEP on rich zone development (Z_{rich}). The stars show the gas ignition points.....	163
Figure 6-19 Effect of SPC-PSEP (EGR=25%, EQR=0.7) on pressure (a,b) and heat release rate (c,d)	164
Figure 6-20 Effect of SPC-PSEP sweep on predicted PM emissions.....	165
Figure 7-1 Pulse-isolation tests results; variation of engine-out PM with NG for single and post injections	169
Figure 7-2 Engine-out methane-PM emissions for different engine parameters	172
Figure 7-3 TSM predictions of engine-out PM compared to SCRE experiments for normal HPDI sweeps and advanced injection strategies.	176
Figure 7-4 PM Size Distributions for baseline, LPI and SPC points. The open/ closed symbols are two repeats of Baseline, LPI or SPC points. The curves are the moving average of each data set.....	179

NOMENCLATURE

AHRR	Apparent heat release rate	D_{phy}	Physical nozzle diameter
A_{cyl}	Cylinder surface area	E	Internal energy
A_f	Soot formation constant	EGR	Exhaust gas recirculation
A_{F_{St}}	Stoichiometric air-fuel ratio	EQR	Global oxygen based equivalence ratio
AHRR	Apparent heat release rate	EQR_I	Local Oxygen based equivalence ratio
A_{hs}	Cylinder head surface area	EOS	The TSM model end of simulation
A_{ox}	Soot oxidation constant	f	Frequency of injection
A_p	Piston surface area	FluxM	Momentum flux
A_{pt}	Frontal surface area of the pressure transducer	FluxZ	Mixture fraction flux
B	Bore	GID	Gas ignition delay
BP	Back pressure	G_{ign}	Gas ignition point
BSFC	Brake specific fuel consumption	GIMEP	Gross-indicated mean effective pressure
CA	Crank angle	GPW	Gas pulse width
CA_c	Centroid of total heat release rate (° ATDC)	GPW1	First gas pulse width in split injections
CA50	50% of total heat release rate (° ATDC)	GPW2	Second gas pulse width in split injections
c_m	Piston speed	GSEP	Separation between first and second gas command signals
COVi	Coefficient of variation of total injected momentum per injection	GSOI	Gas start of injection, command signal
COVs	Coefficient of variation of total injected momentum per second	GSOI2	Second gas start of injection
D_c	Mach disk diameter	H	Enthalpy
DI	Direct-injection	HPDI	High-pressure direct-injection natural gas engine
D_n	Nozzle diameter	h_w	Wall heat transfer coefficient

K_r	Spread coefficient	PSOI	Pilot start of injection
L	Stroke	PT	Pressure transducer
m	Mass	P_t	Tank pressure
Ma	Mach number	Q_w	Wall heat transfer
MAP	Manifold absolute pressure	R	Ideal gas constant
M_c	Momentum rate at the corrected location (Mach disk location)	r	Radial distance from centerline
MIX	Mixture composition (mass based)	R_c	Connecting rod length to crank radius ratio
M_n	Momentum rate at the nozzle	r_c	Compression ratio
M_{pt}	Momentum rate at the surface of pressure transducer	ROI	Rate of injection (mass based)
MROI	Momentum rate of injection	r_s	Swirl ratio
N	Engine rotational speed	S	Soot mass fraction
NG	Natural gas	SCRE	Single cylinder research engine
P	Pressure	Sc_t	Turbulent Schmidt number
P_b	Back pressure (chamber pressure)	SI	Portion of total injected mass in the second injection
PID	Pilot ignition delay	SMPS	Scanning mobility particle spectrometer
P_{ign}	Pilot (diesel) ignition	SOH2	Start of AHRR of second pulse
PM	Particulate matter	SOS	The TSM model start of simulation
P_{pt}	Pressure measured by pressure transducer	S_t	Turbulent effective flame speed
PPW	Pilot pulse width	Stroke	Stroke
PSEP	Pilot separation between the end of diesel injection command and start of the first gaseous command signal	T	Temperature

TEM	Transmission electron microscope	Subscripts	
TEOM	Tapered element oscillating microbalance	a	At ambient
t_{open}	Actual injection duration	air	Averaged air zone
t	Time	b	At boundary of the jet
TPS	Thermophoretic particle sampler	cyl	Averaged cylinder zone
U	Axial velocity	f	Fuel
V	Volume	gsoi	At gas start of injection
v	Characteristic velocity	l	Species "l"
V_c	Clearance volume	ign	Ignition
V_d	Displacement volume	inj	At rail
X	Axial distance from nozzle	intake	In intake
Y	Mass fraction, also shown as [O ₂], [N ₂], [H ₂ O],[CH ₄], [CO], [CO ₂], [H ₂] as the mass fraction of each species	jet	Averaged jet zone
Z	Mixture fraction	map	Mixture fraction map
Greek letters		mix	In mixture, reacting
α	A constant	mix,i	In mixture, inert
ρ	Density	n	At nozzle
φ	Equivalence ratio	sp	Species
		sos	At model start of simulation
		w	Wall

ACKNOWLEDGEMENTS

I would first like to acknowledge the mentorship of my supervisor, Dr. Steve Rogak, for providing guidance and expert opinion on development of this project. I have great appreciation for his contributions to my work. I feel that I have become a better research engineer during the last few years. I would also like to thank my supervisory committee: Dr. Patrick Kirchen at UBC and Dr. Gordon McTaggart-Cowan at Westport Innovations Inc., for providing expert opinion and critically evaluating different parts of this project.

I have enjoyed working on this project alongside an industry partner. I would therefore like to thank all the Westport support engineers including Dr. Ning Wu, Dr. Phil Hill and Dr. Jim Huang for their support and feedback throughout the project.

In addition, I would like to thank Bob Parry, our engine technician, for all the help he has provided maintaining the SCRE. Thanks to Glenn Jolly and Sean Buxton in the instrument shop for helping troubleshoot and fix all of the electrical problems.

Many thanks to my fellow researchers on the APC project: Chris Mabson, Pooyan Kheirkhah and Bronson Patychuk. It was a pleasure working with you. In addition, I would like to thank Ramin Dastanpour for all his help with the TEM image processing. The author also would like to thank intern students working on the momentum measurement project: Yakshu Madaan, Lauriane Helard, Dmitriy Pavlov and Lee Sutton. I would like to thank graduate students in our combustion group James Montgomery, Arka Soewono, Kiego Karakama, Arminta Chicka, Jeremy Rochussen and Jeff Yeo. I would like to thank my supervisors, Dr. Boulouchos, Dr. Schneider and Dr. Wright at ETH Zürich for providing guidance during my internship in Aerothermochemistry and Combustion Systems Laboratory (LAV).

Finally, I must thank my family for their support and encouragement. They helped me to follow my dreams; I owe everything to them. Lastly, thanks to Sara for her unconditional love and support during the last few years and for providing an ear when it was needed.

1 INTRODUCTION

1.1 HPDI Introduction

In heavy-duty applications, the principal advantages of diesel-fuelled compression ignition (CI) engines are favourable fuel efficiency, power density, and reliability. Due to increasingly strict emissions standards there is a need to develop improved engines with low emissions and economic fuel consumption.

Heavy-duty vehicles are defined as vehicles of GVWR (gross vehicle weight rating) of above 8,500 lbs by EPA [3]. Heavy Duty Engines are used for numerous applications including: marine applications, railway applications, on-road applications e.g. heavy-duty trucks, off-road applications, industrial engines and aeronautic applications.

Natural gas (NG) is a leading alternative fuel which is widely available internationally and domestically in Canada. NG is usually cheaper than gasoline or diesel fuel partly due to the lower tax rate of NG fuel e.g. in British Columbia, Canada, since there is currently no federal and provincial tax on NG. Despite short-term infrastructure questions regarding the widespread adoption of natural gas, NG can potentially lead to lower air pollution due to its relatively clean combustion.

The natural gas flame temperature is lower than most hydrocarbons; NG has a lower carbon/energy ratio and a lower possibility of benzene (C_6H_6) ring formation due to no carbon-carbon molecular bonds. These characteristics of NG fuel can potentially lead to lower NO formation, CO₂ emissions and reduce the formation of carcinogenic polycyclic aromatic hydrocarbons (PAH) and solid carbon particles (soot) [4]. However, typical spark-ignition NG engines suffer from reduced efficiency and lower performance when compared to diesel engines [3]. To match diesel engine performance and efficiency while burning NG, Westport Innovations Inc. has developed a system for the high-pressure direct-injection (HPDI) of NG. A small diesel pilot injection (5-10% of the fuel energy) is used to ignite the gas jet, which burns in a non-premixed fashion similar to a conventional diesel engine [4].

The HPDI injector allows for small quantities of diesel fuel and large quantities of natural gas to be delivered at high pressure to the combustion chamber. The injectors are common-rail, hydraulically diesel actuated, and electronically controlled. The injectors can be incorporated into diesel engines with minimal or no modifications to the cylinder head. No special pistons, cams, gas mixer or port injectors are needed. HPDI injectors provide diffusion type combustion and therefore, retain the high power, torque, and efficiency of a diesel engine.

The injector (Figure 1-1) that has been used in the current research is a Westport prototype injector. The injector is a research-level dual-fuel natural gas and diesel injector. The injector is inward-opening and solenoid actuated hydraulically by diesel. Concentric needles, actuated by separate solenoids, were used to allow independent control of the diesel and natural gas timings. The injector is capable of operating with gas pressures in excess of 30 MPa. The injector hardware and drive system are similar to other injectors that have been previously tested at UBC [10].

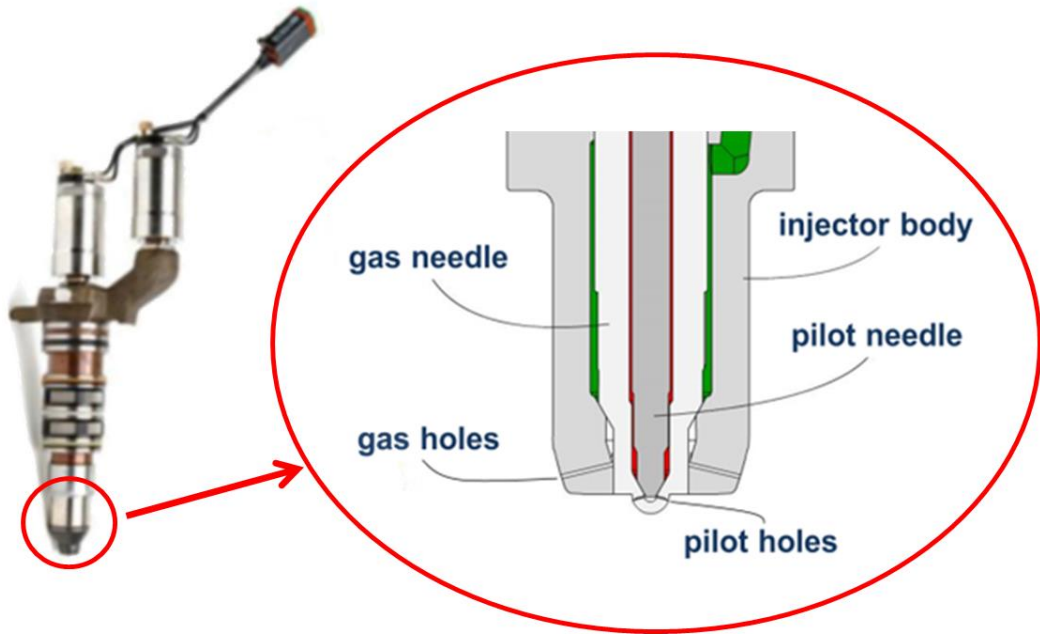


Figure 1-1 HPDI injector and inner structure, show flow passages for gas (green) and pilot fuel (red).

1.2 Motivation for PM Reduction

Particulate Matter (PM) is present in engine exhaust as solid or liquid particles. PM includes soot, adsorbed organic carbon (OC) and other aerosols such as ash particles, metallic abrasion particles, sulfates, and silicates [5]. In addition to soot (elemental or black carbon), there are organic compounds referred to as Semi-Volatile Organic Carbon (SVOC) present in the PM. SVOC are a subset of organic carbon, are mainly alkanes [6] and are present as individually-nucleated particles or as a coating on solid particles. Depending on engine operating conditions, the semi-volatile material contributes to 10-90% of the total mass of the emitted PM in diesel engines [7]. A recent study [8] of an HPDI engine showed that SVOC fraction is correlated with engine load (86%, 47% and 33% for the low, mid and high load modes respectively). Variations in parameters other than load were shown to have a minor effect on SVOC fraction. For partially premixed combustion at high loads, the SVOC fraction increased while total PM was very low compared to the normal HPDI point.

The PM emissions are well known to impact both human health and the climate [9], [10]. Carbonaceous aerosols contribute to global warming by absorbing and scattering sunlight.

Black carbon alone is estimated to have a 20-year Global Warming Potential (GWP) of 3200, and a 100-year GWP of 910 [11]. These particles absorb sunlight and directly heat the surrounding air. Aerosols can also affect cloudiness [12] and change the reflecting surfaces of snow and sea ice so that a lower fraction of solar energy will be reflected (less Albedo) with more absorption of solar heat. These effects contribute to climate changes including thinning arctic ice, permafrost and early springs in the northern hemisphere [13].

Engine exhaust has also long been known to be harmful and can produce carcinogenic and non-carcinogenic health effects. The World Health Organisation (WHO) has estimated that in 2012 around 7 million people died - one in eight of total global deaths – as a result of air pollution exposure [14]. PM contains diverse toxic materials that are assumed to be the main contributors to the negative effects of air pollution on health. Numerous experimental and epidemiological studies have noted a correlation between chronic and even acute exposure to PM pollutants and respiratory and coronary heart diseases [15]–[17]. Health effects have been the main considerations in setting engine emission standards.

The negative effect of PM on climate and human health, as mentioned above, was the main motivation for setting more strict emission standards for vehicles. Heavy-duty engine emissions standards are classified by the size and weight of the vehicles, load and power ratings, and their application. Regulations by the US Environmental Protection Agency (EPA) for heavy-duty CI engines have been in effect since 1974. Since then, PM mass (per unit of engine work) has dropped by a factor of 60, carbon monoxide (CO) by a factor of 3 and NOx by a factor of 8. The current mandatory emission standards for heavy-duty engines were phased-in over the period of 2007-2010. The regulation limits CO to 20.8 g/kW-hr, non-methane hydrocarbon (nmHC) to 0.19 g/kW-hr, NOx to 0.27 g/kW-hr and PM to 0.013 g/kW-hr [3], [5], [18]. Canadian and U.S. federal emission standards including heavy-duty diesel engines are closely aligned [19].

The European Commission has similar regulations that are currently being phased into Euro VI, which places a limit on the number of particles greater than 100nm. This addresses the growing concern of the health effects caused by these small particles. In

Europe, vehicles with a maximum laden mass of more than 3500 kg are classified as heavy-duty and are subject to the emission limits outlined in [20]. Notably, the permissible PM and NOx mass have been dramatically reduced in the most recent regulations and the particle numbers (PN) have been added to the Euro VI standard [5], [20], [21]. HPDI engines produce lower PM and NOx than equivalent diesel engines[4], [22]; however, non-premixed natural gas combustion generates soot [23] and, therefore further reduction in PM is desirable in order to meet future regulations.

Table 1-1- European emission regulations [20], [21]

	Year/Scope	CO (g/kWh)	HC (g/kWh)	NOx (g/kWh)	PM (g/kWh)	PN (1/kWh)
Euro I	1992 ≤ 85 kW	4.5	1.1	8.0	0.612	
	1992 ≥ 85 kW	4.5	1.1	8.0	0.36	
Euro II	1996	4.0	1.1	7.0	0.25	
	1998	4.0	1.1	7.0	0.15	
Euro III	1999 EEV only	1.5	0.25	2.0	0.02	
	2000	2.1	0.66	5.0	0.10	
Euro IV	2005	1.5	0.46	3.5	0.02	
Euro V	2008	1.5	0.46	2.0	0.02	
Euro VI	2013	1.5	0.13	0.40	0.01	8.1x10 ¹¹

Different aftertreatment systems are used in diesel engines to reduce the emission in the exhaust system. A diesel particulate filter (DPF) is a device designed to physically capture PM from the exhaust gas to prevent their release to the atmosphere [24]–[30]. High filtration efficiency, mechanical and thermal durability of the DPFs made them an effective technology for the control of diesel particulate emissions. DPF systems are more effective in removing the solid part of the PM, e.g. soot, rather than non-solid fractions of PM emissions. To control the non-solid fraction of PM, DPF systems are likely to include additional components, typically oxidation catalysts [24]–[26]. However, they need to be periodically cleaned (regenerated) in order to avoid undesirable backpressure in the

engine and to ensure an efficient and safe operation of the vehicle[28]–[30]. Removal of particles, i.e. filter regeneration, can be passive or active[26], [28]–[30]. For most applications passive regeneration is used. Passive regeneration is achieved by promoting oxidation in DPF primarily to carbon dioxide [24]–[26] through the use of a catalyst by promoting combustion with oxygen or combustion with nitrogen dioxide during regular vehicle operation. In the active systems, the regeneration is triggered by increasing the temperature of particulates in the DPF using an energy source (thermal regeneration). The energy can be provided by in-cylinder combustion management e.g. late cycle injections, injecting fuel in the exhaust gas or by electric heating e.g. placing an electric heater upstream of the filter substrate. The coating materials of the DPFs can promote soot oxidation at lower temperatures [28], [29].

The diesel oxidation catalyst (DOC) can promote oxidation of CO, hydrocarbon (HC), the non-solid portion of diesel particulates as well as several HC-driven emissions, such as aldehydes or PAHs, in exhaust gas by oxygen presented in diesel exhaust [24], [26], [31], [32]. DOC system can generate NO₂, if DOC used in front of a DPF in a system, nitrogen dioxide can be effectively used to facilitate the regeneration of diesel particulate filters (passive regeneration) or to enhance the performance of certain types of Selective Catalytic Reduction (SCR) catalysts. SCR has been developed to reduce diesel NOx emissions. Urea-SCR has been selected for many heavy-duty applications [24], [26], [31], [32].

Diesel particulate filters (DPF) are integrated into the exhaust aftertreatment system of the conventional HPDI engines in order to remove PM emissions. Reductions in engine-out soot by in-cylinder injection strategies will reduce the load placed on the aftertreatment system, lowering the frequency of regeneration required and increasing the DPF lifetime. In some applications, exhaust temperatures are too low for passive regeneration. Reducing engine-out PM by in-cylinder injection strategies might be an attractive solution for these cases. By reducing the particulate load on the DPFs, the lifetime of the filters will be improved, adding more reliability and a longer warranty period to the DPFs. Major reduction in PM could enable removal of the DPF from exhaust for some applications. Removing DPF from the exhaust system by lowering the engine-out PM using advanced injection strategies is appealing for the manufacturers and customers.

1.3 Combustion and PM Formation in Direct-Injection Engines

Figure 1-2 shows a typical soot particle produced by the HPDI research engine used in this work, for mid-speed and high load (mode “B75”) captured by a Transmission Electron Microscope (TEM). As shown, the aggregate is composed of chains or clumps of small primary particles or smaller aggregates.

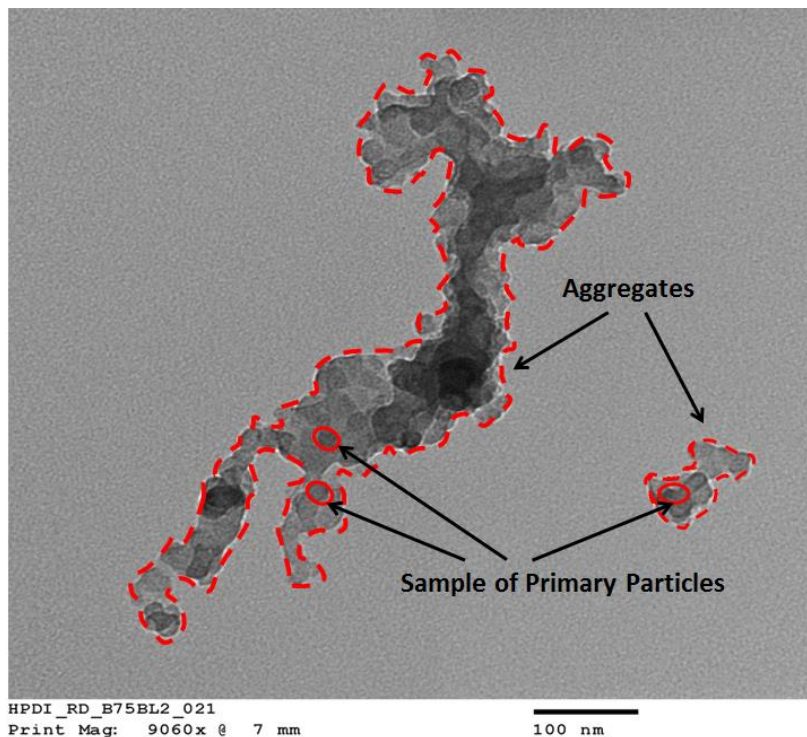


Figure 1-2 Representative engine-out particle from HPDI engine (mode B75 baseline); TEM image.

This section provides a summary of soot formation kinetics described in more detail in references [33]–[38]. A well-known proposed mechanism of PM formation and oxidation inside cylinder suggests six identified processes: pyrolysis, nucleation, coalescence, surface growth, agglomeration, and oxidation. The formation and growth processes, all processes except oxidation, are shown in Figure 1-3. Fuel pyrolysis results in the production of precursors or building blocks for soot with the aid of increased temperatures without significant oxidation even though oxygen species may be present [33]. The precursors are

formed in fuel rich regions of the combustion chamber at elevated temperatures. Because soot formation is so sensitive to local equivalence ratio (EQR_l) and temperature (T), the process is often represented on a φ - T map [39], [40], (discussed later in section 3.7). The major species are acetylene (C_2H_2), propyne (C_3H_4), propene (C_3H_6), and butadiene (C_4H_6) in the formation of soot. Decomposition of these species leads to the production of Polycyclic Aromatic Hydrocarbons (PAH) and growth of soot particles [41].

Nucleation or soot particle inception is the formation of particles from gas-phase reactants. The first particles or nuclei are in the order of 1-2 nm and while being very small in size, serve as the inception point for larger particles to form. Surface growth is the process of adding mass to the surface of a nucleated soot particle. There is no clear distinction between the end of nucleation and the beginning of surface growth. Surface growth is strongly dependant on local temperature, oxygen concentration and the number of reactive sites available. Particle collisions result in the formation of larger particles through coagulation. Coagulation of non-coalescing particles (agglomeration) results in fractal-like soot structures.

Oxidation can take place at any time during the soot formation process from pyrolysis through agglomeration. The most active oxidation species depends on the process and state of the mixture at the time. In diesel engines, the exhausted soot concentration can be orders of magnitude lower than the maximum soot concentration measured during combustion, due to oxidation.

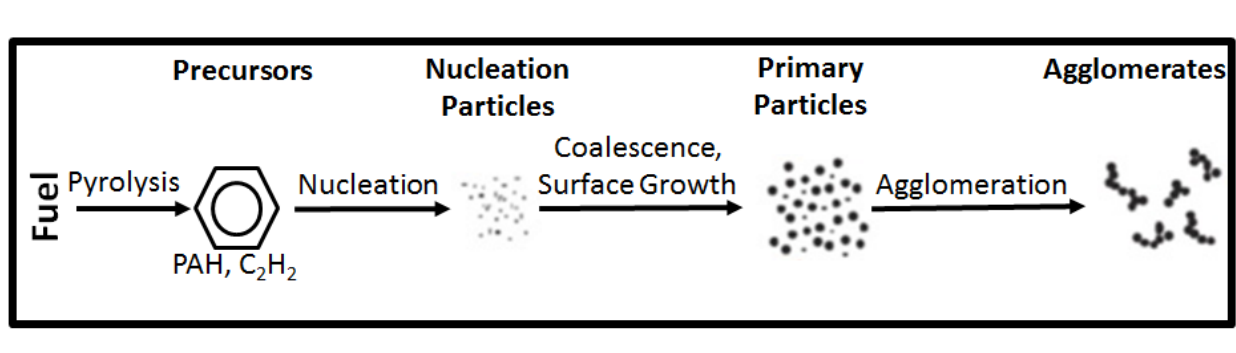


Figure 1-3 Schematic diagram of soot formation process (adapted from [33])

Dec [22] described the soot formation and features of a quasi-steady diesel fuel jet, as shown in Figure 1-4. It should be noted that the original conceptual model applies to conventional diesel conditions for a single injection and assuming free jet with no wall impingement. Also the conceptual model presents a typically long injection with ignition before end of injection (EOI) so that much of the fuel burns during mixing-controlled combustion. After injection, spray penetrates into combustion chamber in a roughly conical jet with entrainment of ambient gas. The thermal energy of entrained hot in-cylinder gases vaporizes the liquid fuel and downstream of the nozzle at some distance the fuel enters the vapor phase. Two stage ignition commences when temperature and charge at some locations in the jet are ready to ignite. The first stage of ignition is weak followed by a highly exothermic second stage of ignition, leading to the “premixed burn” phase of diesel combustion [42], [43]. Polycyclic aromatic hydrocarbon (PAH) and soot-precursor species quickly form in the hot and rich combustion products of the premixed burn ($2 < \text{local equivalence ratio (EQR}_l \text{)} < 5$). A diffusion flame forms on the periphery of the jet in the premixed burn stage of the combustion. Additional soot continues to form in the hot fuel-rich core of the diesel jet after forming a diffusion flame. As the jet enters the “quasi-steady” period, particles continue to form and they move down the turbulent fuel jet toward the head vortex. OH radical attack is known as the primary method of soot oxidation. The main oxidation of the soot aggregates occurs around the periphery of the spray plume and within the flame surface, where the particles oxidized by OH radical and oxygen attack.

Although the conceptual model presented here was very helpful in the understanding of soot formation in direct-injection diesel engines, the actual soot formation process is much more complicated and the physics of soot formation/oxidation in direct-injection engines remains an important research area. The effect of neighboring walls (e.g. cylinder head), impingement, small pulses (where the “quasi-steady” flame is not fully established), compression/expansion and entrainment of the combustion products into the jet are not discussed in details in this conceptual model.

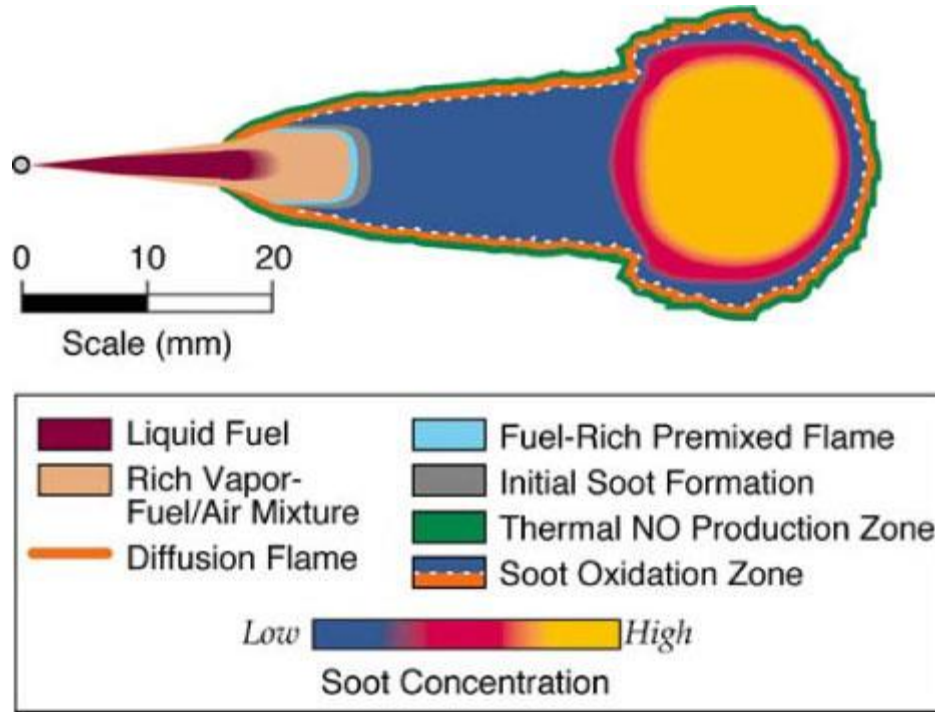


Figure 1-4 Dec's model of combustion and soot formation in diesel jets [42]. Reprinted with permission from SAE paper 970873 Copyright © 1997 SAE International. Further use, copying, sharing or distribution is not permitted without prior written permission from SAE.

There is no conceptual model for HPDI engines in the literature. However, a brief description of gas jet development and combustion process will be introduced here based on previous CFD simulation of HPDI engines in high load, medium speed based on GOLD CFD package. In typical HPDI operation, pilot fuel (diesel) is injected first. The spray and combustion process of the pilot injection is similar to the conceptual model described by the Dec's model; although the lower injection pressure and short pulse will cause the process to deviate from the conceptual model since diffusion flame combustion is not as significant as long pulses with higher injection pressures. For conventional HPDI points at high loads, approximately at the start of combustion of diesel, gas is injected. A gas jet will be quickly formed and penetrate into the cylinder charge. The gas jet will reach the hot zones of diesel ignition products. The gas jet at some locations around the periphery of the jet starts to ignite and the ignition will quickly propagate around the edges of the jet and the diffusion flame will be established. The jet will impinge on the piston surface and move toward the bowl and squish zones of the cylinder. For high loads where the injection is long

enough the mixing controlled combustion lasts even after wall impingement. By the time of the end of injection (EOI), the local EQR in the cylinder decreases quickly in few crank angles after EOI. By more mixing later in the cycle, combustion products will take the major zones of cylinder and the charge will be close to homogeneous.

1.4 Injection Strategies in DI Engines

In direct-injection (DI) engines, the fuel-air mixing process and the injection strategy have a strong effect on combustion and emissions. In-cylinder injection strategies can improve mixing processes, leading to lower engine-out emissions.

Many injection strategies have been described in the literature; including electronic injections, multiple pulsed injections, high injection pressures, slightly premixed combustion and variable fuel rate shape. The injection strategies might be coupled with other engine strategies like advanced exhaust gas recirculation (EGR), variable valve actuation and variable geometry turbochargers.

In early HPDI engines, the effect of a number of diesel and gas holes and their alignment was studied [44]. The engine was found to be unstable in some conditions due to the diesel needle rotating with respect to the gas nozzle. The rotation means that the interlace angle (the circumferential angle between NG and diesel nozzles) changes during operation. It was also found that emissions fluctuate for injectors with equal numbers of gas and diesel holes (6 diesel and 6 NG nozzles), in some conditions. Stability was improved using a number of gas holes different from the number of pilot holes (6 diesel and 7 NG nozzles). The explanation for this was that the diesel needle could rotate within the gas needle, changing the gas-diesel “interlace angle”. With different numbers of gas and diesel holes, there is always a gas-diesel pair closely aligned. A more recent study showed that an equal number of NG and pilot nozzles is not causing combustion instabilities in ISX400 HPDI engines. An injector with 7 NG and pilot nozzles with fixed interlace angle (no rotation of nozzles) was used for the ISX400 HPDI engine with no instability issues [45].

The effect of NG injection pressure on engine performance and engine-out emissions was studied before [46], [47]; by changing NG injection pressure from 18MPa to 30MPa at different operating conditions while all other parameters were held constant. At high loads, higher injection pressures substantially reduced PM, with small increases in NOx. At low loads, injection pressure had no significant impact on either emissions or performance. With very high NG injection pressure [48] significant efficiency improvement and particulate matter reductions can be achieved at high loads. Increases in combustion noise, peak pressure raise rate and higher NOx emission are the drawbacks of higher pressures.

The impact of cooled EGR on HPDI engine performance and gaseous emissions was carried out [49]. The results indicated that the NOx emissions were reduced by 80% of their non-EGR levels by the expense of higher CO and hydrocarbon emissions. PM also increases in conventional HPDI points by increasing EGR [47], [50]. PM increase almost linearly ($R^2=87\%$) by a factor of 10 for EGR change from 0-30% ($[O_2]_{intake}=23-18\%$) in medium speed high load (mode B75) in HPDI engines [8], [51]. Higher EGR (up to >50%) was used in the HPDI engine for parameter sweeps study before[50]. However, in normal HPDI conditions, the EGR would not be set above 30%. A parametric study [8], [51] on an HPDI engine showed that higher EQR (global equivalence ratio calculated from both NG and pilot together) and EGR have the greatest effect on increase in engine-out PM. The mean particles size and number concentrations are most affected by EGR and EQR.

In diesel engines, both peak in-cylinder soot formation and oxidation rates decrease with increasing EGR [52]. At moderate EGR levels (roughly $[O_2]_{intake}=21-10\%$), soot oxidation decreases more rapidly than soot formation, so that exhaust soot emissions are greater than for non-EGR conditions [52]–[54]. At very high EGR level, however, exhaust soot emissions eventually begin to decrease [52]–[54]. The reduction in exhaust soot emissions at high EGR rates is believed to be due to little soot formation during the residence time available [53]. More premixing of the charge due to longer ignition delay in high EGR cases has a major effect on engine-out PM reduction.

A fuel injector prototype for heavy-duty engines was developed [55], [56] to use small amounts of entrained diesel as an ignition promoter in the gas jet. This “co-injector”

simplified the injector construction (only one needle needed) and effectively delayed the gas ignition but resulted in some combustion instabilities and knocking under some operating conditions.

1.4.1 Late Post Injection (LPI) in Diesel Engines

Before discussing LPI, it is helpful to define terminology that will be used throughout this thesis, which is consistent with reference [57]. *Multiple Injection* indicates that fuel is split into two or more portions that are normally of unequal size. A *Split Injection* is a particular case with two injection pulses. *Post injection* refers to a split injection with short injection after a longer main injection. The second pulse usually has less than 20% of the fuel. A *Close-coupled Post Injection* refers to a post injection case where the second injection occurs shortly after the main injection, such that combustion phasing for the second injection is still favourable for thermodynamic efficiency. The threshold for characterizing a post- injection schedule as close-coupled is not well defined [57], but dwells of at most a few crank angle degrees are typical. Finally, *Late post injection (LPI)* refers to post injections where the second short pulse is injected long after the first pulse. As mentioned above, the threshold for defining LPI is not clear in the literature, but discussed later in the thesis.

A post injection can reduce engine-out soot. Post injection was studied in diesel engines [57]–[72]. In particular, post injection can help reduce soot emissions on diesel engines [59], [60], [63]. Close-coupled post injections offer less PM reduction but reduce the fuel consumption penalty [59]. For some experiments post injections with the second pulse immediately injected after the main pulse showed even better fuel efficiency [67], [73] at some modes possibly due to enhancing the air entrainment by the post-injection spray, which increased the combustion rate of the last fractions of fuel in the second pulse in comparison with the case of single long injection [73]. Previous papers have discussed the mechanisms of engine-out PM reduction from close-coupled post injections [57], [63]. There is little consensus within the literature on why close-coupled post injections work, but three main explanations were offered [57]. First, enhanced mixing due to the second

injection could reduce rich burning zones. Second, increasing the local temperature within high PM areas of the cylinder could increase oxidation of soot. Finally, injection duration can be an important parameter on PM formation. This has been seen from the non-linear decrease in engine-out soot when shortening the main injection. A concept related to injection duration effects, is “fuel-replenishment” [61]. Based on computer modeling, it was concluded that as the injection duration increased, more fuel was delivered to the head region creating a larger fuel-rich mixture that supported more soot formation. The “split-flame” concept [60], [62] is based on a distinct “combustion event” for each pulse in a post injection strategy; it was assumed that the fuel from the main injection and the post injection burned separately without interaction. It was shown that the PM from the second injection does not interact with the PM from the main injection and the level of PM in the small second injection is very low; therefore, the level of engine-out PM remains the same as the main injection. The definition of interaction was introduced in the form of a “combustion event”; however, the second pulse can interact with the first pulse by other means as well, such as entrainment of the first pulse by adding turbulence or between different stages of PM formation, e.g. pyrolysis of second pulse and agglomeration of the first pulse. These types of interactions were not discussed in the split flame concept. In the current thesis, interaction between two pulses in a post injection will be studied for two CFD cases based on spatial distribution of PM at different timings.

Late post injection [59] was shown to reduce smoke by up to 60% at the expense of increased fuel consumption by 7% compared to a baseline single injection. LPI has been studied very little due to the large fuel consumption penalty, but the mechanisms of PM reduction were discussed in earlier studies on diesel engines [59], [60], [62]. For strategies with a long separation between injections, the “split flame” concept, as discussed was introduced in the literature [60], [62].

The injection strategies that have been successfully applied to DI diesel engines are not necessarily useful in HPDI natural gas engines. Even if the concept of the injection strategy might be applicable, the trend in response to the engine parameters might be completely different. A study [74] on DI natural gas engine evaluated the potential of using a late gas injection to increase power from a DI natural gas engine using a partially-premixed

combustion strategy. However, one of the main drawbacks of this technique was a substantial increase in PM emissions, attributed to the late injection substantially increasing PM formation. There is no published research on the use of LPI strategies to reduce emissions from direct injection natural gas engines before the current study.

For any direct-injection engine, understanding the performance of the injector is important in interpreting the combustion event and subsequent emissions. For the LPI strategy, investigating the injector performance for small post injections is critical. In almost all post injection strategy studies, deliberate investigation of the injector performance is undertaken e.g. [59]. The injector performance influences turbulence intensity in the combustion chamber, and thus mixing of the gaseous jet with air and subsequent combustion processes. As such, detailed injector testing can provide valuable information to aid engine developers in the production of higher-performance engines, which feature improved emission.

1.4.2 *Partially Premixed Combustion*

1.4.2.1 *Partially Premixed Low-Temperature Diesel Combustion*

In order to reduce particulate matter (PM) and nitrogen oxides (NOx) emissions, low-temperature combustion (LTC) was introduced recently, with variations such as homogeneous charge compression ignition (HCCI) [75], late injection with exhaust-gas recirculation (EGR) and high swirl (MK combustion) [76], and early injection with EGR [77], [78]. Premixing in the current thesis is defined as the lean mixture at the time of ignition. In all LTC strategies premixing is higher and the combustion temperatures are reduced, which further slows NOx formation kinetics. Soot formation rates are also slowed by reducing combustion temperatures [79], [80] while soot oxidation rates decrease even more than formation rates [52], [81]. More EGR is widely used in LTC combustion which decreases the inlet oxygen concentration to 10-19% [40]. By increasing EGR, net PM emission (at the end of formation and oxidation process) increases initially; however, at higher EGR soot formation can become so low that PM emissions decrease even with reduced oxidation. At extreme EGR levels, combustion efficiency is low: unburned

hydrocarbons (UHC) and carbon monoxide (CO) emissions are typically high [43]. PM formation rates are also reduced by the greater premixing that occurs in most of the LTC strategies.

Low-temperature combustion (LTC) in diesel engines can be divided into two categories [40]: those in which the combustion phasing is largely decoupled from injection timing, and those in which the control of the combustion phasing is closely coupled to the fuel injection event. The first category is typically called Homogeneous charge compression ignition (HCCI). These systems are achieved by either pre-mixing to very lean equivalence ratios (EQR <0.5) or by employing extensive EGR. HCCI strategies typically employ long in-cylinder mixing times prior to combustion, often with minimal use of EGR, especially at low-load [43]. Ignition timing is kinetically controlled, and is therefore decoupled from the timing of the fuel injection event.

The second category [40], [43], [82]–[86] is typically called “partially premixed compression ignition” (PPCI) where the charge distributions for PPCI are more heterogeneous at ignition timing than HCCI, and include not only fuel-lean but also fuel-rich mixtures [43]. For conventional diesel conditions, ignition usually occurs before the end of injection; therefore, only a portion of the injected fuel is premixed prior to initiation of combustion. For PPCI strategies, ignition usually occurs shortly after the end of injection, which provides time for some degree of premixing for injected fuel, including fuel from the very end of injection [43]. These systems typically use a low compression ratio, large amounts of cooled EGR or the use of retarded injection timing.

Although LTC can reduce PM and NOx in diesel engines, this strategy still faces challenges including load range limitations, transient and cold-start performance, and increased emissions of CO and unburned hydrocarbons (UHC)[84]. Unburned hydrocarbon emissions using LTC is an ongoing problem and this strategy was investigated in diesel engine studies [83], [85]. According to the experimental results, for the cases where ignition happens close to the end of injection UHC emissions increase due to over-mixing close to the injector at EOI. The majority of UHC emissions from LTC with ignition at EOI arise from incomplete combustion of lean mixtures formed near the injector after EOI [85]. Long ignition delays

can also lead to higher pressure rise rates and noise at high fuelling rates. Combustion noise, associated with a rapid rise of the in-cylinder pressure, can also impose constraints on the required dilution or injection timing, driving further increases in CO and UHC [43].

Typical diesel fuel is a mixture of thousands of chemical species, including single- and multiple-ring aromatics, olefins, and branched- and straight-chain alkanes. The detailed chemical kinetics of ignition for such mixtures under diesel conditions is quite complex. The characteristics of ignition and heat release for LTC conditions are distinctly different from those for conventional diesel combustion [43]. Because of lower temperature combustion, the reactions proceed at slower rate than for conventional diesel combustion. For conventional diesel combustion, the apparent heat release rate (AHRR) can be divided into three parts: ignition delay, premixed burn, and mixing-controlled combustion. For the PPCI condition the premixed burn is more significant (leading to significantly greater levels of combustion noise) with relatively minor mixing-controlled combustion heat release.

A simulation study [43] using the Senkin module of Chemkin to model the PPCI combustion, in a perfectly stirred reactor (PSR) showed that that ignition occurs in two distinct stages for lower oxygen concentration and low initial temperature. The first stage a larger temperature rise. Compared to conventional diesel combustion, PPCI combustion has a slower transition between phases due to lower ambient temperature, leaner mixture and higher dilution level.

In diesel engines, the ignition delay is tightly related to cylinder temperature and pressure. A diesel engine study [82] controlled ignition delay in the engine by adjusting the intake air temperature while keeping the same charge density at TDC. This permitted the study of sooting characteristics at various ignition delays while keeping the same diesel jet penetration. A conceptual image for PM reduction was introduced in their study, illustrated in Figure 1-5, which discusses the correlation between in-cylinder soot distribution and the relative timing of the AHRR peak and End of Injection (EOI). In this figure the color intensity is the representative of the PM concentration. The structure of sooty regions is strongly affected by the ignition delay. The line and borders are the conceptual boundaries of the jet. Since the mixing is different between two cases in this figure, the jet boundaries

should be affected too, however, this effect is not represented in Figure 1-5. The concept was meant to be independent of the specific engine specification. The conceptual figure discusses two main ideas. First, the importance of relative timing between EOI (where the local EQR in cylinder are abruptly reduced) and peak AHRR (roughly the PM formation time) was emphasized. Soot mass in the cylinder starts to be significant enough to be captured optically in the experiment's few crank angles after the ignition, which is roughly the peak premixed AHRR [82]. The second idea of this conceptual figure discusses the soot distributions in the jet for normal and PPCI combustion. This concept divides the soot formation process into two categories.

- Peak AHRR before EOI: starting from peak AHRR, soot forms downstream of the jet in the core of the jet. During EOI ramp-down, the soot formation propagates upstream into the near-injector region. Soot will rapidly oxidize upstream of the jet due to the formation of a lean mixture after EOI. The soot will remain at the head of the jet at the bowl wall and oxidizes slowly.
- Peak AHRR after EOI: Due to a longer ignition delay, the temperature is too low (no ignition yet) for soot formation even after EOI. Starting at AHRR peak, soot will form in the side of the jet head in the jet-jet interaction zones. Since the rich zones generations are mainly prevented in the core of the jet and near the injectors, PM concentrations are much lower for this case. The soot is formed far from the bowl wall. The soot level is significantly lower than that of the "peak AHRR before EOI" case.

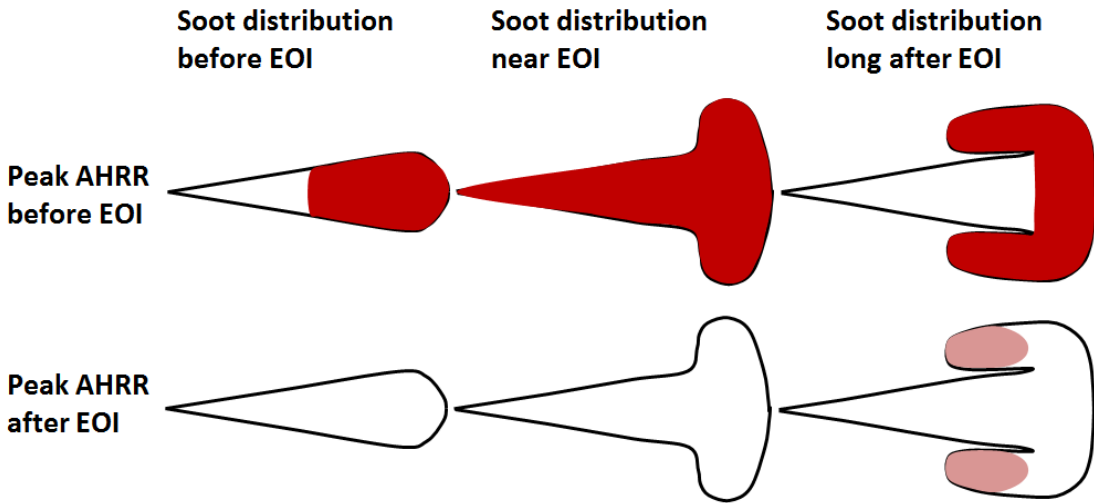


Figure 1-5 Conceptual PM reduction model by premixing (adapted from Ref. [82])

1.4.2.2 Slightly Premixed HPDI Combustion (SPC)

The methods of premixing in HPDI engines are different from those in diesel engines. In HPDI engines, ignition timing is controlled by the diesel injection timing. Adjusting relative timing between diesel and natural gas allows more premixing of the natural gas prior to ignition. This injection strategy is called slightly premixed combustion (SPC) [47], [50], [87], since it is neither fully premixed nor mixing-controlled. The commanded injection timings for HPDI engines are shown in Figure 2-2. Pilot Separation (PSEP) (or Relative Injection Timing (RIT)) will be reduced to reach SPC conditions. The prior literature does not define the RIT threshold for SPC, but instead applies the term to any RIT substantially lower than the baseline value. The charge distribution at ignition, for PPCI in diesel engines, is heterogeneous [87]. More details on charge distribution will be discussed in section 5.3.5. However, PPCI in diesel engines is achieved by slow combustion phasing due to lower ambient temperature and oxygen concentration. Therefore the chemical kinetics of ignition and mixing are tightly coupled. Since SPC, EGR and combustion phasing are close to conventional HPDI values, ambient temperature and oxygen concentration remain almost the same as conventional HPDI combustion ($[O_2]_{intake}=23\text{-}18\%$). Thus the pilot and NG ignition kinetics are essentially unaltered in SPC. By injecting the pilot later, the gas has

more time for premixing before ignition. After gas ignition, the premixed combustion is more significant in SPC than in conventional HPDI.

In the diesel combustion experiments resulting in the conceptual graph of Figure 1-5, more premixing was achieved by lowering the ambient temperature for the jet in the combustion process by adjusting the intake temperature. Similar to PPCI, these experiments also changed the transition of the ignition chemical kinetics. Therefore the combustion and PM formations are different from SPC injection strategy. The results of the conceptual graph will be compared to SPC results in two terms: if the relative timing of EOI and peak AHRR is important for SPC injection strategy too and if the PM contours in the jet is similar to the conceptual graph.

The effect of different parameters, including relative timing of natural gas and pilot, was studied previously [47], [50]. Limited premixing results in a more rapid and more intense combustion event that reduces PM at the expense of higher NOx and hydrocarbon emissions, while the indicated fuel consumption was slightly reduced for a given EGR fraction. A high level interaction between relative timing of gas and pilot was noticed in the experiments. Combining SPC with increased EGR [87] can keep NOx emissions at their baseline levels while still reducing PM significantly. This elevated EGR point still has high total hydrocarbon (tHC) emissions. In an HPDI engine, tHC emissions are dominated by methane. CFD has been used to help to understand the mechanism of PM reduction by SPC. CFD results demonstrated that initiating the gas injection before the diesel pilot reduces the local equivalence ratio in the reaction zone without significantly influencing the temperature.

Methane is difficult to catalytically oxidize in a lean burn environment with low exhaust temperatures [88], [89]. A typical diesel oxidation catalyst (DOC) is not able to treat high methane emissions occurring at low loads in HPDI engines [8]. A fast light-off temperature

(FLT) technique can be helpful to maintain a high exhaust temperature suitable to CH₄ oxidation [88], [90]. In SPC cases of the HPDI engine, EGR increase is not significant to affect late-cycle temperatures especially after mixing the charge later in the cycle.

As mentioned earlier, premixing in the current thesis is defined as the lean mixture at the time of ignition. By this definition, moving toward negative PSEP (or RIT) means more premixing. This will be discussed in more detail in the CFD results of Chapter 5 and the TSM results of Chapter 6.

1.5 Phenomenological Modeling for DI Engines

Improvement of direct-injection (DI) engines has been aided by modelling of jet mixing, penetration and combustion processes. Different types of models have been used. Thermodynamic models, e.g. [91]–[95], consider the entire combustion chamber as a single, homogeneously mixed zone. These models are based on the first law of thermodynamics and mass balances; momentum conservation is not considered and the spatial distribution of composition is neglected. Thermodynamic models are very fast, in the order of few seconds, but do not simulate important in-cylinder phenomena. These models have been used for rough estimation of heat transfer and heat release rates in the engines, especially for homogeneous charge engines rather than DI engines. In contrast, three dimensional CFD simulations, e.g. [96]–[99], are based on the locally-resolved equations for mass, energy and momentum that include detailed physics for spray and combustion phenomena. CFD is computationally expensive which makes it difficult for parametric studies in engine simulation. The complexity of CFD simulation delays the understanding of the link between CFD results and boundary condition of the jet (injection pressure, air density, etc.). Phenomenological engine modeling divides the combustion chamber into multiple zones which are characterized by different temperatures and compositions. The phenomenological model can potentially capture engine pressure, heat

release rates and the injection process based on boundary conditions of the injection. These models are normally fast, in the order of few minutes.

Various phenomenological models are described in the literature for direct-injection engines. The phenomenological model for combustion can be predictive or non-predictive, in terms of simulation of combustion and in-cylinder pressure calculations. Non-predictive combustion models simply calculate the pressure assuming a specific or a correlation for burning rate from the literature or by importing that from an equivalent experimental point. These models are used in investigations where the goal is to study a variable which has little effect on the burning rate. Examples of non-predictive combustion models are the Wiebe model [57] or Chmela and Orthaber's [58]. Arsie et al. [59] developed a non-predictive combustion model for modeling of in-cylinder pressure and soot in DI diesel engines. The model showed good agreement in prediction of AHRR and PM engine-out for two sets of sweeps; however, the model was heavily tuned for both combustion and engine-out PM simulation.

A predictive combustion model calculates the in-cylinder pressure based on some physical sub-models to estimate the burning rate. The predictive models can be used widely in all parametric studies; however, the predictive models typically require more tuning factors in order to provide meaningful results. An example of a predictive model for DI engines is the theory of undisturbed turbulent gas jets as proposed by Abramovich [100] also referenced as the "Cummins engine model" in literature [101], [102]. Another predictive model developed for diesel engines is the "packet model" that was originally proposed by Hiroyasu et al. [103] and later applied and extended by several other authors, e.g. [104]–[109]. The model is described by many discrete "packets". Each packet is tracked from the nozzle and experiences different sub-processes in diesel injection such as fuel atomization and evaporation, fuel-air mixing, ignition, combustion and pollutant formation. The model is also referred to as the DIJet model in GT-Power.

In the Hiroyasu packet model [103], [110] predictions were compared to the data for engine speed, injection timings and swirl ratios sweeps. Predicted pressure diagram, NO and soot emissions showed acceptable quantitative agreement with the data. However, the

total number of packets in the spray can easily reach about 1000 [111], which may cause significant computing costs. To diminish this problem Stiesch and Merker [109] suggested combining spray packets that have similar temperatures. Several papers developed similar phenomenological models. Payri et al. [112] developed a phenomenological model for combustion in direct-injection diesel engines. This model is based on the analysis of the fuel evolution from the injection start until the combustion end. The model has been only used for investigating the influence of the fuel vaporization and air entrainment on the maximum pressure rise and peak pressure. Hountalas et al. [107] developed a phenomenological model for modeling the effect of fuel rate shape on in-cylinder pressure and emissions. This model showed good agreement with experiments for prediction of pressure and AHRR for injection timing sweep; however, the model could not successfully predict the effect of injection timing on engine-out PM. Another phenomenological multi-zone model for prediction of heat release and exhaust emissions in DI Diesel engines was developed [109]. Similarly, this model showed good agreement in prediction of in-cylinder pressure and AHRR; however, prediction of engine-out PM for two case studies that was considered was not close to the experimental measurements. In other work, a multi-zone phenomenological model [105] was employed to study the effect of intake air oxygen concentration on soot and NOx emissions and was compared with one experimental point for AHRR comparison. The model showed the trend in PM changes by changing intake air oxygen concentration. Later Gao and Schreiber [106] used the model to study the effect of EGR and multiple injections on engine-out PM. The results show higher PM for both sweeps; however, the results were not verified with any experiments. Bazari [104] applied the packet model for a parametric study in a DI diesel engine at different load and speeds. The model showed good prediction of AHRR with partial success in prediction of engine speed effect on engine-out PM. However, the effect of load was not well-predicted. Kouremenos [108] developed a multi-zone model for prediction of AHRR, NOx and soot in DI diesel engines similar to the packet model. The model showed good agreement in prediction of the effect of load on AHRR and engine-out PM.

These models had acceptable prediction of pressure and heat release rate, but no consistent results in prediction of any engine emissions. The models were compared with

limited experimental sweeps, and it is not clear if the same model in different studies used the same tuning parameters or not. Although the packet model is used in the academic world for prediction of emissions, it could not be an accepted method in industrial applications and use of the phenomenological models still are limited to simulation of the flow and waves outside of the cylinder.

A lagrangian reacting jet model [113] was applied to n-heptane fuel jets to understand soot formation in diesel engine operating conditions. The model is based on the two-stage Lagrangian (TSL) reacting-jet model of Broadwell and Lutz [114]. The model uses a detailed chemical kinetics in a diffusion-flame reactor and homogeneous core reactor with jet entrainment rates determined by empirical correlations. The model suggests that the equivalence ratio-temperature region of soot precursor formation depends upon parameters such as ambient oxygen concentration, injection pressure, nozzle orifice size, and flame lift-off [113].

For almost all of the phenomenological models, the Hiroyasu soot model is used either as a mean value calculation [115] or for tracking soot in each packet [103]. These models can use predictive or non-predictive combustion models e.g. [115]. The Hiroyasu model is based on two equations for soot formation and oxidation (equations 3-26 and 3-27 in Chapter 3). These equations can be used as mean value calculations or as a source/sink term in a transport equation for soot prediction locally. The formation equation uses fuel as the precursor species. Different forms of the oxidation equation have been used in the literature; original Hiroyasu oxidation model [103] and oxidation rate of Nagle and Strickland-Constable (NSC) [116] (applied in engine simulations before e.g. [61]).

A newer class of model for sprays is based on a one-dimensional (1D) numerical solver in the axis of the jet. By including the necessary physics to simulate the jet, this model enables a straightforward identification of the influence of boundary parameters on the results. An analytical study [117] became an initial step in developing many one-dimensional (1D) models. This analytical model has successfully predicted the penetration of sprays.. Pastor et al. have developed a 1D model to determine the mixture fraction distribution for transient jets during injection[118]. This model is based on setting the injection and

ambient conditions for the jet flow and tracking a conserved scalar in the jet zone, using a 1D axial solver. The distribution of the mixture fraction was calculated based on an assumed radial profile of the jet and spread angle. Musculus and Kattke [119] used a 1D model to predict the entrainment wave after the end of injection (EOI) [119]. The results of the 1D model were later compared with those of a 2D CFD model [120]. The prediction was qualitatively correct but the magnitude of the entrainment wave was different from CFD and experimental data. The peak entrainment predicted by the 1D model was about 70% higher than the 2D CFD model. Later, the model was extended to predict the effect of fuel rate shape on penetration [121]. Variable local spray angle by adjusting the parameters from experimental data is suggested in literature to provide better transient prediction of the spray. Desantes further developed the 1D model of Pastor et al. [122] to predict spray flames under constant environment conditions [122], assuming thermodynamic equilibrium to find local temperature. The penetration increase due to ignition and steady centerline temperature of the jet agreed well with experimental results.

The literature mentioned above applies to DI diesel engines. The only reported phenomenological model for the HPDI was a non-predictive multi-zone thermodynamic method developed to determine combustion rate and NO formation from measured cylinder pressures [124]. This model was adapted from a model for a two-stroke diesel engine [123]. No prior predictive phenomenological model was found in the literature to address the physics of HPDI injection and PM formation.

1.6 Thesis Objectives

The overall objective of this study is to identify injection strategies, which can help to reduce engine-out PM in HPDI engines and study the effect of the injection strategy on other emissions and engine performance (fuel economy, cycle-cycle variability, combustion stability and noise). From the literature, two injection strategies, post injection of gas and Slightly Premixed Combustion (SPC) were selected for further investigation. The effect of these strategies on PM is studied in engine experiments and with the Westport CFD package (GOLD).

Regarding post injection, the following questions are addressed:

- Can a late injection of gas reduce PM in HPDI engines? What are the side effects of this strategy in terms of other emissions and engine performance, particularly on fuel economy?
- Is a close-coupled or late post injection preferable for the HPDI engine?
- How does the performance of the post injection change for a broad range of load and speed in terms of emissions and engine performance?
- How does GOLD predict heat release rate and PM reduction of post injection? What physical processes contribute to low PM of post injections in HPDI engines?

There are a number of open questions related to the SPC strategy for HPDI engines:

- How can we improve the SPC strategy to control PM, NOx and methane together?
- What is the effect of EGR, EQR and pilot mass on SPC strategy on heat release rate, emissions and engine performance?
- What are the defining characteristics of SPC in terms of ignition and injection timing?
- What are the conceptual similarities and differences between premixing strategies for diesel engines and SPC in HPDI engines?
- Can the GOLD CFD model predict heat release rate and PM reduction from SPC with accuracy comparable to its predictions for conventional HPDI combustion?
- What physical processes contribute to low PM of SPC in HPDI engines?

For both LPI and SPC tests, PM morphology and size distribution is studied using Transmission Electron Microscope (TEM) images and scanning mobility particle sizer (SMPS) sampling for both injection strategies. The objective is to compare the PM aggregates, primary particles and number concentration with the baseline (normal HPDI).

One of the objectives of this thesis is to develop a predictive phenomenological model considering simplified physics of the HPDI combustion and soot formation. The model is validated with experiments in literature, CFD and engine tests.

- What are the strengths and limitations of the new phenomenological model? In particular, can this model predict the trends in engine-out PM increase/decrease for wide range of parameters sweeps and for new injection strategies keeping the tuning parameters constant for all the sweeps?
- How is the model performance compared to phenomenological models developed for diesel engines?

Through the experimental and modelling work, an additional goal of this thesis has been to highlight the qualitative similarities and inconsistencies between diesel and HPDI engines in terms of performance of post injection and SPC.

1.7 Thesis Structure

This thesis studies the mechanisms of PM reductions from HPDI engines for injection strategies that have been found useful in the PM reduction during the preliminary studies. Chapters 2 and 3 review the experimental and numerical methods, respectively, used in the investigation.

In Chapter 4, Late Post Injection is studied, first by varying the separation between injections (GSEP) and the portion of fuel in the second injection (SI) at a high-PM mode (medium-speed high-load). The best values of GSEP and SI (referred to later as the “optimized” LPI injection parameters) were selected for further studies of performance and emissions for speed and load combinations. “Pulse isolation” experiments have also been performed to help understand the mechanism of PM reduction in HPDI engines. Multi-injector tests have been performed to show the effectiveness of the LPI injection strategy using other injectors (same injector model). Selected experimental cases were simulated using the in-house CFD package of Westport Innovations Inc. (GOLD). The GOLD results are compared to experimental results. Additionally, the CFD simulations provide more details about combustion events and PM formation zones. In this chapter, interaction is studied for two CFD cases based on spatial distribution of PM at different timings.

In order to test the injector performance for the LPI study, the momentum measurement method is applied to the gas jets, for the first time, and used to evaluate the momentum rate of injection (MROI) of HPDI injectors for single and split injections. A full description of the method applied to HPDI injectors and related literature reviews can be found in reference [2]. This method was used to find the minimum pulse separation (GSEP) between two injections and explain some of the observations of engine experiments.

Chapter 5 focuses on SPC, which is partial premixing of natural gas by adjusting the relative injection timing between NG and diesel. The changes in emission and engine performance for more premixing are studied. The effect of EGR, EQR and pilot mass for normal HPDI and SPC points is studied. Multi-injector tests have been performed to show the effectiveness of the SPC injection strategy using other injectors (same model). This study is an attempt to provide better understanding of PM formation in slightly premixed combustion of natural gas. The normal HPDI points and SPC are modelled using GOLD.

In Chapter 6, the results of the 1D model for prediction of heat release rate and soot emissions from High-Pressure Direct-Injection (HPDI) natural gas engines were compared with the experiments. This “Transient Slice Model” (TSM) models a free jet with variable ambient conditions to resemble engine conditions to determine the evolution of fuel/air mixture fraction in an infinite domain (the jet sub-model). Equilibrium mass fractions are determined from mixture fraction, cylinder pressure and internal energy of cylinder. These mass fractions are rescaled and used in a thermodynamic model of a closed cylinder, considering heat transfer and boundary work. The cylinder and jet models interact throughout the compression and expansion strokes, resulting in predicted cylinder pressures that can be used to determine heat release rate. The temperatures and compositions in the jet are used afterwards to solve a transport equation for soot based on soot formation and oxidation from the Hiroyasu model.

2 EXPERIMENTAL METHODS

This chapter presents the experimental methods used in the current study. The main experimental system used in this study is UBC Single Cylinder Research Engine (SCRE). Details of the engine, control parameters, injection commands, power and emission measurements, variability of the experiments and post processing of the data are discussed here. The injection momentum measurement setup is briefly presented.

2.1 Single Cylinder Research Engine

The UBC Single Cylinder Research Engine (SCRE) is used for this study. Figure 2-1 shows the main features of the SCRE gas flow system including the PM sampling system and the fuel conditioning system. The engine is a 6-cylinder Cummins ISX engine modified so that only a single cylinder fires. Cylinder number six, nearest the flywheel, is the firing cylinder. The short distance between the firing cylinder and flywheel reduces torsional vibration in the crankshaft. The pistons of the non-firing cylinders have been replaced with “dummy” pistons. For non-firing cylinders, only the middle ring was installed to prevent the air leakage while reducing friction. The injectors of the non-firing cylinders have been replaced with “dummy” injectors. The single cylinder has a displacement of 2.5 liters (bore 137 mm, stroke 169 mm, connecting rod length 262 mm). The compression ratio is 17:1 using a piston geometry designed for diesel operation. Speed and load are controlled by an eddy-current dynamometer and an electric motor (to help to overcome friction for conditions where the torque from the firing cylinder is not adequate). Natural gas at up to 30 MPa is provided by a compressor fed with local NG (typical composition ~93-95% CH₄). Day-to-day variation in the local NG composition is a source of variability in the experiments, which will be discussed in section 2.1.2. It can affect the emissions and also the heating values used for fuel consumption calculations. However, it is not currently possible to separately evaluate the effect of day-to-day variation of NG composition. A study [124] on the effect of fuel composition on HPDI engine emissions and fuel

consumption showed that at very high methane concentrations, the effects on emissions and fuel consumptions are minimal. However, by adding more significant amounts of ethane (molar percentage from 1.41% to 6.60-8.62%) or propane (molar percentage from 0.32% to 2.23-3.73%) PM increases dramatically. The commercial NG fuel composition provided for the engine over time is expected to be lower than the changes mentioned above so the changes in emissions should be fairly low.

A separate diesel high-pressure pump provides high pressure diesel for the injector which is then regulated to maintain a pressure 1 MPa above the NG pressure using a dome-loaded pressure regulator, shown in Figure 2-1. Intake air is supplied by an electric air compressor and pneumatic regulators are used to set intake pressure and backpressure and control the intake exhaust gas recirculation (EGR) level of the engine. EGR mass fraction represents the dilution of intake charge by recirculated exhaust.

$$EGR = \frac{m_{EGR}}{m_{EGR} + m_{freshair}} \times 100 \quad 2-1$$

In this equation m_{EGR} is the mass of recirculated exhaust and $m_{freshair}$ is the mass of fresh air in the inlet. Airflow rate (mass of fresh air) is measured with a venturi and confirmed by a hot film anemometer. Airflow measurements are used in the carbon balance and measurements of EGR and EQR. A small sample (1 litre/minute) of the intake flow was drawn from downstream of the intake surge tank to determine the EGR fraction (based on CO₂ measurements) and to measure the intake aerosol loading. EGR mass flow rate is calculated by measuring carbon dioxide in the intake system ([CO₂]_{intake}) and comparing that to fresh air carbon dioxide content ([CO₂]_{fresh}) and wet carbon dioxide in the exhaust ([CO₂]_{exhaust}). More information about the air handling system including EGR, intake air and exhaust, are included in Appendix L.

The relative ratio of fuel and oxidizer is represented by global equivalence ratio defined, based on total fuel (NG and pilot together). When EGR is used, the inlet oxygen concentration is lower which is not defined in the regular definition of equivalence ratio based on fresh air. Global Oxygen-based equivalence ratio is defined where air as oxidizer is replaced with oxygen. The oxygen is the molecular oxygen (O₂ molecule). Global oxygen-

based EQR (EQR) will provide a better representation of fuel and oxidizer ratio when EGR is present, hence it used in this thesis. Mass of fuel is shown by m_{fuel} in this equation, which is energy-based NG and pilot mass together; $m_{fuel} = m_{pilot} + \frac{LHV_{pilot}}{LHV_{NG}} m_{NG}$. In this equation, m_{pilot} is the pilot mass injected per cycle, m_{NG} is the NG mass injected per cycle, N is the engine speed, LHV is the lower heating value of the fuels on mass basis¹.

$$EQR = \frac{\left(\frac{m_{fuel}}{m_{Oxygen}} \right)_{actual}}{\left(\frac{m_{fuel}}{m_{Oxygen}} \right)_{stioch}} \quad 2-2$$

The mass of NG fuel is measured by a coriolis mass flow meter (Promass 80A) in the fuel line. The mass of oxygen is calculated from the oxygen mass fraction in the intake ($[O_2]_{intake}$) considering EGR and intake air flow measurement. The fresh air oxygen mass fraction is set to ~23.2% (slightly adjusted for humidity) and EGR oxygen mass fraction is based on exhaust measurement of oxygen. Further details are discussed in Appendix N.

$$m_{Oxygen} = [O_2]_{intake} (m_{EGR} + m_{freshair}) = [O_2]_{freshair} m_{freshair} + [O_2]_{EGR} m_{EGR} \quad 2-3$$

Diesel fuel is supplied from a small pail on a scale. Most of the diesel flow to the injector is used for injector actuation and then returned to the pail; net changes in weight are used to determine the pilot flow. Appendix M shows the details of the fuel system including components and P&ID drawing of the system.

¹ The heating values for two fuel estimated as: NG heating value= 48810 kJ/kg, diesel heating value=42772 kJ/kg assuming no daily variability of fuel compositions.

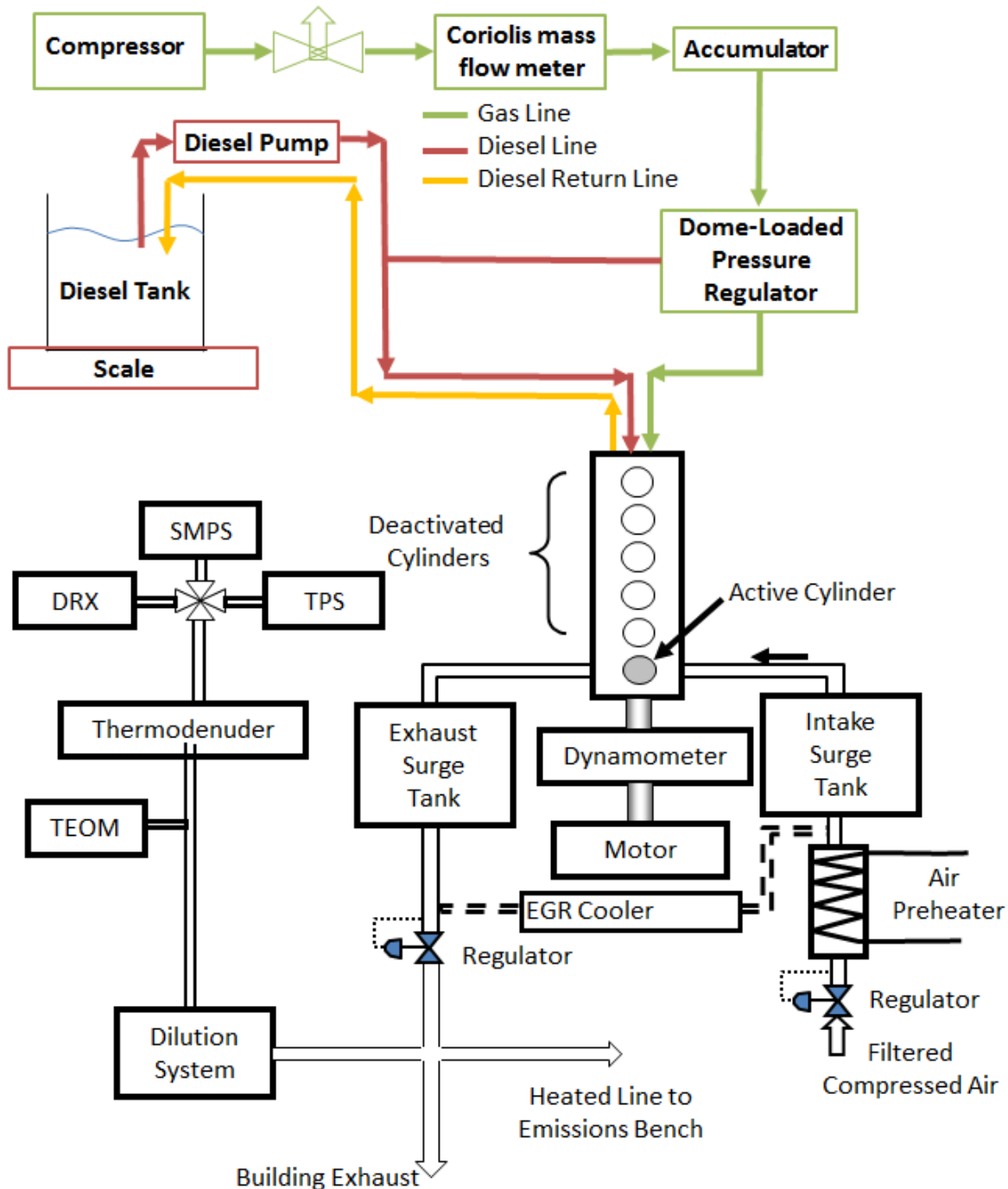


Figure 2-1 Single Cylinder Research Engine (SCRE) gas flow system

This work uses a Westport prototype injector. The injector is a research-level dual-fuel natural gas and diesel injector. The HPDI injector consists of two concentric needles for diesel and natural gas [4]; also shown in Figure 1-1. The injector is electronically

commanded and uses the diesel fuel as the working hydraulic fluid to open and close the needles. The diesel pressure in the control chamber above the gas needle drops when the injection command is sent to the injector, allowing the gas needle to lift. The closing command sent to the injector causes the pressure in the control chamber to increase, closing the gas needle. While the injector is capable of multiple diesel and gas injections, typical operation involves a small diesel injection followed by a single natural gas injection. The engine, injector and fuel specifications are included in Table 2-1.

Table 2-1 SCRE engine, injector and fuel specifications

Engine base type	Cummins ISX, HPDI
Number of cylinders	6 (One cylinder fires)
Cycle	4-stroke
Number of intake valves	2
Number of exhaust valves	2
Swirl ratio	1.5
Bore, stroke, connecting rod length	137 mm, 169 mm, 262 mm
Displacement	2.5 liters
Compression ratio	17:1
Fuel injector type	Common-rail, solenoid actuated, hydraulic diesel actuated
Number of gas/diesel holes & arrangement	9 gas, 7 diesel, equally-spaced
Rail pressure	16-30 MPa
NG fuel	Local BC natural gas (typical composition ~93-95% CH4)
Diesel fuel	Petroleum based diesel fuel

The control parameters are shown in Figure 2-2: pilot start of injection (PSOI), pilot pulse width (PPW), pilot separation (PSEP), gas start of injection (GSOI), gas pulse width (GPW), gas separation (GSEP), second gas start of injection (GSOI2) and second gas pulse width (GPW2). Instead of PSEP, relative injection timing (RIT) will be used in some experiments. It will be discussed in Chapter 5 in more detail. Injection timing parameters were controlled using a custom National Instruments FPGA board through a LabVIEW interface. For the negative PSEP and SPC points presented in Chapter 5, the commanded gas injection is before the end of diesel command.

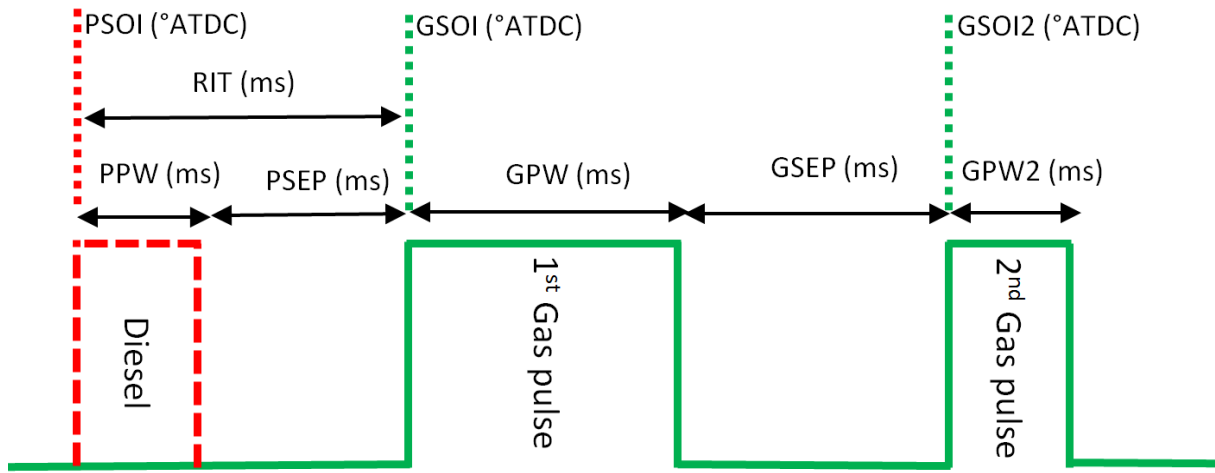


Figure 2-2 Phasing of the injection events. Green is NG commanded signal and red is Pilot commanded signal.

One injector (“Baseline Injector”) has been used for all the experiments presented in this thesis, except for multi-injector tests where several injectors of the same model were tested. The injector-injector variability might affect the performance of an injection strategy in multi-cylinder engine. An internal study by the PhD candidate showed that for all the injectors changing one parameter or applying an injection strategy would affect all the injectors in a similar way. More information about the injector-injector variability will be discussed in chapter 4, 5 and Appendix O.

Injection timing for the pilot and NG pulses, the intake and exhaust pressure, the EGR level, and the common rail gas and diesel pressure can be controlled independently from the

engine torque and speed operating conditions, allowing for experimental flexibility. To monitor the combustion performance, the in-cylinder pressure is recorded using a flush-mounted, water cooled Kistler 6067C piezoelectric transducer, sampled at 0.5° CAD resolution. An average of 45 cycles is used to calculate the indicated pressure and apparent heat release rate. The indicated pressure is used to calculate the gross-indicated mean effective pressure (GIMEP) and gross-indicated specific fuel consumption (GISFC). GIMEP is defined as the total work calculated from IVC to EVO using the cylinder pressure (P_{cyl}) and volume of cylinder. In this equation, V_d is the displacement volume.

$$GIMEP = \frac{\int_{IVC}^{EVO} P_{cyl} dV}{V_d} \quad 2-4$$

Fuel consumption was reported on a diesel energy-equivalent basis:

$$GISFC = \frac{m_{pilot} + \frac{LHV_{pilot}}{LHV_{NG}} m_{NG}}{\frac{N}{2} \int_{IVC}^{EVO} P_{cyl} dV} \quad 2-5$$

GISFC is normalized by the gross-indicated power in this thesis. The ratio of diesel to gas (on an energy basis) is different in various modes but at B75 approximately 5% of the total energy is from diesel injection.

The apparent heat release rate is calculated, based on the first-law of thermodynamics analysis as described in Heywood [7].

$$AHRR = \frac{dQ_{net}}{d\theta} = \frac{\gamma}{\gamma - 1} P \frac{dV}{d\theta} + \frac{1}{\gamma - 1} V \frac{dP}{d\theta} \quad 2-6$$

In this thesis, AHRR is normalized by the displacement volume of the cylinder. Specific heat ratio (γ) of 1.30 is assumed. This poly-tropic exponent is slightly smaller than the average specific heat ratio of air mainly due to heat transfer to the cylinder wall and piston. The integral of the heat release rate (IHR) was used to define the combustion phasing, with the principal timing being the mid-point (CA50). A load cell measures the engine torque on the dyno to provide one more measurement of engine output power, however due to the increased friction from deactivated cylinders, this sensor was not used as the primary

engine load measurement, but we did confirm that trends reported later for GISFC are consistent with those for BSFC.

The gaseous emissions (CO, CO₂, O₂, CH₄, tHC, NOx and intake CO₂ for EGR calculations) measurements are taken from the exhaust system with an AVL CEBII emissions bench. A detailed description of the emissions bench, including span gas and range of each analyzer, is set out in Appendix N and also in reference [55]. The total hydrocarbon (tHC) and CH₄ are measured with individual flame ionization detectors, the NO and NO₂ are measured with chemiluminescence detectors, the O₂ with a paramagnetic detector while the CO and CO₂ are measured by non-dispersive-infrared absorption. At the start of every test day, the emissions bench was calibrated with zero, low and high-span gases (covering the entire measurement range). At the end of every day, the calibrations were checked again to ensure the instrument drift was less than 5%. All test points considered in this work were repeated multiple times on different days using a different sequence of test points. For each point, the data are recorded after the engine is allowed to stabilize for at least 3 minutes after the operating condition is reached.. The measurement duration, after the engine is in steady-state condition, was at least 180 seconds for emission calculations.

The PM sampling system installed on the SCRE is separate from the gaseous measurement system and is based on a 2-stage system using an ejector diluter and an aging chamber. A simplified schematic of the system is included in Figure 2-1. A more detailed schematic drawing is included in Appendix J. The dilution ratio at the first stage is approximately 7:1 and the overall dilution ratio is 12:1, as determined by the CO₂ concentration measurements from the AVL bench and from post-dilution measurements (California Analytical NDIR analyzer model 100).

Particle mass concentration is measured with a tapered element oscillating microbalance (TEOM) [125]. The TEOM (Rupprecht and Patashnick Co., model 1105) provides a continuous and direct mass measurement of the engine PM (both soot and semi-volatile material). PM concentrations are also measured using a DustTrak DRX (DRX) [126]. The DRX (TSI DustTrak DRX™, model 8530) measures light scattering, which can be correlated with aerosol mass for particles of consistent size, morphology, and composition. The DRX is

fast and sensitive to low concentrations, but it does not give a true mass measurement. In this work, we present results for the DRX measurements and note that all trends discussed in this work were apparent in the TEOM measurements as well. It has been shown before [1] that there is a linear correlation between TEOM and DRX measurements. In all of the experiments, a UBC-developed thermodenuder [8], [51] was used upstream of the DRX. The thermodenuder heats the sampled exhaust to 200°C to vaporize the highly volatile OC, sulphuric acid, ammonium sulfate and bisulfate and some of the low volatility OC in the sample [127].

As mentioned earlier, the SVOC fraction of HPDI PM can range from 86% to 33% as load increases [8]. Because the main concern in this thesis is the non-volatile portion of PM, all of the PM measurements in the current study report denuded PM measured by DRX, SMPS or in TEM analysis. The denuded PM mass should correlate with soot predictions of CFD or TSM later in this thesis.

Figure 2-3 shows the correlation between DRX and TEOM for all the points from the baseline injector in this thesis. Generally, the TEOM follows the measurement from DRX with a constant ratio. Part of the scatter in this figure might be due to higher variability of TEOM measurement in the range of current measurements, as discussed in the Table 2-3. From our experience, the DRX is more repeatable at low concentrations and, therefore, in this thesis we used that as a main measurement device.

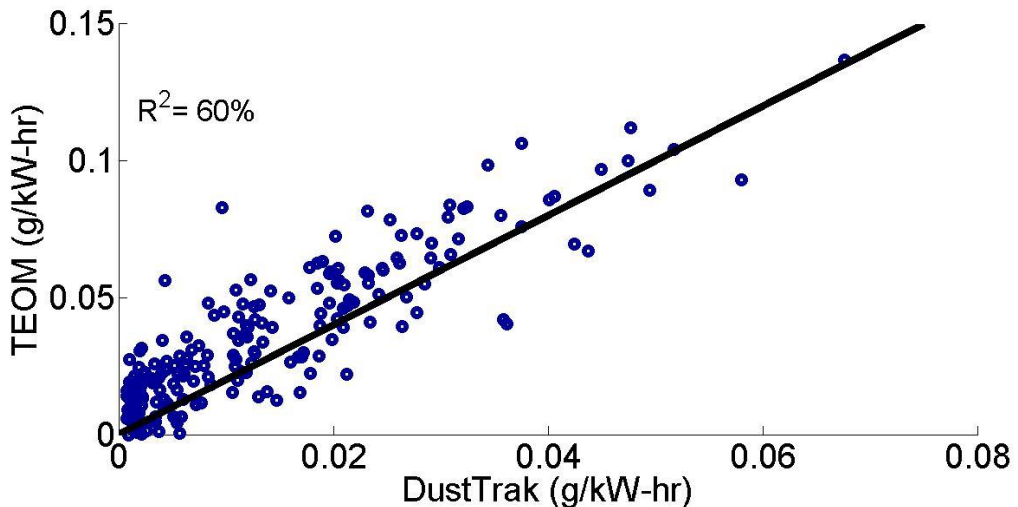


Figure 2-3 PM ratio between TEOM and DRX for all the points in the current study for baseline injector.

Particle number size distributions are measured with a scanning mobility particle sizer (SMPS) spectrometer (TSI, model 3080 Electrostatic Classifier / Model 3025 CPC). A flow is sampled from the diluted exhaust stream, downstream of the thermodenuder, with a differential mobility analyzer. The sheath flow is set at 3 LPM and sample flow at 0.3 LPM. Particles were counted in a condensation particle counter (CPC, TSI Model 3025A) to determine the mobility-equivalent size of the particles. TSI software (AIM) was used to collect the data and a multiple-charge correction was applied to the scans. For all data presented, 3 subsequent scans were averaged.

For particle morphology tests, diluted exhaust from the same connection as the SMPS was used. A thermophoretic particle sampler (TPS) was used to deposit particles onto grids using a temperature gradient. The grids were later imaged with a (Hitachi H7600) transmission electron microscope (TEM). Semi-automated image processing software was used to process the images [128]. At least 42 aggregates and 360 primary particles were counted for each operating point. The method was developed at UBC for automatic determination of the average primary particles and aggregates size measured from the main skeleton of the aggregates.

SMPS and TEM sampling used the denuded line after data was taken with the DRX. A complete description of the PM measurement system can be found in [51], and further discussion of the use of the DRX for engine mass emissions is provided in [129].

The database of the experiments were analyzed by a post processing package that has been developed in the current study (Appendix G) and has been used in parallel studies [45]. The ignition timing has been calculated using a method described in reference [55], [56]. The start of combustion was found as the intercept of the AHRR curve of the combustion event with the zero AHRR axis. This intercept was calculated by finding the slope between 30 kJ/m³-deg and 50 kJ/m³-deg.

2.1.1 Operating Modes

The differences between the SCRE and a production engine, especially in air handling, make direct comparison of the results difficult. The maximum load of the SCRE in terms of GIMEP is about 19.5 bar (~87% of the maximum load). However, previous work showed a strong correlation between trends observed on the SCRE and equivalent multi-cylinder engines. Emissions results are normalized using the gross-indicated power. The fuel consumption is reported on a diesel energy-equivalent basis, and is normalized by the gross-indicated power (Gross-Indicated Specific Fuel Consumption - GISFC).

The test points in this study are based on modes from the European Stationary Cycle (ESC-13), but do not match any of the regulatory test conditions exactly because the SCRE load is based on gross indicated mean effective pressure (GIMEP) and the air handling system of the SCRE can only approximate real multi-cylinder engine (MCE) intake and exhaust conditions. Previous testing indicated that for the SCRE, high-load points have the highest engine-out emissions of PM [4], [87]. As a result, the focus of the current study is on higher loads. Limitations on the SCRE's air handling system restrict the maximum achievable load to less than 90% of an equivalent multi-cylinder engine. In this work we consider operation at low speed ("A"), medium speed ("B") and high speed ("C"). Two load levels (75 and 87% of rated load based on indicated performance) were considered. Most of the tests in the

current thesis are performed on mode B75. The engine parameters normally used to set the points, including permitted range of each parameter, are presented in Table 2-2.

These parameters were developed for the single-cylinder engine and are not intended to represent parameter settings for any specific multi-cylinder engine.

2.1.2 Measurement Variability in SCRE Experiments

Two types of measurement variability can be described: point-to-point (the same point set several times in the same day influenced by how well the point is “set”), and point-over-time (which can be associated with changing hardware calibration on the engine, injector performance or NG composition).

Point-to-point variation can be reduced by setting a permitted range for each parameter. If the parameter is out of the permitted range then the point will not be used for analysis. The permitted range has been set to be as accurate as an operator can set the parameter; ranges are listed in Table 2-2. The effect of the permitted ranges on engine emissions can be found in Table 8 in [8], where a surface regression was developed for all the emissions. The maximum error in engine-out PM in the permitted range is about 7%, and this is controlled primarily by variations of EGR and EQR.

Table 2-2 Mode B75 and permitted range for set parameters

Parameter	B75 Set Point	Permitted variability
Engine Speed (rpm)	1493	15
GIMEP (bar)	16.6	0.3
EGR (%)	18	1.5
EQR	0.61	0.015
GRP (MPa)	25.4	0.3
CA50 (° ATDC)	11	1.5
Pilot mass (mg/inj)	10.5	2.5

Point-over-time variability is due to changing hardware calibrations and changing the combustion event (changing natural gas composition over time or changing the injector

performance over time). Day-to-day variations in the local NG composition is a source of variability in the experiments, however, it is not currently possible to separately evaluate the effect of day-day variation of NG composition in overall point-over-time variability. However, as mentioned before, the effect of this variability on emissions is expected to be fairly low. In order to track the point-over-time variability, every day a low load zero EGR repeatability point (“Repeat Point”, mode A35) and a B75 baseline condition are taken. Additionally the emissions bench is calibrated at the beginning and end of each test day and checked with zero and span gases. Any deviation above 5% from the span gas requires recalibration of the bench.

The average values for the B75 baseline, for all the experiments presented in the thesis using one injector, are included in Table 2-3 with a table of coefficients of variation (COV). COV is defined as the standard deviation of the data set divided by the mean value of the data. Total 52 points are selected between April-December 2014. Generally, the power and pressure related parameters have lower COV compared to the emissions. GISFC and maximum pressure have 1% variations while PM measured by DRX and CO have 17% and 15% variations, respectively. The PM TEOM variation is much higher since the PM concentration is close to the TEOM detection limit. The gaseous emissions measurement devices are calibrated every day (with the acceptable deviation of maximum 5%), so the variations in measurement devices for CO measurements should be small compared to the engine-related variability. DRX is also calibrated, but less often, with a Palas particle generator (PALAS GFG 1000). Therefore, the device variability should be fairly controlled by calibrations. The variations of CO and PM are tightly correlated [45] indicating that the variations reflect real changes in the combustion process, not instrument error.

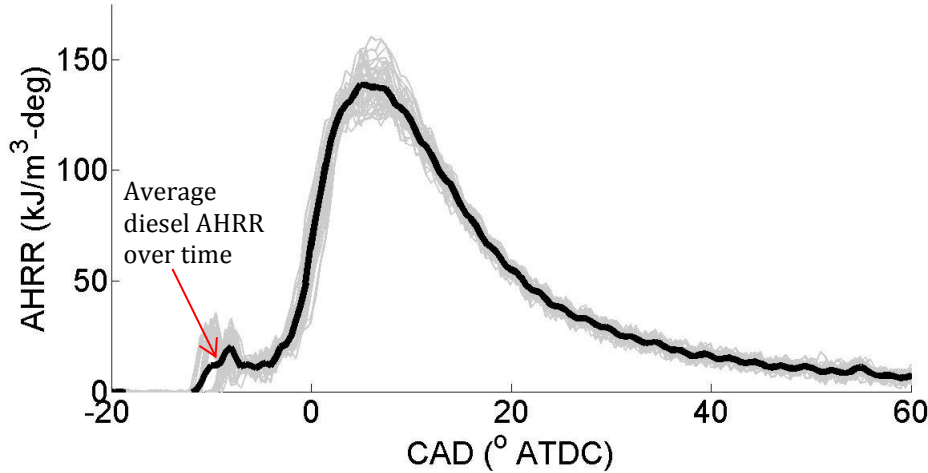
Table 2-3 Mode B75 variations for April-December 2014²

	Average± standard deviation	COV
GISFC (g/kW-hr)	175.78±1.05	1%
P_{max} (bar)	136.75±1.63	1%
P_{max} CAD(°ATDC)	11.34±0.26	2%
(dP/dCA)_{max} CAD(°ATDC)	4.71±0.23	5%
GPW (ms)	1.74±0.05	3%
PM DRX (mg/kW-hr)	20±3	17%
PM TEOM (mg/kW-hr)	40±14	35%
CO (g/kW-hr)	5.46±0.81	15%
NOx (g/kW-hr)	1.35±0.07	5%
CH₄ (g/kW-hr)	0.52±0.04	8%

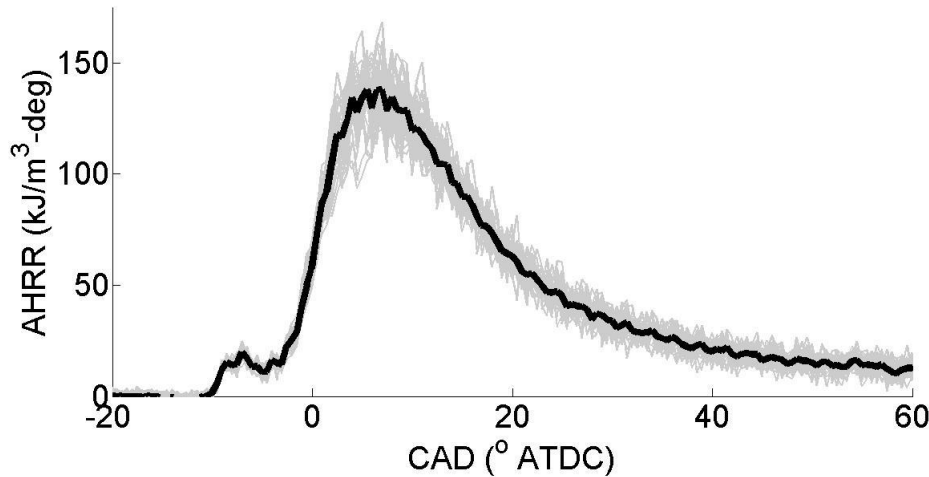
AHRR graphs of the mode B75 points over time (April-December 2014) are shown in Figure 2-4 (a). The AHRR is normalized by the displacement volume of the cylinder. The gray lines are the AHRR calculated from the average pressure (average of 45 cycles) of each point. The average of the all the points from the different dates are shown in the same graph by a black line. The diesel portion of the AHRR is significantly variable over time, which might be due to the injector's performance change over time. Also, the AHRR of the main combustion has changed over time possibly due to the NG composition changes during the course of this study. These combustion differences over time contribute to the overall point-over-time variability.

Figure 2-4 (b) shows the cycle-cycle variations of the AHRR from 45 cycles of one point in one day. The cycle-cycle AHRR graphs show more spikes than the AHRR from the average of the point. The diesel variations, which have been noticed in the point-over-time AHRR graphs, are not significant in cycle-cycle AHRR graphs. Compared with the panel (a), the consistency in (b) shows that the diesel injection variations are more related to variations from week to week, rather than instantaneous changes in injector performance. Different AHRR traces can be also noted in cycle-cycle AHRR graphs close to the AHRR peak.

² For the UBC UBC Baseline Injector. Here, COV is defined as the standard deviation divided by the mean value. $COV = \frac{\sqrt{\frac{1}{N} \sum_{i=1}^N (x_i - \bar{x})^2}}{\bar{x}}$, $\bar{x}_m = \frac{\sum_{i=1}^N x_i}{N}$ where x_i are the data points and N is the number of data points. COV are rounded to the nearest 1%.



(a) Over time variaitons



(b) Cycle-cycle variations

Figure 2-4 AHRR graphs of the mode B75 points (a) Variations over-time; each grey line is the average of 45 cycles of each points and the black line is the average of all B75 points (total 52 points) (b) Cycle-cycle variations; grey curves show individual cycles and the black curve is the average of 45 cycles.

In order to avoid the effect of point-over-time variability, each subject of study is designed in one block of testing (maximum 1-2 weeks). The blocks are designed to need minimum “out of block” comparisons.

2.2 Momentum Measurement Method

Momentum rate measurement will be used in the current study for identifying the minimum effective pulse separation (GSEP) between two gas injections for the LPI strategy. In order to measure the momentum rate of a jet, a dedicated apparatus is used with a pressure transducer (PT) installed in front of the injector nozzle. The gas jet impinges on the PT, as shown in Figure 2-5. The recorded pressure can be used to determine the gas jet momentum. According to free jet theory and experimental measurements in the literature [130], the measured force is equal to the momentum rate of the jet at the nozzle exit. More information about the momentum measurement method for natural gas injectors can be found in reference [2].

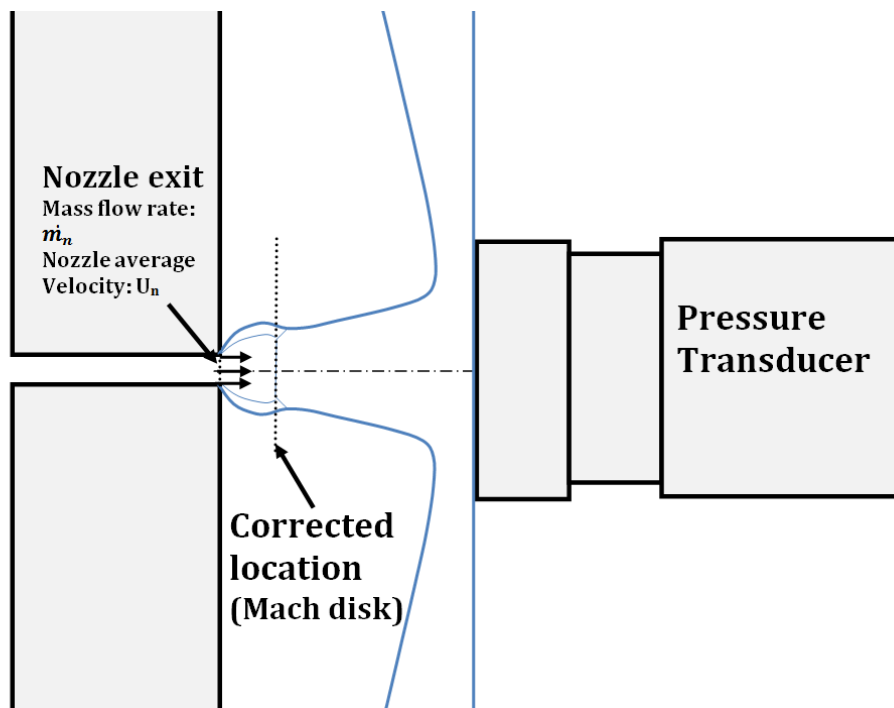


Figure 2-5 Momentum measurement system³

Conservation of momentum requires that the momentum flux to the transducer is equal to the force on the transducer, provided that the jet is deflected perpendicular to its axis and

³ Copyright © 2015 SAE International. This figure is included in this thesis with permission from SAE International. Further use, copying or distribution is not permitted without prior permission from SAE.

pressure outside the jet is nearly uniform. By measuring the average pressure at the PT surface and considering the surface area of the PT (which is larger than the jet diameter at impingement), we can find the momentum rate of the jet at the PT location, which is the same as the nozzle momentum rate according to the measurements in the literature [130]:

$$M_n = M_c = M_{pt} = P_{pt}A_{pt} = \dot{m}_n U_n \quad 2-7$$

In this equation, P_{pt} is the average pressure measured using pressure transducer and A_{pt} is the frontal surface area of the pressure transducer, U_n is the spatial average nozzle velocity, \dot{m}_n is the spatial average nozzle mass flow rate, M_c and M_n are momentum rate at the corrected location (Mach disk location) and at the nozzle, respectively. There is a delay between the injection rate at the injector and the pressure signal, but this is much shorter than the injection duration (considering ~ 400 m/s speed of the jet, it takes ~ 0.01 ms to cover the surface of the PT).

The experiments were performed in the UBC Injection Chamber (IC). The IC is a high pressure chamber machined from a 27cm× 25cm× 25cm block of steel. The ports on the five faces can accept windows or an injector holder. Both the injection gas and the working fluid inside the chamber are nitrogen. The IC windows are designed for a working pressure of 8 MPa. In the current study all of the windows are replaced with steel blanks to allow for chamber pressure up to 12 MPa.

The test matrix of the LPI experiments, presented in chapter 4 is shown in Table 2-4. For some tests, injections were split into two pulses, identified using first gas pulse width (GPW1) and second gas pulse width (GPW2) with a GSEP. In this table P_t is tank pressure, P_b is the back pressure (chamber pressure) and f is frequency of injection.

Table 2-4 Range of parameters selected for the experiments

P _t	P _b	f	GPW1	GSEP	GPW2
[MPa]	[MPa]	[Hz]	[ms]	[ms]	[ms]
26.2	10	5	1.81	0.6, 1.0, 1.3, 1.5, 2.0, 2.5, 3.0	0.6

In a typical experiment, 100 injections are recorded in 20 seconds ($f=5$ Hz); after the injector reaches to its steady-state working conditions. The back pressure is set to 10 MPa for all of the experiments in the current study.

3 MODELLING METHODS

This chapter describes the phenomenological Transient Slice Model (TSM) developed in the current research. TSM is developed to predict the pressure, heat release rate and soot emissions arising from natural gas injections in an engine. Later in this chapter, the GOLD CFD model developed at Westport Innovations Inc. is reviewed.

3.1 Overview of Transient Slice Model (TSM)

This section provides an overview of the TSM model. Section 3.2 provides more information about the jet model including injection specifications, transport of conserved scalars, radial distribution of velocity and mixture fraction, mixture fraction maps, ignition and flame propagation and jet integral calculations. Section 3.3 describes the cylinder thermodynamics model. Section 3.4 provides more information about the soot model in TSM. The tuning parameters are mentioned in section 3.5.

TSM performs computations in two interrelated domains: the “jet” and the “cylinder” (Figure 3-1). In the “jet model”, a jet is injected in a wall-free environment. The nozzle and ambient conditions of the jet are determined to match the cylinder conditions as much as possible. TSM solves the one-dimensional transport equations for momentum and mixture fraction in the jet. The predictions for non-reacting jets are described and validated in Appendix A. The “cylinder model” is a one zone (0-dimensional) thermodynamic model to calculate cylinder pressure. The “mixture fraction map” is a relation (from thermodynamics and species mass conservation) between scalar quantity g_i (such as temperature, density, mass fractions) and the mixture fraction Z , that is $g_i(Z)$.

Model inputs are listed in the flowchart of the model in Figure 3-2. The model starts with engine specifications such as bore and stroke. Additional inputs are the injection timing, injection pressure, pressure and temperature at start of simulation (SOS, the start of simulation, $\theta=-90^\circ$ ATDC), EGR, EQR, engine speed and gas ignition time. Jet and cylinder variables are initialized in the “initialization” function. Cylinder and “ambient” composition

are set according to the SOS mixture composition. Note that the term “ambient” is used to describe the environment of the free jet, which does not perfectly match the cylinder composition, as discussed later. The “injection specification” sub-model provides nozzle velocity, enthalpy, internal energy and density. Velocity and mixture fraction for the jet are calculated based on a 1D numerical solver. The cylinder pressure is used in the thermodynamic calculations to generate mixture fraction maps for the next time step.

In each time step (Figure 3-2), the masses of species generated or consumed in the jet are calculated by the “jet model” and are transferred to the “cylinder thermodynamics model”. The cylinder calculations transfer the cylinder pressure for the calculation of mixture fraction maps for the next time step. Two sets of maps will be generated for reacting and non-reacting parts of the jet in each time step, which are defined by the “ignition and flame propagation” script. The reacting map is generated based on equilibrium; the cells inside the reacting zone will be at equilibrium state. There is no progress variable defined in the model. Therefore the charge is either in non-reacting state or in equilibrium state. This assumption leads to a faster reaction rate compared to the experiments, which can be seen in the AHRR graphs. This higher reaction rate will be partly controlled by defining an effective flame speed, more details of which are presented in sections 3.2.6 and 6.2.1. The jet “ambient” pressure is pressure from the cylinder thermodynamics model and “ambient” temperature ($Z=0$) is set based on calculated motored pressure (an assumption discussed in section 3.3.6) and ideal gas calculations. The jet is divided into “slices” spanning the width of the numerical domain (introduced in Figure 3-3). For each slice, in each time step, we satisfy momentum, mass and state constraints. The simulation runs from start of simulation ($SOS=-90^\circ$) to end of simulation ($EOS=90^\circ$).

The HPDI engine uses diesel as the source of ignition for natural gas, and typically diesel accounts for less than 5% of total injected energy. Most of the PM in the exhaust is from natural gas combustion [23], [131]. In a previous study [23], [131], the contribution of the pilot fuel (a biodiesel blend with higher ^{14}C content than diesel fuel) was determined using accelerator mass spectrometry (AMS) measurements of ^{14}C in the exhaust particulate. The pilot fuel contributes to 4-40% at different modes. However at the high loads ($\sim 60\%$ of load, high PM-forming modes), the pilot contribution was maximum 6%. In the current

study, we do not model the diesel injection, due to its minimal effect on AHRR and total engine-out PM. The ignition timing is taken from engine measurements using a method described in reference [55], [56]. Thus, the effect of diesel ignition timing has been considered indirectly in the model. In reality, the direction of diesel injection as well as relative location of diesel combustion products to the gas jet is an important factor; however, as long as the injector is the same, these effects should be covered by the tuning factors. If the injector or the diesel-gas interlace angle (the circumferential angle between NG and diesel nozzles) changed then the tuning factors would be different too. This limitation of the model might be overcome by adding a diesel injection model to a future version of TSM.

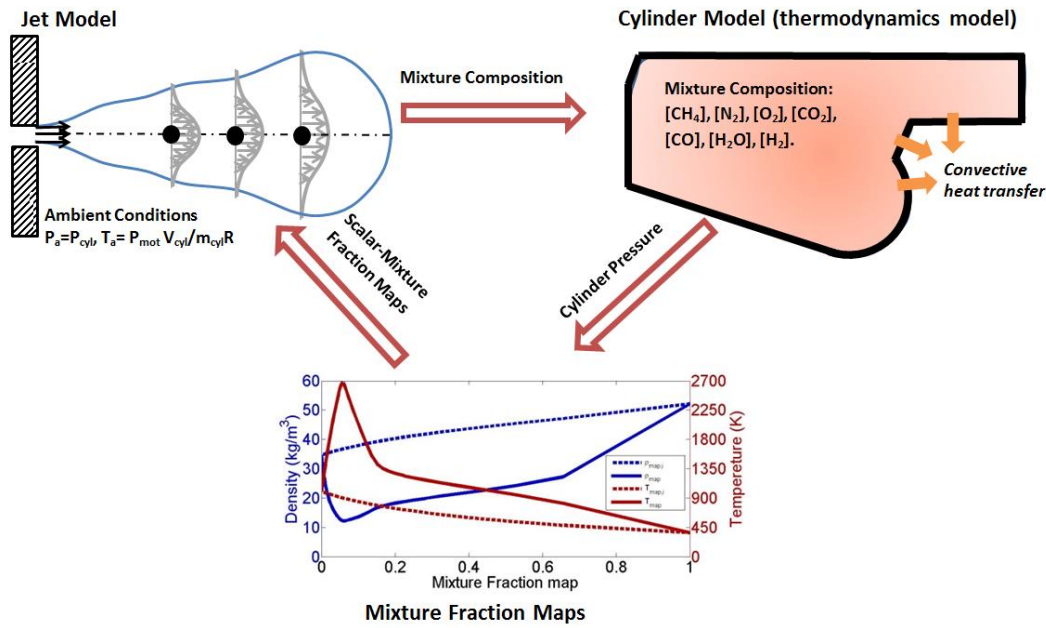


Figure 3-1 Schematic of TSM

Equilibrium mixtures and properties are determined by a thermodynamics script which calls Cantera [132] libraries. Cantera is a suite of object-oriented software tools for problems involving chemical kinetics, thermodynamics, and/or transport processes. It is a C++ based code with interfaces for Python, Matlab, C, and Fortran 90 [132]. Convective heat

transfer, cylinder pressure and temperature will be calculated in the “cylinder thermodynamics model”.

The soot model uses the output of engine simulation (velocity, mixture fraction, temperature, oxygen mass fractions and pressure) and calculates soot based on solving transport equations for soot with source terms from the Hiroyasu model. The soot model is not coupled with the main loop of the jet model.

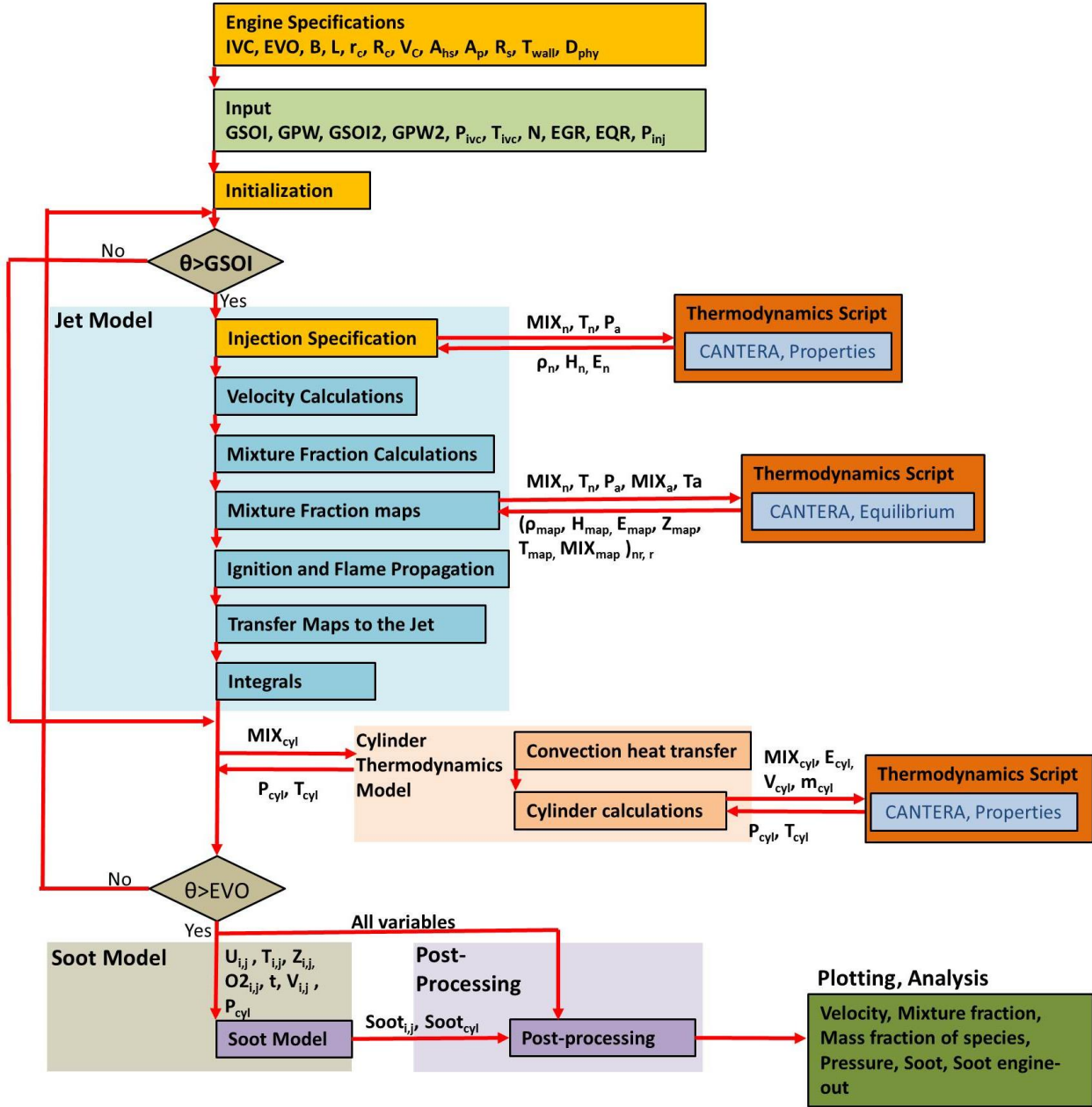


Figure 3-2 Flowchart of the TSM

3.2 The Jet Model

The fuel is injected from the nozzle into an infinite stationary environment. The swirl motion, the effect of walls and impingement are not considered in TSM. Figure 3-3 shows the basic configuration of the model along with the discretization of the model in the axial

direction (slices). The nozzle conditions are described in section 3.2.1. The slices are shown as dashed black lines. The jet in TSM does not have clear boundaries, while in previous versions of this model [118], [119], [121], [122] the boundaries were selected by defining a spread angle. The boundaries of the jet (if required for post processing) are selected based on defining a boundary mixture fraction (Z_b). The boundary mixture fraction may vary depending on the application. The jet spread coefficient will define the jet radial growth in axial direction. Each slice has several points in the radial direction, which are used for calculation of integrals and presentation of the results in radial direction.

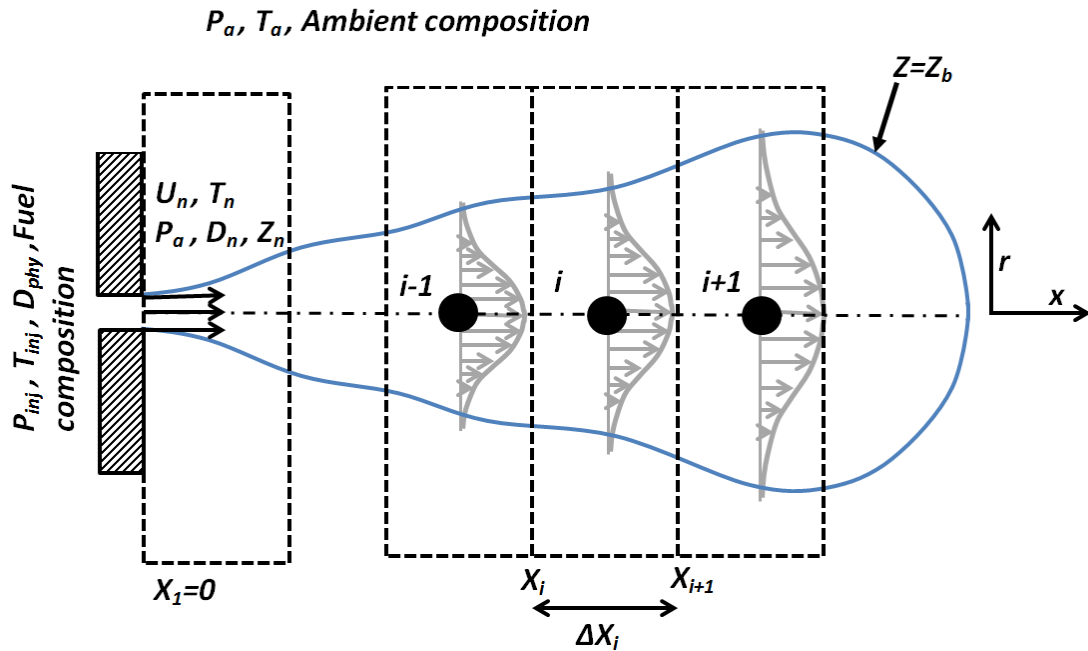


Figure 3-3 Schematic of the jet model

The transport equations are solved in the axial direction (x) of the jet with known radial distributions from the literature. The conservation equations are solved for each slice at each time step. The conserved equations are momentum and mixture fraction. The assumptions for development of this model are:

- Axisymmetric jet; no effect from walls, swirl or neighboring jets

- Self-similar turbulent developed jet. The application of self-similarity to transient jets has been evaluated before [118].
- Pressure is spatially uniform for the entire jet
- Density is calculated based on mixing

As previously mentioned, the jet ambient pressure (Pa) is always the cylinder pressure (P_{cyl}) simulated in the cylinder model (considering the combustion, more details in section 3.3) and ambient temperature (at Z=0) is set based on calculated motored pressure (no combustion, more details in section 3.3.6) and ideal gas calculations. This is not the only way to define the ambient temperature; as an alternative it could be taken as the adiabatic compression temperature up to the cylinder pressure⁴. The ambient composition is set according to the SOS mixture composition.

3.2.1 *Injection Specifications*

The nozzle conditions for NG fuel will be described here (again, TSM does not model the diesel injection). Velocity and mixture fraction of fuel at the nozzle are assumed to be uniform across the nozzle. The velocity at the nozzle is found based on injection pressure, ambient pressure, fuel temperature and mixture composition of the fuel. The Mach number is

$$Ma = \min \left\{ \left[\frac{2}{\gamma - 1} \left(\frac{P_{inj}}{P_a} \right)^{\frac{\gamma-1}{\gamma}} - 1 \right]^{1/2}, 1.0 \right\} \quad 3-1$$

Here, P_a is the ambient pressure for the jet that is set to the cylinder pressure at the start of injection, P_{gsoi} . The nozzle temperature is 370 K (typical engine block temperature) for all the cases. In this equation, γ is the specific heat ratio of methane in nozzle ($\gamma=1.32$). The

⁴ Setting the ambient temperature according to the cylinder pressure leads to higher maximum temperature (close to 3000 K), for combustion products. This is close to the upper limit of Cantera library. This causes instability in the TSM coming from Cantera calculations. In order to avoid it (what?), the “ambient” temperature is set to motored temperature. This assumption results in maximum temperatures closer to CFD calculations, verified at mode B75. The method of setting ambient temperature affects soot calculations as well, and if a different method of setting ambient temperature were used, then the soot tuning constants should be revised. Possibly, if radiation heat transfer and local mixture fraction variations were included, the peak temperatures (at the stoichiometric surface) would remain below 3000K even with higher values of Ta.

ideal gas assumption is reasonable because the compressibility factor is 1-3% at these conditions. The nozzle velocity is:

$$U_n = Ma [\gamma R T_n]^{1/2} \quad 3-2$$

Mach disk expansion with shock waves is a complex phenomenon. Here it is assumed that temperature at the Mach disk location is equal to nozzle temperature, consistent with prior literature [133], [134]. If the flow is sonic at the nozzle, the jet is underexpanded and the “corrected nozzle diameter” is estimated based on [134].

$$D_n = D_{phy} \sqrt{\frac{P_n}{Ma^2 P_a}} \quad 3-3$$

For both subsonic and sonic jets, the pressure at the nozzle will be set to cylinder pressure at the start of gas injection (P_{gs0i}). Density at the nozzle is calculated based on fuel composition, pressure and temperature using thermodynamic relations. The thermodynamics script sets the properties of the gas, required later for calculation of the jet domain (see the flowchart, Figure 3-2). Nozzle momentum and mixture flux will be calculated as:

$$FluxM_n = \rho_n U_n^2 A_n \quad 3-4$$

$$FluxZ_n = \rho_n U_n Z_n A_n$$

In this equation, A_n is the corrected nozzle area based on Equation 3-3. Z_n is the nozzle mixture fraction and it is always 1 in the current thesis.

The jet is assumed to be self-similar except for the cells close to the nozzle. The start of the fully developed region, i.e. end of the potential core and start of self-similarity, can be estimated by the first cell with the centerline value of velocity or mixture fraction less than one ($g_{cl}<1$). For the cells with $g_{cl}>1$, the flux at the cell will be set to nozzle flux value and $g_{cl}=g_n$. Therefore the cells in the potential core are not self-similar.

A gas injection delay of 0.7 ms between the command and the start of opening the needle has been assumed based on our injection studies on the same injectors [2]. In order to

provide the fuel injection rate to the model, the nozzle opening and closing times are specified as inputs to the model. Typical values for the NG injections are a ramp-up of 0.6 ms (start of opening the needle to fully-opened needle) and a ramp-down of 0.6 ms (end of fully-opened needle to fully-closed needle). More details are provided in Appendix A.

3.2.2 Transport of Scalars

The following equation shows the balance of a generic scalar ‘g’ in each slice in the most general form. The fluxes are calculated based on a first order upwind scheme. The functional form of density, g and velocity will be introduced later in sections 3.2.3, 3.2.4 and 3.2.5.

$$\int_{r=0}^{\infty} \rho(x, r, t) g(x, r, t) u(x, r, t) 2\pi r dr \Big|_{i-1}^t - \int_{r=0}^{\infty} \rho(x, r, t) g(x, r, t) u(x, r, t) 2\pi r dr \Big|_i^t = \frac{\int_{r=0}^{\infty} \rho(x, r, t) g(x, r, t) 2\pi r dr \Delta x \Big|_i^{t+1} - \int_{r=0}^{\infty} \rho(x, r, t) g(x, r, t) 2\pi r dr \Delta x \Big|_i^t + \int_{r=0}^{\infty} \rho(x, r, t) g_{gen}(x, r, t) 2\pi r dr \Delta x \Big|_i^t}{\Delta t} \quad 3-5$$

The left hand-side of the equation is the flux of the properties from the inlet and outlet surfaces. The right hand-side of the equation is the variation of the volumes integral over time and a generation term. In this equation $(\cdot)|_i^t$ corresponds to time step ‘t’ and slice ‘i’. Equation (3-5) can be simplified as:

$$FluxG|_{i-1}^t - FluxG|_i^t = \frac{G|_i^{t+1} - G|_i^t - G_{gen}}{\Delta t} \quad 3-6$$

In this equation, $FluxG|_{i-1}^t$ is the inlet flux and $FluxG|_i^t$ is the outlet flux of the parameter “g”. $G|_i^t$ and $G|_i^{t+1}$ are the integrals of the parameter “g” at time step “t” and “t+1”. G_{gen} is the integral of the generation term of parameter “g” in time step “t”. For the balances of momentum and mixture fraction the scalar is conserved and the generation term is zero.

All parameters at $t=0$ and $x=0$ are known. The ambient conditions are set according to the cylinder pressure and temperature. The Equation 3-6 is solved from nozzle downstream for each time, and $G|_i^{t+1}$ is calculated. In order to find the distribution of parameter “g” in time step $t+1$, we use the known radial profile (function F_g) of the parameter from

literature. These functions for velocity and mixture fraction are introduced in equations 3-8 and 3-9.

$$g_{cl}(x)|_i^{t+1} = \frac{G|_i^{t+1}}{\int_{r=0}^{\infty} \rho(x, r, t) Fg(x, r) 2\pi r dr \Delta x} , \quad g(x, r)|_i^{t+1} = g_{cl}(x)|_i^{t+1} Fg(x, r) \quad 3-7$$

The radial distribution for different parameters is based on the self-similarity assumption. The density at time step $t+1$ is unknown, so for a first guess, density at the previous time step is used. After iteration, the density and the parameter values converge. The flux at the inlet of the first slice is set to the nozzle fluxes calculated in equation (3-4). The cells in the potential core are not self-similar, as mentioned earlier.

The calculation of flux integrals in TSM requires a numerical grid. The number of cells in the axial and radial directions is selected based on the mesh-independence study (based on axial velocity, AHRR and engine-out PM; Appendix B). Because the radial distribution functions are known analytically (described below), an analytical approach could be used to speed up calculations in the future, if needed. Each slice has several points in the radial direction, which are used for calculation of integrals and presentation of the results in a radial direction. For discretization of the numerical domain $\Delta x=2D_n$ and $\Delta r=0.5D_n$ are used and a numerical domain is selected with the length of $250D_n$ in the axial direction and width of $40D_n$ in the radial direction.

3.2.3 Radial Distribution of Velocity

For the momentum equation ($g=u^2$) the generation term is zero, assuming momentum is constant in the axial direction of the jet [135]. Based on the self-similarity solution, the radial distribution of axial velocity for a free jet can be estimated as:

$$F_u(x, r) = \exp\left(\frac{-\alpha r^2}{K_r^2 x^2}\right) \quad 3-8$$

For α and K_r , different values are reported in the literature. In the current study, the following constants have been used based on the experiments in the literature: $K_r=0.1$

[135] and $\alpha=\ln(2)$ [135]. For transient jets, the self-similarity assumption is not strictly valid, but as discussed in the results (Appendix A), the predictions resulting from this assumption remain reasonable. The full spread angle of the jet (Θ) was introduced in the literature based on some experiments. This value can be estimated as $\Theta=24^\circ$ [136]. The value of F_u at the jet spread angle, $r/x=\tan(\Theta/2)$, is 0.043.

3.2.4 Radial Distribution of Mixture Fraction

The mixture fraction equation is solved with the same approach as the momentum equation. The generation term in the mixture fraction equation is zero. The mixture fraction radial profile is estimated based on self-similarity of the jet.

$$F_z(x, r) = \exp\left(\frac{-Sc_t \alpha r^2}{K_r^2 x^2}\right) \quad 3-9$$

For many gas mixing applications, the turbulent Schmidt number (Sc_t) was considered near unity [137], [138]. Here Sc_t is taken as 0.7 based on reference [139].

3.2.5 Mixture Fraction Maps

The relation between mixture fraction and scalar properties in the jet is determined in conjunction with the cylinder model (detailed in section 3.3 below). The mixture fraction maps (temperature, density and species as a function of Z) are generated in every 0.1° as the in-cylinder thermodynamic state changes. This value is selected to have minimum computational time with less than 1% error on maximum cylinder pressure compared to the fine times steps of 0.05° . For generating the maps, the enthalpy, temperature and composition at the nozzle ($Z=1$) and ambient conditions ($Z=0$) is required. As mentioned earlier, there is no progress variable defined in the model. Therefore the charge is either in a non-reacting state or in an equilibrium state. Higher reaction rate, due to the equilibrium assumption, will be partly controlled by defining an effective flame speed; more details are presented in sections 3.2.6 and 6.2.1.

The equilibrium gas compositions are determined by Cantera using the thermodynamic properties in the GRI3.0 database. GRI-Mech 3.0 is a mechanism designed to model natural gas combustion, including NO formation and re-burn chemistry [140]. The GRI3.0 database uses 53 species but the TSM module returns only the 7 major species (N_2 , O_2 , CO, CO_2 , H_2O , CH_4 and H_2) to the main loop of the model. Tracking just 7 species results in less than a 0.5% error in the species balance (see Appendix H), it would be easy extend the model later, for example by adding acetylene and NO.

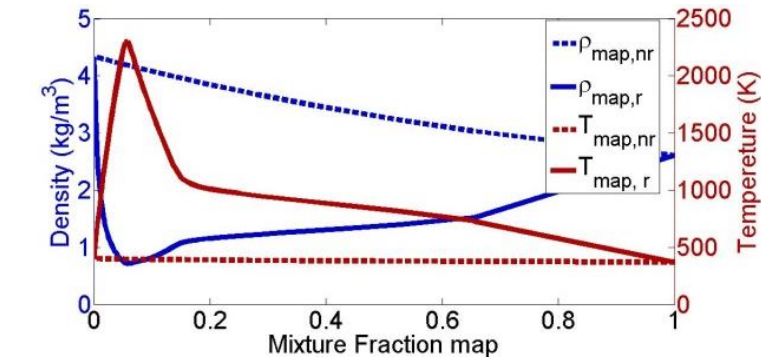
In the generation of mixture fraction maps, a mixture fraction vector ($0 \leq Z_{\text{map}} \leq 1$) is generated. Mass fraction composition, temperature and enthalpy at the nozzle ($Z_{\text{map}}=1$) and ambient ($Z_{\text{map}}=0$) are transferred to the thermodynamics script to calculate maps. The jet might include both non-reacting and reacting cells in any time step; therefore the reacting and non-reacting mixture fraction maps must be defined in each time step. The non-reacting maps ($g_{\text{map,nr}}$) are simple weighted averages for enthalpy H and mass fraction:

$$g_{\text{map,nr}} = (1 - Z_{\text{map}})g_a + Z_{\text{map}}g_n \quad g = H, [\text{O}_2], [\text{CH}_4], [\text{CO}_2], [\text{CO}], [\text{H}_2\text{O}], [\text{H}_2], [\text{N}_2] \quad 3-10$$

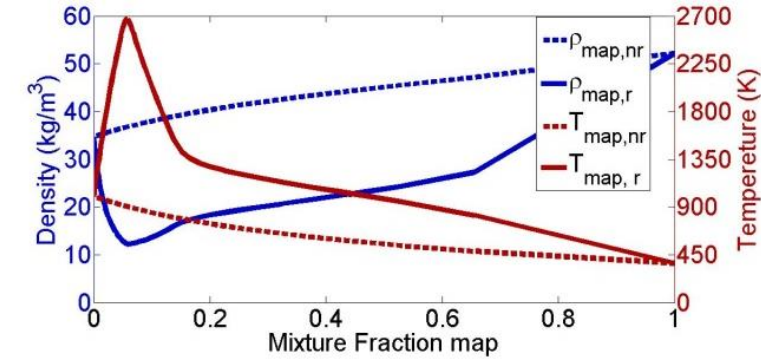
The ambient mixture composition will be set according to the SOS mixture composition (see section 3.3.1 below). Ambient enthalpy is calculated based on ambient pressure and temperature. The ambient pressure of the jet is set to the instantaneous cylinder pressure from the “cylinder model”. The ambient temperature is calculated based on ideal gas law with calculated motored pressure assuming cylinder air as the ambient mixture composition (at $Z=0$). The use of motored pressure to calculate ambient temperature neglects end-gas heating during combustion, but Figure 3-4 shows that mixture fraction maps are nearly identical for widely different ambient conditions. This issue is discussed further in section 3.3.6.

For non-reacting maps ($g_{\text{map,nr}}$), the other mixture properties (temperature, internal energy, density etc.) are found based on pressure ($P_a=P_{\text{cyl}}$), enthalpy ($H_{\text{map,nr}}$) and mixture composition ($[\text{O}_2]_{\text{map,nr}}$, $[\text{CH}_4]_{\text{map,nr}}$, $[\text{N}_2]_{\text{map,nr}}$, $[\text{CO}_2]_{\text{map,nr}}$, $[\text{CO}]_{\text{map,nr}}$, $[\text{H}_2\text{O}]_{\text{map,nr}}$, $[\text{H}_2]_{\text{map,nr}}$) at any Z_{map} at any time step.

For reacting maps ($g_{\text{map},r}$), the elemental mixture is taken from the non-reacting composition at the same mixture fraction (Z_{map}). This mixture is allowed to reach equilibrium at constant pressure ($P_a=P_{\text{cyl}}$) and constant enthalpy ($H_{\text{map,nr}}$) for each time step. Effectively this means that the process linking the non-reacting map to the reacting map is constant pressure and adiabatic. Although this is an oversimplification of the actual combustion, it should be stressed that this calculation is done only to determine mixture fractions and temperatures used in the soot model later. Energy conservation is guaranteed by an energy balance for the whole cylinder, discussed later. The mixture properties (temperature, internal energy, density, mixture composition, etc.) for each mixture fraction are set to their respective equilibrium values. A sample of the mixture fraction maps is shown in Figure 3-4 for SOS-like (a) and TDC-like (b) conditions. In this figure, the dashed lines show the non-reacting maps and the solid lines show the reacting maps. The mass fractions are insensitive to the assumed ambient temperature and pressure, but temperature and density maps, *are* sensitive to these parameters (see footnote in section 3.2.1).



(a) $P_a = 5$ bar, $T_a = 400$ K



(b) $P_a = 100$ bar, $T_a = 1000$ K

Figure 3-4 mixture fraction maps for ambient conditions approximating (a) SOS: $P_a = 5$ bar, $T_a = 400$ K and (b) TDC: $P_a = 100$ bar, $T_a = 1000$ K

In the mixture fraction maps all the mass fractions are calculated based on mixture fraction without regard to spatial coordinates. The next step is to transfer these maps to the jet physical domain in each time step. This is done by finding the mixture fraction for each cell and interpolating the scalars based on the mixture fraction maps. Based on the mixture fraction in each cell the density, temperature and mixture composition of the cell will be found based on the mixture fraction maps. This information is used later to model soot formation and oxidation.

For the next time step, the maps will be created again with different boundary conditions (P_a and T_a); however, the mass fraction of species from the previous time step will not be transferred to the next time step using transport equations.

The radial distribution of mean mixture fraction was considered in the model. However, the effect of local turbulent mixture fraction variation on combustion is not included in this version of TSM. That is, the model bases temperature on the mean mixture fraction at a specific location in the jet. In reality, there could be substantial amounts of over-lean or over-rich material that would not burn, even though the mean value is in the flammability limit.

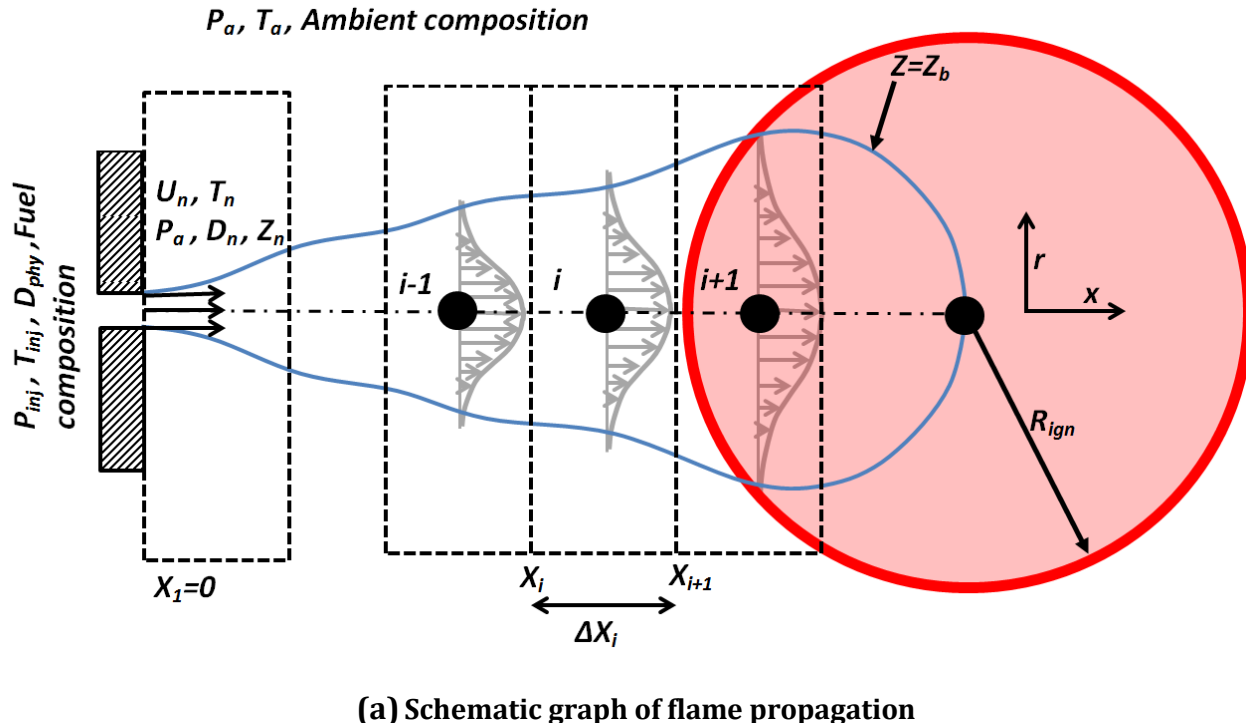
3.2.6 Ignition and Flame Propagation

Ignition timing is taken from the engine measurements, based on the apparent AHRR shape. The start of combustion was found as the intercept of the AHRR curve of the combustion event with the zero AHRR axis [55], [56], as mentioned in section 2.1. To use the TSM in a fully predictive mode, an ignition model would be needed; such a model is proposed in Appendix C.

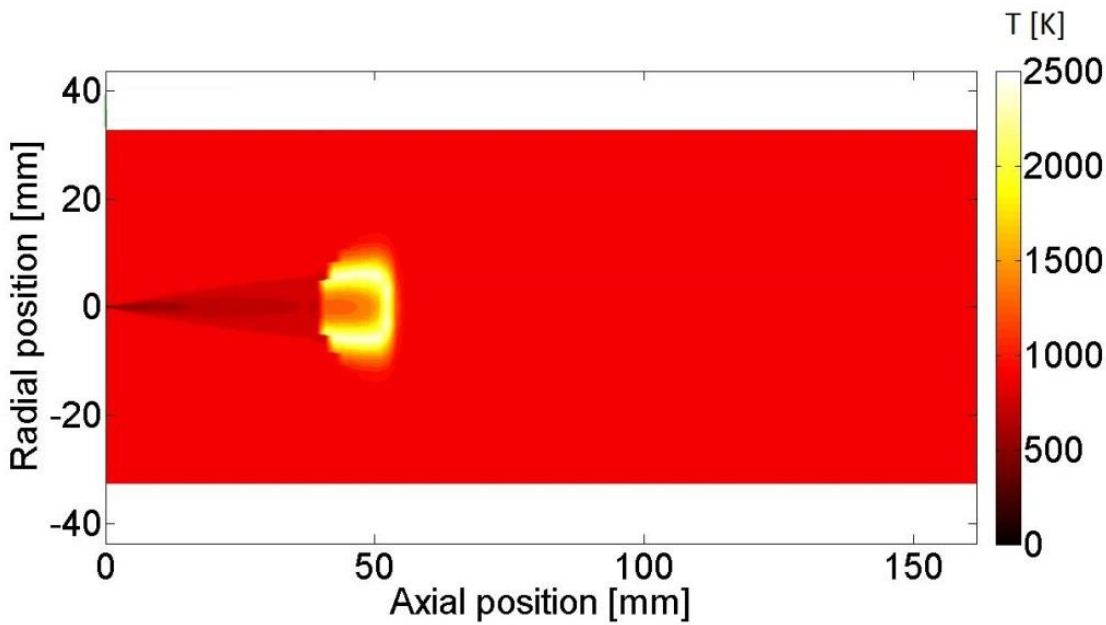
At the time of ignition, the TSM “turns on” combustion in the jet by switching from the non-reacting to reacting equilibrium maps. This process of turning on combustion is a simplified simulation of turbulent flame propagation from an assumed ignition point. At the

ignition time, the tip of the jet (defined as $Z=0.01$)⁵ is selected as the initial ignition site. Based on CFD simulations of HPDI combustion, ignition is expected to occur near the head of the jet.

A circle with increasing radius from the ignition time defines the burning zone; all the cells inside the burning zone are already ignited while the cells outside of the burning zone are still inert mixing. The schematic figure of the ignition model is shown in the Figure 3-5(a). In each time step, some of the cells of a specific slice might be inside the reacting zone. For the cells inside the reacting zone (red circle in the figure) the reacting thermodynamics maps will be used and for the cells outside the reacting zone the inert maps will be used. A parameter called ignition switch ($\text{IgnSw}_{i,j}$) is defined in the model with the values of 0 or 1, the zero value is for the cells outside of the jet and 1 is for all the cells inside the burning zone in each time step. A sample of temperature contour after using the mixture fraction maps for reacting and non-reacting part is presented in Figure 3-5(b).



⁵ At the tip of the jet, mixture fraction gradients are very steep, so any reasonable value of Z in the flammable regime would result in a very similar position. The selection criteria for the tip of the jet is discussed in details in reference [134].



(b) A sample of tempereture distribution after ignition point

Figure 3-5 Ignition and flame propagation (a) Schematic of the ignition model (b) a sample of temperature distribution⁶

The center of the reacting zone circle moves with the tip penetration. The radius of this circle is defined as:

$$R_{ign} = S_t(t - t_{ign}) \quad 3-11$$

The initial value for effective flame speed (S_t) is selected as 20 m/s to match the AHRR slope at the start of ignition for mode B75 baseline (Figure 3-6). S_t is not adjusted to model other engine modes, but later it will be seen that S_t should be adjusted to model SPC combustion, which has a much larger premixed burn. All the tuning parameters of the TSM model can be found in section 3.5.

⁶ The video of the temperature distribution can be found here: https://youtu.be/8y_hwVDENOg

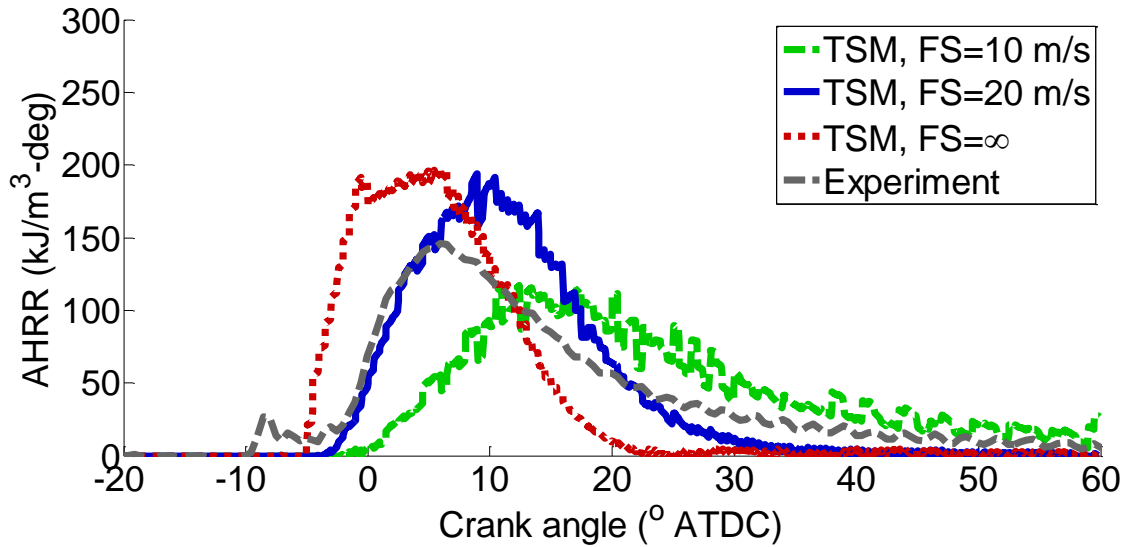


Figure 3-6 Impact of effective flame speed on modelled AHRR

3.2.7 Jet Integral Calculations

The mixture composition in the model is calculated based on the integral of each species in the entire numerical domain. The integral in equation (3-12) is defined as $(Y - Y_a)$ to avoid infinite results in integral calculations of non-zero species in the ambient.

$$Y_{cyl} = \frac{\int_0^{tip} \int_{r=0}^{\infty} \rho(x, r, t) [Y(x, r, t) - Y_a] 2\pi r dr}{m_{cyl}} + Y_a \quad 3-12$$

In this equation Y_a is the species mass fraction in the ambient, $Y(x, r, t)$ is the species mass fraction at any time and location in the domain, ρ is the density in each cell and “tip” is the tip of the jet. The mixture composition of the cylinder is then calculated based on the mass of cylinder and ambient species mass fraction. Appendix D shows a sample calculation for oxygen in non-reacting jets. The ambient species mass fraction is set based on SOS composition. The mixture composition is transferred to the cylinder model.

3.3 Cylinder Thermodynamics Model

The preceding sections described the jet and scalar variations within the jet. The TSM model must also respect conservation laws for the entire cylinder, as discussed below.

3.3.1 Initial Conditions at SOS

The simulation starts from -90° ATDC and ends at 90° ATDC (the model EOS). The pressure, temperature and mixture composition at the SOS are the inputs for the model. These inputs can be manually set by the user or read from a specific experiment. The intake pressure is equal to the experimental pressure reading at -90° ATDC, intake temperature is found based on ideal gas assumption at SOS and the mixture composition at the SOS is set by:

$$\begin{aligned}
 [O_2]_{sos} &= 0.232 \left(1 - \frac{EGR}{100} \right) \\
 &\quad + \frac{EGR}{100} \frac{32(2 - 2EQR)}{32(2 - 2EQR) + 7.56 \times 28 + 2EQR \times 18 + 44EQR} \\
 [N_2]_{sos} &= 0.768 \left(1 - \frac{EGR}{100} \right) \\
 &\quad + \frac{EGR}{100} \frac{7.56 \times 28}{32(2 - 2EQR) + 7.56 \times 28 + 2EQR \times 18 + 44EQR} \\
 [CO_2]_{sos} &= \frac{EGR}{100} \frac{44EQR}{32(2 - 2EQR) + 7.56 \times 28 + 2EQR \times 18 + 44EQR} \\
 [H_2O]_{sos} &= \frac{EGR}{100} \frac{2EQR \times 18}{32(2 - 2EQR) + 7.56 \times 28 + 2EQR \times 18 + 44EQR}
 \end{aligned} \tag{3-13}$$

In this equation, mass fractions of the species ($[O_2]_{sos}$, $[N_2]_{sos}$, $[CO_2]_{sos}$, $[H_2O]_{sos}$) are set based on the input of EGR and oxygen EQR (both from the experimental points, defined in Chapter 2, Equations 2-1 and 2-2. The cylinder pressures (P_{cyl}), temperature (T_{cyl}) and mass fraction of species (Y_i) are equal to the SOS conditions. T_{sos} is calculated based on ideal gas law knowing the inlet mass flow rate.

3.3.2 Cylinder Volume

The volume of the cylinder can be found from the geometry of the engine [7].

$$V_{cyl}(\theta) = V_c \left[1 + \frac{1}{2} (r_c - 1) \left[R_c + 1 - \cos\theta - (R_c^2 - \sin^2\theta)^{1/2} \right] \right] \quad 3-14$$

where r_c is compression ratio, R_c is connecting rod length to crank radius ratio, V_c is clearance volume and V_{cyl} is the cylinder volume.

3.3.3 Cylinder Mass Balance

Between SOS to EOS, the mass of the cylinder is increased by fuel injection.

$$\frac{dm_{cyl}}{d\theta} = \frac{dm_{inj}}{d\theta} \quad 3-15$$

Initial mass can be calculated from conditions at SOS.

$$m_{sos} = \frac{P_{sos} V_{sos}}{R_{sos} T_{sos}} \quad 3-16$$

3.3.4 Cylinder Energy Balance

The energy balance can be written as

$$\frac{dE_{cyl}}{d\theta} = h_n \frac{dm_{inj}}{d\theta} - P_{cyl} \frac{dV_{cyl}}{d\theta} - \frac{dQ_w}{d\theta} \quad 3-17$$

The work done by the piston is known based on the volume change of the cylinder and pressure. If we know the fuel rate shape then we can find the energy entrance rate into the cylinder. Here Q_w is the wall heat transfer discussed below in section 3.3.5. From equation (3-17), we can find the $E_{cyl}|^{t+1}$, which is the cylinder internal energy at the next time step. By calculating the internal energy of the cylinder, specific volume of the cylinder (based on mass and volume of cylinder) and mixture composition of the cylinder (from the jet model,

Equation 3-12), pressure and temperature in the next time step will be calculated by Cantera assuming frozen composition (necessary because the spatial distribution of fuel and air is not considered *in the cylinder model* portion of TSM).

3.3.5 Cylinder Wall Heat Transfer

The wall heat transfer is calculated based on Woschni heat transfer correlations [141], [142]:

$$\frac{dQ_w}{d\theta} = h_w A_{cyl} (T_{cyl} - T_w) \quad 3-18$$

In this equation, h_w is the convective heat transfer coefficient, T_w is the wall temperature and is set to 500K in this model. A_{cyl} is surface area (function of θ), and is defined as:

$$A_{cyl}(\theta) = A_{hs} + A_p + \frac{\pi B L}{2} \left[R_c + 1 - \cos\theta - (R_c^2 - \sin^2\theta)^{1/2} \right] \quad 3-19$$

In this equation, A_{hs} is the cylinder head surface area, A_p is piston surface area, B is bore and L is stroke. Heat transfer coefficient can be estimated by [141], [142]:

$$h_w = 3.26 B^{-0.2} P_{cyl}^{0.8} v^{0.8} T_{cyl}^{-0.53} \quad 3-20$$

where v is characteristic velocity found by:

$$v = 2.28 c_m + 3.24 \times 10^{-3} \frac{V_d T_{ivc}}{P_{ivc} V_{ivc}} (P_{cyl} - P_{mot}) \quad 3-21$$

In this equation, V_d is the displacement volume, P_{mot} is the calculated motored pressure (described in section 3.3.6) and c_m is the piston speed.

$$c_m = \pi N L \sin\theta \left[1 + \frac{\cos\theta}{(R_c^2 - \sin^2\theta)^{1/2}} \right] \quad 3-22$$

where N is rotational speed.

3.3.6 Motored Pressure and Temperature

Motored pressure and temperature calculations are compared with the cylinder pressure in post processing and calculation of the wall heat transfer coefficient. The motored pressure can be found based on assuming a polytropic process. The polytropic index, "n", is estimated by matching the calculated motored pressure to SCRE motored pressure trace, thereby including heat transfer effects. In calculation of motored pressure, blowby is neglected and "n" is 1.35.

$$\frac{dP_{mot}}{d\theta} = -n \frac{P_{mot}}{V_{cyl}} \frac{dV_{cyl}}{d\theta} \quad 3-23$$

The motored temperature (T_{mot}) will be found based on ideal gas law using this pressure, the known volume, and the moles of the unreacted intake charge.

3.4 Soot Model

The output of the velocity, mixture fraction, temperature, oxygen mass fractions and pressure will be used in the soot model. The model is not coupled with the main loop of the jet model, see Figure 3-2. The soot model is a 2D implementation of the commonly-used Hiroyasu model. Radial mass fluxes will be calculated based on the conservation of mass for each cell.

$$FluxX_{in} - FluxX_{out} + FluxY_{in} - FluxY_{out} = \frac{dm_{i,j}}{dt} \quad 3-24$$

In this equation FluxX is the mass flux in axial direction for each cell and FluxY is the mass flux in the radial direction for each cell. The subscript 'in' shows into the cell and 'out' is the flux out of the cell. FluxX for each cell is already known from the velocity calculations and FluxY from, equation 3-24. Assuming the axisymmetric flow $FluxY_{in}$ at any cell in the centerline of the jet is zero. The indices i and j are in axial and radial direction respectively.

The soot transport equation can be written as:

$$\begin{aligned} & FluxX_{in}S_{i-1,j} - FluxX_{out}S_{i,j} + FluxY_{in}S_{i,j-1} - FluxY_{out}S_{i,j} \\ & = \frac{dS_{i,j} + S_{form} - S_{ox}}{dt} \end{aligned} \quad 3-25$$

Fluxes in each cell are known based on equation (3-24).

The soot formation rate is estimated by:

$$S_{form} = Af Z^{c1} P^{c2} \exp\left(\frac{-Taf}{T}\right) \Delta t \quad 3-26$$

The oxidation rate is estimated as:

$$S_{ox} = Aox m_s [O2]^{c3} P^{c4} \exp\left(\frac{-Ta_{ox}}{T}\right) \Delta t \quad 3-27$$

In this equation, m_s is the mass of soot, P is the cylinder pressure calculated from the cylinder thermodynamics model and $[O2]$ is the mass fraction of oxygen in each cell. All the units in these equations are SI; [K] for temperatures and [Pa] for pressures. The parameters used in 3-26 and 3-27 are discussed in the next section.

3.5 Summary of Adjustable Parameters in TSM

TSM employs many sub-models, with the potential for many tunable parameters (Table 3-1). However, most are taken from the literature and there are only 4 parameters tuned in this model: effective flame speed (S_t), soot formation constant (Af), soot oxidation constant (Aox) and the exponent of oxygen in the soot oxidation equation (C_3). Adjusting of the effective flame speed has been shown in Figure 3-6. To select appropriate values for 3 parameters for the soot model, three experimental points have been selected: model B75 baseline where most of the experiments have been performed, B75 with zero EGR where oxidation is much higher compared to the baseline case and repeat mode (35% of load at 1200 rpm, A35) where the soot formation is much lower. Different tuning methods are considered and reported in Appendix B. The results of soot prediction from TSM are compared to denuded PM from DRX measurements. The spatial mesh and crank angle (time step) size for all the simulations have been held constant (Appendix B).

The other 8 parameters were selected and held constant based on previous studies. For the soot model, the constants (C_1 , C_2 , T_{af} , C_4 and T_{aox}) are set based on Reference [103].

Table 3-1 TSM model parameters

	Constant	Value	Sub-model/Equation	Selection method
Tuned	S_t	20 m/s	Ignition and flame propagation, , Equation (3-11)	Based on slope of HRR at the start of ignition for B75
	A_f	100	Soot (formation) , Equation (3-26)	B75, B75-0 EGR, repeat mode
	A_{ox}	$4*10^{-6}$	Soot (oxidation) , Equation (3-27)	B75, B75-0 EGR, repeat mode
	C₃	5	Soot (oxidation) , Equation (3-27)	B75, B75-0 EGR, repeat mode
NO Tuning	K_r	0.085	Velocity, Equation (3-8)	Literature, non-reacting jet
	A	0.63	Velocity, Equation (3-8)	Literature, non-reacting jet
	S_{ct}	0.85	Mixture fraction, Equation (3-9)	Literature, non-reacting jet
	C₁	1.0	Soot (formation) , Equation (3-26)	Literature, Hiroyasu soot models
	C₂	0.5	Soot (formation) , Equation (3-26)	Literature, Hiroyasu soot models
	T_{af}	6313	Soot (formation) , Equation (3-26)	Literature, Hiroyasu soot models
	C₄	1.8	Soot (oxidation) , Equation (3-27)	Literature, Hiroyasu soot models
	T_{aox}	7110	Soot (oxidation) , Equation (3-27)	Literature, Hiroyasu soot models

3.6 CFD Modeling (GOLD)

This thesis has used GOLD, developed at Westport Innovations Inc. by Huang [90]. GOLD is a three-dimensional CFD model incorporating detailed chemical kinetic mechanisms built on OpenFOAM, with additional modules to simulate the combustion of diesel and natural gas in a non-premixed turbulent regime and heat transfer models. The main objective of the modeling is to evaluate the local equivalence ratio, the local temperature and soot concentration during the injection and combustion event and use that information to interpret the experimentally-measured emissions results.

The numerical domain is one-sector region of the combustion chamber including one gas nozzle (of 9 gas nozzles) and one diesel nozzle with periodic boundary conditions for two sides. The simulation starts at -90° ATDC to EVO at 140°. More information about the numerical domain and mesh resolutions can be found in reference [144]. A first-order scheme for time integration and a second-order upwind scheme for spatial integration are employed. The turbulent flow is resolved using a Large-Eddy Simulation (LES) method with one extra transport equation for kinetic energy.

The detailed chemical kinetic mechanisms were implemented through a trajectory-generated low-dimensional manifold (TGLDM) method [145] using detailed chemical kinetic mechanisms for natural gas and heptane (a surrogate for diesel fuel). The mathematical details of the method are beyond the scope of this work and are explained in [145]. Two implementations were developed based on the manifold methods, Intrinsically Low Dimensional Manifolds (ILDM) [145], and Trajectory Generated Lower Dimensional Manifolds (TGLDM) [146]; the latter was implemented in the GOLD [143]. Natural gas was simulated with a modified GRI mechanism [147], [148], while heptane used a Lawrence Livermore National Lab (LLNL) mechanism [149]. The complete mechanism was used to generate the TGLDM libraries. The complete mechanism is time-consuming, however, the chemistry calculations are only performed prior to the simulations to generate the libraries. The libraries are usually used for many cases with similar conditions. During the simulations the whole process is reduced to table-lookup. The interactions between turbulence and chemical reaction were addressed using the conditional source term estimation (CSE) method [150]. The CFD model has been extensively validated against in-cylinder pressure, heat-release, and NOx emissions data from single- and multi-cylinder HPDI natural gas engines and more detail on the model is reported elsewhere [74]. The soot mechanism uses the Hiroyasu model with constants tuned for mode B75. GOLD models soot formation and oxidation in cylinder. The results of soot prediction from GOLD are compared to denuded PM from DRX measurements. More information about the GOLD and implementation of new injection strategies in GOLD can be found in reference [144].

3.7 φ -T Map

The equivalence ratio-temperature map (φ -T map) is used to represent the cylinder state at each time step. The understanding of soot and NOx formation in engines can be aided by examination of combustion process in a φ -T map [39]. This type of analysis consists of a background image where relevant emission contours are generated based on a perfectly stirred reactor (PSR) calculation for an engine relevant resident time. The foreground of these figures shows the instantaneous location of fuel packets on the map. Figure 3-7 is a φ -T map generated for natural gas combustion. The contours show the location where acetylene (a soot precursor) and NOx formation occur for NG. The acetylene and NOx are calculated based on the Cantera Perfectly Stirred Reactor model [132] using the GRI3.0 mechanism for NG (taken as 95.1% of CH₄, 3.7% of C₂H₆ and 1.2% C₃H₈). The selection of the pressure and residence time is based on previous analysis of φ -T map in the literature [40]; residence time was 2ms and pressure (140 bar) was close to the maximum pressure of cylinder. The chemical kinetics was solved at constant temperature in order to generate contours for C₂H₂, CO, and NO. This map has been used in Chapter 5 and earlier theses [45], [144]. The numbers in the φ -T map are concentrations of each species in the combustion mixture of PSR calculations. The numbers are only presented to show the relative position of high and low concentrations of the species.

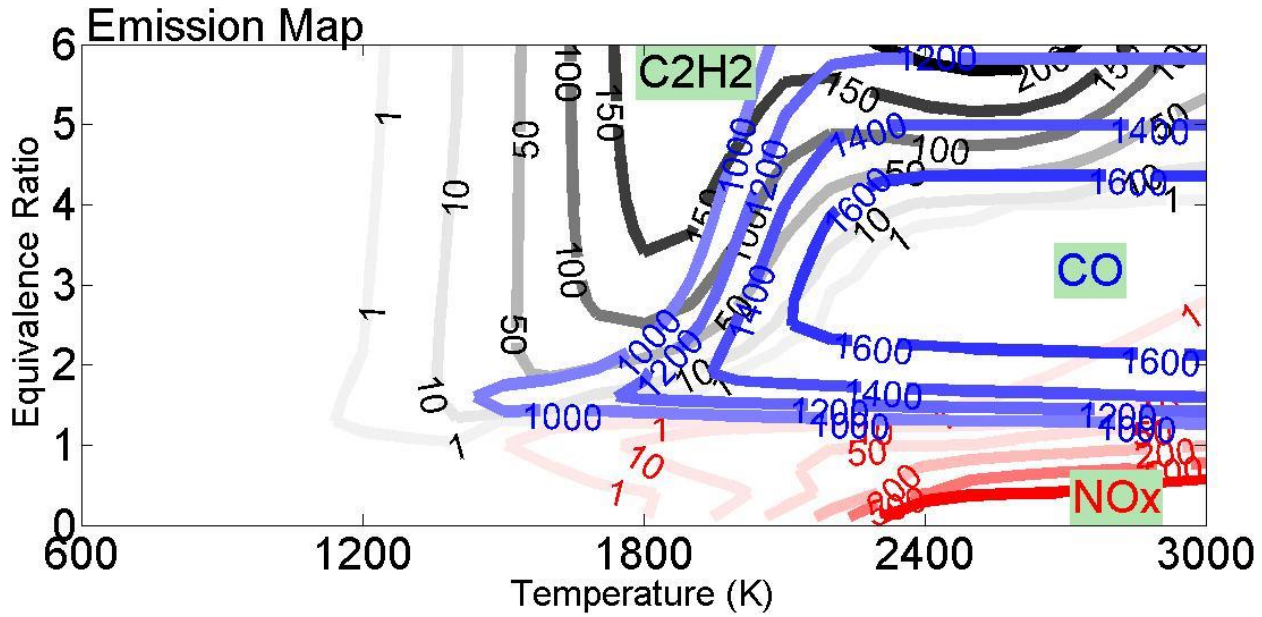


Figure 3-7 φ -T map generated for Natural Gas (96% Methane) at a pressure of 140bar and a residence time of 2 ms. The numbers in the map are the concentration of each species, showing the relative position of high and low concentrations of the species.

Two parameters (Z_{lean} and Z_{rich}) will be defined here to show the rich and lean mixture evaluation in the cylinder. These values will be calculated from CFD and TSM modelling and can be used to show the mixture status at any time. The normalized mass of rich mixture in the chamber is measured by Z_{rich} . In this equation, m_{NG} is the total mass of NG fuel injected in the cycle and Z is the mixture fraction.

$$Z_{\text{rich}} = \frac{\sum_{\text{all cells}} (\rho V Z)_{\text{for } 2 < EQR < 5}}{m_{\text{NG}}} \quad 3-28$$

And Z_{lean} is defined as:

$$Z_{\text{lean}} = \frac{\sum_{\text{all cells}} (\rho V Z)_{\text{for } EQR < 1}}{m_{\text{inj}}} \quad 3-29$$

Z_{rich} and Z_{lean} take values between 0 and 1. Z_{lean} is a monotonically increasing function approaching 1 by the end of the cycle as the injected fuel is completely mixed with the charge. On the other hand, Z_{rich} rises as the injection starts and then drops to zero shortly after the end of injection.

4 RESULTS FOR LATE POST INJECTION

Early in this thesis research, LPI was studied by the author for a range of parameters [1]. That research showed, among other things, that close-coupled injections were not effective for HPDI engines, and motivated the experiments described here.

The main objective of this chapter is to apply post injection to HPDI engines in a systematic study, for the first time, and understand the mechanism of PM reduction in the LPI strategy. The potential application of post injections (close-coupled and late post injections of gas) in HPDI engines is discussed. In the study described in this chapter, the “optimized” LPI point⁷, was found based on gas pulse separation (GSEP; see Figure 2-2) and portion of fuel mass in the second pulse (SI). For example SI=10% indicates that 10% of the NG is injected in the second injection. SI is determined by measuring the total fuel mass flow with and without the second injection. This assumes that the second injection event does not influence the first injection event- an issue discussed below.

The performance of this injection strategy at different engine speed and load combinations was also studied and similar PM reductions were noticed, albeit with slightly higher fuel penalty. PM size and morphology for the LPI strategy has been studied. The mechanism of PM reduction from the LPI injection strategy for HPDI engines is studied by novel “pulse isolation” experiments. Multi-injector tests were performed to show the performance of LPI injection strategy using other injectors of the same model. The experimental results are supported by CFD simulations. It will be shown that LPI in HPDI engines is associated with higher PM reductions and lower fuel penalties compared to diesel engines when equivalent second injection timing and portions of fuel injected in the second pulse.

⁷ Maximum PM reduction with less than 1% fuel consumption penalty in B75 mode in the parameter sweeps

4.1 Experimental Design

4.1.1 Momentum Measurement

A method of momentum measurement for gas injections was developed in order to present transient momentum rate shape during injection timing as discussed in section 2.2, reference [2].

The results for post injections show the momentum rate of the second pulse decreases as the pulse separation (GSEP) decreases and will disappear completely for $GSEP < 0.6\text{ms}$ (Figure 4-1). The first pulse can affect the second pulse when the opening command of the second pulse interferes with the dynamics of the closing needle from the first pulse. In this case, the command signal for the second pulse is actuating the injector while the needle is not fully closed from the first pulse. Another parameter affecting the second pulse is the rail pressure pulsation due to the opening and closing of the needle during the first pulse. From the diesel literature, the rail pressure fluctuations can affect the injected mass and performance of the injection strategy, but the effect is expected to be small and repeatable [59], [151].

For the HPDI injector, momentum measurements show that if $GSEP > 1.3\text{ ms}$ then the first pulse will not affect the second pulse. These results imply that to apply split injection strategies in an engine using the current injector, it is necessary to have at least $GSEP > 1.3\text{ ms}$ for the effective second injection with higher momentum rate and lower variability. The results show that for a small second pulse or small pulse separation the variation is higher and might affect the performance of the post injection strategy in NG engines [2].

The mass of fuel in the second injection for a given pulse width depends on the location of the second pulse in the cycle relative to the first pulse. In the engine experiments, instead of setting the GPW2 constant, the points were set based on SI. This leads to slightly ($\pm 0.05\text{ ms}$) different GPW2 depending on the timing of the second injection. The effect of GSEP on total NG mass flow was also tested on the engine in the preliminary experiments; it was found that for small $GSEP < 1\text{ ms}$ the total NG flow is lower than large GSEP points and the

combustion of the second pulse is less distinct in AHRR graph as well, consistent with the momentum measurement tests.

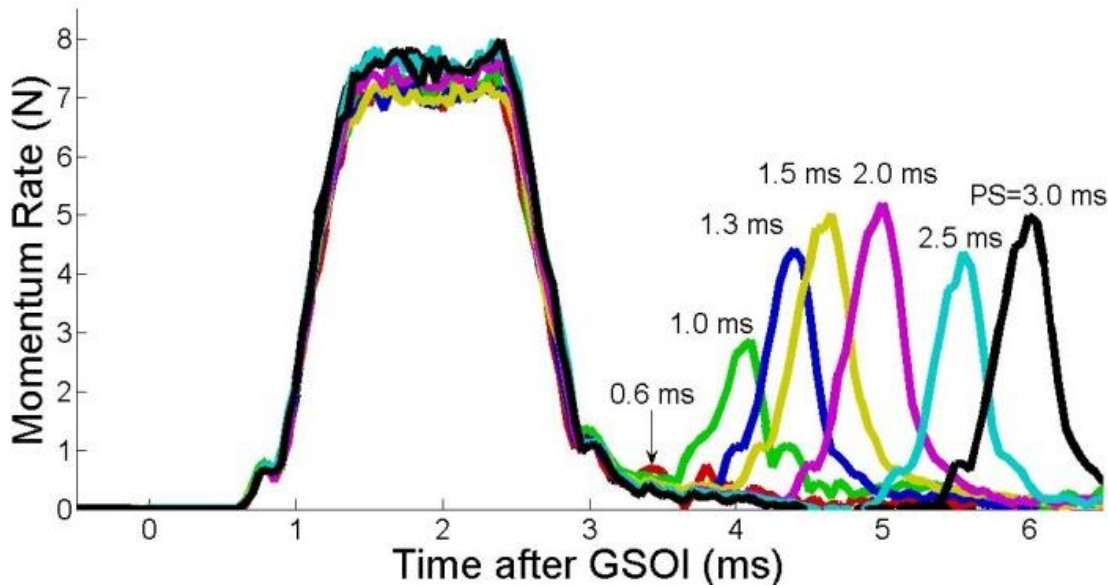


Figure 4-1 Experimental measurement of momentum rate for split injection cases⁸

The variability of small pulses, measured by COV of total momentum per injection, is shown in reference [2]. For small pulses (GPW of 0.6 ms) COV of the total momentum per injection is 2.1% while for longer pulses (GPW of 1.8 ms) this value is 0.9%. Also for small GSEP values ($GSEP < 1.5$ ms) the variability of the pulses is higher as well, as is shown in Appendix R, mainly due to the lower magnitude of the momentum rate for small GSEPs. In this thesis, HPDI post injections with $GSEP \leq 1.5$ ms are called “close-coupled”.

4.1.2 Engine Experiments

The definition of engine operating modes was discussed in Chapter 2. The parameters kept constant for the LPI strategy for each mode were: engine speed, GIMEP, EGR level, oxygen-based equivalence ratio (EQR), gas rail pressure, diesel injection mass (mg/inj.) and pilot

⁸ Copyright © 2015 SAE International. This figure is included in this thesis with permission from SAE International. Further use, copying or distribution is not permitted without prior permission from SAE.

separation (PSEP). Each mode was compared to a baseline single injection strategy that matches PSOI and GSOI. The set parameters for different modes were chosen to provide NOx-PM tradeoffs generally equivalent to those found in a multi-cylinder engine. Emissions results were normalized by the gross-indicated power. Similarly, the fuel consumption was reported on a diesel energy-equivalent basis, and was normalized by the gross-indicated power (GISFC). Since the diesel injection per cycle is constant, the natural gas injection is adjusted to set GIMEP.

Three sets of experiments were run on the SCRE. The first sets of experiments were GSEP and SI sweeps at mode B75. This set of experiments was done to show the effect of GSEP and SI on the engine-out emissions, engine performance, and from this select the best (“optimized”) LPI settings for the SCRE. The optimized GSEP and SI settings are then selected and compared with the single injection strategy; limited PM characterization was done for these conditions. The second set of experiments was designed to understand if the benefits at B75 are also seen at other modes. This is presented in the multi-mode experiments. The third series of tests were “pulse isolation” tests and were performed to answer fundamental questions about PM reduction in HPDI engines. For all experiments all engine points were measured at least twice.

4.1.3 Mode B75 Tests: GSEP and SI Sweeps

These tests were done at mode B75 with the conditions presented in Table 4-1, covering a wide range for the size and timing of the second injection. A total of 25 conditions were run.

The timing for the single injection strategy is set to provide CA50 at 11° ATDC. The injection timing (PSOI and GSOI) of the LPI points are set according to the single injection strategy. The CA50 for the LPI points are later than their equivalent baseline point. If we keep the CA50 constant, that means the first pulse needs to be advanced and therefore the AHRR and pressure of the LPI points would be different from the baseline point even before injection of the second pulse. In our preliminary study [1], we kept the CA50, the LPI points had slightly higher P_{max} due to advancing the first pulse. In the work reported in this

chapter, the first injection timing is kept constant to simplify the interpretation. However, these two methods of controlling the timing are very similar. For the optimized LPI point the CA50 is less than 1° later than the baseline single injection.

The injection timings of the points are included in Appendix Q.

Table 4-1 Summary of the mode B75 GSEP and SI sweep tests

Injection Method (constants)	SI%	GSEP [ms]
Single injection B75* PSEP=0.3 ms, CA50= 11 °CA ATDC	0	-
Late post injection B75* PSOI= -23 ° ATDC, GSOI= -15 ° ATDC	10	1.0, 1.5, 2.0, 2.5, 3.0, 3.5
	15	1.0, 1.5, 2.0, 2.5, 3.0, 3.5
	20	1.0, 1.5, 2.0, 2.5, 3.0, 3.5
	25	1.0, 1.5, 2.0, 2.5, 3.0, 3.5

* engine speed=1500 rpm, diesel mass=11 mg/inj, GIMEP=16.5 bar, EGR=18%, EQR=0.6, NG pressure= 25 MPa.

The parameter sweep ranges (GSEP=1-3 ms and SI=10-25%) are selected based on preliminary LPI studies presented in [1]. As mentioned in the momentum measurement results, the lower GSEP or SI was not possible due to injector limitations. Higher GSEP or SI were not interesting, mainly due to significantly higher GISFC for both cases.

4.1.4 Multi-Mode Tests

Single injection and LPI operation was tested at modes A75, B75, C75 and B87 (Table 4-2). The size of the second injection in LPI was held at SI=15%. The CA50 is first set for the single injection tests in each mode and then the LPI strategies are set based on the same PSOI and GSOI as the single injection strategy. This means that typically, the LPI tests have a later CA50 (for all cases, less than 1° later). For modes other than B75 (RPM other than 1500), two methods were used to set GSEP: a) GSEP=2.0 ms and b) keep separation equal to 18 crank angle degrees. The SI and GSEP for the multi-mode tests were selected based on the best point of the mode B75 experiments. The goal of these tests were not to optimize LPI for each mode but rather show the robustness of LPI strategy in other modes based on

the best point of a high PM-forming mode (B75). The injection timings of the points are included in Appendix Q.

Table 4-2 Summary of the multi-mode tests for single injection and LPI

Mode	Inj. Type	Speed [RPM]	GIMEP [Bar]	EGR [%]	EQR	GRP [Mpa]	Diesel [mg/inj]	PSEP [ms]	CA50 [° ATDC]	GSEP [ms]
A75	S	1200	16.3	15	0.60	25	9	0.4	16	-
	LPI	1200	16.3	15	0.60	25	9	0.4	-	2.0, 2.5
B75	S	1500	16.5	18	0.60	25	11	0.3	11	-
	LPI	1500	16.5	18	0.60	25	11	0.3	-	2.0
C75	S	1750	14.0	18	0.60	25	7	0.4	9	-
	LPI	1750	14.0	18	0.60	25	7	0.4	-	1.7, 2.0
B87	S	1500	19.3	15	0.63	27	10	0.2	11	-
	LPI	1500	19.3	15	0.63	27	10	0.2	-	2.0

4.1.5 Pulse Isolation Tests

The goal of this set of experiments was to better understand the incremental effect of the post injection while keeping the conditions of the first injection as constant as possible. Keeping conditions constant is non-trivial considering EGR effects, so several types of experiments with different “reference points” were used, as discussed below and also in Table 4-3.

The baseline point is a regular mode B75 point and the parameters adjusted to set this point are the same as the multi-mode tests for B75. NG flow, manifold absolute pressure (MAP), back pressure (BP), $[O_2]_{intake}$, PSOI, GSOI from the baseline point will be used to set the other points⁹. MAP is set by adjusting the intake pressure and BP is set by adjusting the back pressure valve. Table 4-3 shows all the data points of this block of testing.

⁹ These values are respectively: NG flow= 7.5 kg/hr, MAP=2.5 bar, BP=1.5 bar, $[O_2]_{intake}=20.5\%$, PSOI=-23°ATDC and GSOI=-15°ATDC.

Table 4-3 Summary of the pulse isolation tests

	Sweep or Point Name	NG flow in the first pulse (kg/hr)	NG flow in the second pulse (kg/hr)	First set point parameter	Second set point parameter
Single Injections	Reference point 1	6.4	-	EGR=18%	EQR=0.6
	Reference point 2	6.4	-	BP= 1.5 (bar)	MAP= 2.5 (bar)
	Single injection sweeps	3.7 to 8.6	-	[O2] _{intake} =20.5%	MAP=2.5 (bar)
LPI Sweeps GSEP=2.0 ms	LPI sweep 1	6.4	0.4 to 2.6	[O2] _{intake} =20.5%	MAP=2.5 (bar)
	LPI sweep 2	7.54	0.7 to 1.1	[O2] _{intake} =20.5%	MAP=2.5 (bar)

* engine speed=1500 rpm, diesel mass=11 mg/inj, NG pressure= 25 MPa, PSOI=-23°ATDC and GSOI=-15°ATDC

Figure 4-2 shows the changes to injection command timings involved in three main sweeps of this block of testing.

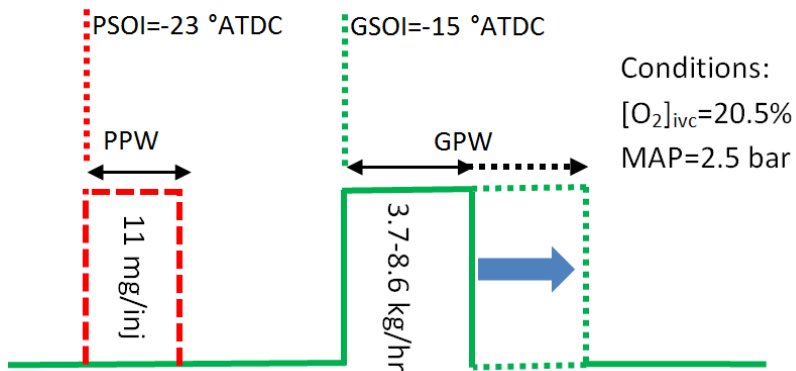
Reference point 1 uses a single injection with 85% of NG flow of the baseline (6.4 kg/hr). MAP and BP were adjusted to match the baseline EGR and EQR (18% and 0.6, respectively).

Reference point 2 uses a single injection and has 85% of NG flow of the baseline, as for Reference point 1. However, now MAP and BP match the baseline values (2.5 bar and 1.5 bar, respectively).

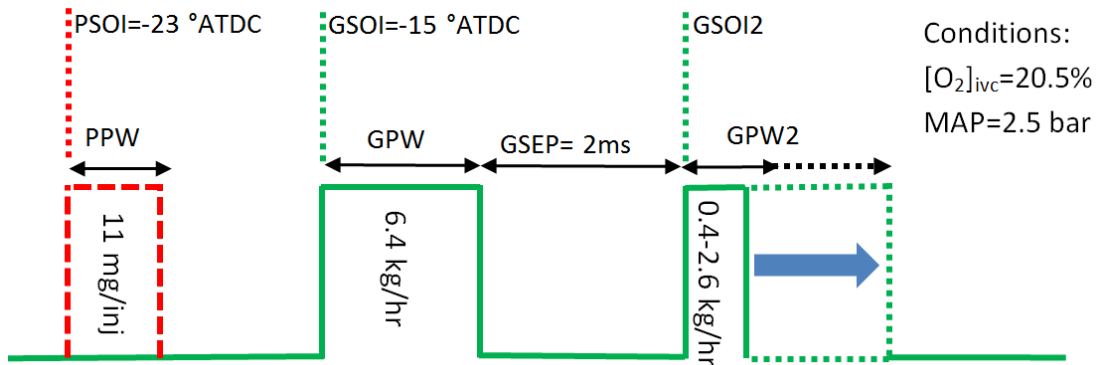
Single injection sweeps have 50-115% (3.7 kg/hr to 8.6 kg/hr) of NG flow of the baseline point. GPW is varied to achieve this point. These points have [O2]_{intake}=20.5% at MAP=2.5 bar, same [O2]_{intake} and MAP as the baseline.

LPI sweep 1 points have 85% of NG flow of the baseline point in the first injection (6.4 kg/hr) and 5-35% of the total fuel of the baseline in the second injection (0.4 kg/hr to 2.6 kg/hr). GPW is fixed and GPW2 is varied to achieve these points. BP will be adjusted for this point to achieve [O2]_{intake}=20.5% at MAP=2.5 bar. GSEP is 2 ms for all the points.

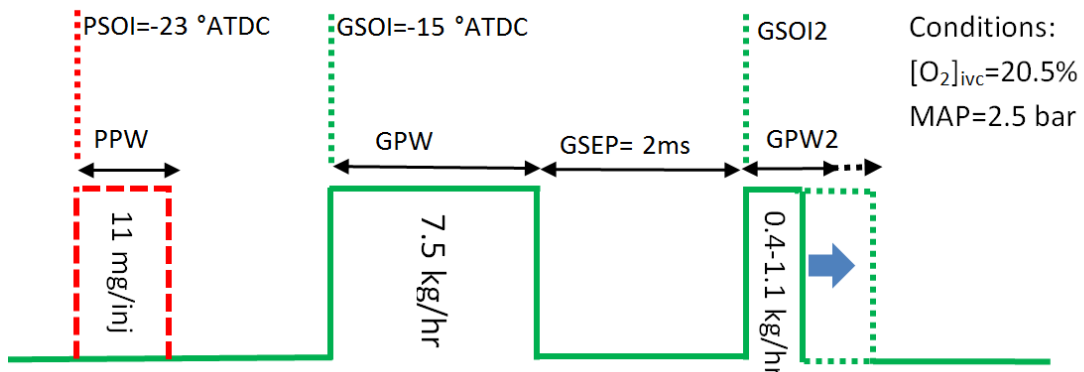
LPI sweep 2 points have 100% of NG flow of the baseline point in the first injection (7.54 kg/hr) and 5-15% of the total fuel of the baseline in the second injection (0.7 kg/hr to 1.1 kg/hr). GPW is fixed and GPW2 is varied. Backpressure is adjusted for this point to achieve $[O_2]_{intake}=20.5\%$ at MAP=2.5 bar (same as baseline). GSEP is 2 ms for all the points.



(a) Single injection sweep



(b) LPI sweep 1



(c) LPI sweep 2

Figure 4-2 Command signals for diesel (red) and gas (green) injections in pulse isolation tests

4.2 Computational Model

The GOLD CFD model (section 3.6 and reference [144]) was used to simulate the HPDI combustion for LPI strategy. In the current study we model the baseline case (PSEP=0.3 ms, EGR=18% and EQR=0.6) and LPI points listed in Table 4-4. The SI for all the LPI strategies is 15%. The CA50 is 11° ATDC for single injection and then the LPI strategies are set based on the same PSOI and GSOI as the single injection strategy. The CA50 of the LPI points are within 1° CAD of the baseline point for SI=15% from the experimental measurements. The injection timing including CA50 is presented in Appendix Q.

Table 4-4 Summary of the CFD tests

Mode	Inj. Type	Speed [RPM]	GIMEP [Bar]	EGR [%]	EQR	GRP [Mpa]	Diesel [mg/inj]	PSEP [ms]	CA50 [° ATDC]	GSEP [ms]
B75	S	1500	16.5	18	0.60	25	11	0.3	11	-
	LPI	1500	16.5	18	0.60	25	11	0.3	-	1.0
	LPI	1500	16.5	18	0.60	25	11	0.3	-	1.5
	LPI	1500	16.5	18	0.60	25	11	0.3	-	2.0

For the CFD cases the physical delay, ramp-up and ramp-down are assumed to be 0.7 ms, 0.6 ms and 0.6 ms respectively (see reference [2]) for both gas injections.

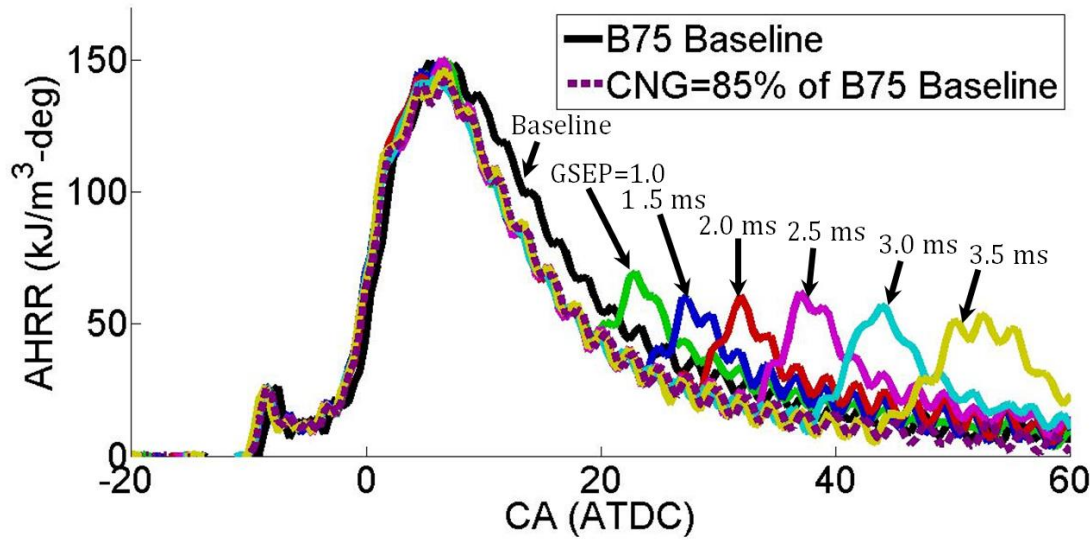
4.3 Results and Discussion

4.3.1 SCRE Experimental Results for Mode B75- GSEP and SI Sweeps

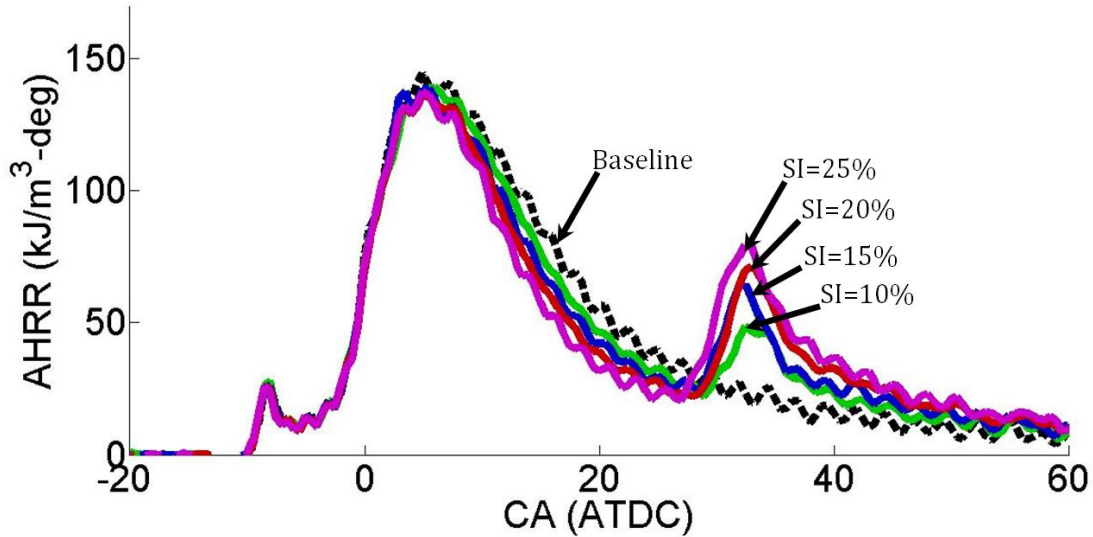
Figure 4-3 show the apparent heat release rates (AHRR) for a range of pulse separation (GSEP) and second injection mass percentage (SI), at engine mode B75. For the cases in Figure 4-3(a), the second injection has 15% of the fuel. The AHRR for the reference single injection strategy is provided for comparison. For the cases in Figure 4-3 (b), the pulse separation (GSEP) is 2.0 ms.

Additional combustion of fuel in the post injection is evident due to a second distinct bump in AHRR of all the experiments with post injections. As the gas pulse separation (GSEP) increases, the AHRR of second injection is delayed. The AHRR of the post injection is wider for the larger separation between two injections. As GPW2 (and SI%) increase, the second combustion event becomes larger and more distinct from the main event. The peak AHRR of second pulse over the no-second pulse case (CNG=85%) increases for larger GSEP cases, showing more distinct heat release for the second pulse for larger GSEPs. However, including the longer tail for the small GSEP cases, the total IHR associated with the second injection is nearly independent of GSEP.

The injection timings of the points are included in Appendix Q. A graph of CA50 and centroid of AHRR (CA_c) is also included in the appendix for both SI and GSEP sweeps. The CA_c increases about 5-6° for both sweeps of parameters while the changes in CA50 is less pronounced.



(a) GSEP Sweeps



(b) SI sweeps

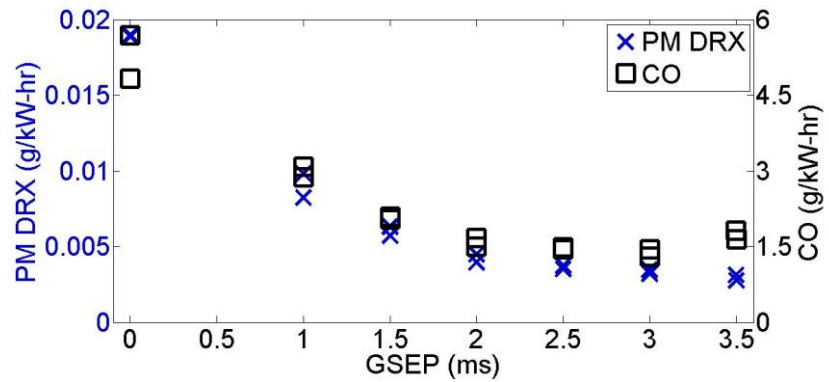
Figure 4-3 B75 heat release rate for (a) GSEP and (b) SI sweeps from SCRE experiments

Figure 4-4 and Figure 4-5 shows the summary of PM, gaseous emissions, and engine performance for different pulse separation (GSEP) at SI=15% and for different second injection mass percentage (SI) at GSEP=2.0 ms. As we increase GSEP, at first PM and CO decrease but soon reach a minimum value for GSEP>2.0ms. This decrease in PM with retarding the second injection was noticed in diesel engines [59] and HPDI engines in our

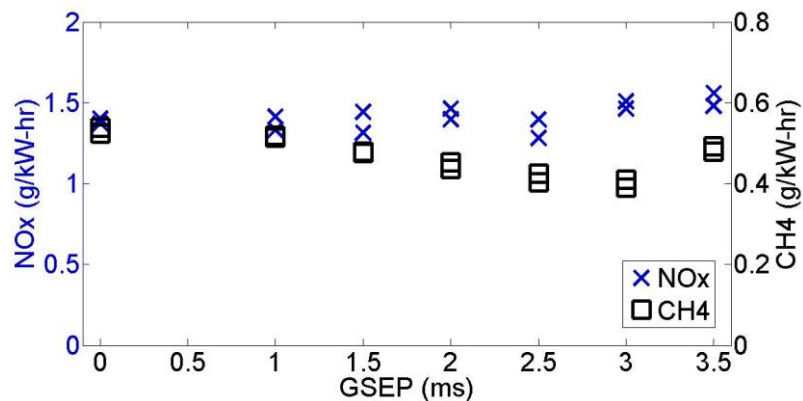
preliminary study [1] as well. As the portion of fuel in the second injection increases from 10% to 25% PM will decrease with a slight slope. Adding the second injection regardless of SI% has a major effect on PM and CO reduction. For all the cases, PM and CO show a strong correlation.

While NOx is almost the same as the baseline case, methane decreases slightly by increasing SI or GSEP. For very late injection of the second injection, methane rises slightly but is still less than the baseline point.

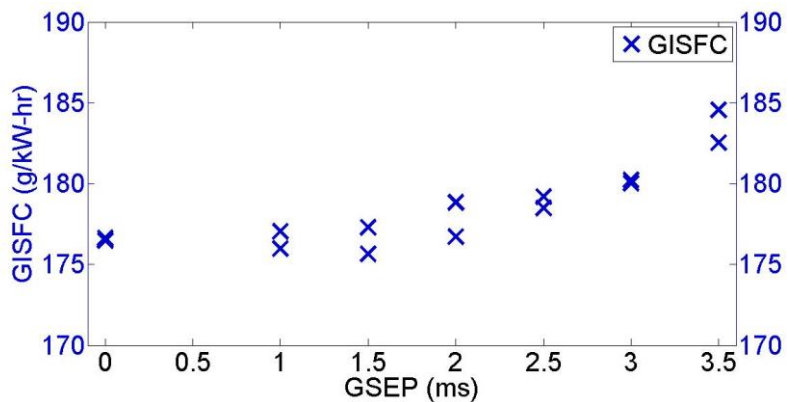
GISFC increase as the second injection is retarded or more fuel is injected in the second injection, however the changes are not significant for $GSEP \leq 2\text{ms}$. For the range of parameters considered, fuel consumption can increase 0-6%. The trend of increasing fuel consumption by retarding the second injection has been reported in previous LPI papers in both diesel [59] and HPDI engines in our first study [1]. The GISFC for the GSEP cases between 1-1.5 ms are very close to the baseline. In the diesel literature [67], [73] for close-coupled (pulse separation less than 1.4 ms), BSFC can remain unchanged possibly due to an increase in entrainment caused by the second pulse[73]. However, the higher entrainment hypothesis cannot be verified based on the current experiments. In the diesel experiments [73] it was shown that for mode A100, the BSFC can remain unchanged for pulse separations up to 1.4 ms. The start of AHRR of the second pulse (SOH2) for these points are as late as $SOH2=37^\circ$ ATDC for $SI=5\%$ and 27° ATDC for 20% of fuel. In HPDI the same GISFC points have SOH2 of 18° ATDC ($GSEP=1\text{ ms}$, $SI=15\%$) and 23° ATDC ($GSEP=1.5\text{ ms}$, $SI=15\%$). The GISFC measurements for these points are consistent with the BSFC reported in the literature.



(a) PM DRX-CO



(b) NOx-CH4



(c) GISFC

Figure 4-4 B75 gaseous emission and engine performance graphs for GSEP sweep, SI=15% from SCRE experiments

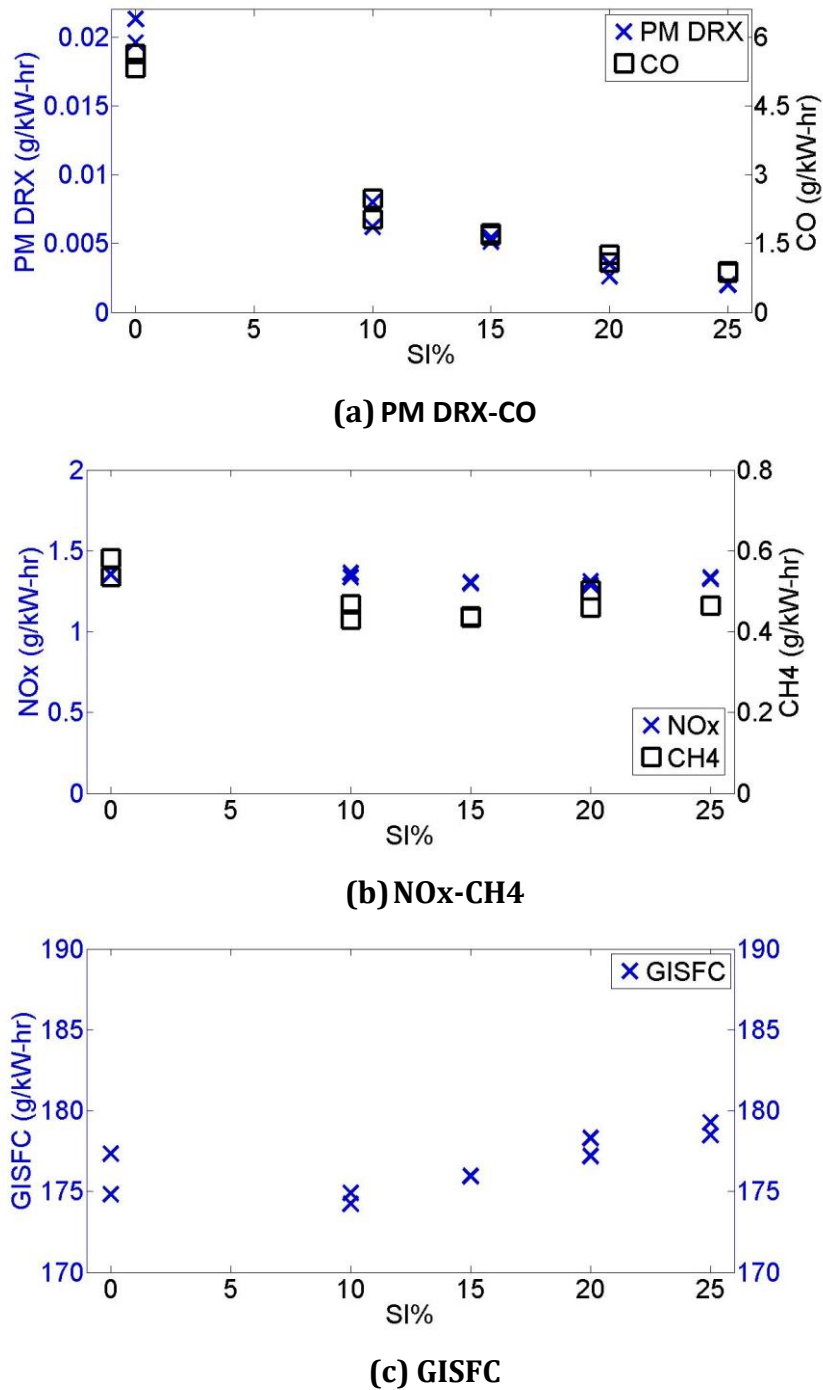


Figure 4-5 Gaseous emission and engine performance graphs for SI sweeps, GSEP=2.0 ms from SCRE experiments

Higher GISFC is expected for post injection cases compared to the baseline. By injecting later in the cycle the part of the heat release rate will happen later in the cycle and the

thermal efficiency will decrease due to deviating from the ideal thermodynamics cycle. Another explanation might be more heat loss from the exhaust for later second pulses, but the measurements show that the exhaust temperature is within the variability of the results ($\pm 5^\circ\text{C}$) for all the points of the GSEP and SI sweeps, so heat loss from the exhaust should be fairly similar for all the points. Further analysis of the pressure can help explain the small effect of LPI on fuel economy. The differential pressure (in-cylinder pressure subtracted from baseline in-cylinder pressure) as a function of CAD is shown in Figure 4-6. The y-axis is the differential pressure. The dashed line is the “only first pulse” case with 85% of the NG mass flow of the baseline case (“reference point 2” in the pulse isolation tests). The blue lines are post injection points with different GSEPs. By shortening the first pulse in post injection cases compared to the baseline, the differential pressure will be negative at first; however, the pressure increases by the start of second pulse heat release, and it rises above the baseline value. The effect of post injection on efficiency, especially for small GSEP cases, are fairly small since the pressure in the cycle will increase above the baseline pressure after the start of the combustion of the second pulse.

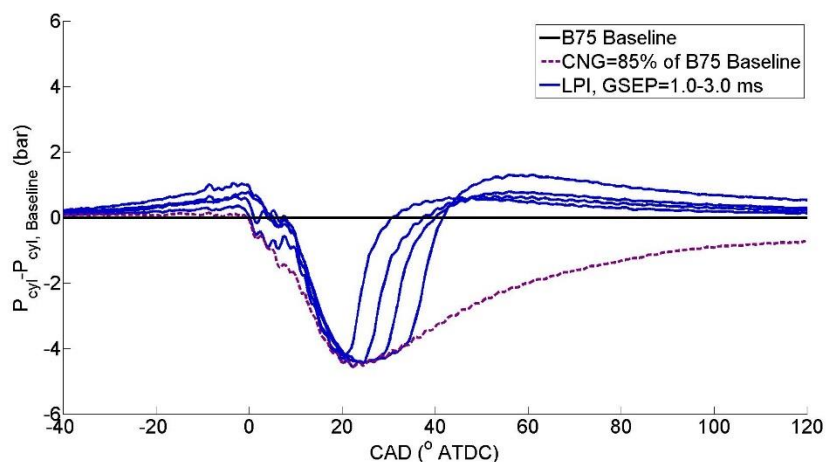


Figure 4-6 In-cylinder pressures subtracted from baseline in-cylinder pressure for post injection (blue lines) and “only first pulse” case (85% of NG flow of the baseline, dashed line).

The SI and GSEP sweeps were used to select “optimum” LPI timings to have maximum PM reduction with less than 1% increase in fuel consumption. Several points met these criteria

with almost the same level of PM reduction but with different GISFC values. The LPI points with small pulse separations or small injections were found to not be repeatable. The optimized point was selected among the points to be highly repeatable, with higher GSEP and higher SI and minimum fuel consumption penalty. These conditions were met for GSEP=2.0ms and SI=15%. Table 4-5 summarizes the emissions and engine performance for the optimized point.

Table 4-5 Comparing optimized LPI point with the baseline

	LPI¹ GSEP=2.0 ms, SI=15%	Baseline
PM DRX (mg/kW-hr)	5	20
NOx (g/kW-hr)	1.4	1.4
Methane (g/kW-hr)	0.45	0.55
CO (g/kW-hr)	1.5	5.5
GISFC (g/kW-hr)	178	176.5
COV of P_{max}	0.7	0.7
dP/dθ_{max} (bar/deg)	4.0	4.0
P_{max} (bar)	136	136
Peak AHRR (kJ/m³-deg)	145	145
Cylinder Exhaust Temperature (°C)	553	546

¹ the best point selected from parameter sweeps of mode B75

The optimized point shows a 75% PM and CO reduction and a decrease in methane by 20% with no change in NOx and only a 1% penalty in fuel consumption. Engine performance including COV of P_{max}, dP/dθ_{max} and P_{max} remain the same as the baseline point. The maximum pressure occurs before the second injection and this additional injection does not change the values of these parameters (P_{max} and dP/dθ_{max}).

The tests for the B75 baseline point and the optimized LPI point were repeated with SMPS and particulate sampling on TEM grids. Based on the LPI and baseline images side by side, comparison of aggregates and primary size is impossible, especially with a high variability in 60 images for each point. The analysis was performed by quantitative image analysis by a semi-automated code. The same procedure as reference [45] and reference [128] is used

in the current study for defining aggregates and primary particles. The geometric mean is calculated based on the particle mobility diameter measured by SMPS. In the TEM analysis, the area of the aggregate is estimated by image analysis then the projected area diameter is calculated based on the area of the aggregate. The SMPS results show that the LPI point produces smaller aggregates and lower concentrations compared to the baseline single injection strategy. This is probably due to different soot formation and/or oxidation caused by LPI strategy. When measuring the aggregate projected area diameter from the TEM grid, the soot aggregates show the same trend as the SMPS results of geometric mean diameter of the particles, namely they are smaller with the LPI strategy. The measurements here also show that smaller aggregates tend to have smaller primary particles, consistent with earlier work [128], [152], [153]. Based on this work, the LPI strategy reduces soot formation and this is seen with smaller aggregates, primary particles, and total number concentration.

Table 4-6 Summary of the results from SMPS and TEM sampling for LPI and baseline points at B75.

Point Name	TEM Primary Particle Mean Diameter(nm)	TEM Aggregate Projected Area Diameter (nm)	SMPS Geometric Mean Diameter (nm)	Concentration #/cm ³
Baseline	32±2	158±12	90 ±4	$2.1 \times 10^6 \pm 2.0 \times 10^5$
LPI	17.0±1	91±6	63±2	$1.1 \times 10^6 \pm 1.0 \times 10^5$

The SMPS size distributions for baseline and LPI points are shown in Figure 4-7. These plots show the size distributions for the non-volatile fraction of the PM after it has passed through the thermodenuder. Solid and open symbols show two size distributions from two repeats for each of baseline or LPI point. The vertical scale for the plots is dN/dlogDp (# of particles / cm³) and has been corrected for dilution. This scaling ensures the area under the curve is proportional to the number of particles in each size bin. The size distributions show lognormal distributions for all the points. For LPI points, the size distribution is shifted toward the smaller particles and the total number concentration is reduced significantly.

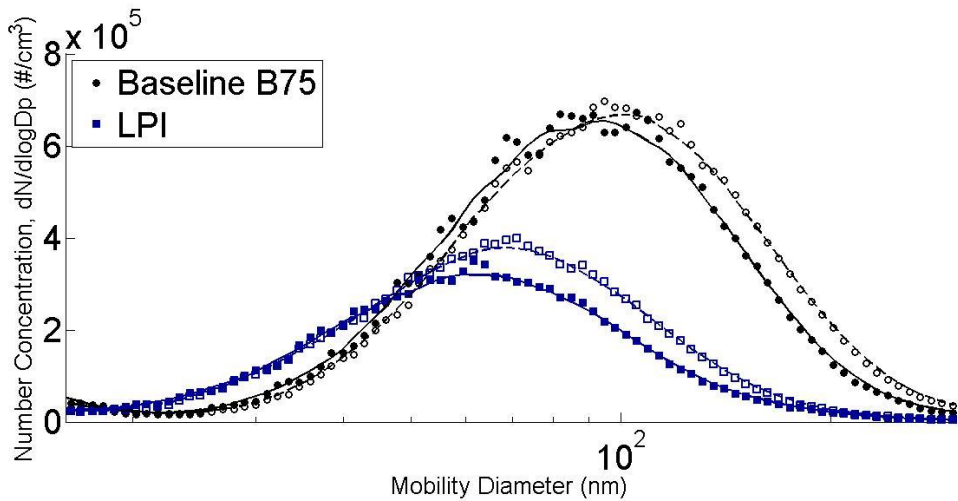


Figure 4-7 PM Size Distributions for baseline and LPI points from SCRE experiments. The open/ closed symbols are two repeats of Baseline or LPI point. The curves are the moving average of each data set

4.3.2 SCRE Experimental Results for LPI Multi-Mode Tests

Table 4-7 shows the emissions and performance measurements for the multi-mode tests (see Table 4-2). The goal of these tests was not to optimize LPI for each mode but rather to show the robustness of LPI strategy in other modes based on the best point of a high PM-forming mode (B75). The SI and GSEP for the multi-mode tests were selected based on the best point of the mode B75 experiments. The LPI point had 15% SI and the pulse separation (GSEP) was selected with two methods: either GSEP=2.0ms or separation equal to 18° crank angle. The difference between the two methods of settings is not significant (2.5-5 degree CAD, minor change in PM and GISFC). This is because of the changes in PM reduction are almost identical for large GSEPs as discussed on Figure 4-4.

The PM reduction for all the modes is significant, although the magnitude of the PM reduction and fuel consumption penalty depends on the mode. For mode A75, LPI will reduce PM only by 30%; however, the PM level on this mode is already very low (near the DRX sensitivity). The PM reductions of the other modes are between 60-80%. Methane emission is reduced for mode B75 and C75 compared to the baseline of the same mode. The fuel consumption penalty varies between modes from 1% to 4% compared to the baseline of the same mode. The highest fuel consumption penalty occurs at the higher loads (B87).

The exhaust temperature of LPI points remains within $\pm 5^{\circ}\text{C}$ of the baseline exhaust temperature, for all the modes.

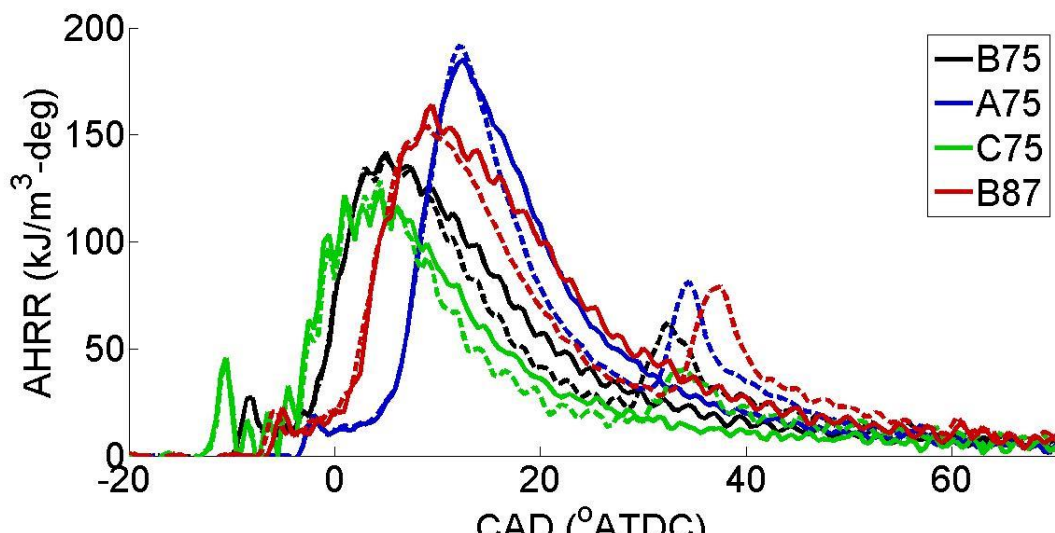
The centroid of AHRR (CA_c) is also included in this table for comparison. Modes A75 and B87 have the latest CA_c compared to the other two modes, B75 and C75.

Table 4-7 Summary of the multi-mode results¹⁰

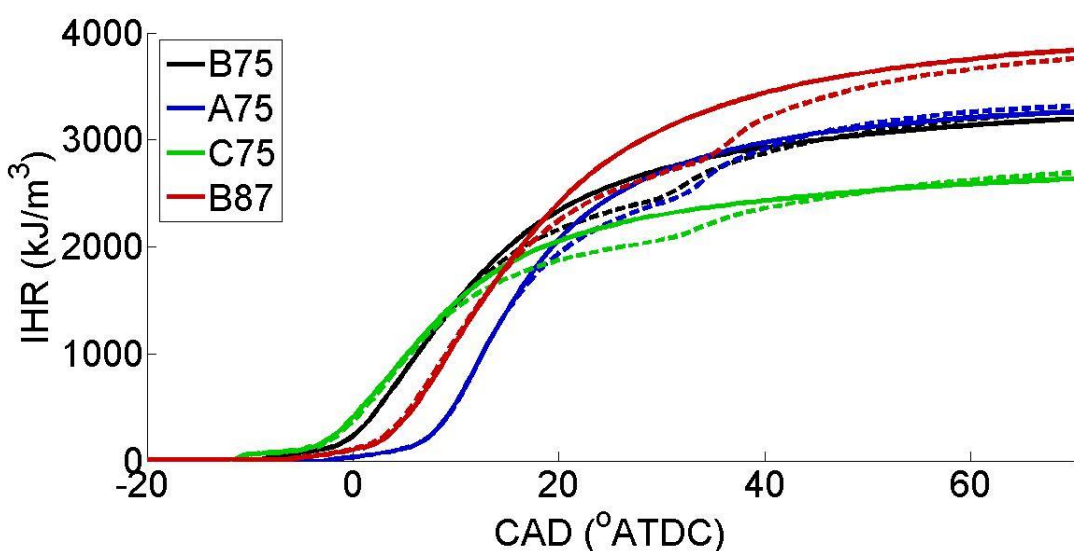
Mode	Inj. Type	PM DRX (mg/kW-hr)	CO (g/kW-hr)	CH_4 (g/kW-hr)	GISFC (g/kW-hr)	CA_c ($^{\circ}\text{ATDC}$)
A75	S	1.1 ± 0.5	0.85 ± 0.19	0.33 ± 0.015	177.4 ± 1.1	20.6 ± 0.1
	LPI	0.8 ± 0.6	0.39 ± 0.04	0.34 ± 0.01	180.8 ± 1.7	23.0 ± 0.6
B75	S	20 ± 1.6	5.5 ± 0.4	0.55 ± 0.032	176.5 ± 1.6	15.4 ± 0.1
	LPI	5 ± 0.2	1.5 ± 0.03	0.45 ± 0.003	178 ± 0.5	18 ± 0.4
C75	S	9 ± 0.4	8.5 ± 0.85	0.68 ± 0.009	173.8 ± 0.75	13.2 ± 0.2
	LPI	2 ± 0.3	1.6 ± 0.1	0.53 ± 0.015	177 ± 1.0	16.0 ± 0.3
B87	S	13 ± 3.8	3.4 ± 0.82	0.4 ± 0.01	178.8 ± 0.5	19.6 ± 0.4
	LPI	5 ± 0.9	1.3 ± 0.22	0.38 ± 0.006	185.9 ± 5.5	21.6 ± 0.1

The apparent heat release rate (AHRR) and integrated heat release rate (IHR) of different modes are shown in Figure 4-8. All the second pulses are at GSEP=2 ms with SI=15%. The combustion of second pulse for B87 mode happens later in the cycle compared to the other modes with more significant heat addition by the second pulse injection. Mode B87 has the highest fuel consumption penalty (4%) among the modes presented in this experiment. The injection timings of different modes are included in Appendix Q.

¹⁰ The measurements in this table are reported as Average \pm (maximum-minimum)/2. The relative changes in BSFC match those of GISFC for all the sweeps including GSEP and SI, pulse isolation tests and multi-mode tests, typically within 1%. An exception to this agreement are the B87 measurements, for which the GISFC penalty from LPI is 4% but the BSFC penalty is only 1.3%. The B87 mode had a much higher COV than other modes, potentially causing the discrepancy.



(a) AHRR



(b) IHR

Figure 4-8 AHRR and IHR of different modes, dashed line is the LPI with GSEP=2 ms and SI=15%.

4.3.3 SCRE Experimental Results for Pulse Isolation Tests

These tests were an attempt to isolate the effect of the 1st and 2nd injections on the PM emissions. Figure 4-9 shows the results of the pulse isolation tests. The unit in the figure is g/hr and not normalized by power since for each point the power level is different and the

goal is to compare PM engine-out mass. PM emissions for reference points (6.4 kg/hr NG flow) do not change depending on which method of controlling the intake charge condition is used (Reference points 1, 2). The results show the PM level, independent of the engine intake charge conditions, is about 0.33 g/hr.

The results here show PM increasing with CNG flow; however, previous multi-mode tests showed that B87 has about 65% of the PM of B75 (single injection in Table 4-7). Part of that is due to normalization (mg/kW-hr in Table 4-7; g/hr in Figure 4-9); however, the main part is due to how the points were set. In multi-mode tests all the conditions are “optimized” (higher GRP, lower PSEP, lower EGR and lower EGR for B87). For pulse-isolation tests all these parameters are kept constant except the CNG flow; please see Table 4-2 and Table 4-3.

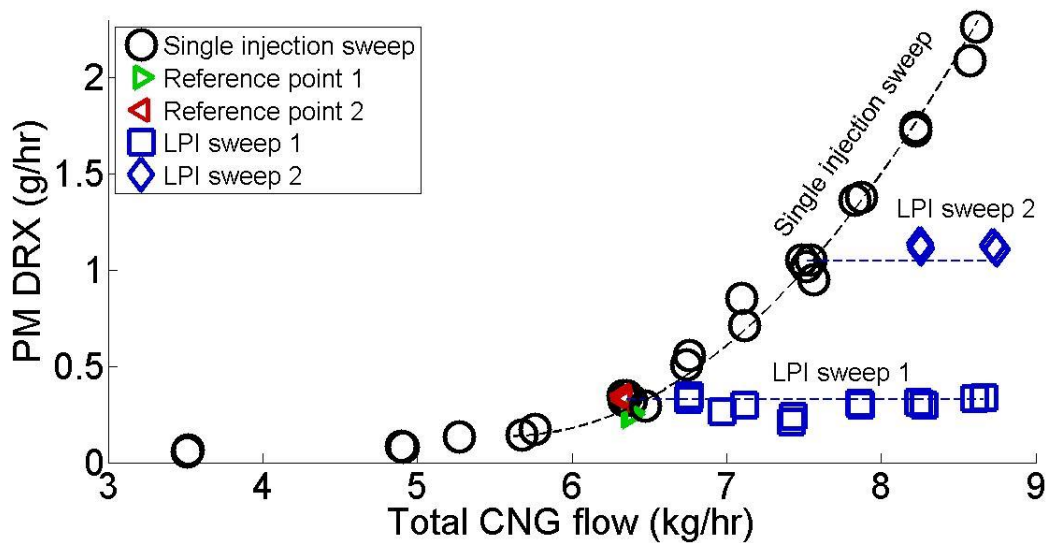


Figure 4-9 Variation of engine-out PM with NG for single and double injections from pulse-isolation SCRE experiments.

Increasing the NG flow in the single injection sweep will increase the PM mass, non-linearly. If we keep the first injection NG mass constant (6.4 kg/hr), increasing the second injection does not change PM mass significantly (LPI sweep 1). A horizontal line is added to

the graph to better illustrate the concept for LPI sweep 1. The LPI sweep 2 also shows the same results, and PM will remain almost constant at the PM level of the main injection. The results here are consistent with previous late post injection experiments in a diesel engine, which showed the PM level of LPI is determined by the PM level of the main injection [59], [60].

The concept of “fuel-replenishment” introduced by Han et al. [61] in diesel engines, discusses the correlation between injection duration and PM formation for single injections. The concept was expanded to the late post injection where, due to the split flame effect, each pulse can be treated as a separate single injection. Pulse isolation tests showed a non-linear increase in engine-out PM with NG flow (or GPW) and also showed that engine-out PM does not change by adding the second pulse; however, not enough evidence is available to confirm or reject the concept of “fuel-replenishment”.

The main PM reduction of the LPI points comes from shortening the first pulse. The pulse isolation tests showed that by reducing 15% of NG flow at mode B75, the PM will be reduced by 75%. The CFD results will be presented later and also show significant reduction. The second pulse has overall minor contribution in net PM mass at exhaust. The two most likely explanations are:

- a) The second pulse does not generate significant PM mass compared to the PM of the first pulse.
- b) PM formation of the second pulse is significant and the extra net PM mass of the second pulse will be balanced by more oxidation from the first pulse due to interaction with the second injection.

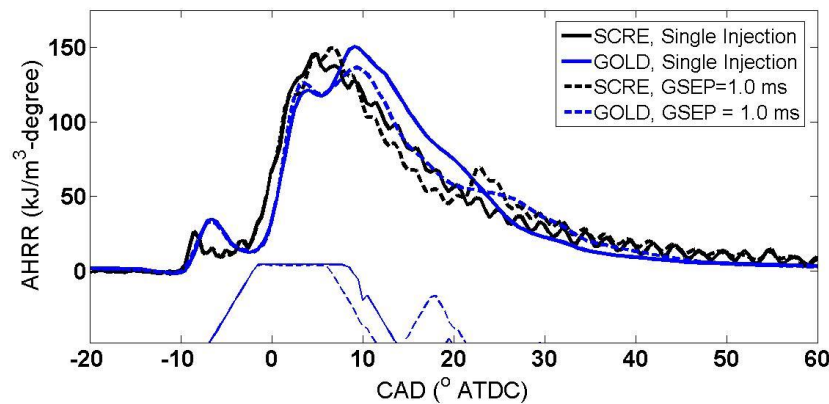
The pulse isolation tests showed that net PM mass is very close to the net PM of the first injection for all the points. Since for all these points the net PM mass is the same as the first pulse. This promotes the first hypothesis while the chances of balancing formation and oxidation between two pulses, for all the points in very different conditions, are rare. Moreover, the CFD results (Figure 4-13) show the PM formation of the second pulse is very

low for large enough GSEPs. The pulse isolation tests and CFD results strongly suggest the first hypothesis; however, not enough evidence is available to refute the second hypothesis.

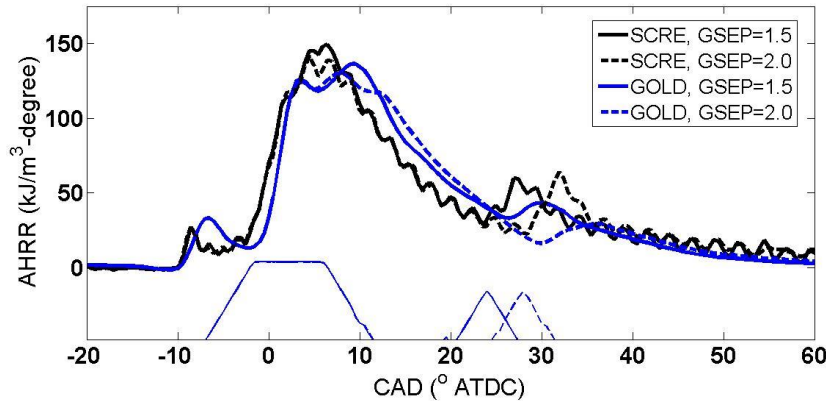
4.3.4 CFD Results and Discussion of LPI Mechanism

The baseline case and selected LPI points (15% of fuel in the second injection with GSEP=1.0, 1.5 and 2.0ms) were simulated by the LES GOLD model. Compared to the description of single injection HPDI combustion presented in section 1.3, the second injection is injected later in the cycle where the ambient density is lower, temperature is higher and part of the combustion products of the first pulse is still close to the injector. The jet quickly ignites as it leaves the nozzle and reaches to the combustion products of the first injection. The diffusion flame will be formed; however, the typical post injections are short (~0.6 ms) and the mixing-controlled combustion ends quickly.

The AHRR graph of the baseline and LPI is shown in Figure 4-10. For both cases the gas injection delay (command to actual injection) is assumed to be 0.7 ms (from Ref. [2]). The rate of injection for each case is also presented at the bottom of the graph. The AHRR of the CFD and experiment are close together except near the AHRR peak. The predicted AHRR of the second injection for LPI is wider and shorter than the measured AHRR. One possible reason for this is the different environment charge composition at the time of the second injection and during the combustion of the second injection.



(a) Baseline and LPI with GSEP=1.0 ms



(b) LPI with GSEP=1.5 ms and GSEP=2.0 ms

Figure 4-10 AHRR for baseline and LPI from CFD simulation compared with the experiments. The narrow lines show the fuel rate shape from CFD.

Emissions at the end of the cycle are compared with the exhaust measurements for the optimized LPI point (SI=15%, GSEP=2.0 ms) in Table 4-8. Although the magnitudes of emissions predicted by CFD are slightly different from SCRE experiments, trends match the experiments. This suggests that despite great simplifications in the soot modelling (e.g., use of Hiroyasu model), the detailed in-cylinder flow and concentration fields from CFD could provide insight into the mechanisms of the LPI strategy.

Table 4-8 Summary of the results from CFD compared to the experiments (SI=15%, GSEP=2.0 ms).

Point	CFD		Experiments	
	Baseline	LPI	Baseline	LPI
PM (mg/kW-hr)	55	28	20	5
NOx (g/kW-hr)	1.08	0.99	1.4	1.4
CH4 (g/kW-hr)	0.43	0.44	0.55	0.45
GISFC (g/kW-hr)	171	175	176.5	178

The evolution of PM in a cycle is shown in Figure 4-11 for baseline and LPI cases. As shown in the figure, the PM formation progresses with the same rate for the single and post injection strategies after the start of injection. However, there is less PM formed (the peak of the curves) for the LPI case due to the reduced injected mass from the first injection. The

CFD results are in agreement with the pulse isolation experiments that showed the main reduction is due to shortening the first pulse. The second injection has a minor effect on PM formation in the cycle; however, the CFD results over-predict the PM of all LPI cases by about 25%.

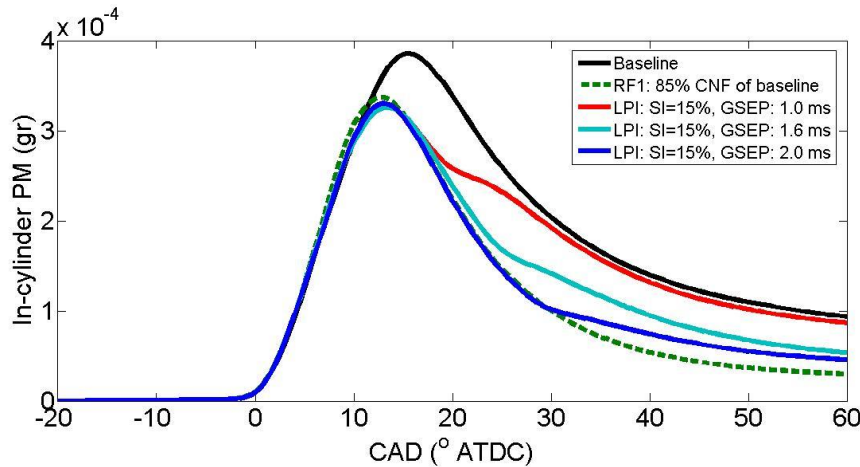


Figure 4-11 Evaluation of PM in the cylinder for baseline and LPI point from CFD simulation.

Experiments show that post injections with small GSEP produce modest PM reductions. This effect is captured by CFD, implying that injector hardware limitations (not considered in CFD) cannot wholly explain the ineffectiveness of close-coupled post injections.

Figure 4-12 shows the contour of PM inside the cylinder for LPI case with SI=15% and GSEP=1.0 ms. The red color intensity in the contour shows the PM concentration. The contours are plotted for the end of fully opened time of the second injection and two degrees after the EOI. The AHRR graphs are also shown with a red dashed line showing the timing of the plot. The contours are generated in two planes, the first one 18 degrees below the fire deck viewed from the top and the second a vertical plane making a 20 degree angle with the centreline and in the direction of the swirl. Soot regions from first and second injections are outlined by red and black contours, respectively. As can be seen from Figure 4-12, when the second pulse is injected there are significant PM zones around the nozzle area and PM from the second injection have substantial interactions with the first injection PM zones.

The second pulse in GSEP=2 ms forms less PM compared to the GSEP=1.0 ms case. Later second pulses, i.e. larger GSEPs, are injected in lower temperature and in-cylinder pressure compared to the close-coupled pulses. This leads to lower PM formation in the LPI points.

Based on predictions for LPI (Figure 4-13) with GSEP=2.0 ms, a large GSEP more distinctly separates the combustion events compared to the small GSEP case. In the present engine geometry with the specific timing and targeting of fuel, most of the formed PM from the first injection ends up in the piston bowl, the beginning of the squish region and close to the nozzle at the end of the injection. If there is a long enough separation between the two injections, the interactions in the above-mentioned regions are fewer. The low PM of the second injection comes from the very short injection width of the second injection (~0.6 ms) and also probably more fresh air for the second injection due to the long injection separation. These results are consistent with the pulse isolation experiments.

Reduced interaction between two pulses is consistent with the concept of “split-flame” concept [60]. However, the second pulse can interact with the first pulse by other means as well e.g. entrainment of the first pulse by adding turbulence or between different stages of PM formation, e.g. pyrolysis of second pulse and agglomeration of the first pulse. These types of interactions in PM formation process cannot be accurately captured by a CFD model based on the Hiroyasu model.

End of fully opened time (18 °ATDC)

2 degrees after EOI (23 °ATDC)

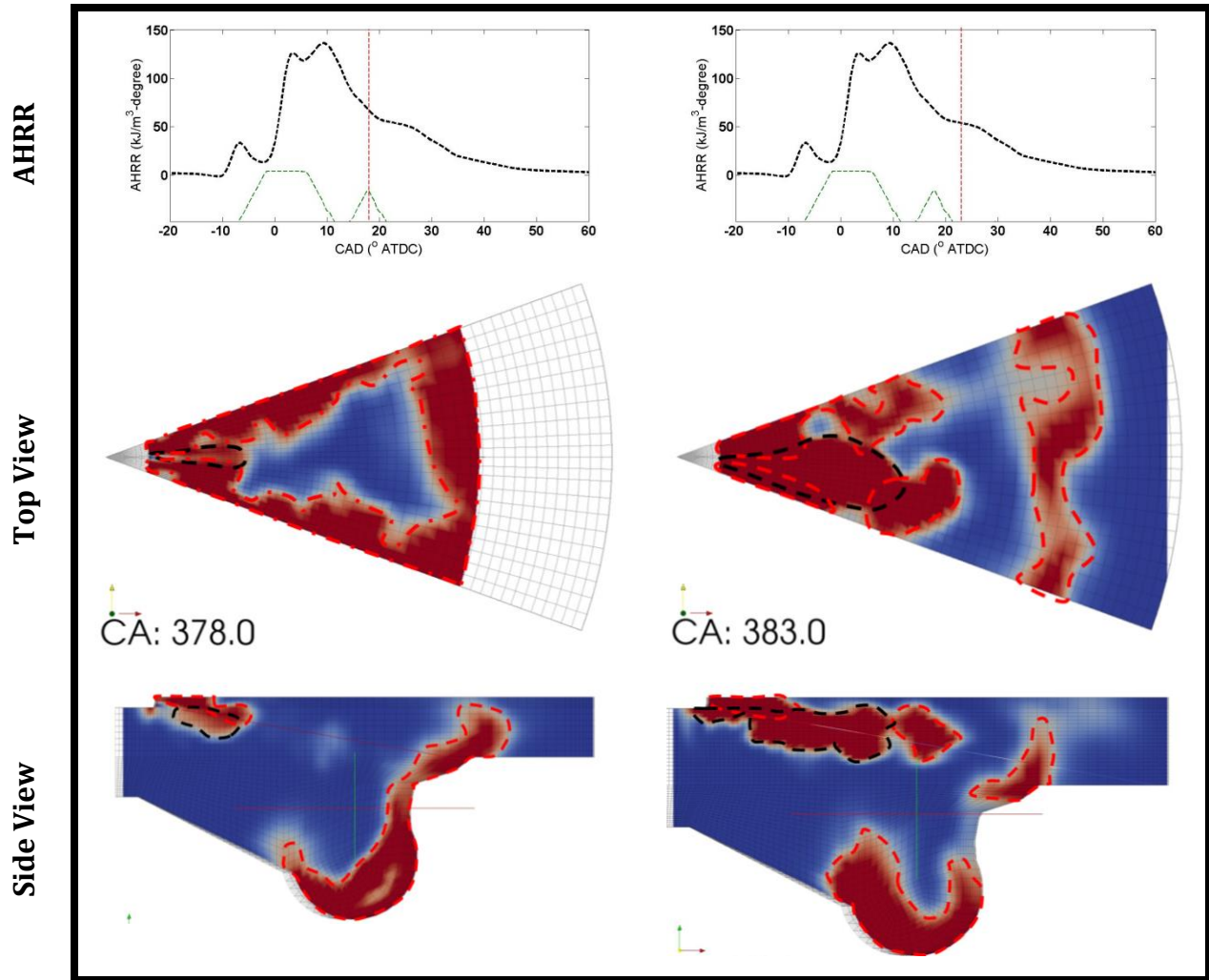


Figure 4-12 In-cylinder PM formation and movement for GSEP=1.0 ms. Soot regions from first and second injections are outlined by red and black contours, respectively. The timing of the presented contour is shown by a red dashed line in the AHRR graph and fuel rate shape graph.

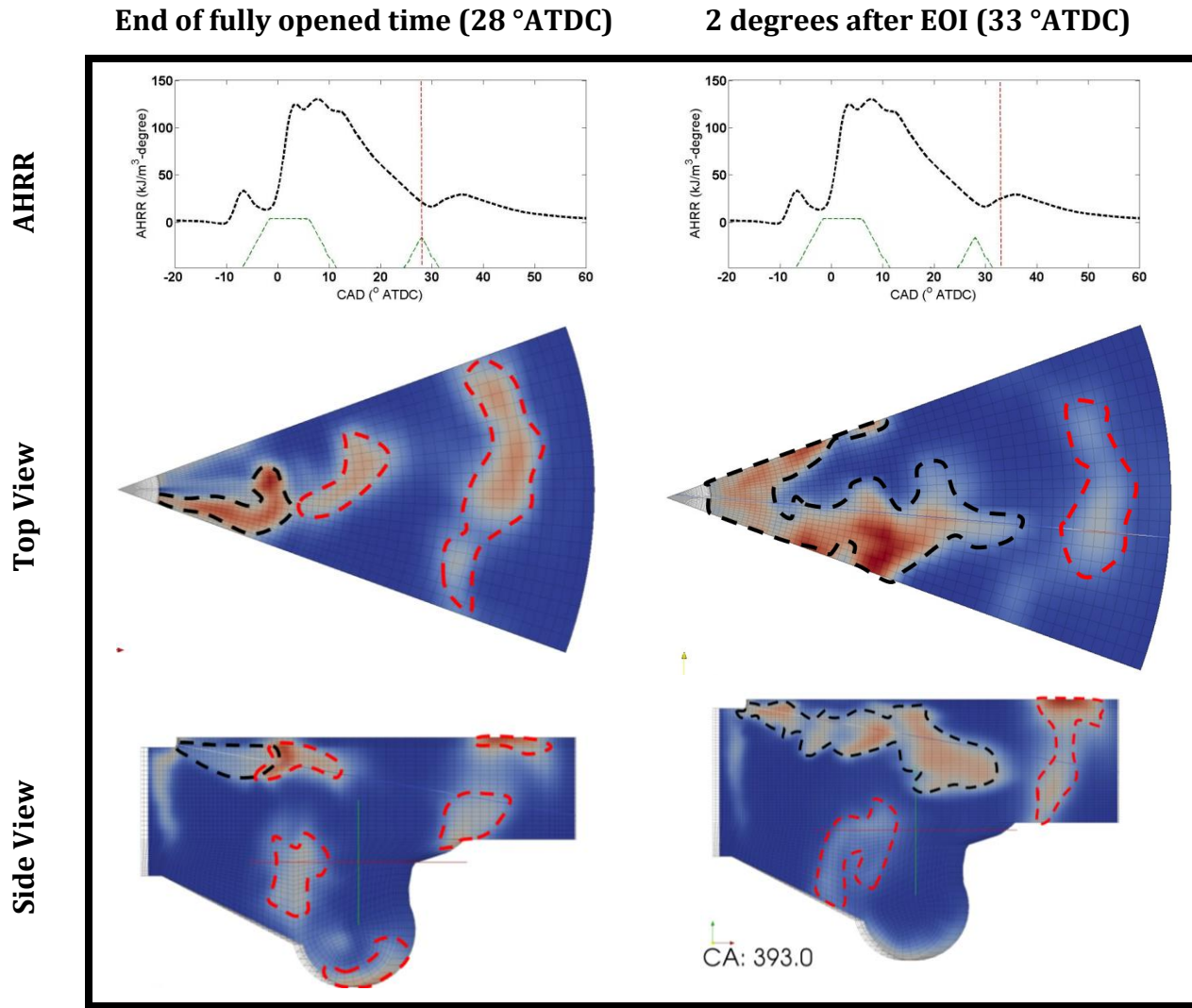


Figure 4-13 In-cylinder PM formation and movement for GSEP=2.0 ms. Soot regions from first and second injections are outlined by red and black contours, respectively. The timing of the presented contour is shown by a red dashed line in the AHRR graph and fuel rate shape graph.

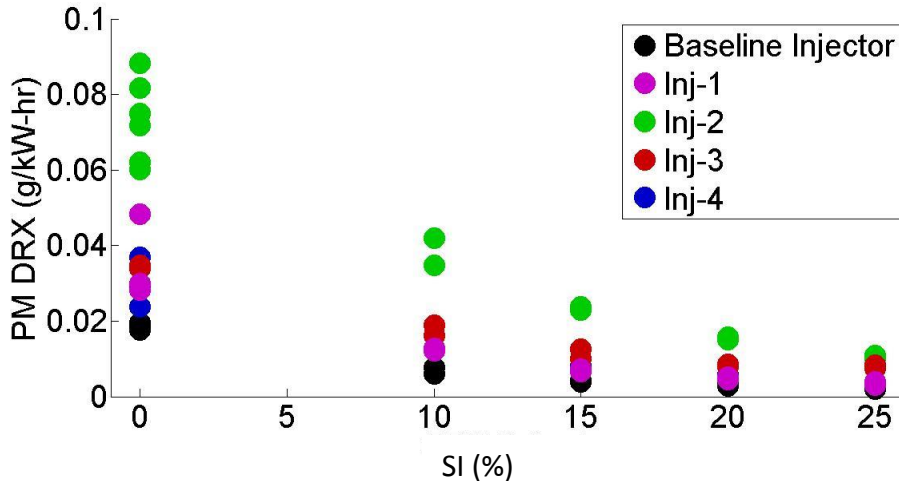
4.3.5 LPI Multi-Injector Tests

Previous results on multi-cylinder engine (MCE) showed differences between the SCRE and MCE. A major reason for this discrepancy might be due to injector-injector variability, especially for more advanced injection strategies where the injector operates close to its limitations. The robustness of the LPI strategy is studied here for five different injectors of the same model of experimental prototype injector used in this work. No attempt was made to adjust or assess the performance of these injectors prior to being tested on the

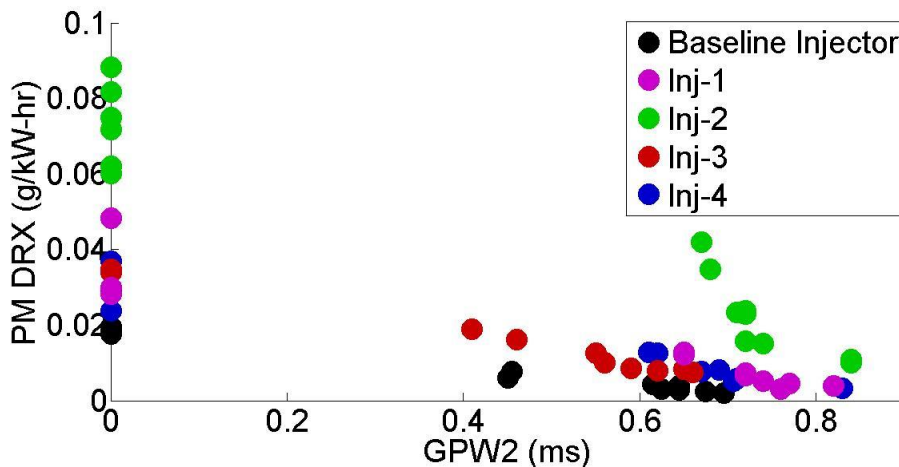
SCRE. This study might also help to better evaluate the performance of LPI strategy in a MCE engine.

Among the injectors' baseline injector is the default UBC-SCRE injector; all the graphs in the current thesis are based on this injector's results except multi-injector tests in this section and similar section in Chapter 5. One of the injectors, Inj-3, has the highest NG mass flow rate for a certain GPW compared to the other injectors. More information about the tests, including the test matrix, is included in Appendix O. For all the injectors GSEP is set to 2 ms, according to the best point of baseline injector, presented in GSEP and SI sweeps. For all the points N=1493 rpm, GIMEP=16.6 bar, EQR=0.61, EGR=18%, GRP=25.4 Mpa and PPW=0.62 ms. For LPI points, PSOI and GSOI are set according to baseline points of each injector. SI was varied between 10-25% for each injector.

Figure 4-14 shows the results of the SI sweep of all the injectors. The same results are presented by changing the x-axis to GPW2. The results show that if the injectors are set based on mass flow distribution suggested by baseline injector results, all the injectors show same trend and same PM reduction magnitude compared to their baseline values. The PM reduction of SI=15% varies between 60-75% between different injectors. TEOM measurements also confirm the results. If all the injectors had the same GPW-NG flow characteristics, then the two graphs in Figure 4-14 would be exactly the same; however, the flow characteristics of the injectors are different. The results in Figure 4-14 (b) are more scattered. That means if we set all the injectors based on GPW2 instead of mass then the effectiveness of the LPI strategy might be affected since at certain GPW each injector inject different fuel mass. The NG flow of the injectors tends to be more variable in small pulses.



(a) PM comparison with same mass distribution for all the injectors



(b) PM comparison with same GPW2 for all the injectors

Figure 4-14 PM comparison for all the injectors in LPI multi-injector tests. GSEP is 2 ms for all the tests.

After some preliminary studies, four injectors were selected for the second block of testing. Injector Inj-4 was removed from the second block since it had similar characteristics to injector Inj-1.

Different methods have been used to set the points on multi-injector tests (Appendix O and an internal report to Westport Innovations Inc.). “Method B” maintained fixed injection command parameters and engine air flow. In this approach, we set the points with matching timings (PSOI, GSOI, PPW, GPW, 2GSOI, 2GPW) and intake airflow (by adjusting MAP and constant EGR) with the baseline injector..

The baseline-B for all the injectors is set by: N=1500 rpm, intake air flow= 205 kg/hr, EGR=18%, PSOI=-23° ATDC, GSOI=-15° ATDC, PPW=0.55 ms, GPW=1.75 ms, GRP=25.4 MPa. For the LPI points, GPW=1.52 ms, GSOI2=20° ATDC and GPW2= 0.6 ms.

Some of the injectors which have higher NG mass flow rates for specific GPW, e.g. Inj-3, will generate much higher PM when all the injectors are commanded with the same GPW. The PM mass of Inj-3 is about seven times higher than the default injector, which is partly due to higher PM of the injector at baseline B75 (Figure 4-14 at SI=0), and partly due to higher EQR and GIMEP of this injector compared to the other injectors due to higher a mass flow rate for certain GPW (see appendix O). The EQR of Inj-3 for baseline-B point is 0.11 higher and GIMEP is about 1.0 bar higher than the default injector. The PM level of Inj-2 injector is about five times higher than the Baseline injector which the main part of that is due to higher engine-out PM at mode B75 (Figure 4-14 at SI=0). The average PM measurement of DRX for all the injectors, shown in Table 4-9, is 46 mg/kW-hr; with high injector-injector variability of 40 mg/kW-hr (defined as (maximum-minimum)/2). Other emissions and engine performances show a much lower variability between the injectors. The study of why these injectors have different PM mass is outside the scope of this thesis.

For the LPI-B points, the PM reduction is 50-75% variable between the injectors compared to their baseline-B values. The lowest PM reduction belongs to the Inj-3 injector where the mass flow of the injector is much different from other injectors. The injector Inj-2 also shows about a 50% PM reduction, since the portion of fuel injected in the second pulse is much lower than other injectors for similar GPW2 (SI=8%).

The average PM reduction of LPI points for all the injectors is 53% compared to their average baseline value, since Inj-2 has very high engine-out PM the reduction is dominated by this injector. Methane emission is about 30% lower compared to the average baseline value. GISFC is about 1% higher on average. NOx, COV of maximum in-cylinder pressure and maximum cylinder pressure gradient will remain almost unchanged based on the average of the four injectors.

The results suggest that LPI might be less effective in terms of PM reduction in a multi-cylinder engine due to injector-injector variability (average of 50% PM reduction

compared to 75% for the best injector). The rest of the emissions and engine performance are consistent with the UBC default injector performance presented in this chapter.

Table 4-9 Emission and injector performance of baseline B75 and LPI point for different injectors¹¹.

Point	Injector	PM DRX (mg/kW- hr)	NOx (g/kW- hr)	CH ₄ (g/kW- hr)	GISFC (g/kW- hr)	COV of P _{max} (-)	dP/dθ _{max} (bar/deg)
Baseline -B	Baseline	13±2	1.21±0.04	0.48±0.02	175.2±0.1	1.0±0.2	4.4±0.1
	Inj-2	61±20	0.94±0.07	0.43±0.08	180.9±0.6	0.7±0.1	4.5±0.1
	Inj-3	93±14	0.97±0.01	0.52±0.05	187.1±0.3	0.7±0.0	4.7±0.2
	Inj-4	17±0.6	1.35±0.04	0.41±0.01	174.5±0.1	0.6±0.1	4.6±0.1
Average Baseline -B	All	46±40	1.12±0.21	0.46±0.06	179.4±6.3	0.8±0.2	4.4±0.2
LPI-B	Baseline	3±0.5	1.11±0.01	0.38±0.01	178.9±1.4	1.0±0.2	4.2±0.1
	Inj-2	28±4	1.13±0.07	0.28±0.01	178.4±1.4	0.6±0.1	4.6±0.2
	Inj-3	49±3	0.85±0.04	0.20±0.02	190.1±0.7	0.7±0.0	4.7±0.1
	Inj-4	9±0.6	1.34±0.04	0.36±0.01	174.4±0.1	0.7±0.0	4.5±0.1
Average LPI-B	All	22±23	1.11±0.25	0.31±0.09	180.5±7.8	0.8±0.2	4.5±0.3

4.3.6 Comparison of the Effect of LPI in Diesel and HPDI Engines

The combustion and PM formation and the oxidation process in HPDI and diesel engines are significantly different. Combustion and PM formation in diesel engines is discussed in Chapter 1 by Dec's conceptual model, and the HPDI combustion process is discussed in section 1.3. The ignition process and chemical kinetics process of two engines are apparently different. Here only the general performance of LPI will be discussed in HPDI and diesel engines.

The HPDI results for LPI are compared here with the results of Bobba and Musculus [59] for a similar size optical Cummins N-14 heavy-duty diesel engine with (B=139.7 mm,

¹¹ The measurements in this table are reported as Average of two repeats± (maximum-minimum)/2 for each injector based on two measurements. The average of all injectors are reported as Average of all injectors± (maximum-minimum)/2

$\text{Stroke}=152.4 \text{ mm}$, $r_c=16$). In reference [59], the engine load and speed were set to GIMEP=9-10bar and engine speed of 1200 rpm. The points with -8 °ATDC for “start of first pulse injection” are selected from their experiments; since it provides close injection timing as current HPDI experiments, considering 0.7 ms injection delay (reference [2]).

One-to-one comparison is not possible between the diesel experiments and current HPDI experiments due to differences in engine geometry, differences in load and speed and type of the engines (optical or thermodynamic engine). However, the trend of engine-out PM and fuel consumption penalty with injection timing will be compared.

The apparent heat release rate (AHRR) of late post injection (LPI) from the HPDI is compared to AHRR of diesel engines in Appendix K. In order to be able to compare the results, the start of AHRR of the second pulse (SOH2) is defined for both engines by visually inspecting the AHRR graphs. The fraction of fuel in the second pulse (SI) in the diesel engine was 17% and for the HPDI 15% of fuel in the second injection. No significant difference in shape and duration of the second pulse AHRR was noticed between the diesel and HPDI engine.

The PM reduction percentage and fuel consumption penalty for the HPDI and diesel engines are shown in Figure 4-15. The plotted percentages are relative to the baseline single injection operation for each engine. In this figure open symbols are diesel engine experiments [59] and solid symbols are the HPDI experiments. The fuel consumption penalty of the HPDI engine is calculated based on GISFC, the same as for the diesel engine.

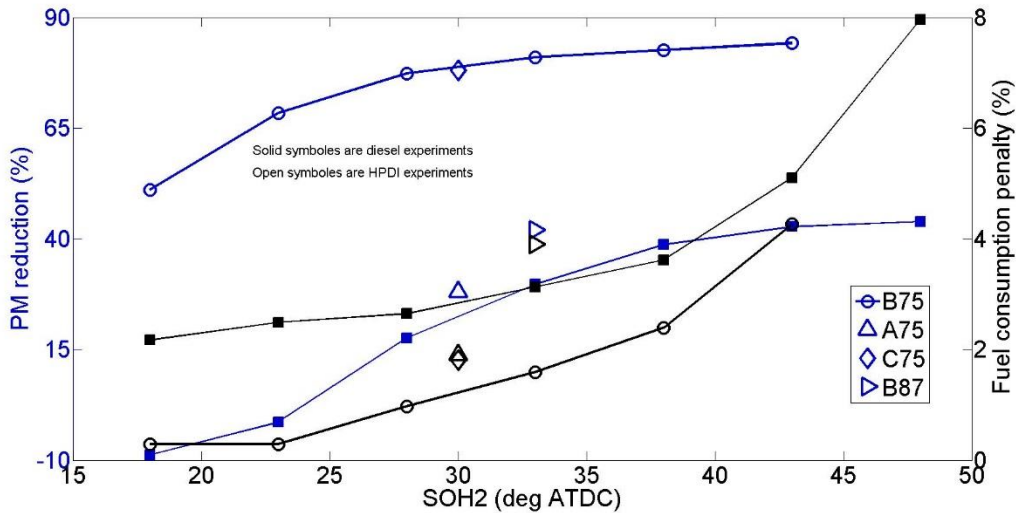


Figure 4-15 Comparison of PM reduction and SFC penalty between diesel experiments [59] and current HPDI engines based on same start of AHRR for second pulse (SOH2). Blue symbols are PM reduction; black symbols are fuel consumption penalty.

Both engines show significant PM reduction with the LPI strategy. The PM reduction reaches to a maximum value for both engines. The PM reduction (over baseline) of the HPDI engine is higher than the diesel engine in equivalent SOH2 for all the modes, especially on high PM-forming modes (B75 and C75) the PM reduction is about 50% higher than the diesel engine at the same timing. However, as mentioned before, these results might not be representative of general HPDI and diesel engines comparison due to differences in the engines and loads. PM formation and the oxidation process in these two engines are significantly different. Moreover these two engines run at significantly different injection pressure (1600 bar for diesel engine vs 250 bar at HPDI engine). In the diesel engine, it is shown that LPI can be more effective for lower injection pressure or high EGR cases where mixing is difficult [59]. This might explain the higher PM reduction of LPI in HPDI engines.

The fuel consumption penalty increases as the second injection is retarded for both engines. The fuel consumption penalty for diesel engine experiments and HPDI experiments are comparable: 3.5% in diesel compared to 1-4% in HPDI experiments for different modes at SOH2=30-35° ATDC. Because soot concentrations are reduced by LPI,

one might expect radiation losses to be lower, but this is expected to have a very small effect on fuel economy¹².

4.4 Conclusions for Late Post Injection

Close-coupled split injections were not consistently beneficial in the current study. These points are associated with lower PM reduction compared to late post injection (LPI) points. Also, close-coupled injections resulted in higher point-point and point-over-time variability. The momentum measurement tests showed the close-coupled injections have high cycle-cycle variability and lower momentum rate.

A parametric sweep at mode B75 revealed that as we retard the second injection, PM and CO decreases significantly at first but approaches a minimum value. As the portion of fuel in the second injection increases, PM decreases slightly. GISFC increased as the second injection was retarded or more fuel was injected in the second injection. The “optimized point” of mode B75 has about 75% PM reduction, NOx is the same; methane is decreased by 20%, CO by 75%. These emission reductions were achieved by about 1% penalty in fuel consumption. Engine performance including COV of P_{max} , $dP/d\theta_{max}$ and P_{max} remained the same as the baseline point.

This “optimized point” selected from the experiments of mode B75 was used for different engine speeds and loads. The goal of these tests was not to optimize LPI for each mode but rather, to show the robustness of the LPI strategy in other modes. The same performance was noticed for all the modes including significant PM reduction and a slight increase in fuel consumption. The PM reduction and fuel consumption penalty of LPI was compared to heavy-duty diesel experiments in the literature. For both diesel and HPDI engines, PM was

¹² Previous experiments showed the radiant fraction (defined as the ratio of radiation heat transfer to total energy of fuel) for higher-sooty, higher-load conditions have peak radiant fractions from 5-10% [142], [143] with an average over-cycle radiant fraction of up to 2.6% for medium engine speed (1300 rpm) [144]. For the modern diesel engines with lower in-cylinder soot, the maximum soot radiant fraction in cycle was at most 2%, causing a reduction in the bulk flame temperature by 25 K [145]; however, the average over-cycle radiant fraction was not reported in this study. Assuming linear correlation between different measurements at different timing of their experiments, the average radiant heat transfer can be estimated up to 1.5%. This means that by removing all the PM from the engine we might improve the thermal efficiency by up to 1.5%. By removing a quarter of the PM from the cylinder (roughly the PM reduction of LPI for 10 to 30 °ATDC, based on the GOLD simulations) the efficiency can be potentially improved by 0.4%.

reduced with a penalty in fuel consumption. As the second injection is retarded, PM approaches a maximum reduction in PM for both engine types. PM reduction in the HPDI engine was higher than in the diesel engine in the equivalent second injection timing especially for high PM-forming modes. The greater PM reduction for the HPDI engine might be due to lower injection pressure and potentially poorer mixing. It has been shown before that the LPI strategy is more effective where mixing is difficult. The fuel consumption penalty arising from LPI for the HPDI engine is comparable with the diesel engine studied by Bobba and Musculus [59]; 3.5% in diesel engine in one mode compared to 1-4% in HPDI multi-mode tests.

PM morphology and size distribution were studied for the optimized LPI point and compared with the baseline point. PM aggregates, primary particles and number concentration were smaller for the LPI point. Previous work on soot morphology analysis showed that smaller aggregates tend to have smaller primary particles, overall these results agree with the literature.

The “pulse isolation” tests showed that the PM level of the LPI cases, for all the points, is close to the PM level formed by a single injection with the same NG flow as the first pulse. The results of “pulse isolation” tests also showed that increasing the NG flow in the single injection sweep will increase the PM mass, non-linearly. The main PM reduction of the LPI points comes from shortening the first pulse and the overall contribution of the second pulse in the engine-out PM is not significant. This might be due to the very low net PM formation (at the end of formation and oxidation process) of the second pulse or balancing the extra net PM formation of the second pulse with possibly more oxidation of the first pulse. Either of these hypotheses could not be proved or rejected based on the current study; however, the results of pulse isolation tests and CFD promoted the first hypothesis.

A three-dimensional CFD based on LES for turbulent flow simulation was used in the current study. The CFD also showed that there is less PM formed for the LPI cases due to the reduction in the injected mass from the first injection combined with the low net PM formation of the second injection. The PM contours of the LPI case showed that most of the formed PM from the first injection ends up in the piston bowl, the beginning of the squish

region and close to the nozzle at the end of injection. For enough separation between injections, the second jet interacts less with the first pulse in the above-mentioned regions compared to the small GSEPs. The low PM of the second injection comes from the short injection duration of the second injection and possibly due to more fresh air available for the second injection because of the long injection separation between two injections. These results are consistent with the concept of a “split-flame” introduced in the literature.

5 RESULTS FOR SLIGHTLY PREMIXED COMBUSTION

The main objective of this chapter is to apply Slightly Premixed Combustion (SPC) strategy (introduced in Chapter 1) to reduce engine-out particulate matter (PM) while controlling both NOx and methane, and understand the mechanism of PM reduction in SPC. Adjusting relative timing between diesel and natural gas injections allows more premixing of the natural gas prior to ignition. The previous literature [47], [50], [87] on HPDI engines showed that significant PM reductions can be achieved at the expense of higher NOx and methane for a given EGR level. Increasing EGR will help to control NOx without increasing PM in the SPC mode; however, these points usually have high methane emissions.

SPC is evaluated here at a steady-state mode using a single-cylinder research engine (SCRE), supported by CFD analysis. The SPC strategy is adjusted to maintain NOx and methane emissions at baseline levels while having very low engine-out PM. This work provides insight into the SPC strategy as a way to “beat” the usual PM-NOx-methane trade-offs found in conventional HPDI combustion.

5.1 Experimental Design

The literature relevant to SPC is reviewed here to motivate the selection of SPC test conditions. Lowering the flame temperature by increasing EGR is an effective method to control engine-out NOx level; however, this tends to increase the PM level due to the PM-NOx trade-off. The low temperature combustion (LTC) strategy used in diesel engines delays ignition and prevents PM formation in the core of the jet (AHRR after EOI in Figure 1-5). The PM-NOx trade-off can be escaped using this strategy; decreasing NOx is not associated with an increase in PM emissions [40], [43], [82], [84]. In previous HPDI studies [47], [50], [87], it was found that combining SPC with increased EGR can keep NOx emissions at their baseline levels, still having significantly lower PM. However, these points usually end up with high methane emissions [47], [50], [87]. Similarly, as reported in the literature of diesel engine experiments, more premixed combustion leads to higher

unburned hydrocarbon emissions [83], [85], the source of unburned hydrocarbon is reported to be over lean charge close to EOI in diesel engine experiments.

The idea of using higher EQR to control methane emission for SPC is tested here. Higher EQR might decrease the potential for over-mixing since there is less air mass in the cycle to lean the mixture. Higher EQR is achieved by reducing the intake pressure while keeping GIMEP constant.

For the normal HPDI points, the pilot mass has a significant effect on the PM engine-out. By increasing pilot mass, PM emissions increase significantly [8], [47], [50]. Pilot mass quantity also affects ignition timing due to the larger ignition source, and because the diesel injection duration increases (indicated by pilot pulse width, PPW). A preliminary study (Appendix E) has been performed to find out whether it is better to control the separation between the end of diesel and start of gas injections (PSEP), or the “relative injection timing” (RIT). RIT is the difference between the pilot start of injection (PSOI) and gas start of injection (GSOI)¹³. It was found that the points with constant PSOI and GSOI, (RIT constant) keep the AHRR similar to the baseline point while we change PPW. For the PPW-PSEP sweep in the current study RIT has been used to set the point instead of PSEP.

These considerations led to experiments that focused on the relative injection timing, EGR, EQR and the strength of the ignition source (indicated by pilot diesel quantity). Engine operating modes were discussed in Chapter 2 and the operating points are summarized in Table 5-1. All the experiments have been done at mode B75 with 1500rpm, GIMEP of 16.5 bar and GRP of 25 MPa. The timing was adjusted keeping CA50 at 11° ATDC for all the cases. Different sweeps of parameters were considered to study the effect of EGR, EQR, combinations of EGR-EQR and pilot mass on the results. By changing PPW from 0.52 ms to 1.02 the ratio of diesel to gas (energy basis) changes from 5%-13%; the natural gas mass is set to meet the GIMEP requirement. Every test was done at least 2 times.

¹³ Note RIT (ms)=PPW (ms)+PSEP (ms).

The $[O_2]_{intake}$ is included in the table for comparison; however, the points were not set based on this parameter.

Table 5-1 Summary of SPC engine experiments. Gas-diesel separation (PSEP) sweeps are combined with other conditions.

	Normal	EGR-EQR Effects			Pilot Effects
		High EGR	High EQR	High EGR-EQR	
EGR [%]	18	25	18	25	18
EQR	0.60	0.60	0.7	0.7	0.6
PPW [ms]	0.62	0.62	0.62	0.62	0.52, 0.62, 0.82, 1.02
PSEP or RIT [ms]	PSEP 0.9, 0.3, -0.3, -0.9, -1.5, -2.1	PSEP= 0.9, 0.3, -0.3, -0.9, -1.5, -2.1	PSEP= 0.9, 0.3, -0.3, -0.9, -1.5, -2.1	PSEP= 0.9, 0.3, -0.3, -0.9, -1.5, -2.1	RIT= 1.5, 0.9, 0.3, -0.3, -0.9, -1.5
$[O_2]_{intake}$	20.5%	19.5%	20%	19%	20.5%

Although there is no abrupt change between mixing-controlled combustion and slightly premixed combustion, for simplicity the points with PSEP=0.9, 0.3 and -0.3 are called “normal HPDI points” and the points with PSEP= -0.9, -1.5 and -2.1 are called slightly premixed combustion (SPC) points. In terms of relative injection timing, the points with $RIT \leq 0$ are called SPC points.

5.2 Computational Model

In order to understand the in-cylinder processes better, GOLD (see section 3.6 and reference [144]) was used to simulate the HPDI combustion for the SPC strategy. In the current study we model the baseline case (PSEP=0.3 ms, EGR=18% and EQR=0.6) and some combination of relative timing and EGR/EQR (Table 5-2).

Table 5-2 Summary of CFD tests*

	Baseline	Case 1	Case 2	Case 3	Case 4	Case 5
EGR [%]	18	25	18	25	18	25
EQR	0.60	0.60	0.6	0.6	0.7	0.7
PSEP [ms]	0.9	0.9	-0.9	-0.9	-0.9	-0.9

*all the cases have PPW=0.62 ms

For the CFD cases the physical delay, ramp-up and ramp-down are assumed to be 0.7 ms, 0.6 ms and 0.6 ms respectively (see reference [2]) for gas injection. The other details of the CFD simulation are mentioned in reference [144].

5.3 Results and Discussion

5.3.1 Effect of Delaying Pilot Injection for Normal EGR and EQR Conditions

Here, the separation between the end of the diesel injection to the start of the gas injection, PSEP, is changed from 0.9 to -2.1 ms (conditions in Table 5-1). The apparent heat release rate (AHRR), the injection rate and ignition points are shown in the Figure 5-1. Note that the baseline PSEP for mode B75 is 0.3 ms. The AHRR changes correspond to changing from more mixing-controlled burn to more premixed burn as we go toward negative PSEP points. The AHRR for normal HPDI points is spread over a wider range in crank angle, while by moving toward more premixed burning AHRR is limited in narrow range of crank angles. The maximum of the AHRR increases with more premixing until PSEP= -1.5ms. This trend has been seen in the diesel engine studies by slightly delaying the ignition [82]. Previous experiments [47] have also shown high intensity combustion for PSEP of -0.6 ms.

Here, the green trace is the expected gas injection profile using a physical delay (0.7 ms) and expected ramp times (0.6 ms up, 0.6 ms down) determined from momentum measurement tests (see reference [2]). The vertical “end of injection” (EOI) line occurs at the end of the green trace. Red and green stars show pilot and gas ignition points determined from the AHRR curve. The ignition point is calculated based on [55], [56], as discussed in Chapter 2.

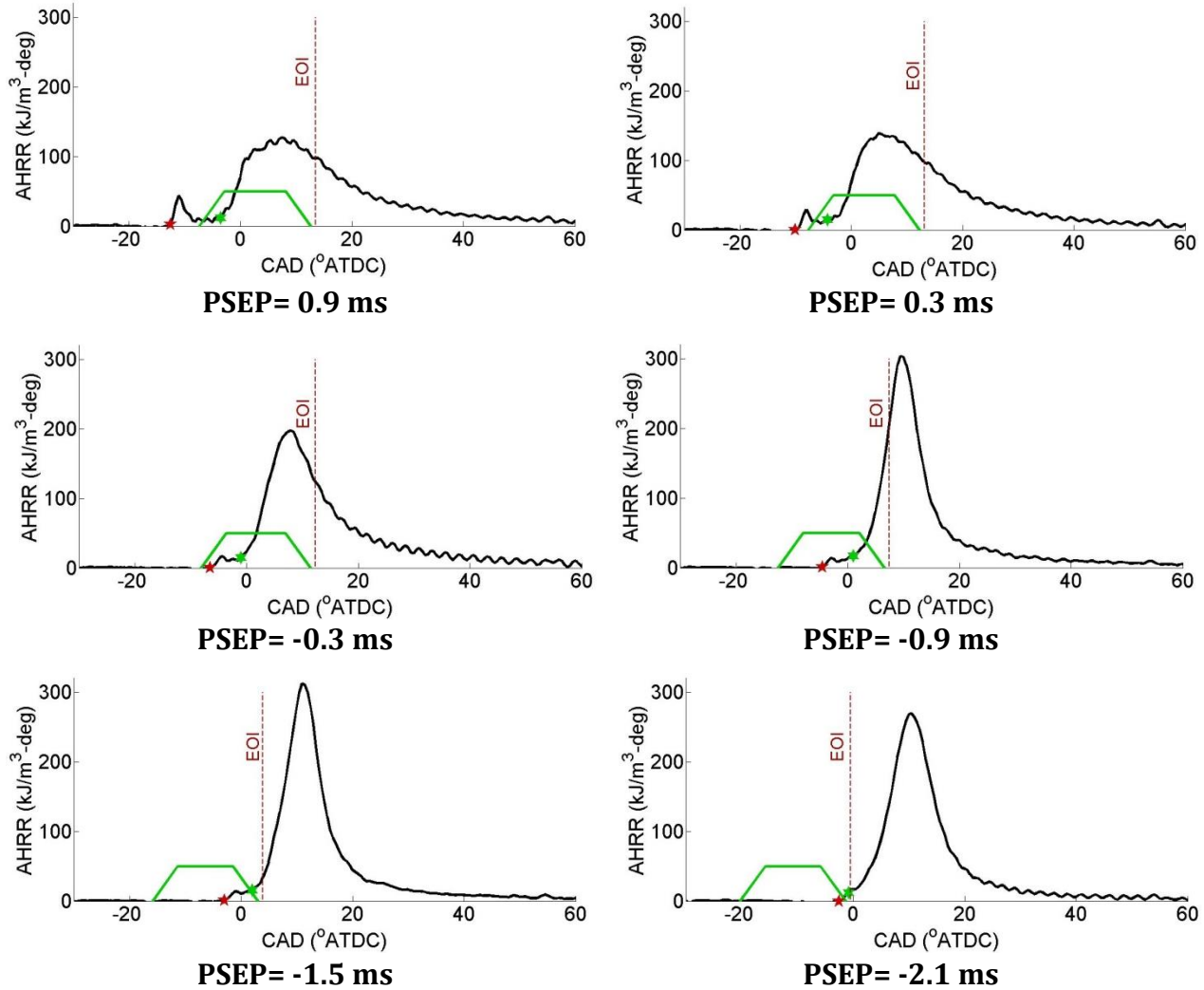


Figure 5-1 Apparent heat release rate (from SCRE experiments) and injection timing for different PSEPs, including gas injection profile (green line, simplified version from momentum measurement tests), diesel ignition (red star) and gas ignition (green star) both from the SCRE experiments.

For normal HPDI points (PSEPs of 0.9, 0.3 and -0.3 ms) peak AHRR occurs before EOI, corresponding to the first category (AHRR peak before EOI) in Figure 1-5. The ignition of NG is before EOI. As we move to negative PSEP values, the peak AHRR is closer to EOI. For SPC points (PSEP=-0.9, -1.5 and -2.1 ms), peak AHRR is after EOI.

Figure 5-2 summarizes the gas ignition and AHRR peaks relative to EOI, in CAD, for all points with the baseline B75 values of EGR, EQR and pilot quantity. The graph is plotted

based on CAD after EOI (end of injection). The EOI ramp-down (0.6 ms) is shown in the same graph as the green band.

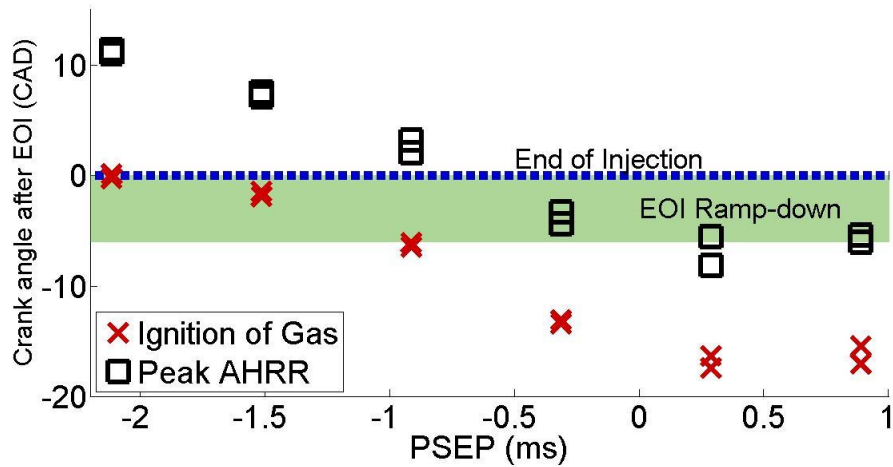


Figure 5-2 Timing of ignition and peak AHRR relative to EOI from the SCRE experiments.

Figure 5-3 shows the engine-out emission and engine performance at different PSEP timing. By moving toward negative PSEP values (more premixing), PM decreases to a value that cannot be measured accurately by the DRX. With respect to the conceptual model of Figure 1-5, almost all the PM is removed when peak AHRR is after EOI, i.e. $PSEP \leq -0.9$ ms. In the experiments resulting in the conceptual graph of Figure 1-5, more premixing was achieved by changing the transition of the ignition chemical kinetics. SPC, on the other hand, achieve more premixing only by shifting the pilot ignition timing relative to NG injection. Despite this major difference, in SPC the relative time of EOI and peak AHRR is an important factor also. This leads us to define a threshold for SPC based on the current studies, which will be discussed later in the chapter.

Carbon monoxide follows a similar trend but is not reduced to zero even for $PSEP = -2.1$ ms. NOx and methane both increase with increasing premixing of NG. Methane is constant for $PSEP \geq -0.9$ ms and suddenly increases for more premixing. The trend in increasing unburnt hydrocarbons by more premixing has been noticed in LTC strategy in diesel engine [83]–[85]. The drawback of this injection strategy is significantly higher NOx and methane emissions [47], [50], [87]. Fuel consumption decreases with slight premixing of NG. Better fuel economy of the negative PSEP points are due to the more sudden and narrow AHRR of

these points. The combustion phasing, defined by CA50, is kept constant for all the points. A graph with all the AHRR traces in one graph is shown in Appendix F. The position of peak will be moved even later in the cycle; however, it will end earlier as well.

Additionally, combustion harshness (indicated by COV or maximum pressure and maximum $dP/d\theta$) increases to a maximum at $\sim PSEP=0.9\text{ms}$. Higher combustion harshness of these points leads to higher engine noise. Similar trends for all the emissions and engine performance have been reported in previous HPDI engine studies on SPC [47], [50], [87].

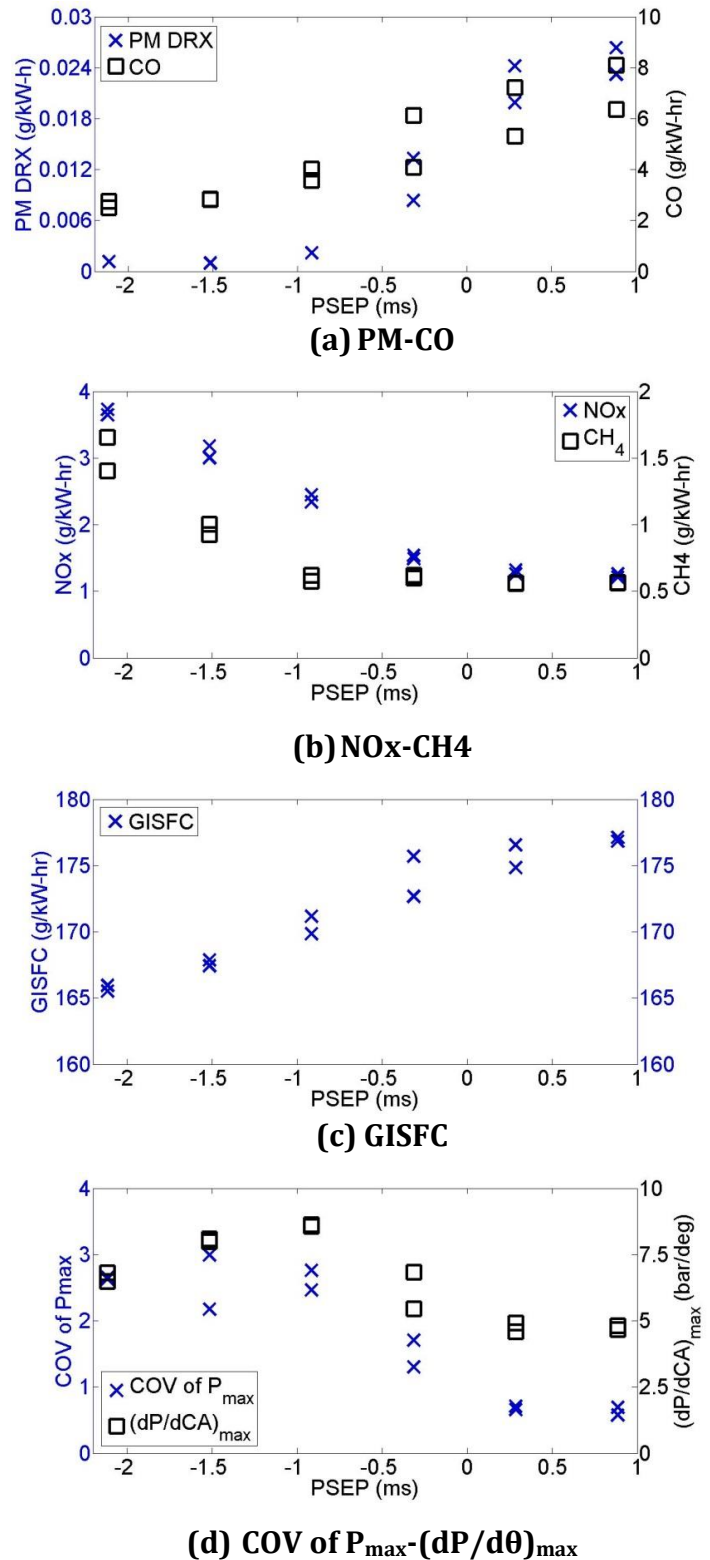


Figure 5-3 Emission and engine performance by changing pilot separation (PSEP), for mode B75 from the SCRE experiments.

5.3.2 PSEP Sweeps at different EGR and EQR

The AHRR for measurements with different EGR and EQR levels for PSEP=-0.9 ms are shown in Figure 5-4. For all the cases at different EGR/EQR levels, combustion duration remains almost unchanged; less than a 1 degree change for a 25 degree duration of combustion defined at 20 kJ/m³-deg. However the peak AHRR changes significantly, about 70 kJ/m³-deg over the average of 300 kJ/m³-deg. By increasing EGR, the peak AHRR is lower, perhaps due to lowering the flame temperature by increasing EGR. Increasing EQR will increase the peak AHRR for SPC points. This might be due to a lower potential for over-mixing at higher EQR. Increasing EGR and EQR together will maintain the AHRR peak close to the original case with EGR=18% and EQR=0.6. The AHRR increase due to the higher EQR is canceled out with the effect of EGR in lowering the AHRR. Note that these experiments are done at fixed engine load (nearly constant fuelling), so to increase EQR, the airflow and cylinder pressure is reduced. This could affect injection behavior slightly.

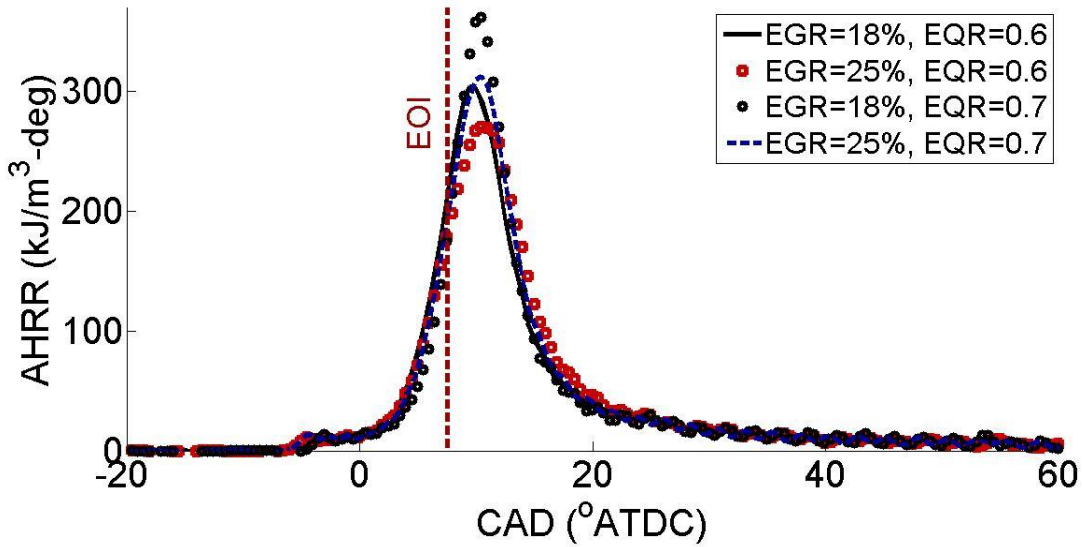


Figure 5-4 Apparent heat release rate for PSEP=-0.9ms and different EGR and EQR levels, CA50=11 ° ATDC for all the cases from the SCRE experiments.

Figure 5-5 (a), (b) and (c) show “ignition dwell”, peak AHRR location, and peak AHRR magnitude for different PSEPs and different EGR-EQR combinations. Ignition dwell is defined as the time from gas ignition to end of injection (Gign-EOI). Ignition and peak AHRR are delayed by 2-3 degrees by increasing EGR for middle PSEP points (PSEP= -0.9 ms, -0.3 and 0.3 ms). As an interesting observation, the peak AHRR magnitude decreases for more

premixed burn at PSEP=-2.1 ms, potentially due to mixing the main portion of the fuel below the stoichiometric. Peak AHRR magnitude in normal HPDI points does not change significantly with EGR or EQR, however, by more premixing, EGR and EQR will affect the the AHRR peak.

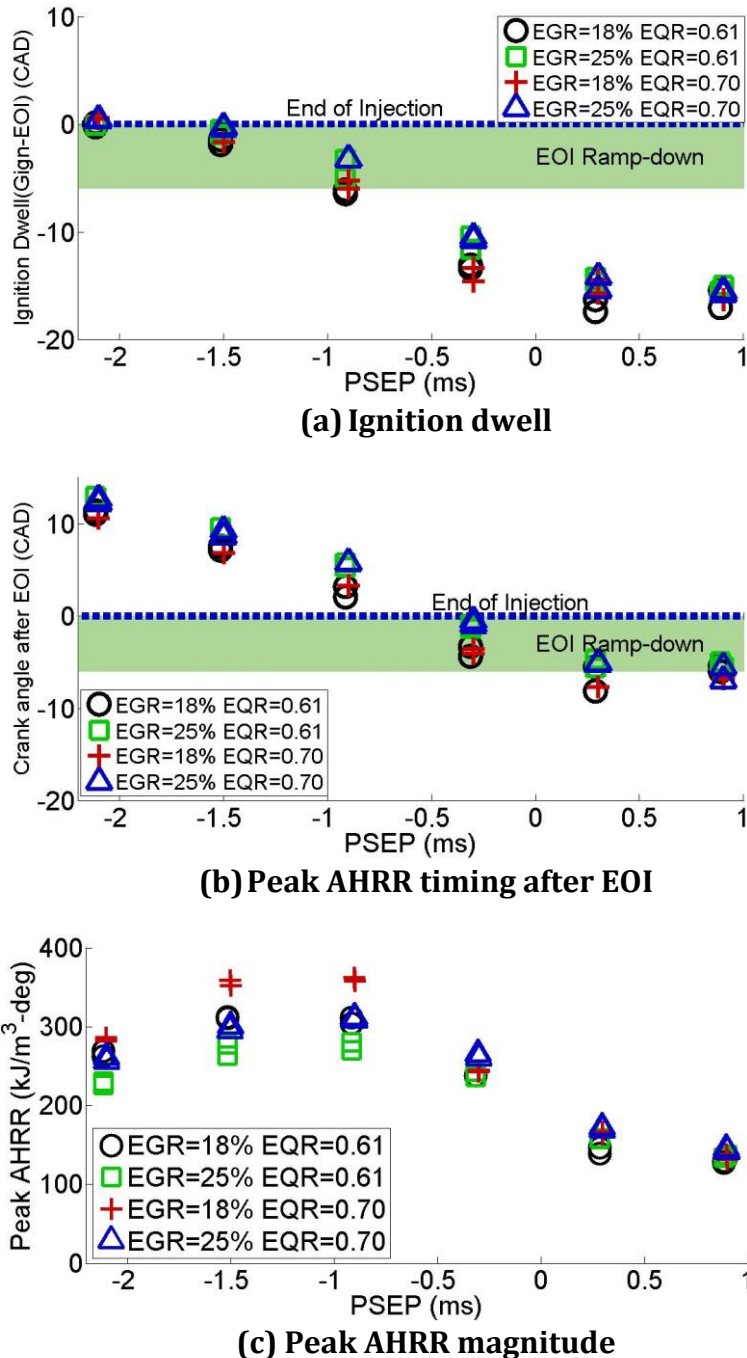


Figure 5-5 Ignition dwell, and peak AHRR timing and magnitude for different PSEPs from the SCRE experiments.

Figure 5-6 (a) shows the engine-out emissions for different EGR and EQR levels. For slightly premixed cases, PM does not increase by changing the in-cylinder environment, which normally increases PM in normal HPDI points, e.g. higher EGR or EQR level. For all

the SPC points, ignition happens after EOI. Appendix I shows the engine-out PM and peak AHRR location of all the SPC experiments. The points with peak AHRR after EOI have very low engine-out PM with low sensitivity to engine parameters.

NOx increases by more premixing of the charge, i.e. moving to negative PSEPs. Increasing EQR has only a minor effect on NOx emission. EGR is increased to reduce the NOx emission (for PSEP=-0.9 ms) back to the baseline point. For these tests, the inlet oxygen concentration is changed from 20.5% to 19%.

For normal HPDI points, methane emission increases as we increase EGR; however, in SPC cases this increase in methane emissions is more significant. Increasing EGR will increase the methane emissions. Increasing EQR, helps to reduce methane at the same PSEP and same level of EGR. Methane emissions for the high EGR and EQR points are close to the level of methane in the baseline point. Carbon monoxide reaches its lowest value at PSEP=-2.1 ms. Emissions formation will be discussed more in φ -T map analysis and the CFD results later.

The premixing has been increased to a level that PM and CO are eliminated but it provides a more lean mixture before ignition which can lead to CH₄ formation. As this more lean mixture is produced before ignition CO is not formed. This will be discussed more in the CFD section of the current chapter.

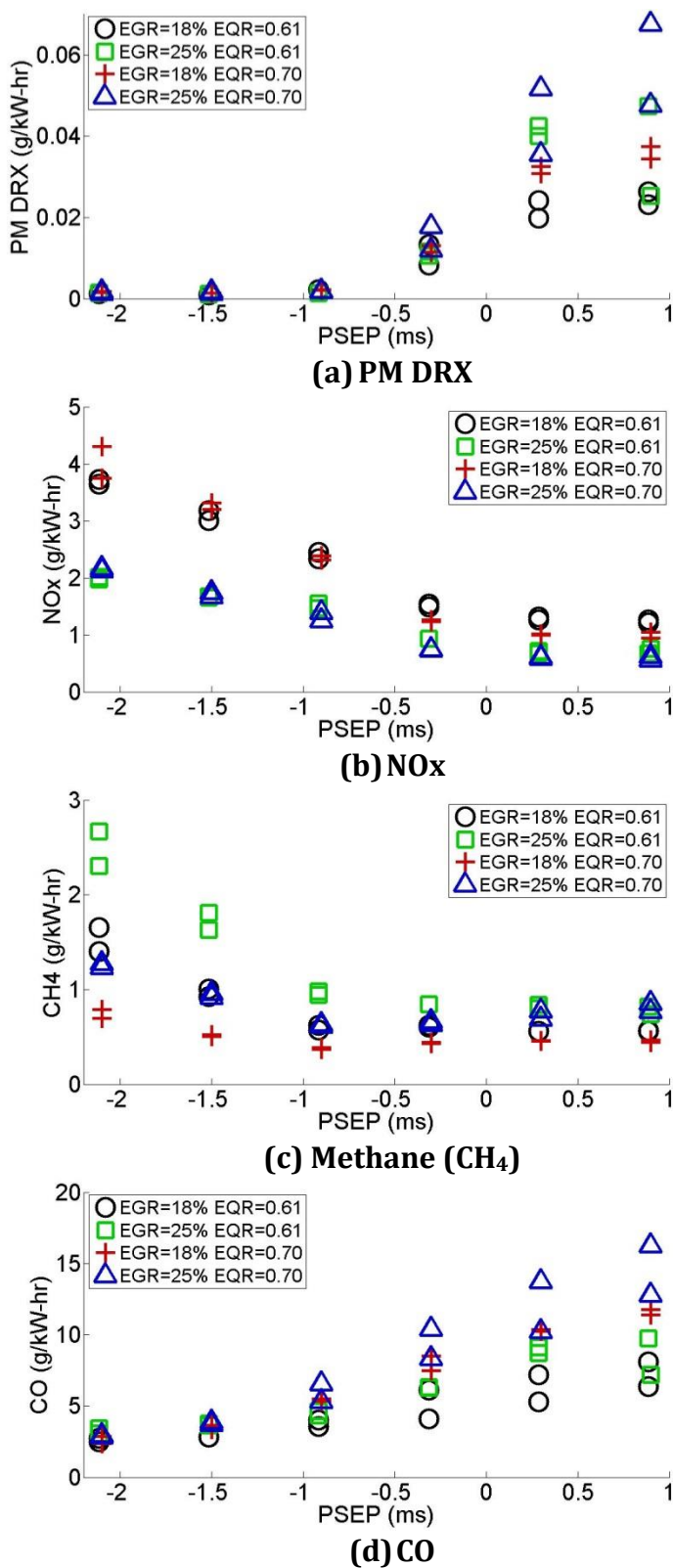


Figure 5-6 Engine-out emission as a function of separation of gas and diesel injections (PSEP) for different engine environment from the SCRE experiments.

Figure 5-7 shows the engine-out methane as a function of ignition dwell (Gign-EOI). This is the same information shown in Figure 5-6 (c), but here it is clearer that for all EGR, EQR conditions, methane emissions rise sharply for Gign-EOI close to zero. The same trend in UHC has been reported in the diesel engine literature [85] for a wide range of diesel operating conditions by Cummins Inc. Based on the optical measurement, long ignition dwells and long mixing times leave very lean, over-mixed regions close to the nozzle due to the end of injection rapid mixing and this contributes significantly to UHC emissions for LTC diesel engines [83], [85]. We cannot verify the source of methane in our experiments; however, the significance of EOI in methane increase is reported here as an interesting observation.

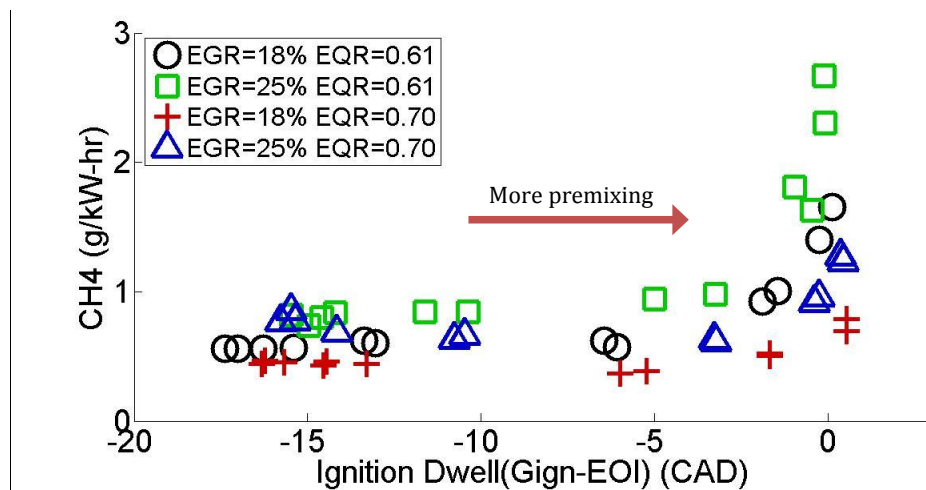


Figure 5-7 Engine-out methane versus ignition dwell from the SCRE experiments.

Engine performance for different PSEP is shown in the Figure 5-8. By moving toward more premixing, fuel efficiency is generally improved, as in Figure 5-3 and previous experiments [47], [50], [87]. This might be due to the narrow range of AHRR close to TDC. The combustion phasing, defined by CA50, is kept constant for all the points. The position of peak for the normal PSEP sweeps will be moved even later in the cycle; however, it will end earlier as well (see Appendix F). Changing EGR and EQR mainly changes the AHRR peak magnitude as mentioned before.

Increasing EQR will increase fuel consumption at the same PSEP for normal HPDI points. However, for SPC points increasing EQR has an insignificant effect on fuel consumption based on GISFC (any changes in pumping work are not incorporated into the GISFC results). As for the normal PSEP sweep, the COV of maximum pressure and maximum $dP/d\theta$ increase with more premixing and then slightly decrease for PSEP=-2.1ms. By increasing premixing, the effect of engine parameters, e.g. EGR and EQR, on the peak pressure rise rate and variability of maximum pressure would be more significant. The exhaust temperature is within the variability of the results ($\pm 5^\circ\text{C}$) for all the points of the parameter sweeps.

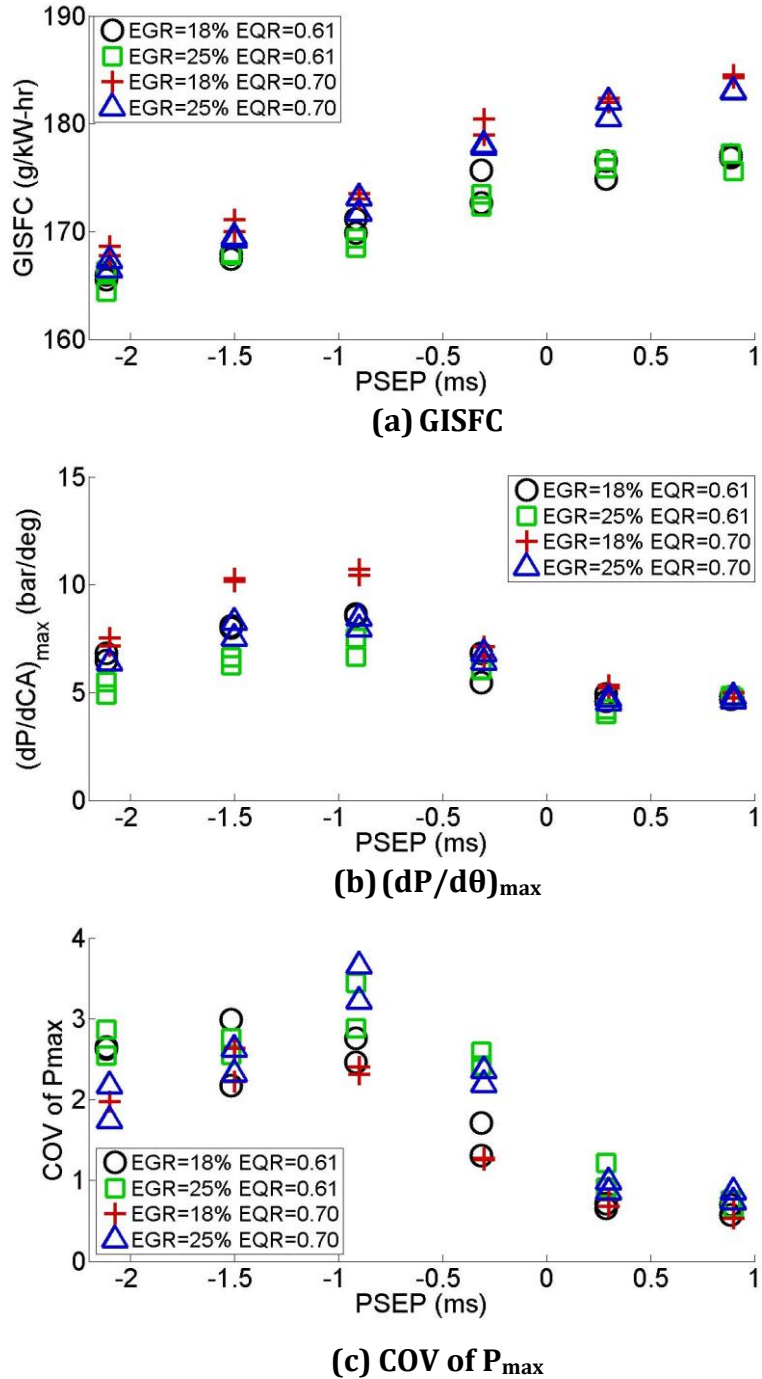


Figure 5-8 Engine performance for different engine environment from the SCRE experiments.

5.3.3 SCRE Experimental Results for Effect of Pilot Quantity on SPC

The effect of pilot mass on PM is shown in Figure 5-9. As discussed earlier, the relative injection timing (RIT) is a better way of characterizing injection timing than PSEP, when

pilot pulse width changes (Appendix E). For the SPC cases, with RIT<0, the pilot mass has no measurable effect on the PM emissions. Previous work with HPDI shows that most of the PM comes from the natural gas not diesel [131], for high PM modes. In the current experiments by more premixing of natural gas injection almost all of the PM is removed as well, while the pilot injection occurs in almost the same environment as the baseline. This is in general agreement with the previous experiments [131].

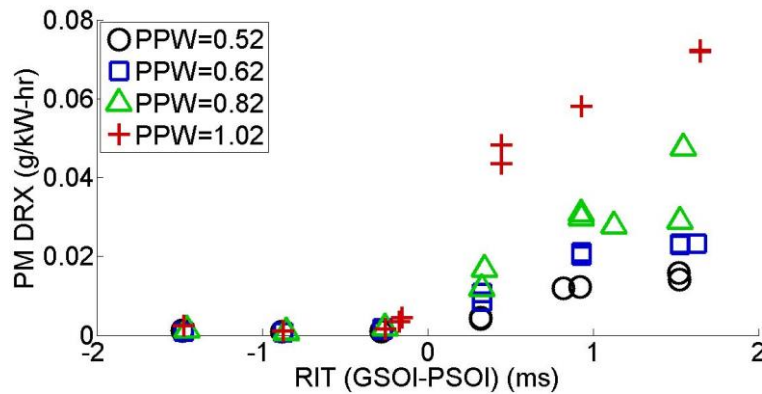


Figure 5-9 Engine-out PM for different PPW-PSEP sweep from the SCRE experiments.

5.3.4 Optimized Slightly Premixed Combustion and PM Characterization from the SCRE Experiments

From the parameter sweeps discussed above, an “optimized point” (i.e. best point of the SPC cases in the current parameter sweeps) was selected to have the lowest PM with almost the same NOx and CH₄ as the baseline point (PSEP=0.3, EGR=18% and EQR=0.6). The high EGR-EQR point (EQR = 0.7 EGR = 25%) with PSEP of -0.9ms was selected due to significant PM reduction and same level of NOx and methane as the baseline point (Table 5-3). The optimized SPC point shows a 90% reduction in PM and a 2% improvement in fuel economy with almost the same level of NOx, methane and CO emissions. The drawback of this point is cycle-to-cycle pressure variations and a higher peak pressure rise rate in the cycle; both of which are referred to as higher combustion harshness in the current thesis. Higher combustion harshness of the SPC points leads to higher engine noise as well.

Table 5-3 Comparing optimized SPC point with the baseline

	SPC ¹	Baseline
PM DRX (mg/kW-hr)	2	22
NOx (g/kW-hr)	1.3	1.3
Methane (g/kW-hr)	0.60	0.55
CO (g/kW-hr)	5.8	6
GISFC (g/kW-hr)	172.5	176
COV of Pmax	3.5	0.6
dP/dθ_{max}	8.0	5.0
P_{max} (bar)	136	139
Peak AHRR (kJ/m³-deg)	310	145
Cylinder Exhaust Temperature (°C)	536	539

¹ PSEP=-0.9, EGR=18%, EQR=0.7, the best point selected from parameter sweeps of mode B75

The baseline B75 (0.3ms PSEP 18%EGR 0.61EQR) and optimized SPC point were repeated for more detailed analysis of the PM characteristics, using an SMPS and collecting PM on TEM grids. A sample TEM image was included in Chapter 1, Figure 1-2; noting the soot aggregates and primary particles. For each operating point at least 40 aggregates were measured using the semi-automatic particle sizing algorithm. More information about the TEM analysis can be found in reference [45], [128].

Results from the image processing and SMPS scans are included below in Table 5-4. Similar to LPI analysis in Chapter 4, SMPS geometric mean and TEM aggregate projected area diameter are calculated. The SMPS shows that the SPC condition produces much smaller soot aggregates and a much lower concentration of particles. The TEM analysis also shows that the SPC point produces much smaller soot aggregates with smaller primary particles. Previous work on soot morphology analysis shows that smaller aggregates tend to have smaller primary particles [128], [152], [153]. Overall these results agree with the previous studies.

Table 5-4 Summary of the results from SMPS and TEM sampling for SPC and baseline points

Point Name	TEM Primary Particle Mean (nm)	TEM Aggregate Projected Area Diameter (nm)	SMPS Geometric Mean (nm)	Total Concentration #/cm ³
B75 Baseline	32±2	158±12	90 ±4	$2.1 \times 10^6 \pm 2.0 \times 10^5$
B75 SPC	15±1	82±5	51±1	$0.7 \times 10^6 \pm 0.5 \times 10^5$

These results show that in addition to reducing aggregate size (which is correlated with reducing soot mass) the primary particles are also reduced, possibly indicating that the surface growth, coagulation and agglomeration processes are slowed relative to baseline strategy.

The SMPS size distributions for the non-volatile fraction of the PM are shown in Figure 5-10 for baseline and SPC points. The same graph was presented for LPI points in Chapter 4, Figure 4-7. Solid and open symbols show two size distributions from two repeats for each of baseline or SPC point. The size distributions show lognormal distributions for all the points. For SPC points, the size distribution is shifted toward the smaller particles and the total number concentration is reduced significantly.

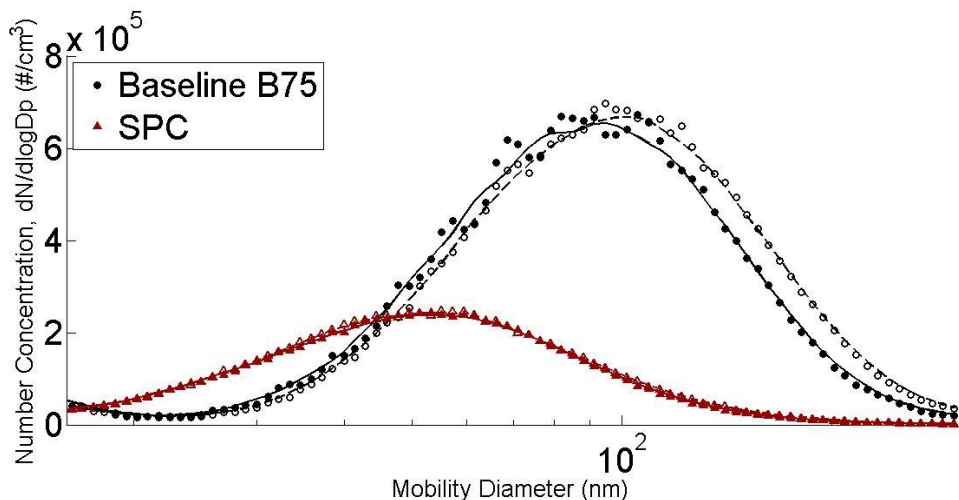


Figure 5-10 PM Size Distributions for baseline and SPC points. The open/ closed symbols are two repeats of Baseline or SPC points from the SCRE experiments. The curves are the moving average of each data set.

5.3.5 CFD Results and Discussion of SPC Mechanism

The baseline point and some SPC points ($\text{PSEP}=-0.9$ ms with different EGR-EQR levels) were simulated using GOLD. The AHRR graphs of baseline and SPC conditions are shown in Figure 5-11. There is good agreement between CFD and measurement for the baseline condition, but not for SPC. For the SPC case, the gas ignition delay was not be predicted correctly with the model, possibly because the TGLDM library was originally designed for normal HPDI combustion with dominant mixing-controlled combustion. More information about the TGLDM libraries is mentioned in section 3.6 and reference [143]. Revising these kinetics libraries for gas-diesel mixtures is a complicated task outside the scope of this thesis, therefore, in this study we delayed the diesel injection to bring AHRR closer to its experimental value [144]. As a result, for the SPC case we did not model any specific PSEP value, since the rate of reaction in CFD (from the AHRR graph of CFD simulation) is much higher than the experiments. Because of this, methane and NOx emission predictions are not considered reliable and not reported here.

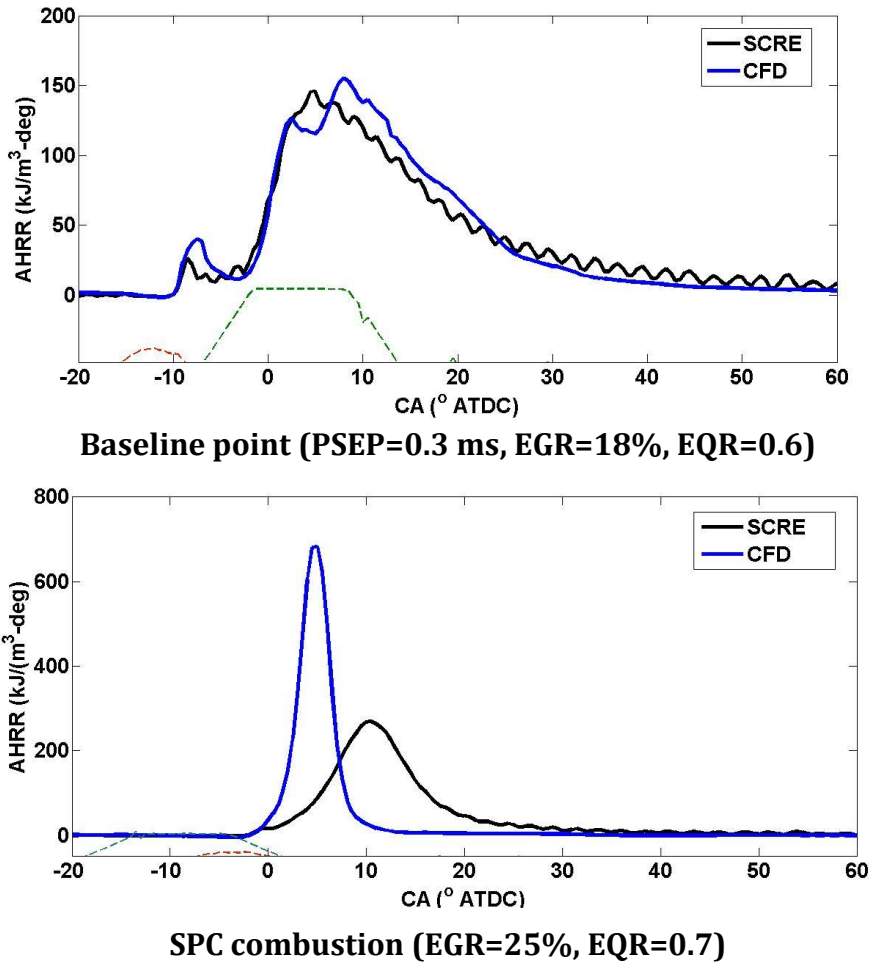


Figure 5-11 Predicted (CFD) apparent heat release rate of baseline and SPC case compared with the experiments. The green dashed line is the NG fuel rate shape and the red dashed line is the pilot fuel rate shape.

The evolution of PM in a cycle is shown in Figure 5-12 for baseline and SPC cases. PM formation in the cycle for baseline PSEP=0.3 ms and the same case with higher EGR is shown in the graph. By increasing the EGR, PM is formed more in the cycle; however, the main effect of EGR is on reducing the oxidation of PM in the cycle. For the SPC case, much less PM is formed in the cylinder and the PM will be oxidized quickly in the cylinder after EOI. Higher EGR or EQR will increase the PM formation in the cycle slightly in the SPC cases, but still the engine-out is much less than baseline. This trend has been noticed in the experiments as well.

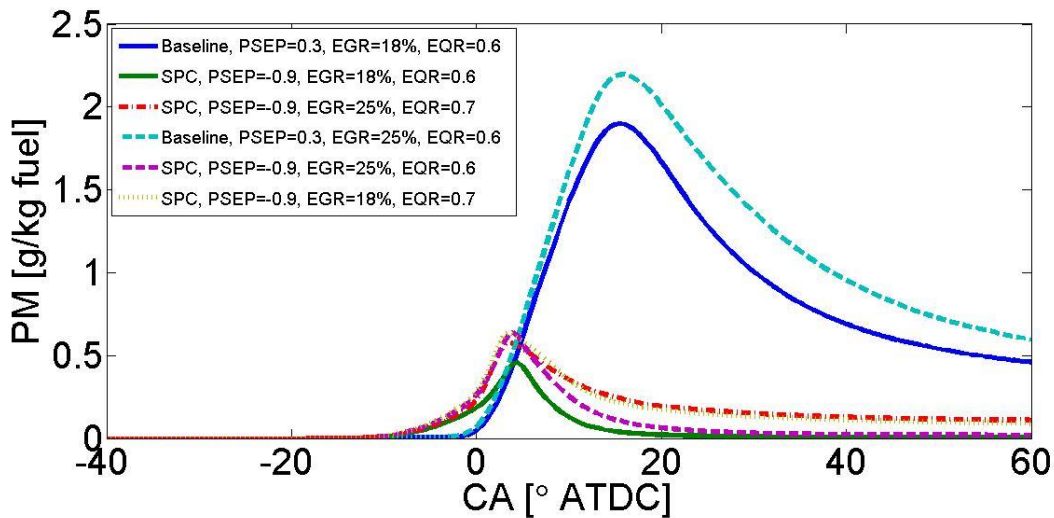


Figure 5-12 PM as a function of crank angle for different mixing controlled and SPC cases from the CFD simulations.

Although the CFD appears to confirm the importance of relative timing on PM emissions, consistent with the conceptual graph presented in Figure 1-5, this picture could not be compared with SPC combustion by CFD results since CFD could not predict the ignition point correctly and therefore could not be expected to predict PM spatial distribution accurately.

Based on the discussion above, CFD misses some important aspects of SPC combustion and PM spatial distribution are highly unreliable. Therefore, the remainder of the discussion focuses on the evolution of the mixture distribution in the cylinder, which is nearly independent of the chemistry. Figure 5-13 shows the normalized mixture fraction mass in “rich zone”, Z_{rich} ($2 \leq \varphi \leq 5$), and “lean zone”, Z_{lean} ($\varphi \leq 1$), as a function of CAD. These variables are defined in equations 3-28 and 3-29. The ignition points are shown in the figure by red stars. For the baseline HPDI combustion, the ignition point is before development of the rich zone in the cycle so it is more likely that soot will be formed by rich zone development. For the SPC case (EGR=25%, EQR=0.7), however, due to a longer ignition delay, ignition is almost at the end of rich zone development so less soot will be formed. The penetration of the jet for the SPC case is higher than the baseline point since the gas is injected in lower air density for SPC case [144]. This higher penetration of the SPC cases can be noticed from the

lower rich zone peak in Figure 5-13; however, almost all of this reduction in the rich zone happens before the ignition point and cannot be the main reason for PM reduction in SPC. Delaying the ignition to the end of rich zone peak is the main reason for PM reduction of these points based on the current graph.

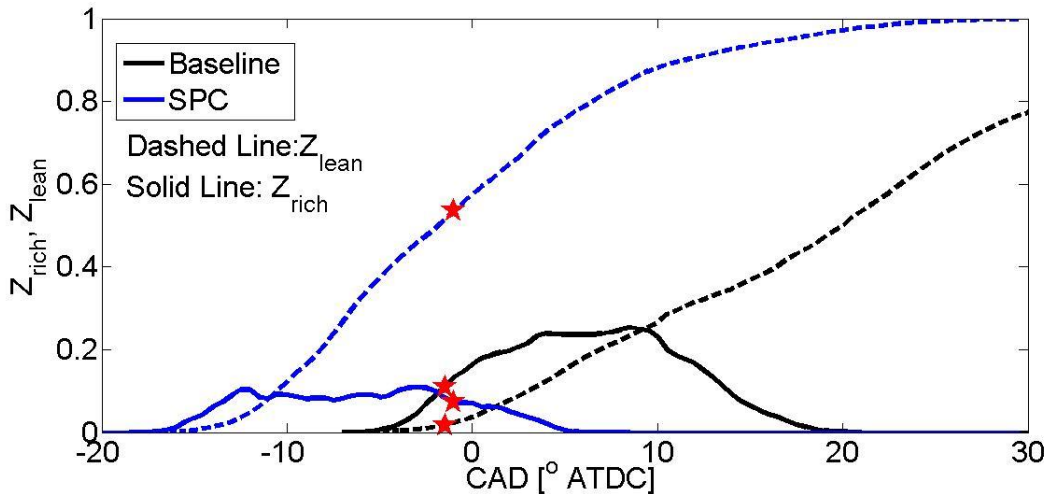


Figure 5-13 Development of rich zone and lean zone in the cycle for baseline and SPC case from the CFD simulations. The stars are the NG ignition points.

Premixing can be defined by different metrics. It can be defined as the level of Z_{lean} at the ignition timing. For this metric a CFD study or phenomenological model is always required. Based on this metric Z_{lean} is about 55% for SPC case while it is under 5% for the baseline case. The current study suggests the importance of relative timing of ignition (or peak AHRR) and end of injection. Related to this finding, another metric could be the fuel injected portion at the time of ignition (SPC factor=100% when ignition is at the EOI). To define this metric, knowledge of injector behaviour is required (momentum measurement or fuel rate shape).

EQR distribution of the jet at the ignition point of the baseline case and the SPC case (EGR=25%, EQR=0.7) are shown in Figure 5-14. At gas ignition time, there is still significant fuel in the rich zone for the baseline point; over 50% of the fuel is within $2 < \text{EQR} < 5$. For the SPC point, over 90% of the fuel is under EQR of 2, therefore the potential for soot formation is mainly eliminated. These values will be used to generate a conceptual φ -T map for the baseline and SPC case.

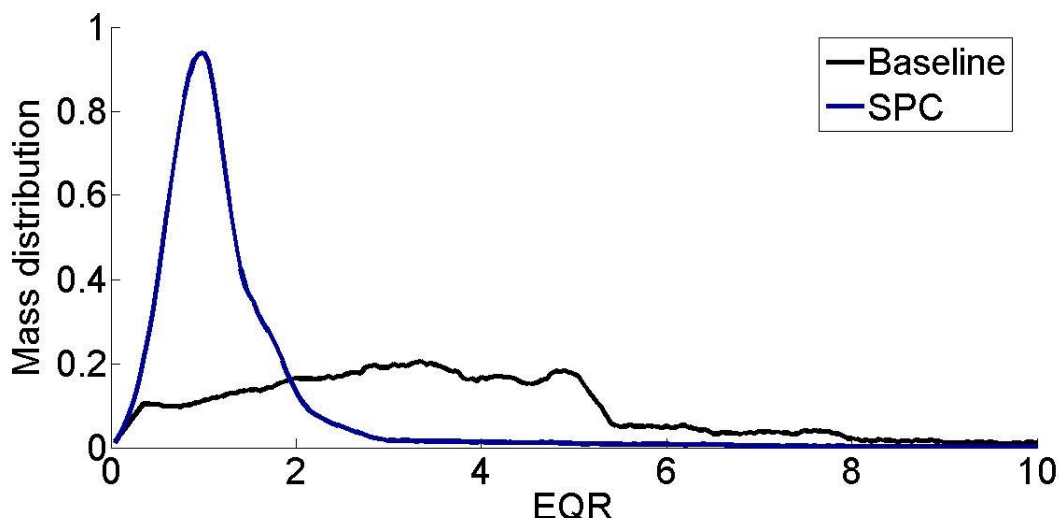


Figure 5-14 EQR distribution of baseline and SPC case at the ignition time from the CFD simulations.

An understanding of soot and NOx formation in engines can be aided by examination of the combustion process in a φ -T map [39]. It is a useful qualitative approach for visualization of soot and NOx formation in DI engines [40]. Figure 5-15, is a φ -T map generated for natural gas combustion, according to details described in section 3.7. The contours show the location where acetylene (soot precursor) and NOx formation occur for natural gas fuel. The green dashed line shows the non-reacting adiabatic mixing of fuel with ambient air. The fuel temperature is assumed 370 K with an ambient temperature of 1000K (roughly the temperature at TDC). The solid red line on the map is the adiabatic flame temperature calculated for these fuel/air temperatures and oxygen mass fraction of 20.5% (intake oxygen of the baseline point), while the dashed red line is the adiabatic flame temperature in the same conditions but oxygen mass fraction of 19% (intake oxygen of the SPC point, which has higher EGR).

CO also can be formed in the lean zone at a lower temperature as well [40], [43]. Based on the SPC experiment presented in this chapter, decreasing CO by more premixing might suggest rich zones are the main source of CO formation in these conditions. The engine-out CO does not reach zero for more negative PSEP cases; the remaining CO might be the CO generated in the premixed zone. However, we cannot confirm the portion of CO formation in the rich and lean zone separately, based on the engine experiments.

The fuel will be mixed with air according to the adiabatic mixing line before the ignition point. Two different combustion processes have been added to the plot for comparison of baseline and SPC case; shown in Figure 5-15. The location of the premixed burning (horizontal lines) in the graph is estimated based on the CFD results from Figure 5-14. The average EQR at the ignition time for baseline case is about 3, while for SPC it is slightly above stoichiometric mixture. The real premixed burning is a cloud rather than a single line; however, for simplicity the line is shown based on average EQR at the ignition time from CFD. In this conceptual graph, the dark blue arrows approximate the baseline (normal HPDI) case. The orange arrows show the cases with later ignition and higher EGR. More charge is premixed before ignition so the premixed burning would be a governing part of the combustion. Premixed combustion is followed by mixing-controlled combustion. It should be noted that for the range of EGR changes in these experiments, the inlet oxygen concentration is changed from 20.5% to 19% and accordingly, the adiabatic flame temperature will be reduced by less than 100 K. In the LTC in diesel engines the adiabatic flame temperature will be reduced by 300-700 K by reducing the inlet oxygen concentration to 10-15% [40]. The EGR in our experiments increased just slightly to maintain the NOx level of the baseline point, while for diesel LTC is used to control the ignition point as well.

For the baseline combustion, the mixing-controlled combustion passes from the PM formation zone and later moves to the NOx formation zones. For the SPC case, the average local EQR is below the PM forming zone therefore the PM formation of SPC points is minimal. In reality, since the premixed burning is not a single line, some packets of fuel will still pass the PM formation zone. The lower flame temperature due to higher EGR generates less NOx compared to an SPC case with lower EGR.

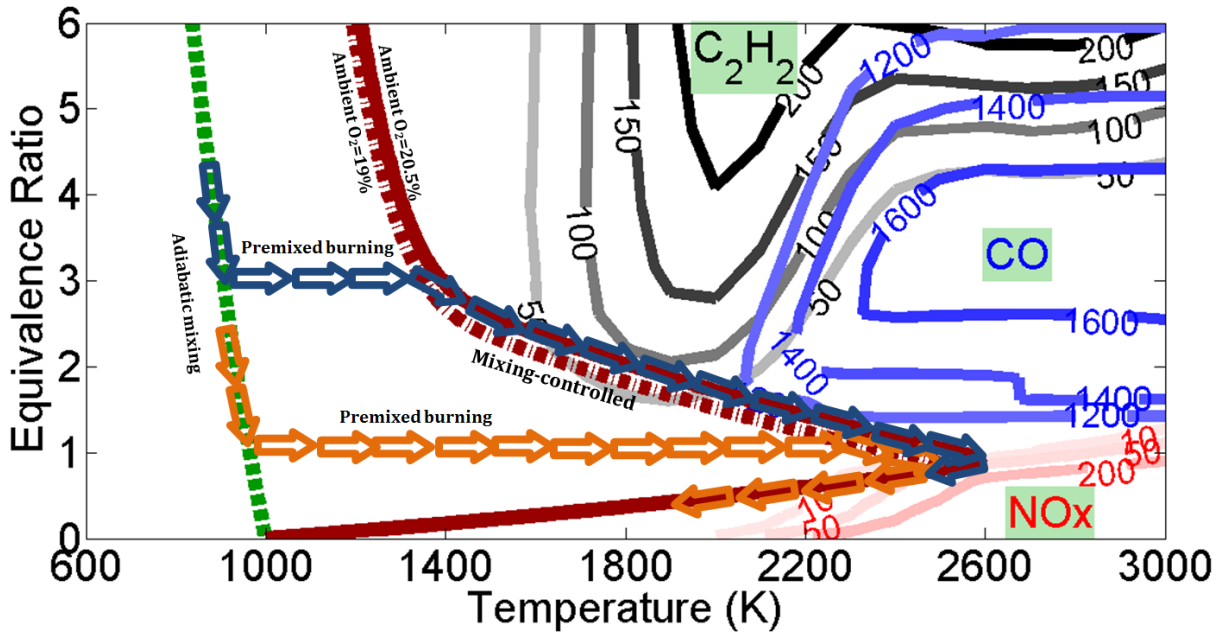


Figure 5-15 φ -T map computed for 2 ms residence time at 140 bar. The fuel temperature is 370 K and ambient temperature is 1000K. The simulation is based on GRI3.0 mechanism. The contour numbers show the concentration of each species based on a PSR simulation. The blue combustion path line is the conceptual baseline combustion while the orange line is the SPC conceptual combustion line.

5.3.6 SPC Multi-injector tests

Four injectors (Baseline Injector, Inj-1, Inj-2 and Inj-3) were selected for multi-injector tests. Inj-1, -2, and -3 were the same model of experimental prototype injector as the baseline injector. The robustness of the SPC strategy will be studied here for different injectors of the same model. The baseline Injector is the default UBC-SCRE injector; all the graphs in the current thesis are based on this injector's results except multi-injector tests presented in Chapter 4 and the current section. One of the injectors, Inj-3, has the highest mass flow rate for a specific GPW between the injectors. More information about the injectors and test matrix are included in the Appendix O.

The baseline-B for all the injectors are set by: N=1500 rpm, intake air flow= 205 kg/hr, EGR=18%, PSOI=-23° ATDC, GSOI=-15° ATDC, PPW=0.55 ms, GPW=1.75 ms, GRP=25.4 MPa. For the SPC points, N=1500 rpm, intake air flow= 175 kg/hr, EGR=25%, PSOI=-20° ATDC,

GSOI=-23° ATDC, PPW=0.55 ms, GPW=1.52 ms, GRP=25.4 MPa. Chapter 4 described the variability of the injectors and the different approaches to simulating a multicylinder engine (including the choice of baseline-B).

For the SPC-B points, the PM reduction is about 85% for all the injectors compared to their baseline values. This leads to an average PM reduction of ~85% for the average of the injectors compared to an average of the injectors in baseline-B. Methane emission is about the same compared to their baseline values. The average fuel economy is 2-3% better. NOx is slightly lower when method B is used, since the EQR and GIMEP of Inj-3 is higher than other injectors. COV of maximum in-cylinder pressure and maximum cylinder pressure gradient will remain similar to the baseline injector based on the average of the four injectors.

The results suggest that SPC strategy is less dependent on injector-injector variability than the LPI strategy. All the emissions and engine performance for SPC points (relative to the baseline B75) were very close for all the injectors. This might be because SPC is based on more premixing; therefore, injection history is less effective for the SPC strategy.

Table 5-5 Emission and injector performance of baseline B75 and SPC point for different injectors¹⁴.

Point	Injector	PM (mg/kW- hr)	NOx (g/kW- hr)	CH ₄ (g/kW- hr)	GISFC (g/kW- hr)	COV of P _{max} (-)	dP/dθ _{max} (bar/deg)
Baseline-B	Baseline e	13±2	1.21±0.04	0.48±0.0 2	175.2±0. 1	1.0±0.2	4.4±0.1
	Inj-2	61±20	0.94±0.07	0.43±0.0 8	180.9±0. 6	0.7±0.1	4.5±0.1
	Inj-3	93±14	0.97±0.01	0.52±0.0 5	187.1±0. 3	0.7±0.0	4.7±0.2
	Inj-4	17±0.6	1.35±0.04	0.41±0.0 1	174.5±0. 1	0.6±0.1	4.6±0.1
Average Baseline -B	All	46±40	1.12±0.21	0.46±0.0 6	179.4±6. 3	0.8±0.2	4.4±0.2
SPC-B	Baseline e	2±0.1	1.25±0.05	0.51±0.0 1	168.6±0. 6	3.0±0.0	8.4±0.6
	Inj-2	10±0.4	1.29±0.13	0.40±0.0 1	172.6±0. 5	2.7±0.1	9.3±0.1
	Inj-3	15±3	0.73±0.01	0.54±0.0 1	184.1±0. 8	4.9±0.4	7.6±0.1
	Inj-4	3±0.3	1.72±0.07	0.40±0.0 1	168.1±0. 6	2.3±0.4	10±0.1
Average SPC-B	All	7.5±8	0.99±0.54	0.46±0.0 7	173.4±8. 0	3.2±1.3	8.3±1.2

5.4 Conclusions for Slightly Premixed Combustion

Previous experiments [47], [50], [87] in HPDI engines show that by injecting the gas slightly before the diesel, PM can be reduced significantly at the expense of increased NOx and methane emissions for a given EGR level. Combining SPC with increased EGR limits NOx emissions while maintaining very low PM, but elevated EGR increases methane emissions. In the current study, SPC was further studied, with a focus on the use of higher

¹⁴ The measurements in this table are reported as Average of two repeats± (maximum-minimum)/2 for each injector based on two measurements. The average of all injectors are reported as Average of all injectors± (maximum-minimum)/2

EQR to limit methane emissions. One of the main contributions of the current study was to provide more information about the fundamental mechanism of PM reduction using SPC strategy in HPDI engines by engine experiments and CFD simulation. One aspect of this study is an investigation of ignition point location relative to end of injection (EOI) and injection event, to define a threshold for the SPC points.

By more premixing of NG, i.e. moving toward negative PSEP values, PM emissions decrease to a very low level, NOx and methane emissions both increase, fuel consumption decreases, combustion harshness (indicated by COV or maximum pressure and maximum $dP/d\theta$) increases too. Combustion harshness reduces slightly for $PSEP < -0.9\text{ms}$. These are consistent with previous experiments [47], [50], [87] in HPDI engines. Higher combustion harshness also can lead to higher engine noise as well.

The AHRR peak increases by more premixing from $PSEP=0.9$ to $PSEP=-0.9$, then reduces slightly for more premixed burn at $PSEP=-2.1\text{ ms}$, potentially due to mixing the main portion of fuel below stoichiometric.

For all the SPC cases, the combustion duration changed by less than 4%. However the peak AHRR changes significantly, about $70\text{ kJ/m}^3\text{-deg}$ over the average of $300\text{ kJ/m}^3\text{-deg}$. By increasing EGR the peak AHRR is reduced while the ignition delay is constant. Increasing EQR increases the peak AHRR for slightly premixed cases. This may be due to reducing the potential of over-mixing because of less mass of air in the cycle.

The PM/NOx trade-off is escaped for the SPC strategy. PM does not change for SPC cases by changing in-cylinder environment, which normally increases PM in normal HPDI points, e.g. higher EGR level. NOx increases by more premixing of the charge, i.e. moving to negative PSEPs. Increasing EGR controls NOx potentially by decreasing the flame temperature. CO reaches to its minimum value at $PSEP=-2.1\text{ms}$ while PM reaches its minimum value at $PSEP=-0.9\text{ms}$. CO is formed in regions of that jet that are rich but not as rich as needed for PM formation. After the end of injection local EQR of the jet reduces by time, as it takes longer for the jet to reduce maximum EQR in the core of the jet below the CO formation zone.

Methane stays almost unchanged with more premixing, i.e. delaying the ignition, until the ignition happens after EOI; then the methane level sharply increases. For normal HPDI points, EGR increases methane emissions slightly, however in SPC cases; increasing EGR increases methane formation significantly. Increasing EQR, on the other hand, reduces methane at the same PSEP and same level of EGR. Methane emissions for the high EGR and EQR points are close to the level of methane in the baseline point.

The “optimized SPC point” of the mode B75 (maximum PM reduction with the same NOx and methane level as the baseline of the SPC cases in the parameter sweeps) shows a 90% reduction in PM and a 2% improvement in fuel efficiency with almost the same level of NOx, methane and CO. The drawback of this point is cycle to cycle variations and a higher peak pressure rise rate in the cycle which can lead to higher engine noise levels. The morphology of the soot at the optimized SPC strategy shows smaller aggregates, primary particles, and number concentration of particles than the baseline strategy.

As mentioned in the literature review in Chapter 1, PPCI combustion and the PM formation process in diesel engines are significantly different from SPC in HPDI engines. Despite this difference, the relative position of ignition and EOI, as suggested in the literature (Figure 1-5), seems to be important for the HPDI engine as well.

CFD simulation was used to help understand the PM reduction mechanism in SPC. Although the ignition of gas cannot be predicted correctly, CFD showed, for SPC cases, much less PM is formed in the cylinder and the PM will be oxidized quickly in the cylinder after EOI. Higher EGR or EQR will increase the PM formation in the cycle slightly, but will have minor effect on PM by the end of cycle. This trend has been noticed in the experiments as well. The EQR distribution of the jet at the ignition point for the baseline case and the SPC case were compared. At gas ignition time, there is still significant fuel in the rich zone for the baseline point; over 50% of the fuel is within $2 < EQR_l < 5$. For the SPC point, over 90% of the fuel is under EQR_l of 2, therefore the potential for soot formation is mainly eliminated.

6 RESULTS FOR TRANSIENT SLICE MODEL

This chapter presents the results of the transient slice model (TSM), introduced in Chapter 3. For a wide range of engine conditions, measurements from the SCRE are compared with predictions from TSM for PM, pressure and AHRR.

6.1 Experimental Points to be Modeled by TSM

Fifty points have been selected from the SCRE experiments to be compared with the TSM model. These points cover the sweeps of engine parameters (EGR, EQR, GRP, NG flow, load and speed, CA50 and PSEP) as well as the non-conventional injection strategies: LPI and SPC (Table 6-1). As mentioned in Chapter 3, four TSM parameters were adjusted to match measurements for 3 engine conditions, and then held constant for all model-measurement comparisons. TSM takes the ignition time from the SCRE measurement and does not model the pilot combustion. The end of simulation (EOS) for all the points is set to 90° ATDC, as mentioned in Chapter 3; however, all the results (except LPI sweep) are presented up to 60° ATDC.

Table 6-1 TSM cases used for validation

Experiment Sweeps	Variable	Constants
EGR	EGR=0, 6, 1, 18, 24, 40, 60 and 80 ^{15%}	Mode B75 (GIMEP=16.5 bar, N=1500 rpm), EQR(0.6), CA50 (11° ATDC) , P _{inj} (25 MPa), PSEP(0.3 ms)
EQR	EQR=0.50, 0.54, 0.58, 0.62, 0.70	Mode B75 (GIMEP=16.5 bar, N=1500 rpm), EGR(18%), CA50 (11° ATDC) , P _{inj} (25 MPa), PSEP(0.3 ms)
NG flow	NG=1.7,3.5, 5.0, 5.75, 6.5, 7.5, 7.9, 8.2, 8.6 kg/hr	N (1500 rpm), [O ₂] _{intake} (0.205), CA50 (11° ATDC) , P _{inj} (25 MPa), PSEP(0.3 ms)
Gas rail pressure	GRP=22, 25, 29 MPa	Mode B75 (GIMEP=16.5 bar, N=1500 rpm), EGR (18%), EQR(0.6), CA50 (11° ATDC), PSEP(0.3 ms)
Mode	Mode: A25, A75, B75, C75, B25, B50	All parameters are optimized for best emission and fuel economy
CA50	CA50: 7, 9, 11, 13, 15 ° ATDC	Mode B75 (GIMEP=16.5 bar, N=1500 rpm), EGR (18%), EQR(0.6), P _{inj} (25 MPa), PSEP(0.3 ms)
PSEP	PSEP= 0.9, 0.3, -0.3, -0.9, -1.5, -2.1 ms	Mode B75 (GIMEP=16.5 bar, N=1500 rpm), EGR (18%), EQR(0.6), CA50 (11° ATDC) , P _{inj} (25 MPa)
LPI-GSEP	GSEP=1.0, 1.5, 2.0, 2.5, 3.0 ms	Mode B75 (GIMEP=16.5 bar, N=1500 rpm), EGR (18%), EQR(0.6), CA50 (11° ATDC) , P _{inj} (25 MPa), PSEP(0.3 ms)
SPC-PSEP	PSEP= 0.9, 0.3, -0.3, -0.9, -1.5, -2.1 ms	Mode B75 (GIMEP=16.5 bar, N=1500 rpm), EGR (25%), EQR(0.7), CA50 (11° ATDC) , P _{inj} (25 MPa), PSEP(0.3 ms)

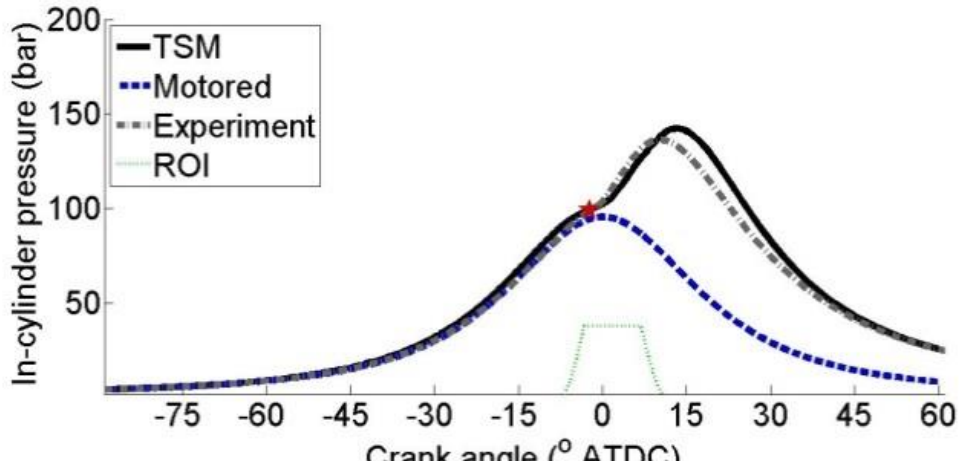
The engine measurements show substantial point-over-time variability, as mentioned in Chapter 2. This means that if the DRX measurement for the baseline point changes with time, the TSM should be recalibrated. In order to avoid this complication, and to separate model errors from measurement errors, the experimental measurements are normalized by the B75 baseline measurement. Recall that the soot prediction of TSM will be compared to denuded PM measurement from DRX.

¹⁵ No experiments are available for EGR=40, 60 and 80%. The ignition point for these cases are set according to EGR=24% case.

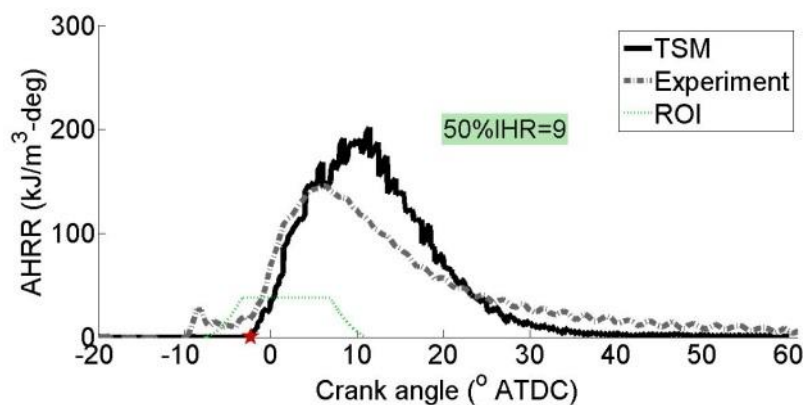
6.2 Results and Discussion

6.2.1 B75 Pressure and Heat Release Rate

Mode B75 is used for most experiments, since it generates more soot than most of the other modes. Figure 6-1 shows the pressure and AHRR compared to the experiments. The peak pressure and AHRR predicted by TSM are slightly higher and later than the measured values. This is due to instantaneous equilibrium assumption, which leads to a high burning rate for methane. This is only partly controlled by the effective flame speed; the shape of the AHRR still does not match at the end (Figure 3-6).



(a) Pressure

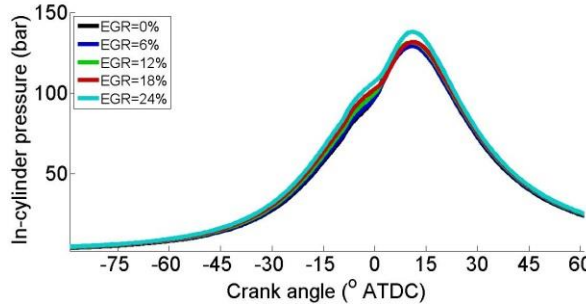


(b) AHRR

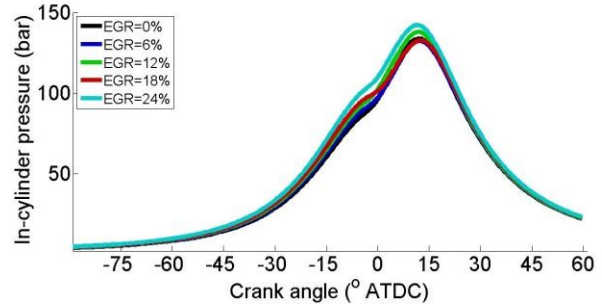
Figure 6-1 Pressure and AHRR of mode B75 compared to the TSM results. The star means the NG ignition point from the SCRE experiment. The green dashed line in the TSM fuel rate shape.

6.2.2 EGR Sweep

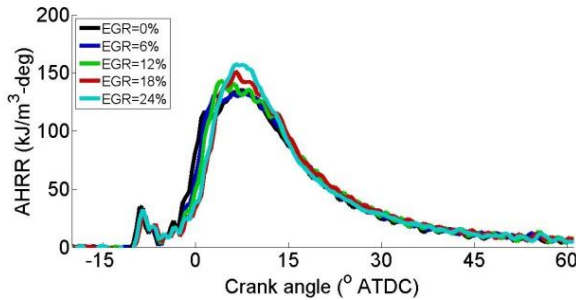
Pressure and AHRR from the experiments are compared to TSM results in Figure 6-2. TSM predictions show good agreement with the experiments in showing the trend in pressure change. AHRR does not change significantly with EGR sweep in SCRE experiments and the TSM AHRR graphs are also similar.



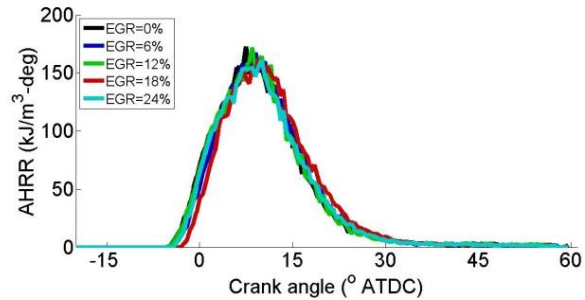
(a) Pressure experiments



(b) Pressure TSM



(c) AHRR experiments



(d) AHRR TSM

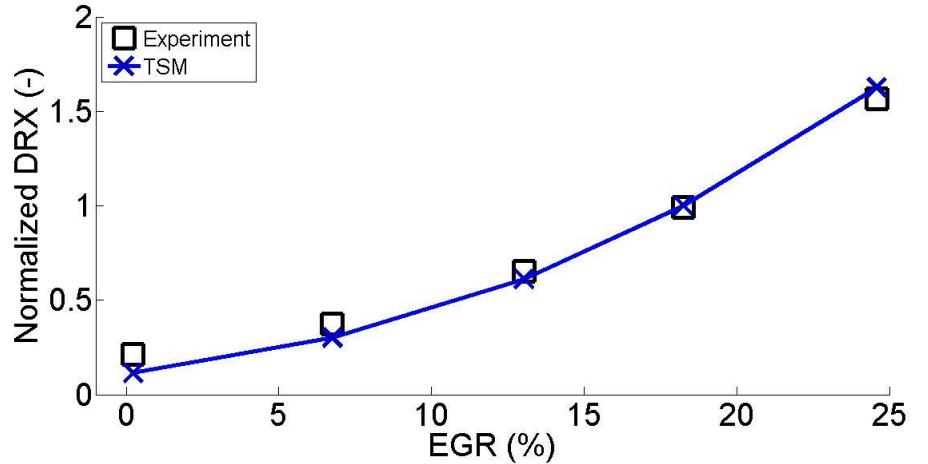
Figure 6-2 Effect of EGR on pressure (a,b) and heat release rate (c,d) for EGR=0-24% at mode B75.

PM predictions are compared with the DRX measurements in Figure 6-3 (a). The engine-out PM predictions are very good but recall that two points in this graph were tuned to match the experiments, as discussed in chapter 3 (0 and 18% EGR).

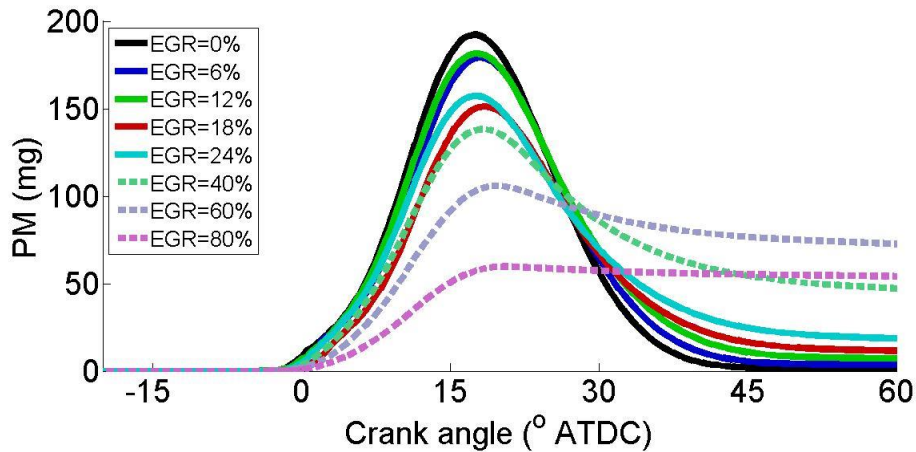
As mentioned in the literature review, in diesel engines, both peak in-cylinder soot formation and oxidation rates decrease with increasing EGR [52]. At moderate EGR levels (roughly $[O_2]_{intake}=21\text{-}10\%$) , soot oxidation decreases more rapidly than soot formation, so that exhaust soot emissions are greater than for non-EGR conditions [52]–[54]. At higher EGR level, however, exhaust soot emissions eventually begin to decrease, reaching low levels at high EGR rates [52]–[54]. A reduction in exhaust soot emissions at high EGR rates is believed to be due to little soot formation during the residence time available [53] and more premixing due to a larger ignition delay also plays an important role.

The PM-CAD graphs for different EGR are shown in Figure 6-3 (b), including EGR=40, 60 and 80% cases which cannot be run in our engine. PM formation decreases slightly; however, PM oxidation decreases more rapidly and engine-out PM increases as a result of

this balance (EGR=0-60%). However for much higher EGR (80% here) the formation rate is about 1/3 of the low EGR cases and engine-out PM starts to decrease. More investigation of these extra cases can be performed in a future study. Although the effect of EGR on diesel and HPDI engines are fundamentally different (in diesel engines ignition and EGR are tightly coupled), a similar qualitative effect has been noticed.



(a) Engine-out PM of TSM compared to DRX measurements



(b) PM-CAD graph

Figure 6-3 Effect of EGR on predicted PM emissions at mode B75. The PM-CAD graph is for EGR=0-80%.

6.2.3 NG Flow Sweep

The effect of gas flow (load) on pressure, AHRR and PM is shown in Figure 6-4. The peak pressure of the experiments is constant for higher NG flow rates; however, for TSM pressure will increase with increasing NG flow, which is due to the equilibrium assumption of the model controlled by an effective flame speed. In reality, after a certain injection duration, combustion rate approaches a mixing-controlled limit. For TSM the mixing controlled limit is, in effect, due to the assumption of equilibrium and an effective flame speed while neglecting progress variable in reaction. Despite this difference, TSM predicts

both pressure trends correctly. The AHRR trend also follows the trend of SCRE AHRR by increasing NG flow.

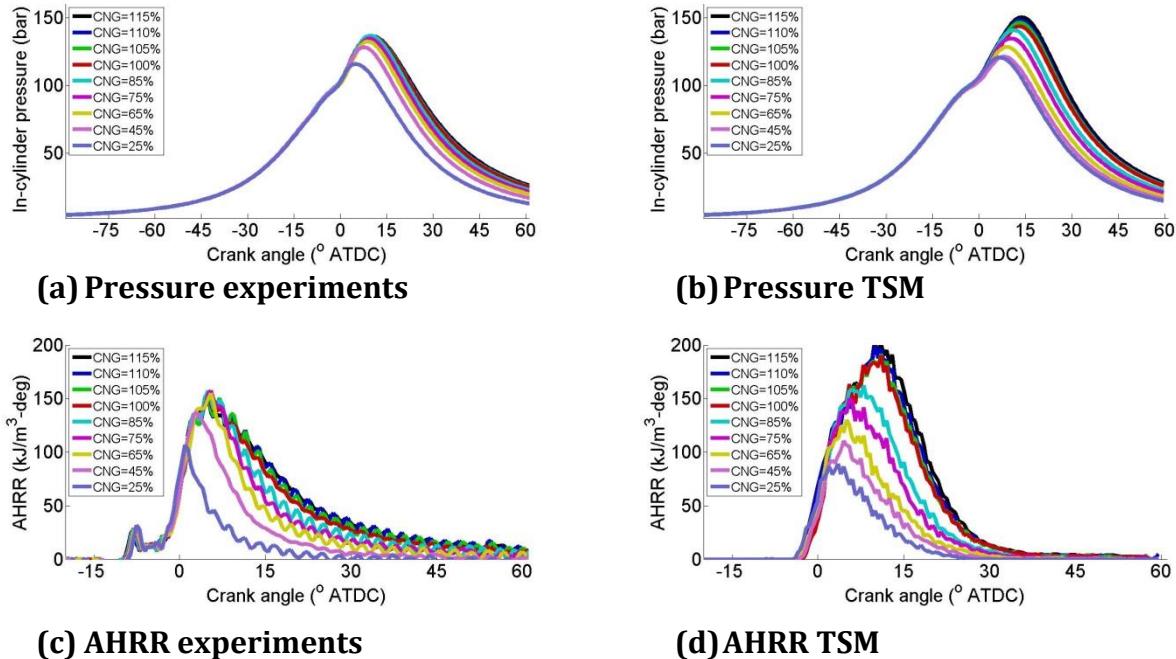
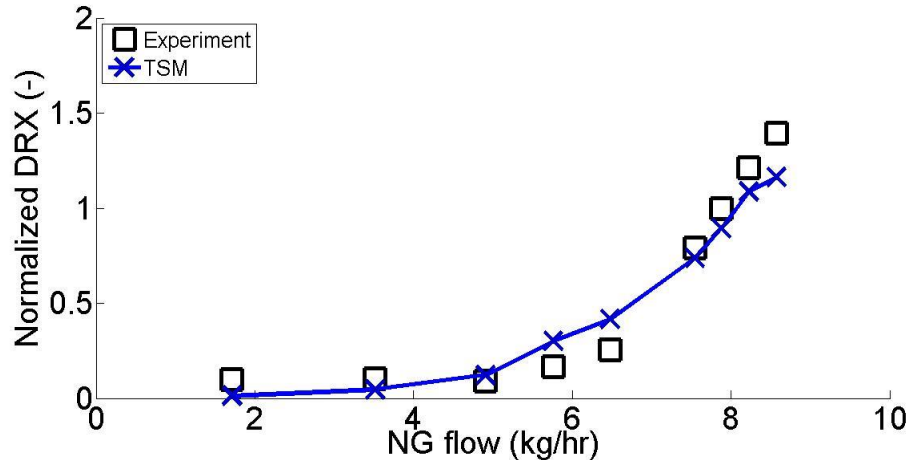
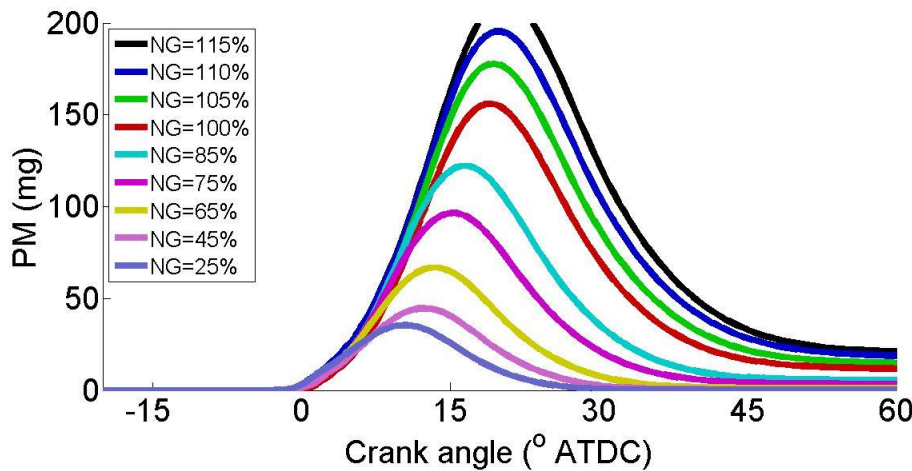


Figure 6-4 Effect of NG flow on pressure (a,b) and heat release rate (c,d) for NG flow=25-115% of the baseline mode B75.

The PM predictions are compared with the DRX measurements in Figure 6-5 (a). For very a high NG flow, the engine-out PM prediction of TSM is lower than the experiments, possibly related to the errors in the AHRR prediction. Beside this difference, for most of the points engine-out PM prediction of TSM is close to the measurements. The PM-CAD graph shows that the formation of the PM increases with increasing NG flow.



(a) Engine-out PM of TSM compared to DRX measurements

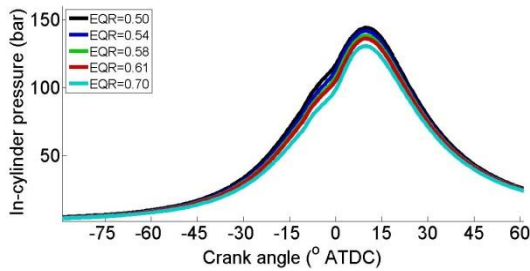


(b) PM-CAD graph

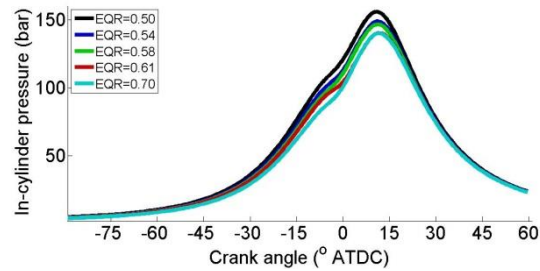
Figure 6-5 Effect of NG flow on predicted PM emissions for NG flow=25-115% of the baseline mode B75.

6.2.4 EQR Sweep

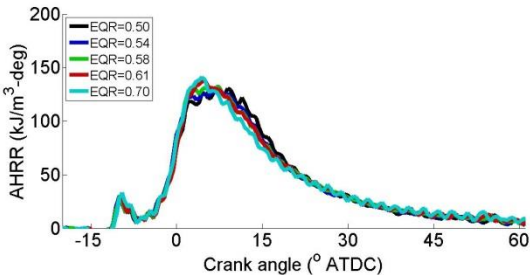
Measured pressure and AHRR are compared to the TSM results in Figure 6-6. By decreasing EQR through higher intake pressure, the in-cylinder pressure is increased in both SCRE experiments and TSM. The AHRR of the experiments and TSM are not sensitive to EQR.



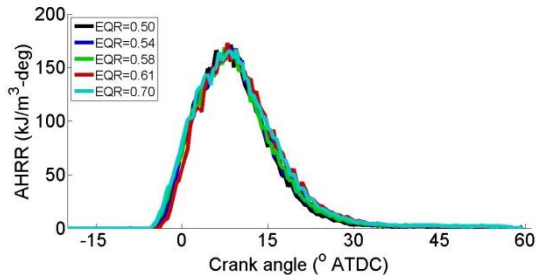
(a) Pressure experiments



(b) Pressure TSM



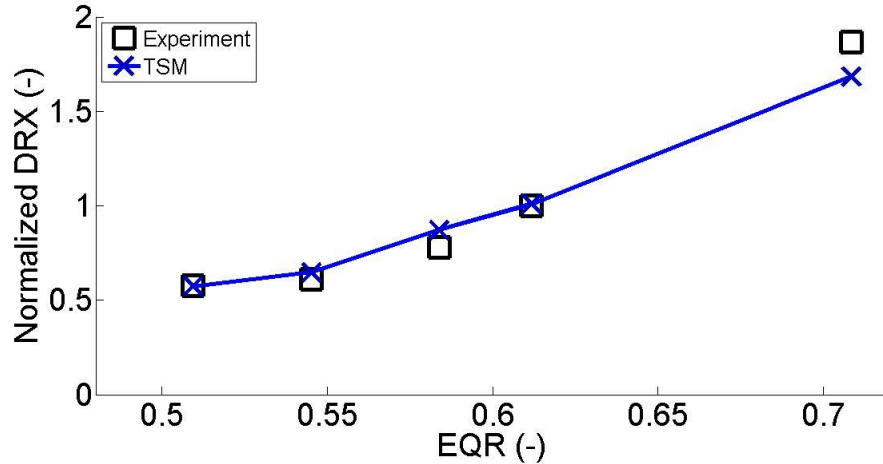
(c) AHRR experiments



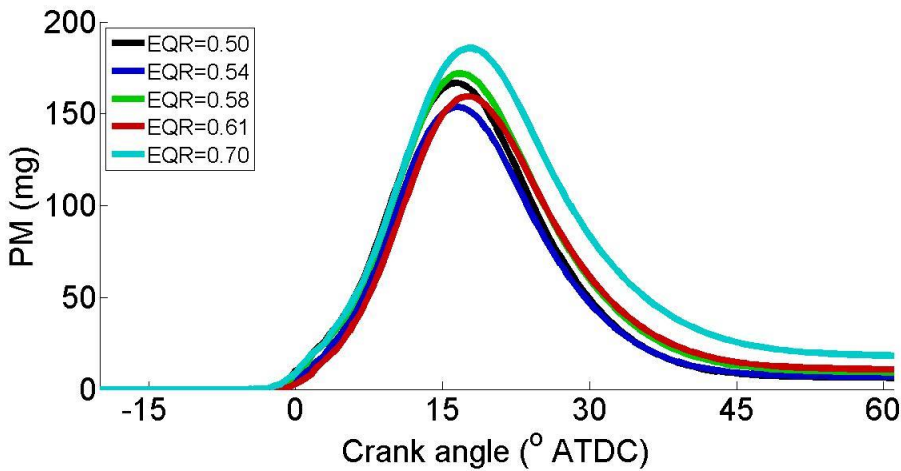
(d) AHRR TSM

Figure 6-6 Effect of EQR on pressure (a,b) and heat release rate (c,d) for EQR=0.5-0.7 at mode B75.

TSM can predict the trend in increasing PM by increasing EQR. The results are presented in Figure 6-7(a); for EQR values lower than the baseline (0.61), the TSM prediction is very close to the experiments. For high EQR, the PM prediction is slightly lower than the experiments. The PM-CAD graph shows higher in-cylinder PM for higher EQR cases; however, the peak in-cylinder PM does not consistently change with EQR.



(a) Engine-out PM of TSM compared to DRX measurements

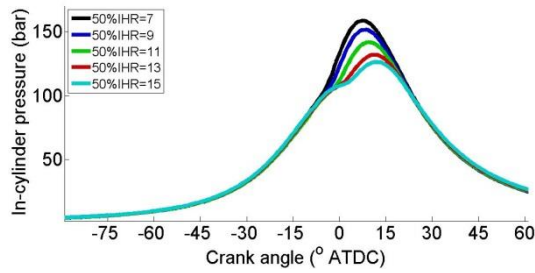


(b) PM-CAD graph

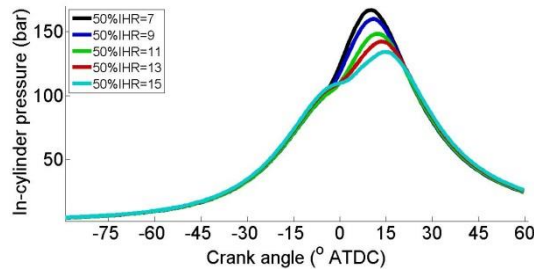
Figure 6-7 Effect of EQR on predicted PM emissions for EQR=0.5-0.7 at mode B75.

6.2.5 Timing (CA50) Sweep

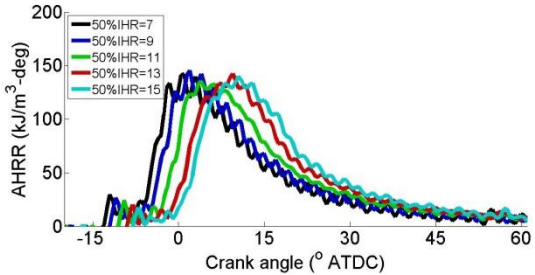
Measured pressure and AHRR are close to the TSM results (Figure 6-8). Maximum in-cylinder pressure decreases by retarding the CA50. TSM correctly shows that as the injection is delayed, the peak pressure will be lower and delayed. The CA50 of the TSM and the experiments are different due to the difference in the AHRR shape.



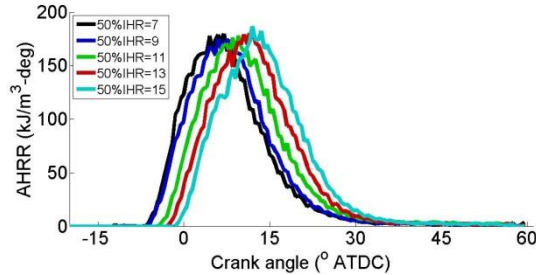
(a) Pressure experiments



(b) Pressure TSM



(c) AHRR experiments

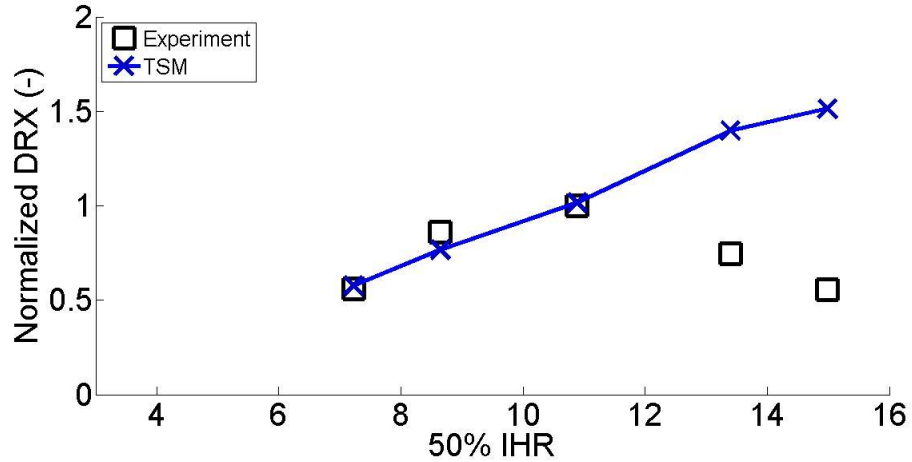


(d) AHRR TSM

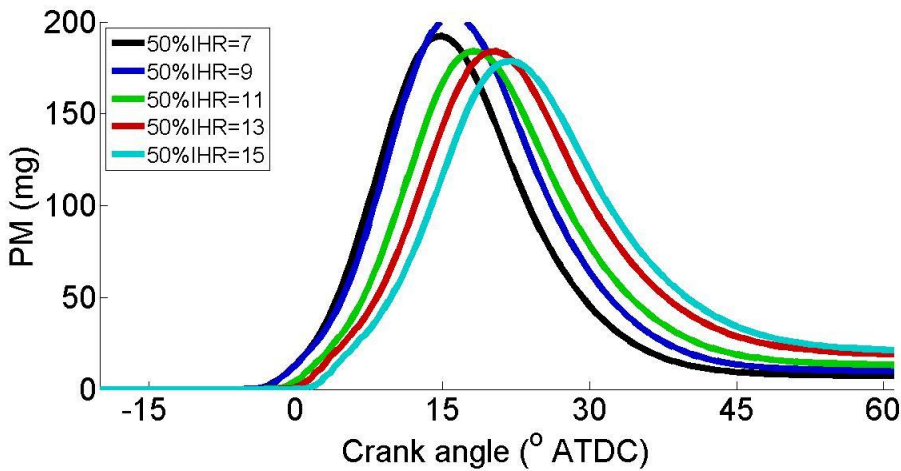
Figure 6-8 Effect of timing on pressure (a,b) and heat release rate (c,d) for CA50=7-15° ATDC at mode B75.

TSM can capture the engine-out PM increase that occurs when timing is changed from 5 to 11° ATDC; with a further increase in CA50, the predicted PM still increase while measured PM will decrease (Figure 6-9 (a)). As the injection is delayed, the piston location will change; therefore this changes the impingement timing. The PM decrease for higher CA50 might be due to the wall impingement effect, which has not been modelled in TSM.

The in-cylinder formation and oxidation of the CA50 sweep is shown in Figure 6-9 (b). In-cylinder PM formation increases from CA50=7 to CA50=9° ATDC and then decreases for all later combustion phasing (9-15° ATDC); however, the engine-out PM is constantly increasing since the oxidation time is reduced by later combustion. It is not clear that this deviation in the simulation from the experimental measurements is due to the wall impingement effect of ineffective PM oxidation modeling.



(a) Engine-out PM of TSM compared to DRX measurements

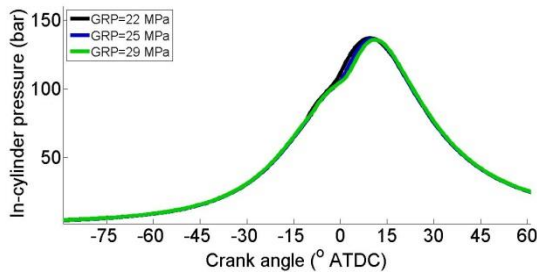


(b) PM-CAD graph

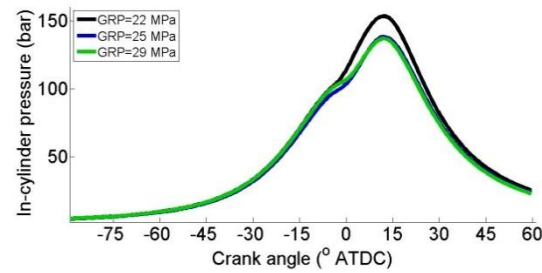
Figure 6-9 Effect of combustion timing (CA50) on predicted PM emissions for CA50=7-15° ATDC at mode B75.

6.2.6 Gas Rail Pressure (GRP) Sweep

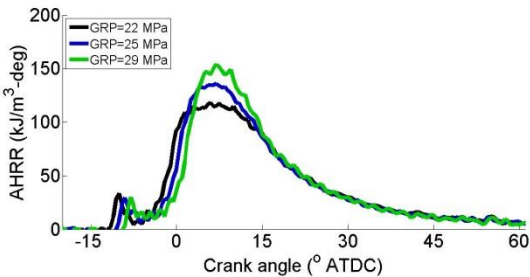
Peak AHRR from experiments increases due to higher mixing by increasing GRP; however, this is not captured by TSM. Figure 6-10 shows the pressure and AHRR of the experiments and the TSM results. As discussed in Chapter 3, a higher reaction rate of TSM due to the equilibrium assumption is controlled by selecting an effective flame speed. Since the reaction is controlled by a flame speed rather than the mixing by itself, the effect of GRP cannot be captured by the model.



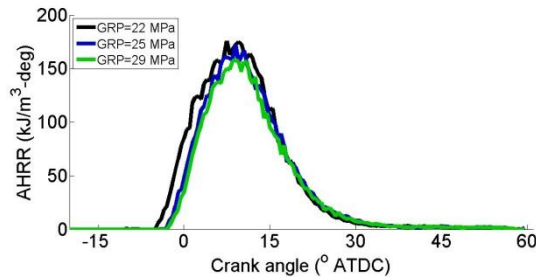
(a) Pressure experiments



(b) Pressure TSM



(c) AHRR experiments



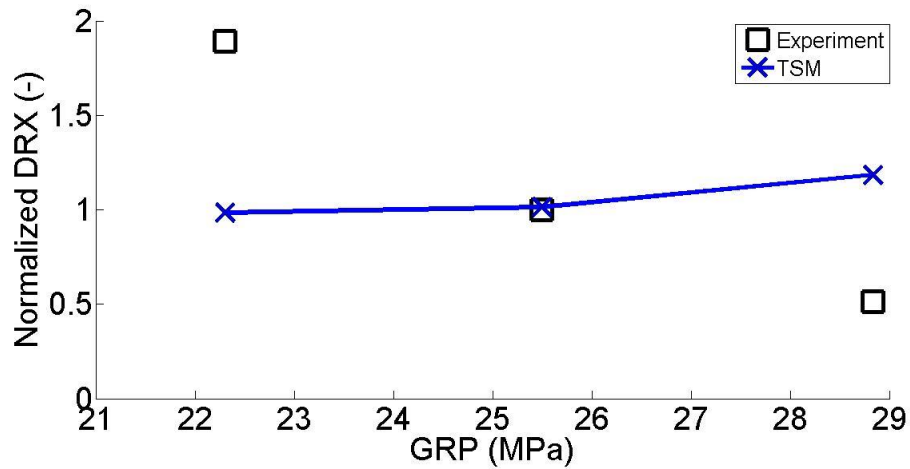
(d) AHRR TSM

Figure 6-10 Effect of GRP on pressure (a,b) and heat release rate (c,d) for GRP=22-29 MPa at mode B75.

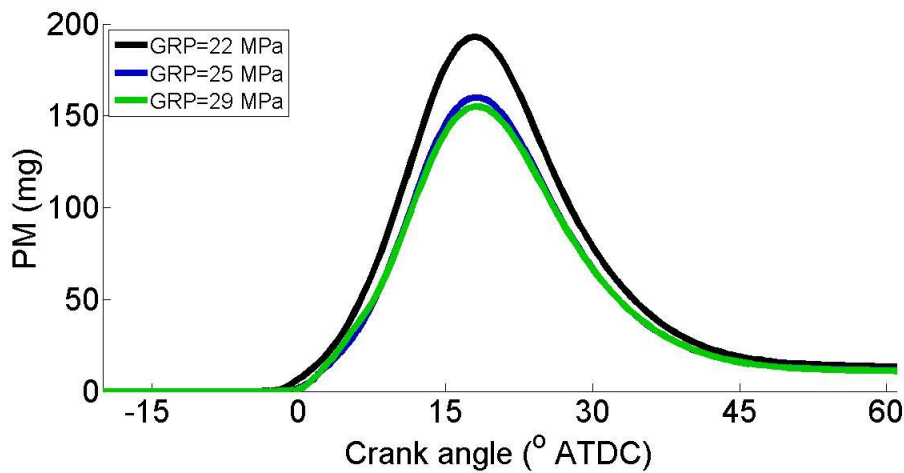
TSM cannot predict the PM reductions with GRP observed experimentally (Figure 6-11 (a)). Several factors might contribute to incorrect engine-out PM prediction of TSM, besides the incorrect prediction of AHRR by TSM. The turbulence effect on mixing has not been modeled correctly in TSM and more generally for all phenomenological models [111]. Pressure dependent injector dynamics were considered another potential factor. A study of the effect of ramp-up/down on engine-out PM by TSM, presented in Appendix 0, showed that faster opening and closing of the nozzle can help to reduce PM by ~15% for reducing ramp-up/down from 0.8 ms to 0.4 ms; however, this can only explain a small part of this deviation. The turbulence effect of GRP on the jet shape can be simplified in the model by changing the jet spread coefficient. More studies are required to find the dependency of the jet spread coefficient to GRP.

The PM-CAD graph shows that formation of the PM decreases with increasing the GRP; there is a sharp decrease for GRP=22 to 25 MPa and a slight decrease for GRP=25 to 29 MPa. Similar to the high EGR sweep and the CA50 sweep, it might suggest that the soot

oxidation model in TSM should be modified; however, as mentioned above the turbulence effect might be important as well.



(a) Engine-out PM of TSM compared to DRX measurements

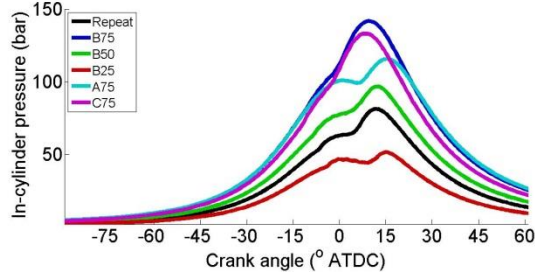


(b) PM-CAD graph

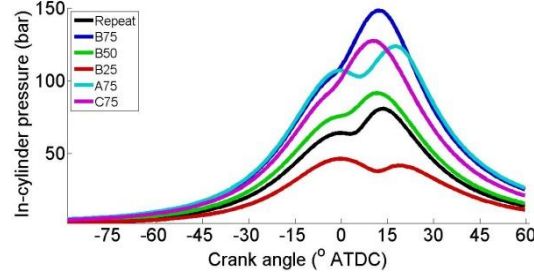
Figure 6-11 Effect of GRP on predicted PM emissions for GRP=22-29 MPa at mode B75.

6.2.7 Mode Sweep

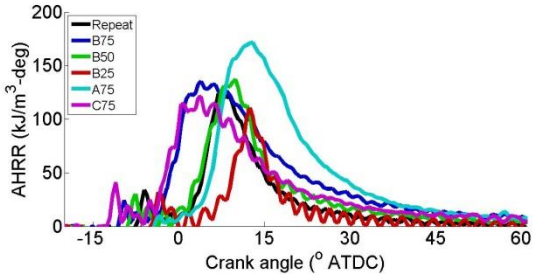
Pressure and AHRR of the experiments compared to the TSM results are shown in Figure 6-12. Pressure changes with the mode sweep show good agreement between TSM and engine experiments. AHRR of TSM, although different in shape, shows the trend by changing the mode.



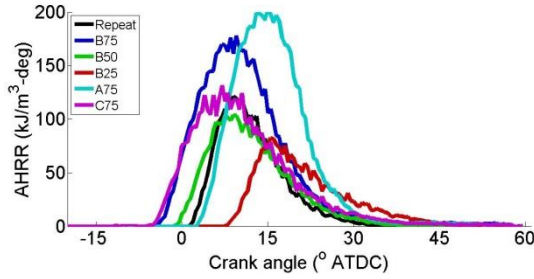
(a) Pressure experiments



(b) Pressure TSM



(c) AHRR experiments



(d) AHRR TSM

Figure 6-12 Effect of load and speed on pressure (a,b) and heat release rate (c,d) for different modes.

Engine-out PM shows a good match for some points, as shown in Table 6-2. The TSM simulation shows low PM for mode A35 and B25. For some other modes, relative engine-out PM compared to the B75 is captured as well; but the absolute value of engine-out PM is different from the experiments. The effect of turbulence intensity and wall impingement are not modeled in the TSM, which might partly explain why the effect of engine speed cannot be captured.

Table 6-2 Normalized PM for different modes

Mode	Normalized DRX, SCRE experiments	Normalized DRX, TSM simulation
A35	0.09	0.03
A75	0.15	0.78
B25	0.06	0.2
B50	0.1	0.6
C75	0.72	0.93

The PM-CAD graph of different modes is shown in Figure 6-13. By increasing the load, peak in-cylinder PM increases as well. Both A75 and C75 have lower peak in-cylinder PM compared to B75 point.

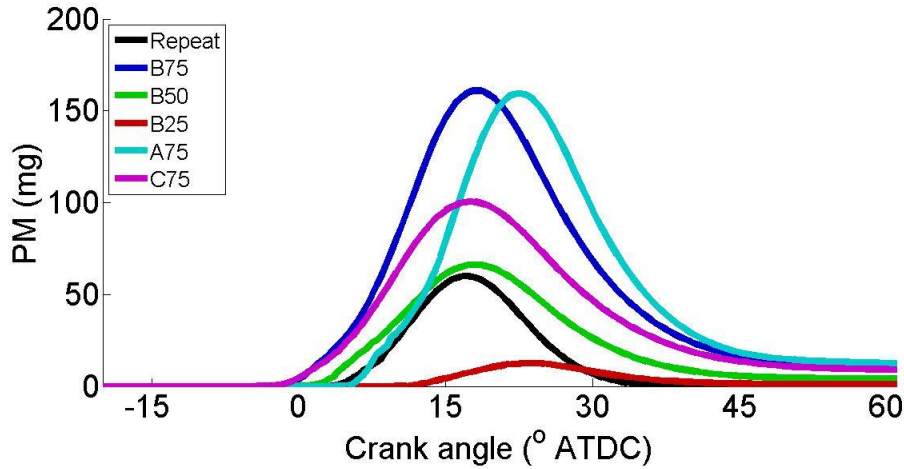
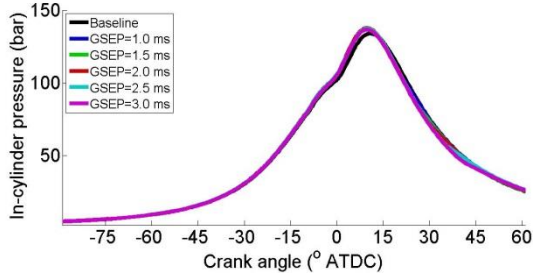


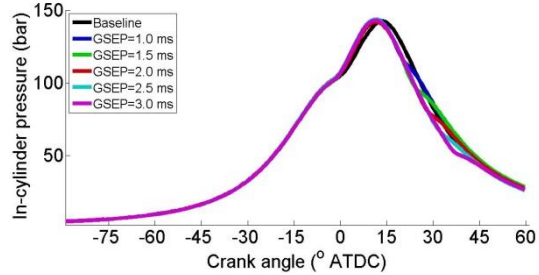
Figure 6-13 Effect of load and speed on PM-CAD graph.

6.2.8 LPI-GSEP Sweep

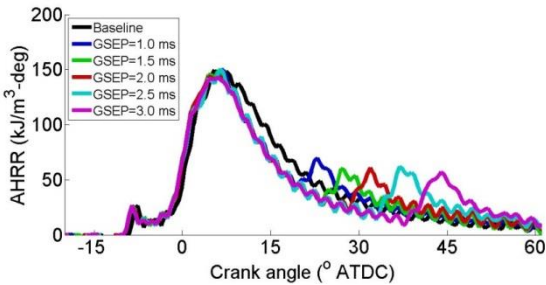
For the split injection cases, the pressure predictions are good. As shown in Figure 6-14, AHRR of the second pulses in TSM simulation shows a sharp rise with a high peak for AHRR of the second pulse, while in the experiments the AHRR of the second pulse has a lower peak value. This difference between TSM and experiments might be due to the ignition delay of the second pulse and also the difference in location of the start of ignition for the first and second pulse. The ignition delay was not defined for the second pulse, so the second pulse ignites if it is within the reaction zone. The reaction rate was controlled for the first pulse by defining an effective flame speed and location of the ignition at the tip of the jet. By the time the second pulse is injected, for large GSEPs, the second pulse reacts as it is injected.



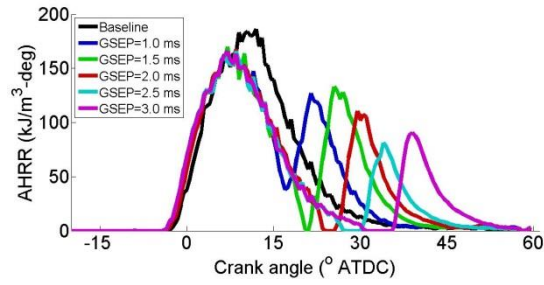
(a) Pressure experiments



(b) Pressure TSM



(c) AHRR experiments

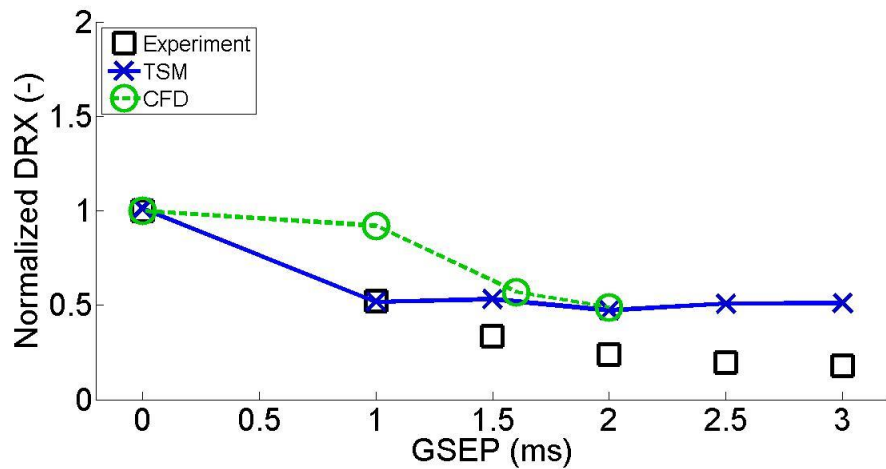


(d) AHRR TSM

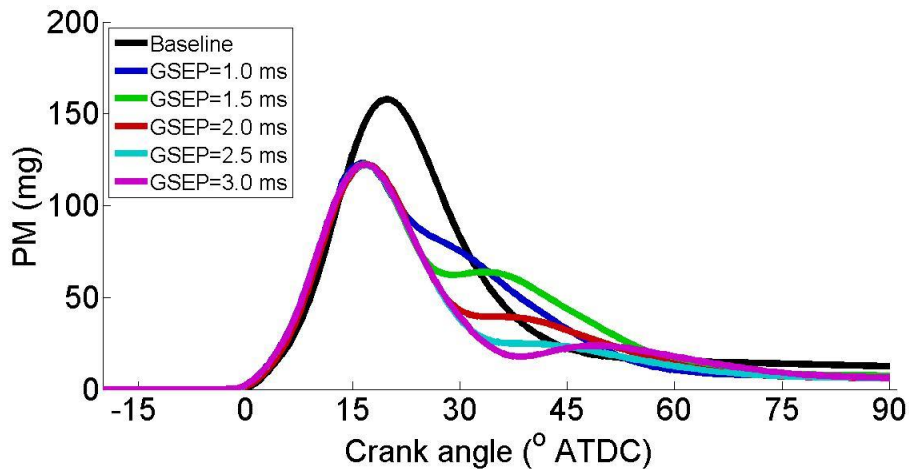
Figure 6-14 Effect of GSEP on pressure (a,b) and heat release rate (c,d) of LPI points for GSEP=1-3 ms at mode B75.

TSM correctly shows a large PM reduction for all the post injection cases; however, TSM cannot predict the trend of engine-out PM with GSEP correctly. The CFD results presented in chapter 4 (section 4.3.4) are included in the graph for comparison with TSM results. Both CFD and TSM show the same results for GSEP=1.5-2 ms; however, the TSM prediction of close-coupled pulses (GSEP=1 ms) is closer to the experimental data.

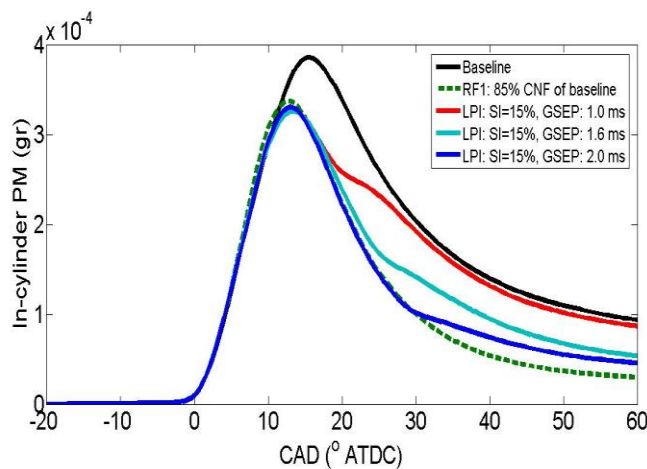
The PM-CAD graph of TSM and CFD results (presented before in section 4.3.4) are shown as well. In-cylinder PM traces of LPI in TSM cross the baseline case and later more oxidation of PM causes engine-out PM for LPI cases to be lower than the baseline. However, for CFD the in-cylinder PM is always lower than the baseline case.



(a) Engine-out PM of TSM compared to DRX measurements and CFD results



(b) PM-CAD graph of TSM



(c) PM-CAD graph of CFD (same graph as Figure 4-11)

Figure 6-15 Effect of GSEP on predicted PM emissions for GSEP=1-3 ms at mode B75.

6.2.9 PSEP Sweep

Cylinder pressure and AHRR for the experiments and TSM are shown in Figure 6-16. By moving toward the negative PSEP, combustion is shifted to the slightly premixed rather than non-premixed. In the experiments, ignition is delayed by injecting diesel fuel later in the cycle. After ignition, the pressure rise would be sharper and reaches to approximately the same peak pressure as normal HPDI points. In the TSM model, ignition was delayed; however, the pressure gradient was the same as the non-premixed cases with lower peak pressure. The effective flame speed was defined constant in the model, however, for slightly premixed cases the effective flame speed should be set to higher values to model the increased burning rate associated with the large premixed mass at ignition time, see Figure 5-14.

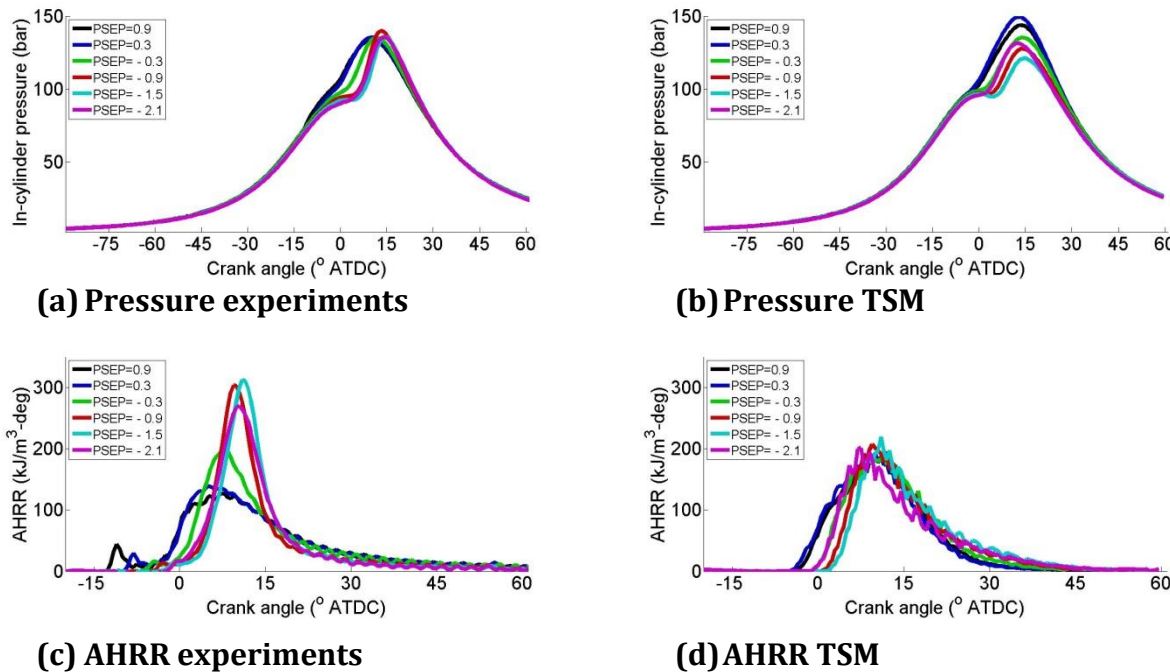
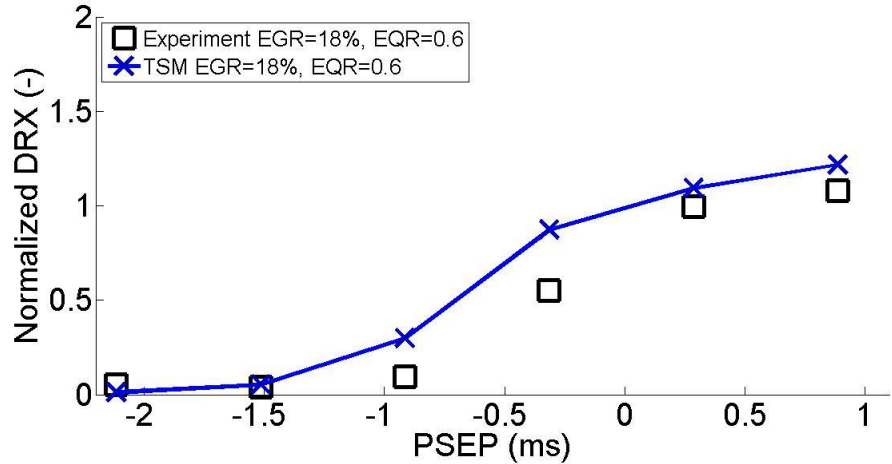
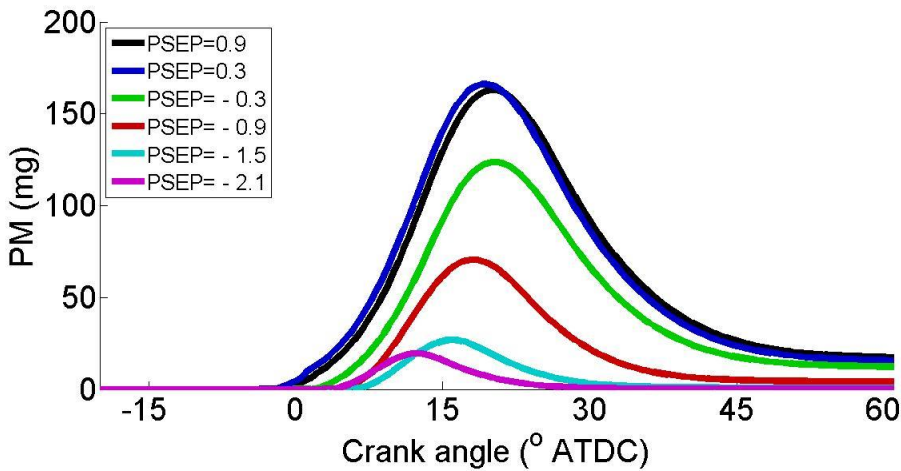


Figure 6-16 Effect of PSEP on pressure (a,b) and heat release rate (c,d) for PSEP=-2.1-0.9 ms at mode B75.

As is shown in Figure 6-17, the trend in PM reduction by moving toward negative PSEP values is well-captured by the model, although for PSEP= -0.9 and -0.3 ms the engine-out PM of TSM is higher than the experiments. PM-CAD graph of the TSM shows lower PM formation in the cylinder by moving toward negative PSEP (more premixing).



(a) Engine-out PM of TSM compared to DRX measurements



(b) PM-CAD graph of TSM

Figure 6-17 Effect of PSEP on predicted PM emissions for PSEP=-2.1-0.9 ms(EGR=18%, EQR=0.6) at mode B75.

The normalized mixture fraction mass (Z_{rich}) in “rich zone” ($2 \leq \varphi \leq 5$) is shown in Figure 6-18. The rich zone can be interpreted as a potential soot forming mass after the ignition point (the integral of Z_{rich} from ignition point). Looking at the Z_{rich} graphs, for different PSEP values ignition is shifted to the end of the Z_{rich} zone by moving toward the slightly premixed cases, this means much lower potential for PM formation in engine. This analysis is consistent with CFD analysis of the SPC cases presented in section 5.3.5.

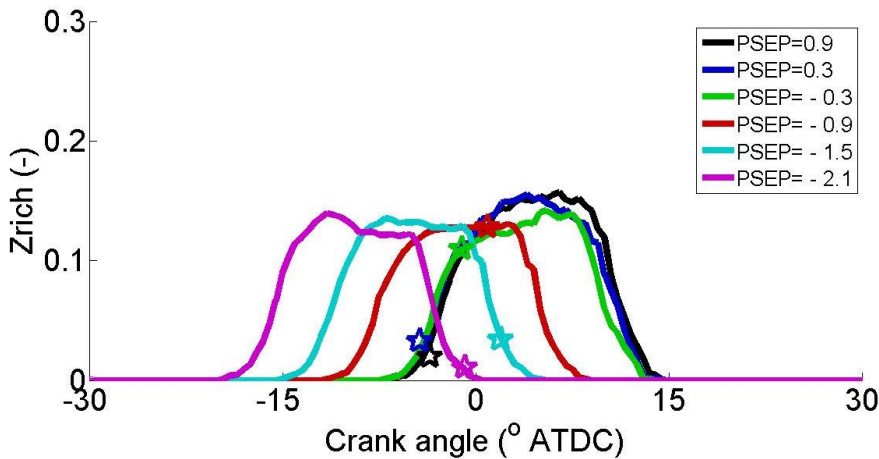
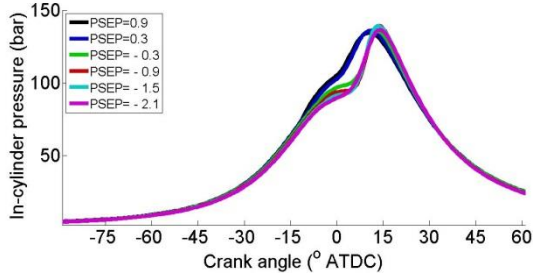


Figure 6-18 Effect of PSEP on rich zone development (Z_{rich}). The stars show the gas ignition points.

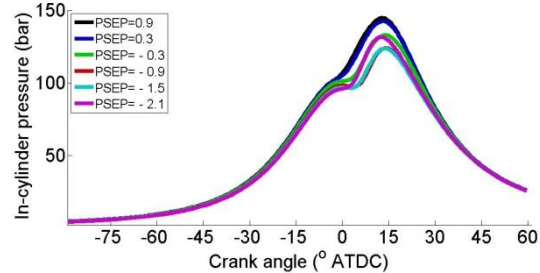
As mentioned in Chapter 5, premixing can be defined as the Z_{lean} at the ignition time. For TSM these values are 0.5% for $\text{PSEP}=0.9$ ms, 0.5% for $\text{PSEP}=0.3$ ms, 4% for $\text{PSEP}=-0.3$ ms, 18% for $\text{PSEP}=-0.9$ ms, 30% for $\text{PSEP}=-1.5$ ms and 35% for $\text{PSEP}=-2.1$.

6.2.10 SPC-PSEP Sweep

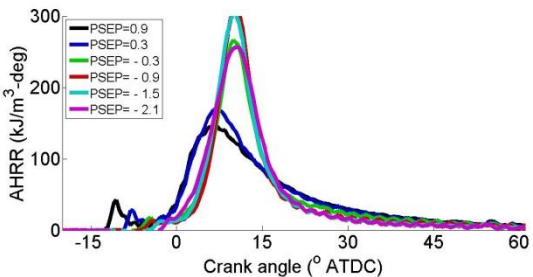
SPC cases considered here have negative PSEPs with higher EGR and EQR to control the NOx and methane engine-out levels as mentioned in Chapter 5. The pressure and AHRR of the SPC cases in SCRE experiments follow the same trend as the normal PSEP sweep, although the magnitude of the peak AHRR is different in the SCRE experiments. For the SPC cases, as with the negative PSEP cases, the AHRR is not well-captured by the TSM model. The same tuning constants as all other points have been used for the SPC points as well.



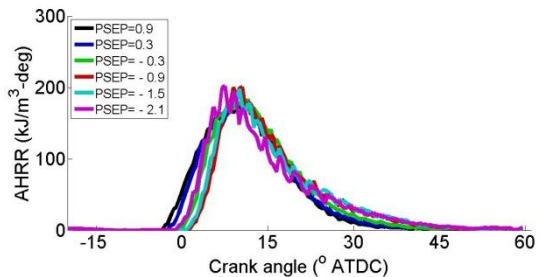
(a) Pressure experiments



(b) Pressure TSM



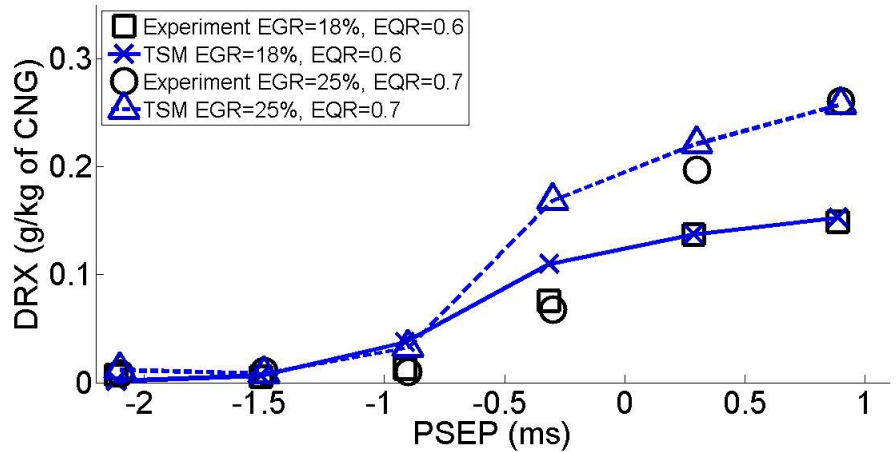
(c) AHRR experiments



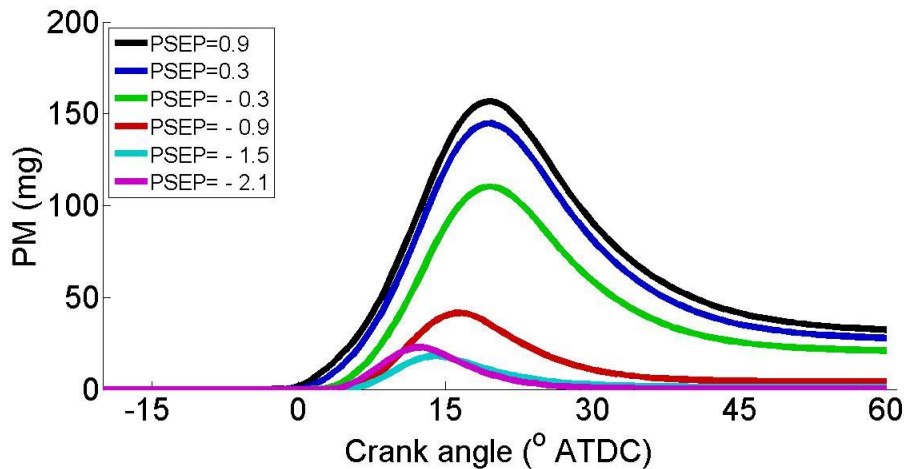
(d) AHRR TSM

Figure 6-19 Effect of SPC-PSEP (EGR=25%, EQR=0.7) on pressure (a,b) and heat release rate (c,d)

Engine-out PM of these cases is compared to the experiments in Figure 6-20 (a). The trend in PM reduction by moving toward the negative PSEP is well-captured by the model, even if the EQR and EGR are much higher than the baseline point. These results are in agreement with the experimental results and the mechanism of PM reduction in SPC cases, as discussed in Chapter 5. PM-CAD graph of SPC-PSEP sweep (EGR=25%, EQR=0.7) also shows the same trend as the normal PSEP sweep (EGR=18%, EQR=0.6) in reduction of the peak in-cylinder PM by moving toward negative PSEP values.



(a) Engine-out PM of TSM compared to DRX measurements



(b) PM-CAD graph of TSM (EGR=25%, EQR=0.7)

Figure 6-20 Effect of SPC-PSEP sweep on predicted PM emissions.

6.3 Conclusions for the Transient Slice Model

A novel quasi-1D phenomenological model of HPDI combustion and soot formation has been developed. The goal of this work has been to provide better understanding of PM formation mechanism in the HPDI engine and evaluate the model performance in PM prediction for conventional, LPI and SPC operation.

The model simulates a free jet based on 1D numerical solver for momentum and mixture fraction. The nozzle and the ambient conditions of the free jet were set to model the jet

inside the cylinder. The model used a one zone thermodynamics model to calculate the pressure and temperature of the cylinder based on mass fractions calculated by the jet model. Soot was predicted by solving transport equation for soot using formation and oxidation terms from Hiroyasu model.

To test the model, over fifty experimental points were selected in very different conditions. One set of tuning factors (4 constants) was used for all points. TSM results show good agreement in prediction of pressure trace and AHRR, considering the deviation discussed before, for most of the cases. Engine-out PM trends with changing the engine parameters are well-captured in the TSM for EGR, EQR, NG flow, PSEP and the effect of load in mode sweeps. The effect of gas rail pressure (GRP) on engine-out PM cannot be captured by the model, perhaps due to the turbulence effect that is not well-modeled in the TSM or rough estimation of AHRR from the TSM is not enough to see the effect on engine-out PM.

For more advanced injection strategies e.g. LPI and SPC, the TSM shows good performance in the prediction of engine-out PM. For LPI points, the low PM level of LPI cases could be predicted by the model. In SPC simulations, the trend in PM reduction for negative PSEPs even for high EGR/EQR points is well-modeled by the TSM.

Due to the equilibrium assumption, the AHRR is typically higher in the model. For engine experiments, chemical kinetics leads to the more progressive start of combustion while in the TSM model the model simply shifts from inert to reacting conditions, as ignition starts. We have controlled the ignition propagation by defining the effective flame speed, however, due to a difference in the physics of the flame propagation in real engine conditions, the AHRR does not perfectly match. However, differences due to these limitations seem to be minor when we tried to simulate engine cases including the engine-out PM.

Comparing the performance of the model with the packet model for the diesel engines, the jet dynamics in TSM was validated with many experiments, while for the packet model the comparison was limited to engine AHRR and engine-out emissions. The AHRR simulations for both models are acceptable for many cases. The TSM prediction of engine-out PM was compared to many experimental sweeps with one set of tuning factors.

7 CONCLUSIONS

Two unconventional HPDI injection strategies (LPI and SPC) were selected and developed for a single-cylinder research engine. The mechanisms of non-volatile PM reduction were studied in a single-cylinder research engine with the aid of large-eddy simulations and a new phenomenological model. The results presented in this thesis are based on a research-level dual-fuel natural gas and diesel injector (the “UBC Baseline Injector”, except where specifically indicated otherwise).

7.1 Late Post Injection

The effect of post injection of gas on HPDI engine performance and emissions was studied for a range of speeds, loads and injection parameters. One of the main contributions of the current study is to provide a better understanding of the mechanism of PM reduction using LPI strategy in HPDI engines using “pulse isolation” tests and CFD simulation.

Momentum measurement experiments showed that the baseline injector could not operate practically for gas pulse separations (GSEP) < 1 ms, and even for “close-coupled” ($1 \text{ ms} < \text{GSEP} < 1.5 \text{ ms}$) where the engine could run, the post injections were characterized by low and variable momentum rate. In engine tests, these points are associated with lower PM reduction compared to late post injection (LPI) points.

To compare the effects of LPI on multiple modes, an “optimized point” was selected from the B75 GSEP/SI sweeps. The selection was based on maximum PM (75%) reduction and less than a 1% fuel consumption penalty) for B75, and the injection parameters were not tuned for the other modes considered (A75, B75, C75 and B87). Although the magnitude of PM reduction or fuel consumption penalty was different for each mode, PM reductions were significant (60-80%) in all modes, except for mode A75 which already has PM emissions close to the minimum measurement limit. Methane emission was reduced by 20% for mode B75 and C75 compared to the baseline of the same mode. Fuel consumption penalty varies between modes from 1% to 4%, highest penalty in higher load (B87), compared to the baseline of the same mode. The combustion of second pulse for B87 mode

happens later in the cycle compared to the other modes with more significant heat addition by the second pulse injection. The exhaust temperature of LPI points remains within $\pm 5^{\circ}\text{C}$ of the baseline exhaust temperature, for all the modes based on exhaust temperature measurements. This shows that heat loss from exhaust for LPI points is not significantly different from the baseline point in the range of parameter sweeps in the current study.

One of the main contributions of this thesis was to use novel “pulse isolation tests” to help understand the mechanism of PM reduction using late post injection of gas. Figure 7-1 shows the results of the pulse isolation tests. Increasing the NG flow in the “single injection sweep” increases the PM mass significantly, consistent with prior literature on HPDI combustion. However, it is shown that this increase in PM is non-linear. A key new finding is that if we keep the first gas injection mass constant, increasing the second injection does not change engine-out PM significantly (LPI sweep 1 and LPI sweep 2).

The main PM reduction of the LPI points comes from shortening the first pulse. The pulse isolation tests showed that by reducing 15% of NG flow, the PM will be reduced by 75%. The CFD results also confirmed this finding. The second pulse has an overall minor contribution in net PM mass at exhaust. Possible explanations are:

- a) The second pulse does not form significant PM mass.
- b) PM formation of the second pulse is significant; however, the extra net PM mass of second pulse will be balanced by more oxidation from the first pulse due to interaction with the second injection.

The pulse isolation tests showed that the net PM mass is very close to the net PM of the first injection for ALL the points in the pulse isolation tests. This supports (but does not prove) the first explanation because the chance of balancing formation and oxidation between two pulses, for ALL the points at very different conditions seems low. Moreover, the CFD results (figure 4-10) show the PM formation of the second pulse is very low for large enough GSEPs. For the LPI points, the last portion of the fuel is injected into lower temperature and lower in-cylinder pressure conditions compared to the close-coupled pulses. This leads to lower PM formation in the LPI points.

CFD also showed that the interactions between two pulses for large GSEPs are less than the small GSEPs in terms of spatial PM interactions in the cylinder. This CFD observation is in line with the split-flame concept in the literature of the diesel engines. However, it is not clear to what extent it contributes to overall low engine-out PM mass of the LPI strategy. The pulse-isolation experiments and CFD, as discussed, suggest that this less interaction between pulses might not be a first-order effect in justifying low PM of LPI points. The interaction between two pulses might be in various parameters e.g. entrainment or between different stages of PM formation, e.g. pyrolysis of the second pulse and agglomeration of the first pulse, however these interactions cannot be captured by the CFD model based on the Hiroyasu model.

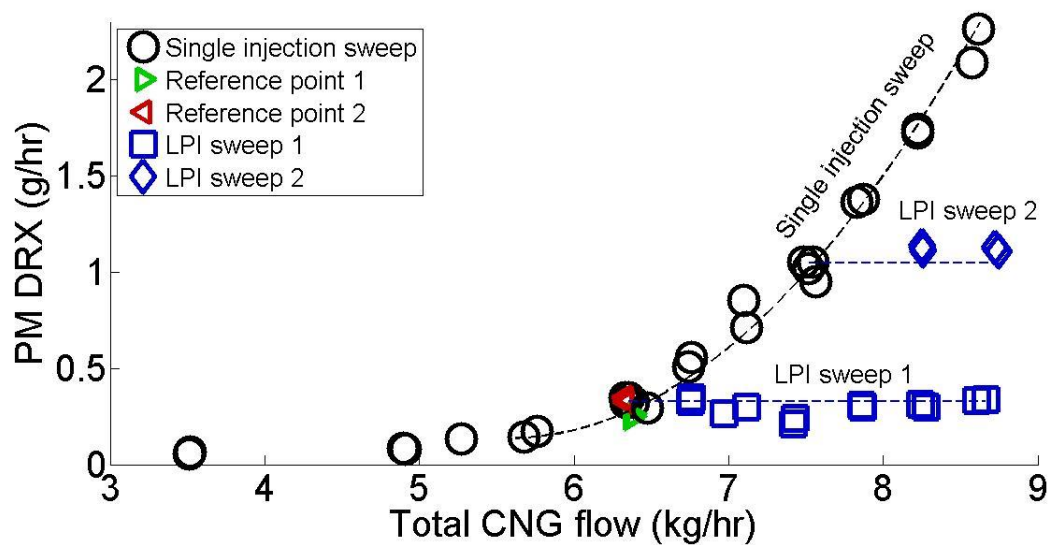


Figure 7-1 Pulse-isolation tests results; variation of engine-out PM with NG for single and post injections

The effects of LPI in the HPDI engine were compared to heavy-duty diesel experiments in the literature. One-to-one comparison was not possible due to differences in engine geometry, differences in load and speed, the PM instrumentation used, and type of the engines (optical or thermodynamic engine). However, for both diesel and HPDI engines, PM was reduced with a penalty in fuel consumption. As the second injection is retarded, PM

approaches to a maximum reduction in PM for both engine types. PM reduction, compared to baseline, of the HPDI engine was higher than the diesel engine in the equivalent second injection timing, for all the modes. The greater effectiveness of LPI in the HPDI engine might be due to significantly lower injection pressure of the HPDI engine; lower injection pressure might imply that the extra mixing from a split injection would have greater effects. The fuel consumption penalty for diesel engine experiments was comparable with HPDI experiments.

The sensitivity of LPI to injector variability was investigated at mode B75 by testing five different injectors from the same injector model. The results show that if the injectors are trimmed to match the desired 15% SI, the injectors show a 60-75% PM reduction compared to their baseline values. However, if we instead fix the commanded injection timing to match the baseline injector, each injector will have SI ranging from 8 to 15% and at the lowest SI, PM reduction is not significant. A second set of experiments was performed to compare the performance of LPI points in different injectors when the same injection timing and air handling condition has been used for all the injectors. These experiments evaluate what the impact on emissions would be if injectors with different performance are run under equivalent commanded injection and air handling values. The results suggest that LPI might be less effective in terms of PM reduction in a MCE engine due to injector-injector variability (average of 50% PM reduction compared to 75% for the best injector). The other emissions and fuel consumption penalty are consistent with the UBC default injector performance in the tests on the single cylinder research engine.

7.2 Slightly Premixed Combustion

For HPDI, slightly premixing the natural gas by delaying the pilot injection until after the natural gas injection has started is known to reduce PM at the expense of NOx and CH₄ penalties [47], [50], [87]. Adding EGR has been shown to reduce NOx without increasing PM, but further impaired CH₄. This thesis demonstrated, for the first time, that by increasing the EQR, the CH₄ penalty from SPC could be eliminated without impacting the reduction in PM or causing an increase in NOx. One of the main contributions of the current

study was providing more information about the fundamental mechanism of PM reduction using SPC strategy in HPDI engines by engine experiments and CFD simulation. All the SPC experiments were performed at mode B75.

The “optimized SPC point” (i.e. best point of the SPC cases with maximum PM reduction and same NOx and methane level as the baseline in the parameter sweeps at mode B75) removed over 90% of the PM with a 2% improvement in fuel efficiency while having almost the same level of NOx and methane. The drawback of this point is cycle to cycle variations and higher peak pressure rise rate in the cycle. A higher peak pressure rise and cycle to cycle variations of pressure lead to higher engine noise as well. These experiments were performed for a range of $18 \leq EGR \leq 25$, $0.6 \leq EQR \leq 0.7$ and $-2.1 \leq PSEP \leq 0.9$ ms. Based on the current experiments, combustion harshness (identified by a higher peak pressure rise rate and higher cycle-cycle variability of maximum pressure) is maximum at $PSEP = -0.9$ ms. It can be reduced by more or less premixing ($PSEP > -0.9$ ms or $PSEP < -0.9$ ms). However, by more premixing NOx and methane would be higher and for $PSEP > -0.9$ ms PM is not minimized. Higher EGR can also result in a lower peak pressure rise; however, cycle to cycle variations of pressure and also NOx would be higher.

By allowing more time for the NG to mix with air (negative PSEP), methane emissions increase significantly, for different EGR and EQR levels (Figure 7-2). This graph shows the results from different sweeps in a PM-methane graph. The color shows the RIT timing, as an indication of premixing. EGR increases methane emissions. Increasing EQR, on the other hand, reduces methane at the same PSEP and same level of EGR. Methane emissions for the high EGR and EQR points will be back to the baseline value for $PSEP = -0.9$ ms.

The PM/NOx trade-off is escaped for the SPC strategy. PM does not increase for SPC cases by changing in-cylinder environment e.g. higher EGR level, higher EQR or higher pilot mass, which normally increases PM in non-premixed combustion. As shown in Figure 7-2; PM is very low for all the SPC points ($RIT < 0$) on the right side of the graph, below the lower reliable detection limit of DRX. For normal HPDI points ($PSEP > -0.3$ ms), there parameters

affect engine-out PM significantly. The baseline, optimized LPI and SPC points¹⁶ are also included in the graph for comparison.

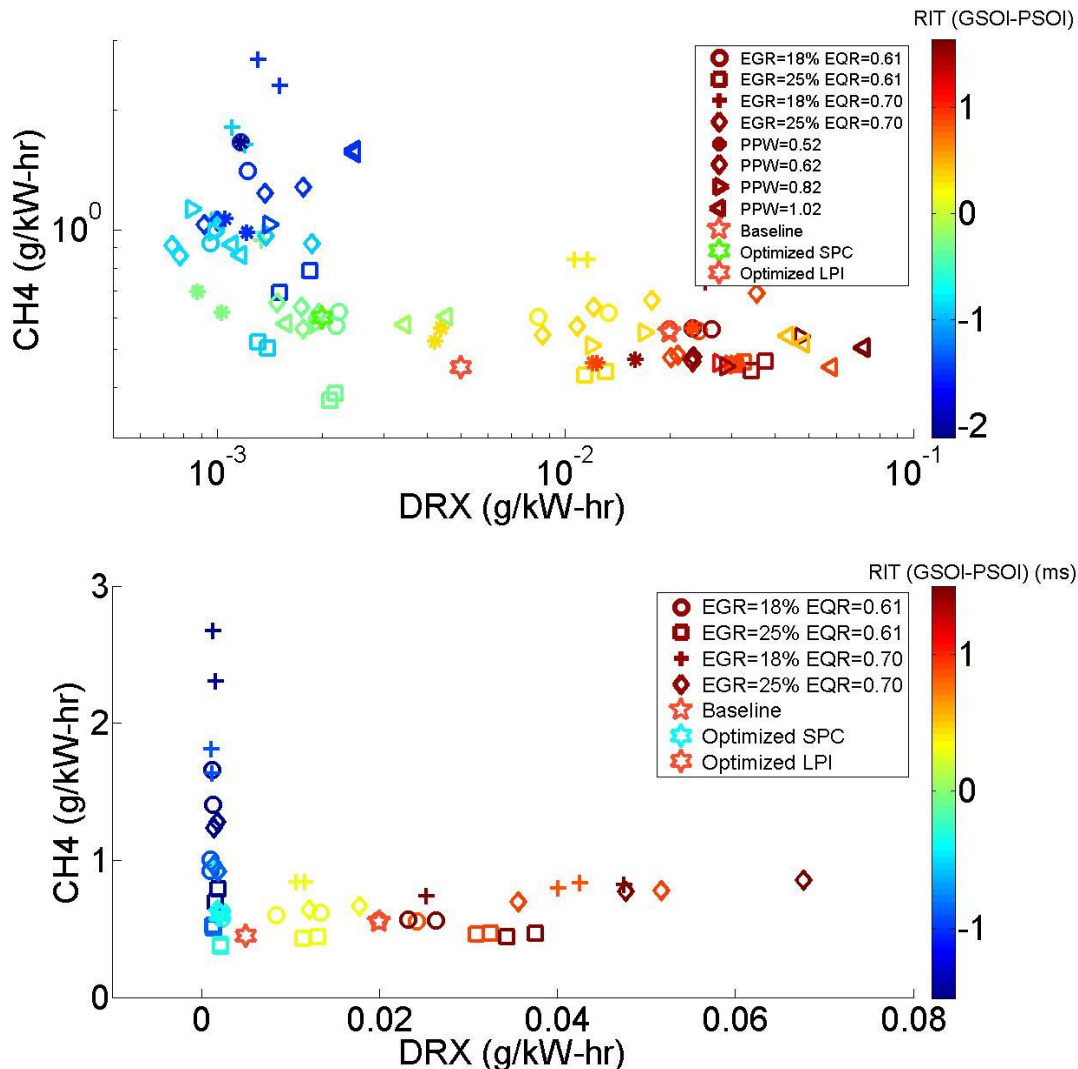


Figure 7-2 Engine-out methane-PM emissions for different engine parameters

CFD simulation was used to model SPC. Although the ignition of gas cannot be predicted correctly, CFD captured the main trends in PM emissions. For SPC cases, much less PM is formed in the cylinder and the PM will be oxidized quickly in the cylinder after EOI. Higher EGR or EQR will increase the peak PM formed in-cylinder slightly, but have almost no effect

¹⁶ i.e. best point of the LPI/SPC cases in the parameter sweeps of mode B75

on PM by the end of cycle. This trend has been noticed in the engine-out PM from the experiments as well. The EQR distribution of the jet at the ignition point for the baseline case and the SPC case were compared. At the gas ignition time, there is still significant fuel in the rich zone for the baseline point; over 50% of the fuel is within $2 < \text{EQR} < 5$ (defined as Z_{rich}). For the SPC point, the Z_{rich} is less than 10%, therefore the potential for soot formation is mainly eliminated.

The conceptual graph presented in Figure 1-5 emphasizes the importance of the relative location of ignition (or peak AHRR) and end of injection. Despite the fundamental differences between SPC and LTC in diesel engines in terms of combustion and the PM formation process, this relative timing is important for the HPDI engine as well and can be used to define the SPC thresholds in future. More experiments might be required to confirm this for a wide range of parameters e.g. different modes, gas rail pressures and CA50. Figure 1-5 also suggests that LTC results in a distinctive spatial pattern of PM formation, but whether or not this applies to SPC could not be determined in this work.

The robustness of the SPC strategy was verified by testing different injectors from the same injector model, at mode B75. The same method as LPI multi-injector tests was used to compare the performance of the SPC strategy in different injectors when the same injection timing and air handling condition was used for all the injectors. The results suggest that SPC strategy is less affected by injector-injector variability than the LPI strategy: all the emissions and engine performance were very close for all the injectors. This might be because SPC combustion is less coupled with the injection timing compared to the baseline points, expecting less mixing-controlled combustion and more premixed combustion, therefore injection history might be less effective for SPC strategy compared to LPI.

The main parameter in defining diesel-to-gas injection timing is PSEP, defined from the end of pilot command signal to the start of gas signal. Based on the tests in the current study, presented in Appendix E, for any sweep of parameters RIT (defined from the start of the command signal to the start of the gas signal) is a more effective parameter in comparing the cases since the start of combustion for diesel and gas will be kept constant.

Premixing can be defined by different metrics. It can be defined as the level of lean mixture (Z_{lean}) at the time of ignition; however, for this metric a modeling study is always required. Moving toward the negative PSEP (or RIT) will increase the premixing as shown in the CFD and TSM simulations of the current study. The current study suggests the importance of relative timing of ignition (or peak AHRR) and end of injection. Related to this finding, another metric could be fuel injected portion at the time of ignition (SPC factor=100% when ignition is at the EOI). For defining this metric, knowledge of injector behaviour is required (momentum measurement or fuel rate shape).

7.3 Transient Slice Model (TSM)

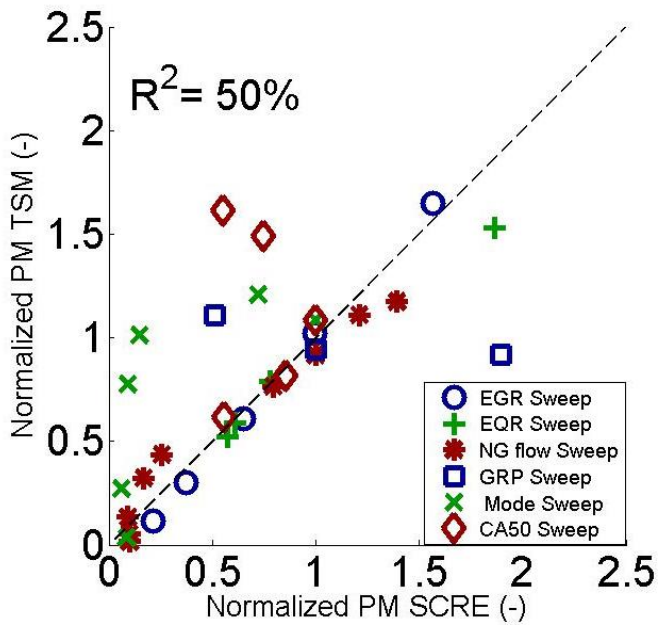
A novel quasi-1D phenomenological model (TSM) of HPDI combustion and soot formation has been developed. The goal of the model is to provide better understanding of PM formation mechanism in the HPDI engine and evaluate the model performance in PM prediction of advanced injection strategies, which were identified in the current thesis.

The model simulates a free jet based on 1D numerical solver for momentum and mixture fraction. This type of phenomenological model was developed in the literature for non-reacting jets with recent development of the model for reacting jets. TSM expands the abilities of the 1D models to engine simulation and prediction of engine-out PM. This model simulates a free jet and adjusts the nozzle and the ambient conditions of the free jet to approximate the jet inside the cylinder. The jet reactions are “turned on” according to the experimentally measured ignition time and an “effective flame speed”. A new aspect of the model is the interaction between free jet simulation, cylinder thermodynamics model and generating mixture fraction maps for each time step, as three main sub-models of the TSM.

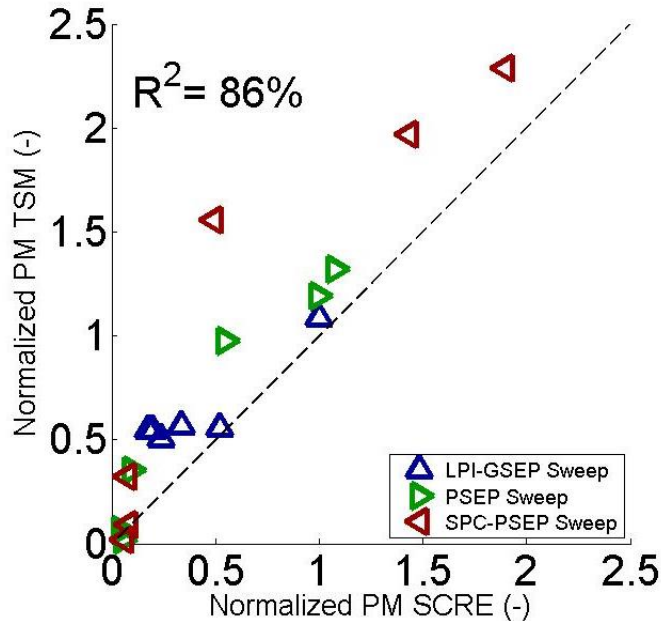
To test the model, fifty experimental points were selected from very different engine operating conditions. Figure 7-3 shows all the simulated cases using TSM compared with experimental measurements of denuded PM of DRX. TSM was tuned by adjusting 4 parameters that were then kept constant for all the points. The dashed line is the perfect match between experiments and simulation. Different symbols and colors indicate different

parameter sweeps. For some of the points, e.g. effect of load on mode sweeps, even if the PM magnitude is not close to the experiments, the trend in changing the PM is well-captured by the model. The relatively low R^2 on the graph is mainly due to later CA50 points and the effect of GRP.

TSM predictions of pressure and AHRR for most of the cases are similar to the measurements; however the AHRR change with GRP could not be captured by the model. For SPC cases a modification in the effective flame speed factor was suggested to match the experiments better. Engine-out PM trends with changing the engine parameters are well-captured in the TSM for EGR, EQR, NG flow, PSEP and the effect of load in mode sweeps. The effect of gas rail pressure (GRP) on engine-out PM cannot be captured by the model; perhaps due to simplification of turbulence effect in TSM.



(a) Normal HPDI Cases



(b) Advanced injection strategies

Figure 7-3 TSM predictions of engine-out PM compared to SCRE experiments for normal HPDI sweeps and advanced injection strategies.

For LPI points the lower engine-out PM of the LPI points was captured by the model as well. However, more details of the LPI strategy, e.g. the PM reduction trend with GSEP,

could not be predicted by the model. In SPC simulations, the trend in PM reduction for negative PSEPs even for high EGR/EQR points is well-modeled by the TSM, except for PSEP=-0.3 ms.

Compared to packet models developed previously for diesel engines, the TSM has a number of new features. The jet dynamics in TSM were validated with many experiments and focus on gas jets, naturally. The AHRR simulations for both packet models and TSM are acceptable for many cases, but the TSM has been compared with an especially broad range of engine operating conditions and gives reasonable PM predictions with very minimal tuning.

7.4 Conclusions Drawn from all Chapters

LPI and SPC both reduced PM emissions from the HPDI engine, but in different ways. Here the results will be compared to the baseline point at mode B75, a high PM-forming mode (Table 7-1). LPI achieved the significant PM reduction with a 1% penalty in fuel economy for the optimized point (selected among the mode B75 points). This injection strategy can be used for the cases where this slight increase in fuel consumption can be tolerated given its significant PM, CO and moderate decrease in engine-out methane. SPC also shows a major reduction in engine-out PM due to negative PSEP. Through the use of a higher EGR and EQR, NOx and methane emissions are maintained at their baseline levels. This injection strategy also shows improvement in fuel economy. The drawback of the injection strategy was combustion harshness (cycle-cycle variability and higher peak pressure rise rate). The combustion harshness leads to higher engine noise production as well. The numbers for LPI and SPC are the values of emissions and engine performance normalized by the baseline value.

Table 7-1 Baseline B75 values and LPI and SPC measurements normalized by corresponding baseline values

Emissions and Engine Performance	Baseline B75 ¹	LPI Baseline ²	SPC Baseline ³
PM DRX	20±1 (mg/kW-hr)	0.25	0.1
NOx	1.4±0.1 (g/kW-hr)	1.0	0.93
Methane	0.55±0.05 (g/kW-hr)	0.82	1.09
CO	5.5±0.6 (g/kW-hr)	0.3	1.05
GISFC	176.5±1 (g/kW-hr)	1.01	0.98
COV of P_{max}	0.7±0.05 (-)	1.0	5.0
dP/dθ_{max}	4.0±0.3 (bar/deg)	1.0	2.0
P_{max}	136±2.0 (bar)	1.0	1.02
Peak AHRR	145±5 (kJ/m ³ -deg)	1.0	2.1
Cylinder Exhaust Temperature	553±10 (°C)	1.0	1.0
TEM Primary Particle Mean	32±2 (nm)	0.55	0.45
SMPS Geometric Mean	90±4 (nm)	0.70	0.55
Total Particle Concentration	2.1×10 ⁶ ±2.0×10 ⁵ (#/cm ³)	0.52	0.33

¹ Baseline in this table is the average of two blocks of testing, LPI and SPC together.

² The best LPI point selected from the experimental points at mode B75, GSEP=2.0 ms, SI=15%.

³ The best SPC point selected from the experimental points at mode B75, PSEP=-0.9 ms, EGR=18%, EQR=0.7.

For baseline, LPI and SPC combustion at B75, PM morphology and size distribution were studied using TEM images and SMPS sampling. The SMPS size distributions are shown in Figure 7-4 (in all cases with the semi-volatile portion removed, corrected for dilution). Solid and open symbols show two sizes of distributions from two repeats for each baseline, LPI or SPC point. For both LPI and the SPC point, the size distribution is shifted toward the smaller aggregates and the total number concentration is reduced significantly. Primary particle diameters (from TEM) were also smaller for the optimized LPI/SPC point. Previous

work on soot morphology analysis showed that smaller aggregates tend to have smaller primary particles [128]; these results agree with those studies.

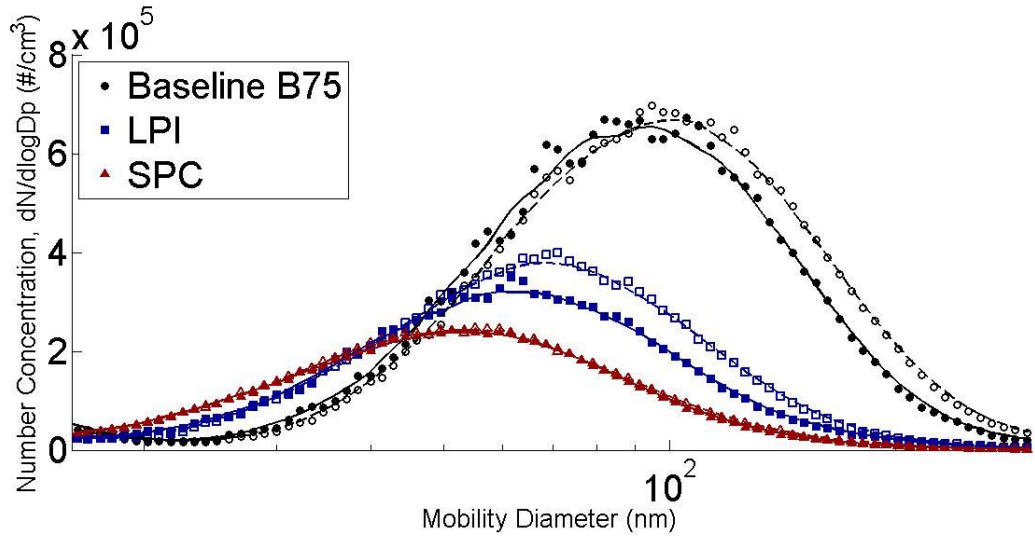


Figure 7-4 PM Size Distributions for baseline, LPI and SPC points. The open/ closed symbols are two repeats of Baseline, LPI or SPC points. The curves are the moving average of each data set.

CFD correctly predicted the trends in PM emissions for each injection strategy, but not all of the details could be captured by CFD correctly. For LPI strategy the simulated AHRR of the second pulse was too low and broad. The difference between engine-out PM and simulated PM might be explained by a lower heat release rate of the second pulse from CFD prediction and thus, a longer residence time of fuel in the core of the jet. In the SPC case, the CFD model was not able to predict the diesel ignition point correctly. The CFD package was originally designed for non-premixed combustion modeling, therefore, before applying the model to SPC, substantial modification might be needed.

The TSM model could predict the engine-out PM from many parameter sweeps (EGR, EQR, NG flow, effect of load, some of the CA50 points, PSEP, LPI and SPC sweeps). All these predictions were achieved by modeling a free jet without the wall interactions. It might show that for many of these parameters, engine-out PM is not mainly affected by the geometric effects. However, TSM cannot capture the effects of parametric changes that are likely to affect turbulence levels in the engine.

In spite of the differences in combustion and PM formation of diesel and HPDI engines, discussions above suggest that concepts developed in the diesel literature can be useful in explaining HPDI phenomena. Conversely, the HPDI studies can also be helpful in providing better understanding of the emission formation and ignition phenomena in general engine applications due to more control over the ignition timing for HPDI engines. The models specifically developed for each of diesel or HPDI engine can be adapted to the other engine application.

8 RECOMMENDATIONS FOR FUTURE WORK

The current thesis provides insights into two injection strategies and designing a phenomenological model in a direct injection natural gas combustion system. Based on this, the following sections provide recommendations related to engine test methodology, expanded engine tests, model development and finally product development.

8.1 Recommendations for Engine Testing and CFD Methodology

The main parameter in defining diesel-to-gas injection timing is PSEP, defined from the end of the pilot command signal to the start of the gas signal. When varying pilot quantity, it is important to recall that the pilot and gas start-of-injection (PSOI and GSOI) timings are effectively being changed as well. As a result, ignition timing effects are introduced as well as changes in pilot quantity, which can confound the results. Future testing should work to ensure that both effects (pilot quantity and pilot start of injection timing) are evaluated. It might also slightly improve variability of the engine experiments. Currently for setting the points, PSEP and diesel mass will be kept constant. If an adjustment in PPW is required to set the diesel mass, start of gas command would be variable. Applying RIT can eliminate this source of variability in the results.

Optical engine experiments could be very helpful in increasing the understanding of emission reduction in engines. The metal engine experiments do not provide any details about the in-cylinder phenomena or time resolved variation of emissions, which are essential for understanding any new injection strategies. CFD on the other hand, can provide in-cylinder details; however, it should be fully validated first. The CFD results do not match experiments exactly in many cases which makes the interpretation of the results complicated. Moreover, some technical aspects, e.g. the injector performance, cannot be easily implemented in the CFD package unless an equivalent experiment is available. Some of the fundamental questions related to the mechanism of PM reduction for LPI and SPC could be answered by engine experiments and/or CFD simulation. Optical engine experiments can provide another tool for the understanding of in-cylinder phenomena.

The CFD provided in-cylinder information that could not be obtained without an optically accessible engine. Therefore, for a new concept tested in SCRE, it is useful to run CFD cases. The ignition point of SPC cases could not be correctly predicted by the GOLD CFD package, therefore, the spatial distribution of PM and sources of high methane and NOx emissions for SPC points could not be studied in detail. A future study should examine the SPC strategy again with GOLD package specially modified for partially premixed combustion. In general, the limitations and strengths of the CFD model should be carefully documented for each case for future reference as this should eventually provide a map showing where CFD can be useful.

8.2 Recommendations for Areas for Future Engine Testing

LPI showed higher fuel consumption penalty for mode B87 compared to mode B75. Further studies are required to study the effect of LPI in full load conditions. Since at high loads the second pulses are larger and later in the cycle (GPW1 is larger with constant GSEP), the fuel consumption penalty of higher loads might be higher.

This thesis shows that the knowledge of injection timing parameters (delay, ramp-up, ramp-down) can be very critical in designing an injection strategy or in interpretation of the results. The variability of the injections is also as important as the average fuel rate shape. This information should be known before any engine experiments on a new injector or testing under unconventional injector conditions. Injector testing (rate tube or momentum measurement) should be included in future experiments. By regularly testing the injector, part of the variability due to injector performance changes can be tracked as well.

The pulse isolation tests were performed for one EGR and EQR, and further development of the results could be beneficial in improving the understanding of PM formation in HPDI engines. A single injection sweep at different EQR and EQR (or $[O_2]_{intake}$) by increasing NG flow (or GPW) can help us to estimate the net PM formation of each pulse at different conditions e.g. at which NG flow level the PM formation starts to be significant for lower

$[O_2]_{intake}$ levels? Another aspect of this development might be more LPI experiments with a higher mass flow rate or different GSEPs e.g. at which level of SI the PM of second pulse starts to be significant? Is this the same level as single injection sweep at this $[O_2]_{intake}$ level? If the pulse-isolation were performed for the close-coupled pulses how would the graph be different?

Measurement of particle size distributions for the of pulse isolation tests could be beneficial in understanding the mechanism of PM reduction in LPI. If the size distribution of LPI is close to its single injection pulse (here 85% of fuel in B75), then it would provide an extra evidence for minimal contribution of second pulse in PM generation. Moreover, the size distribution of close-coupled pulses can provide more information as well (unimodal or bimodal, symmetrical or unsymmetrical).

Premixing can be defined by different metrics. It can be defined as the level of Z_{lean} at the ignition timing; however for this metric a modeling study is always required (CFD or TSM). The current study suggests the importance of relative timing of ignition (or peak AHRR) and end of injection. Related to this finding, another metric could be fuel injected portion at the time of ignition (SPC factor=100% when ignition is at the EOI). For defining this metric, the knowledge of injector behaviour is required (momentum measurement or fuel rate shape).

The performance of SPC on the other modes was not considered in the current study. The main characteristics of SPC are major PM reduction, slightly better fuel economy, and higher combustion harshness. SPC is also more effective in high-PM forming modes, since one major benefit of SPC is PM reduction. A multi-mode test of SPC is required to define the performance of the injection strategy and also examine the importance of relative timing between peak AHRR (or ignition) and EOI. Depending on the results, a transition between conventional HPDI to SPC can be commanded to the injector for certain modes.

On a turbo-charged production engine, EGR and EQR are not independent parameters. Future work needs to evaluate the limitations imposed by a turbo-charged production engine air handling system on a multi-cylinder engine, and look at ways of optimizing the injection strategy to accommodate the achievable EGR and EQR levels.

Higher cycle-cycle variation of pressure and higher maximum pressure gradient of SPC points can lead to higher noise in the engine operation as well. All these effects are addressed as higher “combustion harshness” for SPC points. The performance of SPC on different injection timing (e.g. changing CA50) or different injection pressures has not been considered in the current study. A future study should consider the effect of CA50 and injection pressure on performance of SPC strategy and possibly to reduce combustion harshness of the SPC points.

8.3 Recommendations for Phenomenological Model Development

A goal of this study was to develop a phenomenological model with minimum tuning factors, in order to make the model as general as possible. This goal was substantially reached with the Transient Slice Model, but the performance of TSM can be improved by developing a systematic parameter tuning process so that all tuned parameters end up within the uncertainty range of the literature, and also make use of the full dataset. This might be by genetic algorithms or simulated annealing, to minimize the difference between measurements and predictions.

TSM prediction can be improved by better modeling of ignition and flame propagation. The ignition model can be a physical model, similar to Appendix C, so that TSM can be used to predict emissions and AHRR for cases that have not been run on the engine. The flame propagation is modeled as the switching between reacting and non-reacting maps according to a single effective flame speed; a model that includes more physical effects could be used. The new model could include the effect of laminar flame speed in propagation of the ignition; therefore the reaction zone would propagate faster in close to stoichiometric conditions and slower in rich and lean mixture.

TSM ignores variations in local mixture fraction and turbulence. The effect of local mixture fraction variation could also be considered in the model to improve the performance of the

model. Finally, including a wall impingement model (similar to that in Appendix A) might help improve predictions for varying gas rail pressure, engine speed and injection timing.

The TSM could be run for each experimental point for any ongoing or future studies. The model is relatively simple compared to CFD with a modular structure that can be modified easily. The model could be used to predict the fluid mechanics of the jet including entrainment and penetration, PM-CAD and engine-out PM prediction, mixture fraction development and analysis, premixing definition by lean mixture (Z_{lean}) and potential for soot formation by z_{rich} integral from the ignition point

8.4 Recommendations for Product Development

To apply the LPI strategy to a production engine the following steps need to be carefully considered. First, LPI shows a significant PM reduction with a fuel consumption penalty. While the injection strategy is beneficial for high-PM forming modes, for low-PM forming modes LPI offers no significant benefit with an extra penalty in fuel economy. This issue can be addressed by applying the injection strategy to high-PM forming modes. The injector can be commanded to apply the second injection when it is required, typically at high NG flow (or GPW) with EGR for medium or high engine speed. The pulse isolation tests can be used to define the boundaries based on NG flow for this transition.

To implement LPI, it must be recognized that an inconsistent injector, in terms of mass flow rate for a command signal, can degrade the performance of the injection strategy significantly. As a result, to get the best advantages from LPI, the stability and part-to-part repeatability of the mass flow for the secondary injection will need to be carefully controlled during injector development and validation.

Close-coupled pulses were not effective in the current study; however, if future injectors can provide repeatable quality of injection for close-coupled pulses, these points might be interesting due to their smaller fuel consumption penalties. Momentum measurement

results showed short GSEPs have a lower momentum rate during injection and a higher variability. Faster opening/closing and more repeatable injector series enhances the performance of the close-coupled and maybe LPI points too. This should be investigated in more detail including considering new designs for injectors to better perform in this injection strategy.

In this thesis, injection strategies have been defined and evaluated that demonstrate substantial PM reductions while minimizing impacts on other engine emissions and fuel consumption. Both CFD and a novel phenomenological model have been used to evaluate the fundamental causes for the reduced PM emissions. In both LPI and SPC, better mixing of the directly injected natural gas has reduced PM emissions, while careful operating condition selection has mitigated other undesirable side-effects. The results from this work can be used for future engine development as well as providing valuable guidance for further research tool development. The TSM model, developed in this work, can be expanded to provide both enhanced interpretation of experimental results and a fast, low-cost method for evaluating HPDI combustion concepts.

BIBLIOGRAPHY

- [1] E. Faghani, B. Patychuk, G. McTaggart-Cowan, and S. Rogak, "Soot Emission Reduction from Post Injection Strategies in a High Pressure Direct-Injection Natural Gas Engine," *SAE Tech. Pap. 2013-24-0114*, Sep. 2013.
- [2] E. Faghani, P. Kirchen, and S. N. Rogak, "A Fuel Momentum Measurement Device for Natural Gas Engine Injections," *SAE Tech. Pap. 2015-01-0915*, 2015.
- [3] "United States Environmental Protection Agency, Heavy Duty Emission Regulations." [Online]. Available: <http://www.epa.gov/OMS/climate/regulations-heavy-duty.htm>. [Accessed: 01-Aug-2015].
- [4] G. P. McTaggart-Cowan, "Pollutant Formation in a Gaseous-Fuelled, Direct Injection Engine," Doctoral Thesis, The University of British Columbia, 2006.
- [5] I. A. Khalek, T. L. Bouger, P. M. Merritt, and B. Zielinska, "Regulated and Unregulated Emissions from Highway Heavy-Duty Diesel Engines Complying with U.S. Environmental Protection Agency 2007 Emissions Standards," *J. Air Waste Manage. Assoc.*, vol. 61, no. 4, pp. 427-442, Apr. 2011.
- [6] C. Seigneur, "Current Understanding of Ultrafine Particulate Matter Emitted from Mobile Sources," *J. Air Waste Manage. Assoc.*, vol. 59, no. 1, pp. 3-17, Jan. 2009.
- [7] J. B. Heywood, *Internal Combustion Engine Fundamentals*. New York: McGraw-Hill, 1988.
- [8] B. D. Patychuk, "Particulate Matter Emission Characterization From a Natural Gas High-Pressure Direct-Injection Engine," MASc Thesis, The University Of British Columbia, 2013.
- [9] Y. J. Kaufman, D. Tanré, and O. Boucher, "A satellite view of aerosols in the climate system," *Nature*, vol. 419, no. 6903, pp. 215-23, Sep. 2002.
- [10] J. H. Seinfeld and S. N. Pandis, *Atmospheric Chemistry and Physics: From Air Pollution to Climate Change*. John Wiley & Sons, 2012.
- [11] T. C. Bond, S. J. Doherty, D. W. Fahey, P. M. Forster, T. Berntsen, B. J. DeAngelo, M. G. Flanner, S. Ghan, B. Kärcher, D. Koch, S. Kinne, Y. Kondo, P. K. Quinn, M. C. Sarofim, M. G. Schultz, M. Schulz, C. Venkataraman, H. Zhang, S. Zhang, N. Bellouin, S. K. Guttikunda, P. K. Hopke, M. Z. Jacobson, J. W. Kaiser, Z. Klimont, U. Lohmann, J. P. Schwarz, D. Shindell, T. Storelvmo, S. G. Warren, and C. S. Zender, "Bounding the role of black carbon in the climate system: A scientific assessment," *J. Geophys. Res. Atmos.*, vol. 118, no. 11, pp. 5380-5552, Jun. 2013.
- [12] M. Z. Jacobson, "Short-term effects of controlling fossil-fuel soot, biofuel soot and gases, and methane on climate, Arctic ice, and air pollution health," *J. Geophys. Res.*, vol. 115, no. D14, p. D14209, Jul. 2010.
- [13] J. Hansen and L. Nazarenko, "Soot climate forcing via snow and ice albedos," *Proc. Natl. Acad. Sci. U. S. A.*, vol. 101, no. 2, pp. 423-428, 2004.
- [14] WHO, "7 million premature deaths annually linked to air pollution." [Online]. Available: <http://www.who.int/mediacentre/news/releases/2014/air-pollution/en/>. [Accessed: 15-May-2015].
- [15] M. Brauer, G. Hoek, H. A. Smit, J. C. de Jongste, J. Gerritsen, D. S. Postma, M. Kerkhof, and B. Brunekreef, "Air pollution and development of asthma, allergy and infections in a birth cohort," *Eur. Respir. J.*, vol. 29, no. 5, pp. 879-888, May 2007.
- [16] B. Brunekreef and S. T. Holgate, "Air pollution and health," *Lancet*, vol. 360, no. 9341, pp.

1233–42, Oct. 2002.

- [17] M. Franchini and P. M. Mannucci, "Air pollution and cardiovascular disease," *Thromb. Res.*, vol. 129, no. 3, pp. 230–4, Mar. 2012.
- [18] "Heavy Duty Emission Standards." [Online]. Available: <https://www.dieselnet.com/standards/us/hd.php>. [Accessed: 01-Aug-2015].
- [19] "Environment Canada, Heavy-duty Vehicle and Emission Regulations." [Online]. Available: <http://canadagazette.gc.ca/rp-pr/p2/2013/2013-03-13/html/sor-dors24-eng.html>. [Accessed: 01-Aug-2015].
- [20] "Council of the European Communities, Directives and Regulations - Motor Vehicles." [Online]. Available: http://ec.europa.eu/enterprise/sectors/automotive/documents/directives/motor-vehicles/index_en.htm. [Accessed: 20-May-2008].
- [21] "Diesel net engine regulations." [Online]. Available: <https://www.dieselnet.com/standards/eu/hd.php>. [Accessed: 01-Aug-2015].
- [22] J. Harrington, S. Munshi, C. Nedelcu, P. Ouellette, J. Thompson, and S. Whitfield, "Direct Injection of Natural Gas in a Heavy-Duty Diesel Engine Reprinted From : Diesel Engine Experiments," in *International Spring Fuels & Lubricants Meeting & Exhibition Reno, Nevada May 6-9, 2002*, 2002.
- [23] H. L. Jones, S. N. Rogak, and W. K. Bushe, "Source Apportionment of Particulate Matter from a Diesel Pilot-Ignited Natural Gas Fuelled Heavy Duty DI Engine," *SAE Tech. Pap. 2005-01-21*, 2005.
- [24] "Diesel Particulate Filter (DPF)." [Online]. Available: <https://www.dieselnet.com/tech/dpf.php>. [Accessed: 01-Aug-2015].
- [25] W. Majewski, "Diesel Particulate Filters," *Diesel Part. Filters. DieselNet Technol. Guid. www. DieselNet. com. Copyright© Ecopoint Inc. Revis. 1*, 2001.
- [26] W. Majewski and M. Khair, *Diesel emissions and their control*. Society of Automotive Engineers, 2006.
- [27] M. Khair, "A review of diesel particulate filter technologies," *SAE Tech. Pap. 2003-01-2303*, 2003.
- [28] C. Görsmann, "Catalytic Coatings for Active and Passive Diesel Particulate Filter Regeneration," *Monatshefte für Chemie - Chem. Mon.*, vol. 136, no. 1, pp. 91–105, Jan. 2005.
- [29] S. Lorentzou, C. Pagkoura, A. G. Konstandopoulos, and J. Boettcher, "Advanced Catalyst Coatings for Diesel Particulate Filters," *SAE Tech. Pap. 2008-010-0483*, 2008.
- [30] A. G. Konstandopoulos, M. Kostoglou, E. Skaperdas, E. Papaioannou, D. Zarvalis, and E. Kladopoulou, "Fundamental Studies of Diesel Particulate Filters: Transient Loading, Regeneration and Aging," *SAE Tech. Pap. 2000-01-1016*, 2000.
- [31] A. Russell and W. S. Epling, "Diesel Oxidation Catalysts," *Catal. Rev.*, vol. 53, no. 4, pp. 337–423, Oct. 2011.
- [32] H. J. Stein, "Diesel oxidation catalysts for commercial vehicle engines: strategies on their application for controlling particulate emissions," *Appl. Catal. B Environ.*, vol. 10, no. 1–3, pp. 69–82, Sep. 1996.
- [33] D. R. Tree and K. I. Svensson, "Soot processes in compression ignition engines," *Prog. Energy Combust. Sci.*, vol. 33, no. 3, pp. 272–309, Jun. 2007.

- [34] O. I. Smith, "Fundamentals of soot formation in flames with application to diesel engine particulate emissions," *Prog. Energy Combust. Sci.*, vol. 7, no. 4, pp. 275–291, Jan. 1981.
- [35] B. S. Haynes and H. G. Wagner, "Soot formation," *Prog. Energy Combust. Sci.*, vol. 7, no. 4, pp. 229–273, Jan. 1981.
- [36] I. Glassman, *Combustion*. Academic Press, 1997.
- [37] I. Glassman, "Soot formation in combustion processes," *Symp. Combust.*, vol. 22, no. 1, pp. 295–311, Jan. 1989.
- [38] H. Palmer, C. Cullis, and P. W. Jr, "Chemistry and Physics of Carbon," Vol. 1 *Marcel Dekker*, New York, 1965.
- [39] T. Kamimoto and M. Bae, "High Combustion Temperature for the Reduction of Particulate in Diesel," in *SAE Technical Paper 880423*, 1988.
- [40] S. Kook, C. Bae, P. C. Miles, D. Choi, and L. M. Pickett, "The Influence of Charge Dilution and Injection Timing on Low-Temperature Diesel," *SAE Tech. Pap. 2005-01-3837*, 2005.
- [41] G. Blanquart, P. Pepiot-Desjardins, and H. Pitsch, "Chemical mechanism for high temperature combustion of engine relevant fuels with emphasis on soot precursors," *Combust. Flame*, vol. 156, no. 3, pp. 588–607, Mar. 2009.
- [42] J. E. Dec, "A Conceptual Model of DI Diesel Combustion Based on Laser-Sheet Imaging," *SAE Tech. Pap. 970873*, 1997.
- [43] M. P. B. Musculus, P. C. Miles, and L. M. Pickett, "Conceptual models for partially premixed low-temperature diesel combustion," *Prog. Energy Combust. Sci.*, vol. 39, no. 2–3, pp. 246–283, Apr. 2013.
- [44] G. Li, P. Ouellette, S. Dumitrescu, and P. G. Hill, "Optimization Study of Pilot-Ignited Natural Gas Direct-Injection in Diesel Engines," *SAE Tech. Pap. 1999-01-3556*, Oct. 1999.
- [45] C. W. J. Mabson, "Emissions Characterization of Paired Gaseous Jets in a Pilot-Ignited Natural -Gas Engine," MSc Thesis, The University Of British Columbia, 2015.
- [46] G. P. McTaggart-Cowan, H. L. Jones, S. N. Rogak, W. K. Bushe, P. G. Hill, and S. R. Munshi, "The Effects of High-Pressure Injection on a Compression-Ignition, Direct Injection of Natural Gas Engine," *J. Eng. Gas Turbines Power*, vol. 129, no. 2, p. 579, 2007.
- [47] G. P. McTaggart-Cowan, W. K. Bushe, S. N. Rogak, P. G. Hill, and S. R. Munshi, "PM and NO_x reduction by injection parameter alterations in a direct injected, pilot ignited, heavy duty natural gas engine with EGR at various operating conditions," *SAE Tech. Pap. 2005-01-1733*, 2005.
- [48] G. McTaggart-Cowan, K. Mann, J. Huang, A. Singh, B. Patychuk, Z. X. Zheng, and S. Munshi, "Direct Injection of Natural Gas at up to 600 Bar in a Pilot-Ignited Heavy-Duty Engine," *SAE Tech. Pap. 2015-01-0865*, 2015.
- [49] G. McTaggart-Cowan, W. K. Bushe, P. G. Hill, and S. R. Munshi, "NO_x reduction from a heavy-duty diesel engine with direct injection of natural gas and cooled exhaust gas recirculation," *Int. J. Engine Res.*, vol. 5, no. 2, pp. 175–191, Jan. 2004.
- [50] G. McTaggart-Cowan, W. Bushe, and S. Rogak, "Injection parameter effects on a direct injected, pilot ignited, heavy duty natural gas engine with EGR," *SAE Tech. Pap. 2003-01-3089*, 2003.
- [51] B. Patychuk and S. Rogak, "Particulate Matter Emission Characterization from a Natural Gas Fuelled High Pressure Direct Injection Engine," in *Proceedings of the ASME 2012 Internal*

Combustion Engine Division Fall Technical Conference, ICEF2012, 2012.

- [52] E. Huestis, P. A. Erickson, and M. M. P. B., "In-Cylinder and Exhaust Soot in Low-Temperature Combustion Using a Wide-Range of EGR in a Heavy-Duty Diesel Engine," *SAE Tech. Pap. 2007-01-4017*, 2007.
- [53] K. Akihama, Y. Takatori, K. Inagaki, S. Sasaki, and A. M. Dean, "Mechanism of the Smokeless Rich Diesel Combustion by Reducing Temperature," *SAE Tech. Pap. 2001-01-0655*, Mar. 2001.
- [54] R. Wagner, J. Green, and T. Dam, "Simultaneous low engine-out NO_x and particulate matter with highly diluted diesel combustion," *SAE Tech. Pap. 2003-01-0262*, 2003.
- [55] B. S. Brown, "High-pressure direct-injection of natural gas with entrained diesel into a compression-ignition engine," MSc Thesis, The University of British Columbia, 2008.
- [56] B. S. Brown, S. N. Rogak, and S. Munshi, "Multiple Injection Strategy in a Direct-Injection Natural Gas Engine with Entrained Diesel," *SAE Tech. Pap. 2009-01-1954*, Jun. 2009.
- [57] J. O'Connor and M. Musculus, "Post Injections for Soot Reduction in Diesel Engines: A Review of Current Understanding," *SAE Tech. Pap. 2013-01-0917*, 2013.
- [58] C. Barro, F. Tschanz, P. Obrecht, and K. Boulouchos, "Influence of Post-Injection Parameters on Soot Formation and Oxidation in a Common-Rail-Diesel Engine Using Multi-Color-Pyrometry," in *ASME 2012 Internal Combustion Engine Division Fall Technical Conference*, 2012.
- [59] M. Bobba, M. Musculus, and W. Neel, "Effect of Post Injections on In-Cylinder and Exhaust Soot for Low-Temperature Combustion in a Heavy-Duty Diesel Engine," *SAE Tech. Pap. 2010-01-0612*, 2010.
- [60] J. M. Desantes, J. Arrègle, J. J. López, and A. García, "A Comprehensive Study of Diesel Combustion and Emissions with Post-injection," *SAE Tech. Pap. 2007-01-0915*, 2007.
- [61] Z. Han, A. Uludogan, G. J. Hampson, and R. D. Reitz, "Mechanism of Soot and NO_x Emission Reduction Using Multiple-injection in a Diesel Engine," *SAE Tech. Pap. 960633*, 1996.
- [62] S. Molina, J. M. Desantes, A. Garcia, and J. M. Pastor, "A Numerical Investigation on Combustion Characteristics with the use of Post Injection in DI Diesel Engines," *SAE Tech. Pap. 2010-01-1260*, 2010.
- [63] J. O'Connor and M. Musculus, "In-Cylinder Mechanisms of Soot Reduction by Close-Coupled Post-Injections as Revealed by Imaging of Soot Luminosity and Planar Laser-Induced Soot Incandescence in a Heavy-Duty Diesel Engine," *SAE Tech. Pap. 2014-01-1255*, Apr. 2014.
- [64] A. Vanegas, H. Won, C. Felsch, M. Gauding, and N. Peters, "Experimental Investigation of the Effect of Multiple Injections on Pollutant Formation in a Common-Rail DI Diesel Engine," *SAE Tech. Pap. 2008-01-1191*, Apr. 2008.
- [65] S. Mendez and B. Thirouard, "Using Multiple Injection Strategies in Diesel Combustion: Potential to Improve Emissions, Noise and Fuel Economy Trade-Off in Low CR Engines," *SAE Int. J. Fuels Lubr. 2008-01-1329*, vol. 1, pp. 662–674, Apr. 2008.
- [66] Y. Zhang and K. Nishida, "Vapor/Liquid Behaviors in Split-Injection D.I. Diesel Sprays in a 2-D Model Combustion Chamber," *SAE Tech. Pap. 2003-01-1837*, May 2003.
- [67] Y. Hotta, M. Inayoshi, K. Nakakita, K. Fujiwara, and I. Sakata, "Achieving Lower Exhaust Emissions and Better Performance in an HSDI Diesel Engine with Multiple Injection," *SAE Tech. Pap. 2005-01-0928*, Apr. 2005.
- [68] S. K. Chen, "Simultaneous Reduction of NO_x and Particulate Emissions by Using Multiple

- Injections in a Small Diesel Engine," *SAE Tech. Pap. 2000-01-3084*, Aug. 2000.
- [69] H. Yun and R. D. Reitz, "An Experimental Investigation on the Effect of Post-Injection Strategies on Combustion and Emissions in the Low-Temperature Diesel Combustion Regime," *J. Eng. Gas Turbines Power*, vol. 129, no. 1, p. 279, Jan. 2007.
 - [70] H. Yun, Y. Sun, and R. D. Reitz, "An Experimental and Numerical Investigation on the Effect of Post Injection Strategies on Combustion and Emissions in the Low-Temperature Diesel Combustion Regime," in *ASME 2005 Internal Combustion Engine Division Spring Technical Conference*, 2005, pp. 25–35.
 - [71] M. Badami, F. Mallamo, F. Millo, and E. E. Rossi, "Experimental investigation on the effect of multiple injection strategies on emissions, noise and brake specific fuel consumption of an automotive direct injection common-rail diesel engine," *Int. J. Engine Res.*, vol. 4, no. 4, pp. 299–314, Jan. 2003.
 - [72] A. Helmantel, J. Somhorst, and I. Denbratt, "Visualization of the Effects of Post Injection and Swirl on the Combustion Process of a Passenger Car Common Rail DI Diesel Engine," in *Design, Application, Performance and Emissions of Modern Internal Combustion Engine Systems and Components*, 2003, pp. 631–640.
 - [73] F. Payri, J. Benajes, J. V. Pastor, and S. Molina, "Influence of the Post-Injection Pattern on Performance, Soot and NOx Emissions in a HD Diesel Engine," *SAE Tech. Pap. 2002-01-0502*, Mar. 2002.
 - [74] S. Munshi, G. McTaggart-Cowan, H. J., and P. Hill, "Development of a Partially-Premixed Combustion Strategy for a Low-Emission, Direct Inject High Efficiency Natural Gas Engine," in *Proceedings of the ASME ICE Division Fall Technical Conference, ICEF2011-60181*, 2011.
 - [75] F. Zhao, "Homogeneous charge compression ignition (HCCI) engines: key research and development issues," *Soc. Automot. Eng.*, 2003.
 - [76] S. Kimura, O. Aoki, H. Ogawa, S. Muranaka, and Y. Enomoto, "New combustion concept for ultra-clean and high-efficiency small DI diesel engines," *SAE Tech. Pap. 1999-01-3681*, 1999.
 - [77] T. Kanda, T. Hakozaki, T. Uchimoto, J. Hatano, N. Kitayama, and H. Sono, "PCCI operation with early injection of conventional diesel fuel," *SAE Tech. Pap. 2005-01-0378*, 2005.
 - [78] K. Okude, K. Mori, S. Shiino, and T. Moriya, "Premixed compression ignition (PCI) combustion for simultaneous reduction of NOx and soot in diesel engine," *SAE Tech. Pap. 2004-01-1907*, 2004.
 - [79] H. Kellerer, R. Koch, and S. Wittig, "Measurements of the growth and coagulation of soot particles in a high-pressure shock tube," *Combust. Flame*, vol. 120, no. 1, pp. 188–199, 2000.
 - [80] R. Dobbins, "Soot inception temperature and the carbonization rate of precursor particles," *Combust. Flame*, vol. 130, no. 3, pp. 204–214, 2002.
 - [81] C. Park and J. Appleton, "Shock-tube measurements of soot oxidation rates," *Combust. Flame*, vol. 20, no. 3, pp. 369–379, 1973.
 - [82] M. K. Bobba, C. L. Genzale, and M. P. B. Musculus, "Effect of Ignition Delay on In-Cylinder Soot Characteristics of a Heavy Duty Diesel Engine Operating at Low Temperature Conditions," in *SAE Technical Paper 2009-01-0946*, 2009.
 - [83] T. Lachaux and M. P. B. Musculus, "In-cylinder unburned hydrocarbon visualization during low-temperature compression-ignition engine combustion using formaldehyde PLIF," *Proc. Combust. Inst.*, vol. 31, no. 2, pp. 2921–2929, Jan. 2007.
 - [84] M. P. B. Musculus, "Multiple Simultaneous Optical Diagnostic Imaging of Early-Injection Low-

Temperature Combustion in a Heavy-Duty Diesel Engine," in *SAE Technical Paper 2006-01-0079*, 2006.

- [85] M. P. B. Musculus, T. Lachaux, L. M. Pickett, and C. A. Idicheria, "End-of-Injection Over-Mixing and Unburned Hydrocarbon Emissions in Low-Temperature-Combustion Diesel Engines," *SAE Tech. Pap. 2007-01-0907*, 2007.
- [86] J. O'Connor and M. Musculus, "Optical Investigation of the Reduction of Unburned Hydrocarbons Using Close-Coupled Post Injections at LTC Conditions in a Heavy-Duty Diesel Engine," *Sae Tech. Pap. 2013-01-0910*, Apr. 2013.
- [87] G. P. McTaggart-Cowan, K. Mann, N. Wu, J. Huang, and S. R. Munshi, "Particulate Matter Reduction from a Pilot-Ignited, Direct Injection of Natural Gas Engine," in *Proceedings of the ASME Internal Combustion Engine Division's 2012 Fall Technical Conference (ICEF2012)*, 2012.
- [88] E. Wirojsakunchai, T. Aroonsrisopon, K. Wannatong, and N. Akarapanjavit, "A Simulation Study of an Aftertreatment System Level Model for Diesel Dual Fuel (DDF) Engine Emission Control," *SAE Tech. Pap. 2009-01-1966*.
- [89] P. Gélin and M. Primet, "Complete oxidation of methane at low temperature over noble metal based catalysts: a review," *Appl. Catal. B Environ.*, vol. 39, no. 1, pp. 1–37, Nov. 2002.
- [90] A. Noipheng, N. Waitayapat, T. Aroonsrisopon, E. Wirojsakunchai, T. Thummadetsak, and K. Wannatong, "Experimental Investigation of Applying Raw Fuel Injection Technique for Reducing Methane in Aftertreatment of Diesel Dual Fuel Engines Operating under Medium Load Conditions," *SAE Tech. Pap. 2011-01-2093*, 2011.
- [91] M. Gerstle and G. Merker, "Transient simulation of marine diesel engine systems by improved characteristic cylinder map interpolation," *Trans. Mar. Eng. C- 111*, vol. 111, pp. 129–138, 1999.
- [92] G. Heider, K. Zeilinger, and G. Woschni, "Two Zone Calculation Model for the Prediction of NO Emissions From Diesel Engines," *Proc. 21st Cimac Conf.*, 1995.
- [93] I. Stiesch, "Thermodynamic Models," *Model. Engine Spray Combust. Process.*, vol. Springer B, pp. 5–39, 2003.
- [94] G. Merker and C. Schwarz, *Technische Verbrennung: Simulation verbrennungsmotorischer Prozesse*. Stuttgart: Teubner, 2001.
- [95] K. Schreiner, "Equivalent Combustion Rate with the Polygon-Hyperbola Function: Investigations into the Dependence of the Parameters in the Performance Map," in *Proc 5th Symposium, "The Working Process of the Internal Combustion Engine," Technical University Graz, Austria*, 1995.
- [96] J. Ferziger and M. Peric, *Computational methods for fluid dynamics*. Springer Science & Business Media, 2012.
- [97] J. Abraham, "What is adequate resolution in the numerical computations of transient jets?," *SAE Tech. Pap. 970051*, 1997.
- [98] C. Baumgarten, J. Stegemann, and G. Merker, "A new model for cavitation induced primary break-up of diesel sprays," *Zaragoza*, vol. 9, no. 11, 2002.
- [99] H. Pitsch, M. Chen, and N. Peters, "Unsteady flamelet modeling of turbulent hydrogen-air diffusion flames," *Symp. Combust. Elsevier*, vol. 27, no. 1, pp. 1057–1064, 1998.
- [100] G. Abramovich, *The Theory of Turbulent Jets*. MIT Press, Cambridge, 1963.
- [101] S. M. Shahed, W. S. Chiu, and V. S. Yumlu, "A Preliminary Model for the Formation of Nitric

Oxide in Direct Injection Diesel Engines and Its Application in Parametric Studies," *SAE Tech. Pap.* 730083, Feb. 1973.

- [102] W. S. Chiu, S. M. Shahed, and W. T. Lyn, "A Transient Spray Mixing Model for Diesel Combustion," *SAE Tech. Pap.* 760128, 1976.
- [103] H. Hiroyasu and K. Toshikazu, "Development and Use of a Spray Combustion Modeling to Predict Diesel Engine Efficiency and Pollutant Emissions," *Bull. JSME*, vol. 26, no. 214, 1983.
- [104] Z. Bazari, "A DI Diesel Combustion and Emission Predictive Capability for Use in Cycle Simulation," *SAE Tech. Pap.* 920462, 1992.
- [105] Z. Gao and W. Schreiber, "A phenomenologically based computer model to predict soot and NO_x emission in a direct injection diesel engine," *Int. J. Engine Res.*, vol. 2, no. 3, pp. 177–188, Jan. 2001.
- [106] Z. Gao and W. Schreiber, "The Effects of EGR and Split Fuel Injection on Diesel Engine Emission," *Int. J. Automot. Technol.*, vol. 2, no. 4, pp. 123–133, 2001.
- [107] D. T. Hountalas, D. A. Kouremenos, E. G. Pariotis, D. Ag, T. Engine, and D. Dep, "Using a Phenomenological Multi-Zone Model to Investigate the Effect of Injection Rate Shaping on Performance and Pollutants of a DI Heavy Duty Diesel Engine," *SAE Tech. Pap.* 2002-01-0074, 2002.
- [108] D. A. Kouremenos, C. D. Rakopoulos, and D. T. Hountalas, "Multi-Zone Combustion Modelling for the Prediction of Pollutants Emissions and Performance of DI Diesel Engines," *SAE Tech. Pap.* 970635, 1997.
- [109] G. Stiesch and G. P. Merker, "A Phenomenological Model for Accurate and Time Efficient Prediction of Heat Release and Exhaust Emissions in Direct-Injection Diesel Engines," *SAE Tech. Pap.* 1999-01-1535, May 1999.
- [110] H. Hiroyasu, T. Kadota, and M. Arai, "Development and Use of a Spray Combustion Modeling to Predict Diesel Engine Efficiency and Pollutant Emissions : Part 2 Computational Procedure and Parametric Study," *Bull. JSME*, vol. 26, no. 214, pp. 576–583.
- [111] G. Stiesch, *Modeling Engine Spray and Combustion Processes*. 2013.
- [112] F. Payri, J. Benajes, and F. V. Tinaut, "A phenomenological combustion model for direct-injection, compression-ignition engines," *Appl. Math. Model.*, vol. 12, no. 3, pp. 293–304, 1988.
- [113] L. M. Pickett, J. A. Caton, M. P. B. Musculus, and A. E. Lutz, "Evaluation of the equivalence ratio-temperature region of diesel soot precursor formation using a two-stage Lagrangian model," *Int. J. Engine Res.*, vol. 7, no. 5, pp. 349–370, Jan. 2006.
- [114] J. E. Broadwell and A. E. Lutz, "A Turbulent Jet Chemical Reaction Model: NO_x Production in Jet Flames," *Combust. Flame*, vol. 114, no. 3–4, pp. 319–335, Aug. 1998.
- [115] P. Kirchen and K. Boulouchos, "Development and Validation of a Phenomenological Mean Value Soot Model for Common-Rail Diesel Engines," *SAE Tech. Pap.* 2009-01-1277, Apr. 2009.
- [116] J. Nagle and R. F. Strickland-Constable, "Oxidation of Carbon between 1000-2000 C," in *Proceedings of the fifth carbon conference* vol. 1 No. 1, New York: Pergamon, 1962.
- [117] J. Naber and D. L. Siebers, "Effects of Gas Density and Vaporization on Penetration and Dispersion of Diesel Sprays," *SAE Tech. Pap.* 960034, Feb. 1996.
- [118] J. Pastor, J. Javierlopez, and J. Garcia, "A 1D model for the description of mixing-controlled inert diesel sprays," *Fuel*, vol. 87, no. 13, pp. 2871–2885, Oct. 2008.

- [119] M. M. P. B. Musculus and K. Kattke, "Entrainment Waves in Diesel Jets," *SAE Tech. Pap. 2009-01-1355*, 2009.
- [120] S. Singh and M. P. B. Musculus, "Numerical Modeling and Analysis of Entrainment in Turbulent Jets After the End of Injection," *J. Fluids Eng.*, vol. 132, no. 8, p. 081203, 2010.
- [121] L. M. Pickett, J. Manin, R. Payri, M. Bardi, and J. Gimeno, "Transient Rate of Injection Effects on Spray Development," *SAE Tech. Pap. 2013-24-0001*, Sep. 2013.
- [122] J. M. Desantes, J. V. Pastor, J. M. García-Oliver, and J. M. Pastor, "A 1D model for the description of mixing-controlled reacting diesel sprays," *Combust. Flame*, vol. 156, no. 1, pp. 234–249, Jan. 2009.
- [123] P. G. Hill and B. Douville, "Relating Burning Rate and NO Formation to Pressure Development in Two-Stroke Diesel Engines," *J. Energy Resour. Technol.*, vol. 119, no. 2, p. 129, Jun. 1997.
- [124] G. P. McTaggart-Cowan, S. N. Rogak, S. R. Munshi, P. G. Hill, and W. K. Bushe, "The influence of fuel composition on a heavy-duty, natural-gas direct-injection engine," *Fuel*, vol. 89, no. 3, pp. 752–759, Mar. 2010.
- [125] M. S. Gilbert and N. N. Clark, "Measurement of particulate matter from diesel engine exhaust using a tapered element oscillating microbalance," *Int. J. Engine Res.*, vol. 2, no. 4, pp. 277–287, Jan. 2001.
- [126] S. K. Cheung, S. T. Elder, and R. R. Raine, "Diesel Particulate Measurements with a Light Scattering Photometer," *SAE Tech. Pap. 2000-01-1136*, Mar. 2000.
- [127] H. Burtscher, U. Baltensperger, N. Bukowiecki, P. Cohn, C. Hüglin, M. Mohr, U. Matter, S. Nyeki, V. Schmatloch, N. Streit, and E. Weingartner, "Separation of volatile and non-volatile aerosol fractions by thermodesorption: instrumental development and applications," *J. Aerosol Sci.*, vol. 32, no. 4, pp. 427–442, Apr. 2001.
- [128] R. Dastanpour and S. N. Rogak, "Observations of a Correlation between Primary Particle and Aggregate Size for Soot Particles," *Aerosol Sci. Technol.*, vol. 48, no. 10, pp. 1043–1049, Aug. 2014.
- [129] M. M. Maricq, "Monitoring Motor Vehicle PM Emissions: An Evaluation of Three Portable Low-Cost Aerosol Instruments," *Aerosol Sci. Technol.*, vol. 47, no. 5, pp. 564–573, May 2013.
- [130] B. C. R. Ewan and K. Moodie, "Structure and Velocity Measurements in Underexpanded Jets," *Combust. Sci. Technol.*, vol. 45, no. 5–6, pp. 275–288, Mar. 1986.
- [131] H. L. Jones, "Source and Characterization of Particulate Matter from a Pilot-Ignited Natural Gas Fuelled Engine," MASc Thesis, The University of British Columbia, 2004.
- [132] G. Goodwin, "An open source, extensible software suite for CVD process simulation," in *Proceedings of CVD XVI and EuroCVD Fourteen*, 2003, 2003.
- [133] Y. Ra, S. C. Kong, R. D. Reitz, and C. J. Rutland, "Multidimensional Modeling of Transient Gas Jet Injection Using Coarse Computational Grids," *SAE Tech. Pap. 2005-01-0208*, 2005.
- [134] P. Ouellette and P. G. Hill, "Turbulent Transient Gas Injections," *J. Fluids Eng.*, vol. 122, no. 4, pp. 743–753, Dec. 2000.
- [135] N. Rajaratnam, *Turbulent Jets*. Elsevier, 1976.
- [136] J. O. Hinze, "Turbulence," in *Turbulence*, 2nd ed., McGraw-Hill, 1975.
- [137] H. A. Becker, H. C. Hottel, and G. C. Williams, "The nozzle-fluid concentration field of the round, turbulent, free jet," *J. Fluid Mech.*, vol. 30, no. 2, pp. 285–303, 1967.

- [138] D. D. R. Dowling and P. E. P. Dimotakis, "Similarity of the concentration field of gas-phase turbulent jets," *J. Eng. Gas Turbines Power*, vol. 218, pp. 109–141, 1990.
- [139] I. Yimer, I. Campbell, and L.-Y. Jiang, "Estimation of the Turbulent Schmidt Number from Experimental Profiles of Axial Velocity and Concentration for High-Reynolds-Number Jet Flows," *Can. Aeronaut. Sp. J.*, vol. 48, no. 3, pp. 195–200, Sep. 2002.
- [140] G. P. Smith, D. M. Golden, M. Frenklach, N. W. Moriarty, B. Eiteneer, ...& Goldenberg, M., and Z. Qin, "GRI3. 0 mechanism version 3.0 7/30/99," 1999..
- [141] G. Woschni, "A Universally Applicable Equation for the Instantaneous Heat Transfer Coefficient in the Internal Combustion Engine," *SAE Tech. Pap. 670931*, 1967.
- [142] K. Sihling and G. Woschni, "Experimental investigation of the instantaneous heat transfer in the cylinder of a high speed diesel engine," *SAE Tech. Pap. 790833*, 1979.
- [143] J. Huang, "Natural gas combustion under engine-relevant conditions," Doctoral Thesis, The University of British Columbia, 2006.
- [144] P. Kheirkhah, "CFD modeling of injection strategies in a High-Pressure Direct- Injection (HPDI) natural gas engine," MSc Thesis, The University of British Columbia, 2015.
- [145] U. Maas and S. B. Pope, "Simplifying chemical kinetics:," *Combust. Flame*, vol. 88, no. 3–4, pp. 239–264, Mar. 1992.
- [146] S. B. Pope and U. Maas, "Simplifying Chemical Kinetics: Trajectory-Generated Low-Dimensional Manifolds," *Mech. Aerosp. Eng. Rep. FDA*, vol. 93–11, 1993.
- [147] J. Huang and W. K. Bushe, "Experimental and kinetic study of autoignition in methane/ethane/air and methane/propane/air mixtures under engine-relevant conditions," *Combust. Flame*, vol. 144, no. 1–2, pp. 74–88, Jan. 2006.
- [148] J. Huang, W. K. Bushe, P. G. Hill, and S. R. Munshi, "Experimental and kinetic study of shock initiated ignition in homogeneous methane–hydrogen–air mixtures at engine-relevant conditions," *Int. J. Chem. Kinet.*, vol. 38, no. 4, pp. 221–233, Apr. 2006.
- [149] M. Mehl, W. J. Pitz, C. K. Westbrook, and H. J. Curran, "Kinetic modeling of gasoline surrogate components and mixtures under engine conditions," *Proc. Combust. Inst.*, vol. 33, no. 1, pp. 193–200, 2011.
- [150] H. Steiner and W. K. Bushe, "Large eddy simulation of a turbulent reacting jet with conditional source-term estimation," *Phys. Fluids*, vol. 13, no. 3, p. 754, Mar. 2001.
- [151] A. D. Michailidis, R. K. Stobart, and G. P. McTaggart-Cowan, "Fuel-Line Stationary Waves and Variability in CI Combustion During Complex Injection Strategies," in *ASME 2010 Internal Combustion Engine Division fall technical conference. American Society of Mechanical Engineers*, 2010.
- [152] U. Mathis, M. Mohr, R. Kaegi, A. Bertola, and K. Boulouchos, "Influence of Diesel Engine Combustion Parameters on Primary Soot Particle Diameter," *Environ. Sci. Technol.*, vol. 39, no. 6, pp. 1887–1892, Mar. 2005.
- [153] M. Arai, K. Amagai, T. Nakaji, and S. Hayashi, "Primary and Aggregate Size Distributions of PM in Tail Pipe Emissions form Diesel Engines," *JSME Int. J. Ser. B*, vol. 48, no. 4, pp. 639–647, 2005.
- [154] A. Verhoff, "The two-dimensional, turbulent wall jet with and without an external free stream," *Princet. Univ NJ*, 1963.
- [155] H. Tanabe and G. T. Sato, "Experimental Study on Unsteady Wall Impinging Jet," *SAE Tech.*

Pap. 900605, 1990.

- [156] H. J. Hussein, S. P. Capp, and W. K. George, "Velocity measurements in a high-Reynolds-number, momentum-conserving, axisymmetric, turbulent jet," *J. Fluid Mech.*, vol. 258, no. 1, p. 31, Apr. 2006.
- [157] W. R. Quinn, "Upstream nozzle shaping effects on near field flow in round turbulent free jets," *Eur. J. Mech. - B/Fluids*, vol. 25, no. 3, pp. 279–301, May 2006.
- [158] J. R. Birch, A. D., Brown, D. R., Dodson, M. G., & Thomas, "The turbulent concentration field of a methane jet," *J. Fluid Mech.*, vol. 88, no. 3, pp. 431–449, 1978.
- [159] D. Dowling and P. Dimotakis, "Similarity of the concentration field of gas-phase turbulent jets," *J. Fluid Mech.*, vol. 218, 1990.
- [160] E. Faghani and S. N. Rogak, "Phenomenological Simulation of Non-Premixed Gas Jet Flames Including Soot Formation and Oxidation," in *ASME 2012 Internal Combustion Engine Division Fall Technical Conference. American Society of Mechanical Engineers*, 2012.
- [161] F. P. Ricou and D. B. Spalding, "Measurements of entrainment by axisymmetrical turbulent jets," *J. Fluid Mech.*, vol. 11, no. 1, pp. 21–32, 1961.
- [162] P. G. Hill and P. Ouellette, "Transient Turbulent Gaseous Fuel Jets for Diesel Engines," *J. Fluids Eng.*, vol. 121, no. March 1999, pp. 93–101, Mar. 1999.
- [163] P. Ouellette and P. Hill, "Turbulent transient gas injections," *J. Fluids Eng.*, vol. 122, no. December 2000, pp. 743–753, 2000.
- [164] H. Fujimoto, G. S. Hyun, M. Nogami, K. Hirakawa, T. Asai, and J. Senda, "Characteristics of free and impinging gas jets by means of image processing," *SAE Tech. Pap. 970045*, 1997.
- [165] Y. Wakisaka and A. Azetsu, "Effect of Fuel Injection Rate Shaping and Injection Pressure on Intermittent Spray Combustion," *SAE Tech. Pap. 2000-01-2793*, no. 724, 2000.
- [166] D. N. Assanis, Z. S. Filipi, S. B. Fiveland, and M. Syrimis, "A Predictive Ignition Delay Correlation Under Steady-State and Transient Operation of a Direct Injection Diesel Engine," *J. Eng. Gas Turbines Power*, vol. 125, no. April 2003, pp. 450–457, 2003.

APPENDICES

Appendix A: Non-Reacting TSM and Validation

A phenomenological model, called transient slice model (TSM) is developed to evaluate transient gas injections. A one-dimensional numerical solver is used to solve transport equations for momentum, mass fraction and enthalpy. This model is capable of simulating fuel-air mixing and gas penetration under transient conditions. The model can also predict the jet after end of injection, effect of rate of injection, wall impingement and injection in variable environment. The model is based on mixing-controlled assumption and self-similarity for conserved properties. TSM is extensively validated with both CFD simulation and experimental measurements from literature. The model provides simple but reliable phenomenological model to predict gas jets in a wide range of applications with built-in thermodynamics allowing easy change in chemistry and boundary conditions of the problem.

Impingement Model (included for possible future development of TSM)

Figure A-1 shows different regions of an impinging jet on a flat surface. In region (b) –the impingement region- there is a pressure rise in the vicinity of the stagnation point reducing the free jet velocity; starting at 0.85H to the wall surface (i.e. inside the red box). Upon impingement, the pressure on the wall surface rises to cancel the axial momentum of the jet. Given this, applying the momentum balance equation to the impingement region, the net normal force on the wall is calculated based on the total momentum of the jet at the 0.85H. Given the work of Beltaos and Rajaratnam [135], the pressure force at the impingement region increases linearly to the stagnation pressure, suggesting the following force distribution in this region.

$$F_i = \frac{x_i - x_1}{x_2 - x_1} \times F_{wall} = \frac{x_i - x_1}{x_2 - x_1} \times \int_{0.85H} \rho U^2 dA \quad (A-1)$$

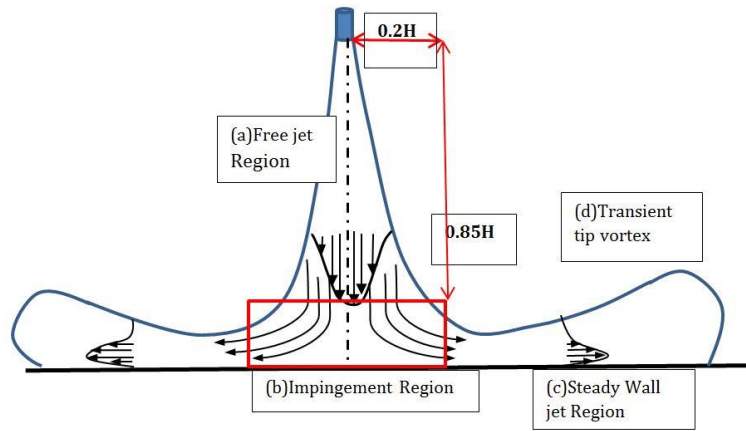


Figure A-1: Schematics of an impinging jet in the model

Knowing the pressure distribution, the force balance (momentum equation) at each cell could be written considering the extra flux coming from the impingement in the impingement zone.

$$FluxM|_{i-1}^t - FluxM|_i^t + (\mathbf{F}_{i-1}^t - \mathbf{F}_i^t) = \frac{M|_i^{t+1} - M|_i^t}{\Delta t} \quad (A-2)$$

After obtaining axial velocity at the impingement region, the exit mass flux at each slice is calculated from based on the mass balance of each cell inside the wall impingement zone.

$$\dot{m}_e = \int_{in} \rho U dA - \int_{out} \rho U dA \quad (A-3)$$

The exit mass generates an effective velocity in the wall direction, inducing an effective momentum flux for the wall jet. In other words, the initial momentum at the beginning of the wall jet is the sum of the individual exit momentum fluxes from the impingement slices.

Wall jet PDFs

The dimensionless velocity profile is estimated using the profile from literature [154]. The spread coefficient for wall jet ($K_{r,i}$) is reported [135] slightly different from the free jet; the value of $K_{r,i}=0.087$ is a commonly accepted value. The numerical values of A and B are 1.48 and 0.68 respectively.

$$PDF_u(x, r) = A \left(\frac{y}{K_{r,i}x} \right)^{\frac{1}{7}} \left[1 - \text{erf} \left(B \frac{y}{K_{r,i}x} \right) \right] \quad (\text{A-4})$$

According to Tanabe and Sato [155], the concentration profile in the wall jet maintains a Gaussian distribution peaked at the wall vicinity.

$$PDF_z(x, r) = \exp \left(\frac{y}{0.23x} \right) \quad (\text{A-5})$$

Model Validation

TSM is developed to predict the HPDI engine parameters, namely cylinder pressure, heat release rate, and PM. The current study is focusing on the abilities of the model in prediction of non-reacting jets for different conditions. The validations of these cases are required to make sure the model can effectively perform in more challenging environment in engine.

The mesh sensitivity calculations has been performed on the model and discussed in Appendix B. For the rest of the study here we use the mesh size of $\Delta x=2D_n$, $\Delta y=0.5D_n$. Although the model has the ability of adopting a stretching mesh, a uniform mesh size is selected since the uniform mesh shows good performance in our preliminary studies.

The constants of the model are not further adjusted to match the experimental results and the initial values from literature, mentioned in the theory of the model, will be used for the entire paper and future studies of the model.

Steady Air-Air Jet, Velocity Comparison

The TSM results of velocity for non-reacting steady jet are presented and compared with the experiments. The results are taken long after the start of injection to make sure the jet is steady state in the computational domain. For validation of the results the experimental

data of Hussein et al. [156] and Quinn [157] are used, where a jet of air is injected into an atmospheric quiescent medium in room temperature. Figure A-2 shows the centerline and radial profile of axial velocity of the free jet compared with experimental measurements. In centerline velocity comparison, TSM and experiments show good agreement in far-field of the jet, however, in near-field TSM slightly deviate from the experimental data. The main assumption of TSM is self-similarity of the jet which is not fully established yet in near-field of the jet [118], [135]. The radial profile of the velocity in TSM is assumed to be Gaussian in and it is in agreement with experimental data.

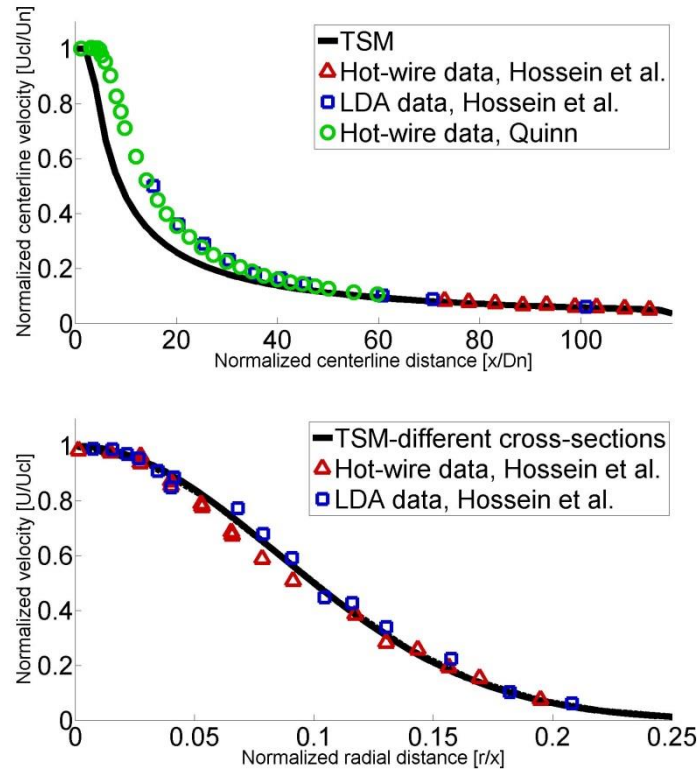


Figure A-2: Comparison of the free jet velocity profile with the experimental measurements

Steady Methane-Air Jets, Mass Fraction Comparison

One of the important quantities govern the behaviour of the combustion in the non-premixed flames is the mixture fraction distribution of the fuel. Mixture (mass) fraction distribution is closely coupled with the entrainment and mixing behaviour of the jets. For

validation, the experimental results of Birch and Brown [158] is selected for axial mass fraction comparison with TSM model. In their study, the concentration distribution of a round turbulent methane jet is measured by means of Raman Spectroscopy. The experimental data of Dowling and Dimotakis [159] is also used for further investigating the mixture fraction distribution in radial direction.

Figure A-3 show the centerline decay of mass fraction and radial distribution of mass fraction compared to experimental data. Similar to velocity field, TSM can predict the far-field of the jet where self-similarity is fully established with good accuracy; however it shows slight deviation in near-field. The general agreement between the model and experimental data is acceptable. Radial distribution of mass fraction compared with experimental data, the experimental data and Gaussian profile selected for mass fraction are very close.

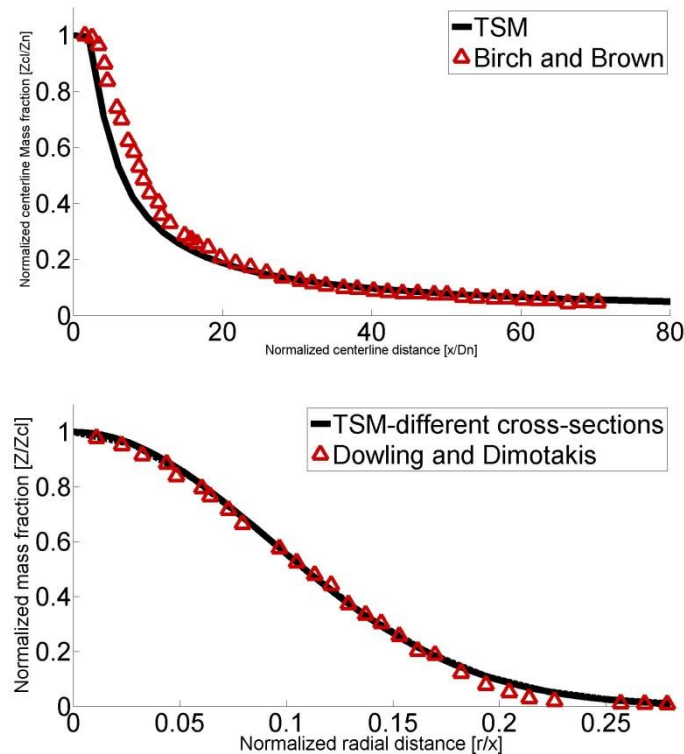


Figure A-3: Comparison of the free jet mass fraction profile with the experimental measurements

Steady Methane-Hot Air Jet, Mixing Temperature Comparison

Mixing temperature prediction of the model has been compared with previous CFD simulation [160]. Mixing temperature will be found based on gas composition and enthalpy of the cell using thermodynamics script in the model. Mixing temperature is important for calculation of reacting flow later, since it would be used as initial temperature for equilibrium calculations. The results of axial mixing temperature comparison have been shown in Figure A-4. Similar to mass fraction and velocity, mixing temperature prediction is also close to CFD for far-field while for near-field there is a minor deviation from CFD results.

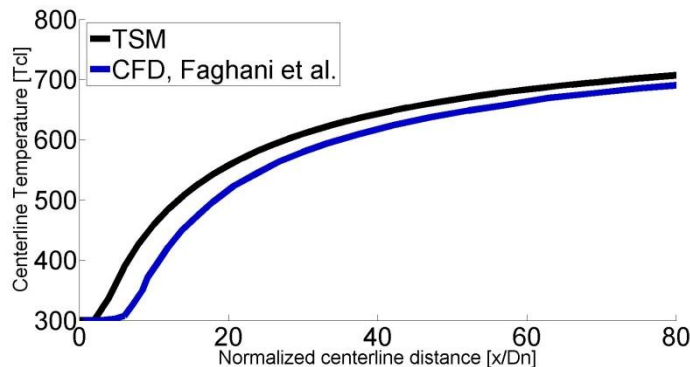


Figure A-4: Normalized axial profile of mixing temperature distribution.

Steady N₂-CO₂-H₂ Jets, Entrainment Comparison for Different Density Ratios

Entrainment rate is the amount of air entrained by jet from ambient and it has a governing effect on the process of mixture formation and combustion in direct-injection engines. Furthermore, entrainment as an integral quantity is an indicator of whether or not the overall scalar distribution is well predicted. The experimental results of Ricou and Spalding [161] is chosen for validation in this section. Their experiments have been performed using different materials and consequently different density ratios. The results of their experiments with different nozzle and ambient compositions are summarized in an experimental correlation. The TSM results of different density ratios will be compared to

Ricou and Spalding experimental correlation. In TSM, the composition of the injection (N2, CO2 and H2) is changed to set the density ratios (nozzle to ambient) from 0.6 to 2.7.

Figure A-5 shows the TSM results of entrained mass versus the dimensionless axial distance for three different nozzle-ambient density ratio compared to the correlation developed by Ricou and Spalding. The non-dimensional results of entrainment from TSM are in agreement with the experimental correlation. The TSM over-predict the entrainment by 6%, however it is within the data scatter of the experiments used for development of the experimental correlation.

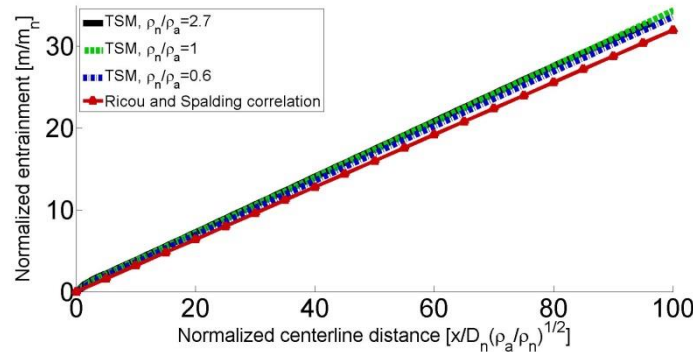


Figure A-5: Scaled entrainment of free jets versus axial distance from the nozzle

Transient N₂-CO₂-H₂ Jets, Penetration Comparison for Different Density Ratios

TSM model is developed to predict the transient behaviour of gaseous jets should be able to predict the penetration rate of jets in a free environment at different density ratios. In this section the experimental work of Ouellette and Hill [162], [163] is used to validate the TSM results in prediction of penetration rate. In TSM, the composition of the injection (N2, CO2 and H2), same as the entrainment comparison case, is changed to set the density ratios (nozzle to ambient) from 0.6 to 2.7.

Figure A-6 shows the normalized penetration for different density ratios. The experiments show penetration of the jet increase slightly from the normalized scale introduced in Ref. [163]. TSM prediction shows a good agreement with experimental results considering the scattered of the experiments. Moreover TSM can predict the minor effect of density ratio

change in the normalized penetration graphs. For lower density ratios (0.6) penetration is lower as it is shown in the experimental results too, higher density ratios show higher normalized penetration rate. The TSM results in prediction of penetration go beyond the experimental correlation.

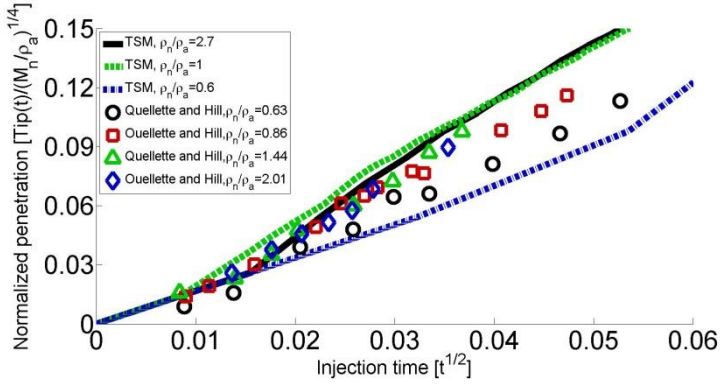


Figure A-6 Scaled penetration rate versus square root of time.

Decelerating Air-Air Jet, Entrainment Comparison after EOI

End of injection is accompanied with a sudden increase of entrainment rate at the tail of the jet. It is known as “entrainment wave”. Singh and Musculus [120] discussed the rate of entrainment of an interrupted jet after the end of injection relative to a non-interrupted jet (still injecting) and identified this phenomena. The increase of entrainment rate manifests itself as a peak in the entrainment curve propagating towards the tip of the jet with a speed twice the speed of the tip of the jet [120]. In this section TSM results are compared with the 1D model of Musculus and 2D CFD simulations with a KIVA V3 code.

Figure A-7 (a and b) show the results of CFD and 1D model from SANDIA [120]. Both CFD and TSM models can predict the presence of entrainment wave after EOI. However, the 1D model predicts it with higher peak (2.5 instead of 1.5) and the tip of the jet has a sudden decrease in entrainment, where CFD simulation shows a gradual decrease. In 1D model the entrainment wave is traveling faster than CFD model. Figure A-7(c and d) shows the entrainment of TSM model after EOI as a function of distance for the same case. The case with square shape fuel rate shape is just shown to show the effect of fuel rate shape on the entrainment wave after EOI. The model captures the presence of the entrainment wave

after EOI. For the case with square shape pulse, peak of the entrainment wave is high and it travel faster than CFD predictions. TSM results with ramp down in fuel rate shape, shows the peak of the entrainment wave around 2 which is still higher than CFD (1.5) but lower than previous 1D model (2.5) and TSM square shape pulse results. The tip of the entrainment wave is not as steep as previous 1D model. Although there are small differences in prediction of the current model, but generally TSM can capture entrainment wave after EOI with the same, if not better, than previous 1D models.

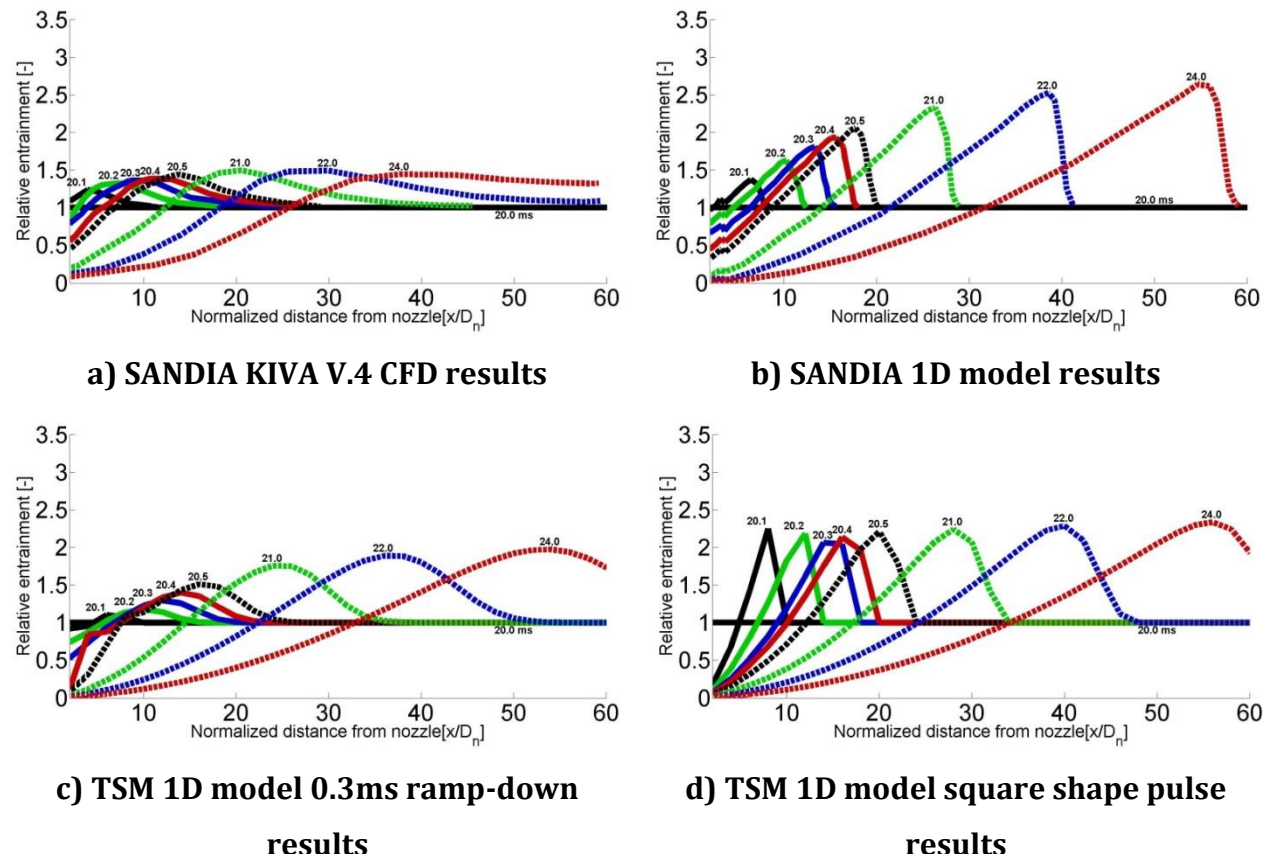


Figure A-7: Entrainment after EOI

Steady Impinging Air-Air Jet, Velocity Comparison

This case study focuses on the velocity profile of an impinging jet right above the wall. Figure A-8 shows the axial velocity decay of an impinging jet for different nozzle-wall distances (H/D_n). Even though the near-field of the jet is modeled, the agreement with the

literature data is reasonably well. The slight under-prediction of the velocity was also observed in the previous free jet cases.

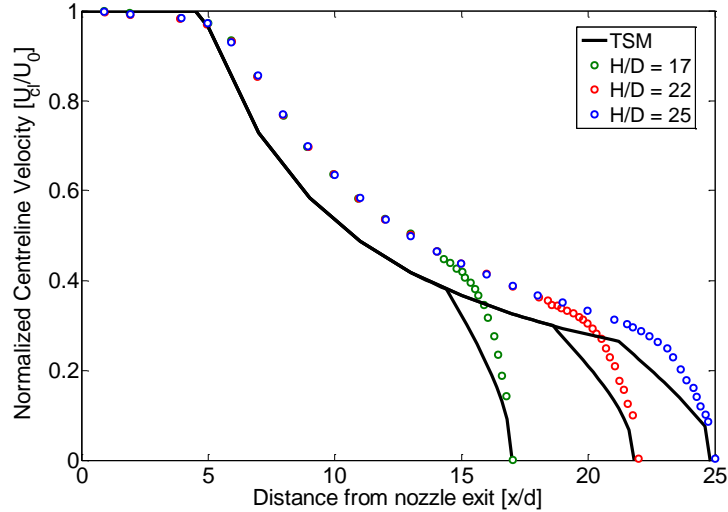


Figure A-8: Axial velocity decay of an impinging jet for different wall distances

Transient Impinging C₂H₂-Air Jet, Jet Penetration Comparison

Experimental measurements [164] and simple dimensional analysis show that the penetration rate of a wall jet is much less compared to the free jet. Correlated with the rate of mixing and heat transfer to the piston surface, penetration is a key characteristic of the free and wall jet. Figure A-9 shows the predictions of TSM for the penetration of the free and wall jets previously studied by Fujimoto et al. [164]. TSM correctly predicts less penetration of the jet after impingement. However, the level of error is very high for the short wall distances (Red curve, wall/diameter ratio: 12.5). As the wall distance increases (Red curve, wall/diameter ratio: 18.75), the TSM predictions model the wall jet penetration with a better accuracy.

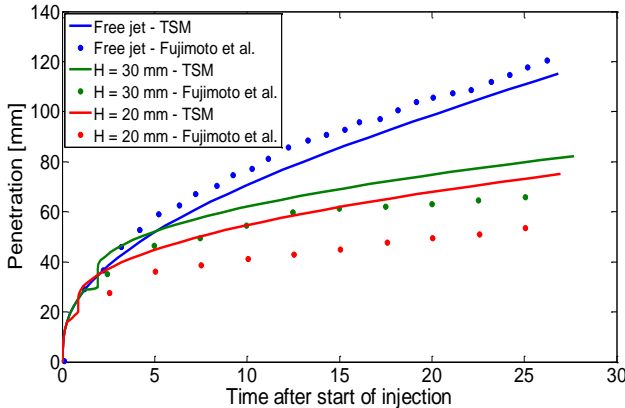
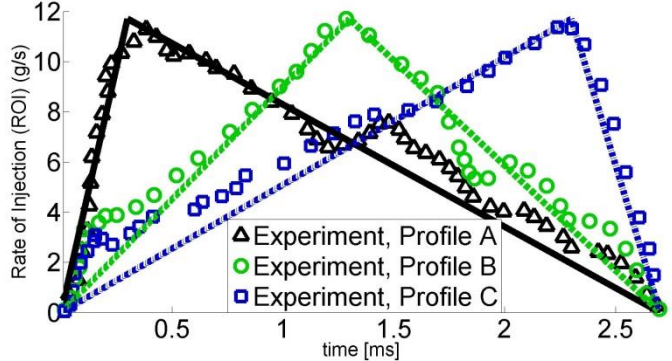


Figure A-9. Penetration of free and impinging jets; TSM prediction compared with literature data [164]

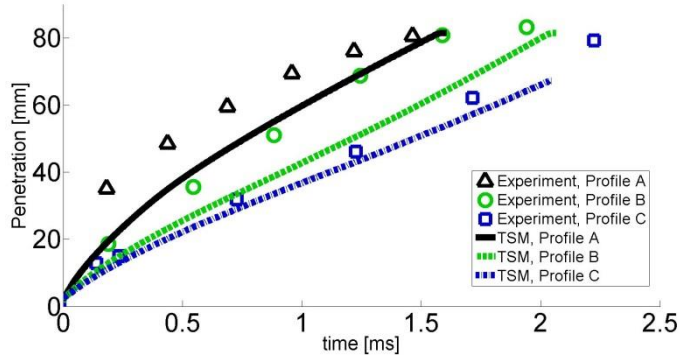
Pulsed Air-Air Jet, Fuel Rate Shape Effect on Penetration Rate

TSM has the capability of accepting fuel rate shape from the experiments, if available. The shape of mass injection ramp-up and ramp-down affects penetration and mixing [121]. The effects of fuel injection rate shape on diesel spray has been considered in the literature before [121], [165]. Wakisaka and Azetsu [165] considered three different ROI profile with pulse duration of 2.7ms for all of the cases. The injection rate shaping used in the study was triangular, with different slopes of injection rate rise and fall. The injection period, peak injection rate and total amount of fuel injected for all tests were the same. The profiles A, B and C had peak injection rate at start, middle and end of injection, respectively. There is no equivalent gas injection study in the literature; instead we produced the profiles to qualitatively compare the results. Figure A-10(a) shows the fuel rate shape from the experiments and the TSM model using the linear fuel rate shape between start and maximum fuel delivery rate and end of injection. In the TSM model, instead of diesel injection, we injected a hypothetical gas with same density as diesel. The case study here might not be representative of the experimental case [165]; however the trend of penetration change with fuel delivery rate should be the same for both gas and spray injections.

Based on the spray results [165], the jet from profile A penetrate faster, then profile B and finally profile C. Profile A start of penetration is closer to the scale of time in experimental correlations ($t^{0.5}$ [162]) while profile B and C start with linear growth with time and then would be closer to the time scale of $t^{0.5}$. Penetration rate of three different profiles for ROI has been shown in Figure A-10(b). TSM predicts profile A to have higher penetration rate, then profile B and finally profile C, as it is measured by experiments. Moreover, penetration from profile A is closer to the scale of time in experimental correlations ($t^{0.5}$) while profile B and C start with linear growth with time and then would be closer to the time scale of $t^{0.5}$. The point-point comparison of the results is not possible since the fuel composition and state is different.



(a)



(b)

Figure A-10: a) ROI of experiments and TSM model, b) Penetration of the different ROI cases

Cold Injection in Variable Environment, Penetration and Mixing Rate Comparison

The TSM model is compared to the results of in-cylinder CFD simulations. The CFD simulation is done using GOLD [87]. The CFD program is based on OpenFoam combined with in-house chemistry and heat transfer models. The ignition model in the code is disabled in order to compare the non-reacting injection in a variable environment with CFD. The CFD code is run in engine conditions with swirl and wall-impingement. Although the CFD simulation and TSM are simulated in different conditions, in our engine simulation with TSM model no swirl motion and simple wall impingement on the flat surface are assumed. Figure A-11 (a) shows the total mass of the jet in TSM model and CFD for different Z_b values. The results show TSM predicts the lean mixture less than the CFD value especially for later timing in cycle.

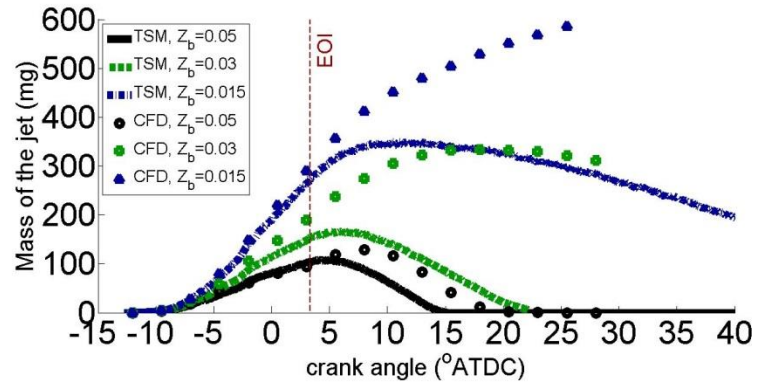


Figure A-11. entrainment of the jet compared to CFD simulation

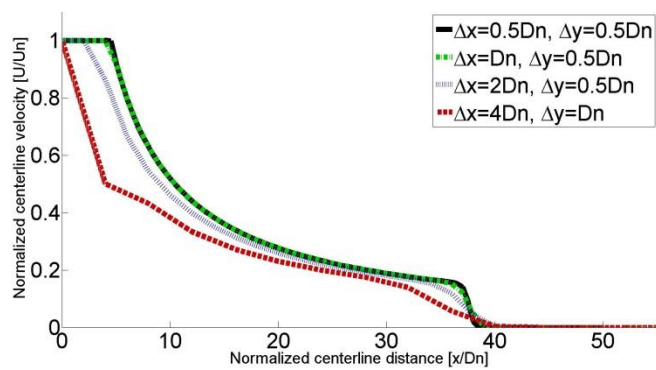
Appendix B: Mesh Sensitivity, Computational Time, and Parametric Tuning of TSM

TSM Mesh Sensitivity

The jet is divided into “slices” spanning the width of the numerical domain. Each slice has several points in the radial direction, which are used for calculation of integrals and presentation of the results in radial direction. The domain dimensions are selected large enough to ensure the jet does not cross these boundaries for engine time scales. The volume of the cells is scaled with the compression or expansion of the cylinder. This is done to consider the effect of compression and expansion on the mesh size. This mesh compression/expansion is similar to the engine simulation using CFD stretching mesh.

$$V_{i,j}|^{t+1} = V_{i,j}|^{GSOI} \frac{V_{cyl}}{V_{cyl}|^{GSOI}} \quad \text{B-1}$$

Four different mesh resolutions have been considered: 1) $\Delta x=4D_n$, $\Delta y=D_n$ 2) $\Delta x=2D_n$, $\Delta y=0.5D_n$ 3) $\Delta x=D_n$, $\Delta y=0.5D_n$ 4) $\Delta x=0.5D_n$, $\Delta y=0.5D_n$. The results of axial (x) and radial (y) velocity are shown in Figure B-1. While the coarse mesh ($\Delta x=4D_n$, $\Delta y=D_n$) has significant deviation from the fine mesh, close to the nozzle and at the head of the jet, all other mesh resolutions are very close. The medium mesh ($\Delta x=2D_n$, $\Delta y=0.5D_n$) shows small deviation from converged mesh in prediction of potential core of the jet, but on farfield of the jet this case is similar to converged mesh too. For the rest of our study here we use the medium mesh ($\Delta x=2D_n$, $\Delta y=0.5D_n$).



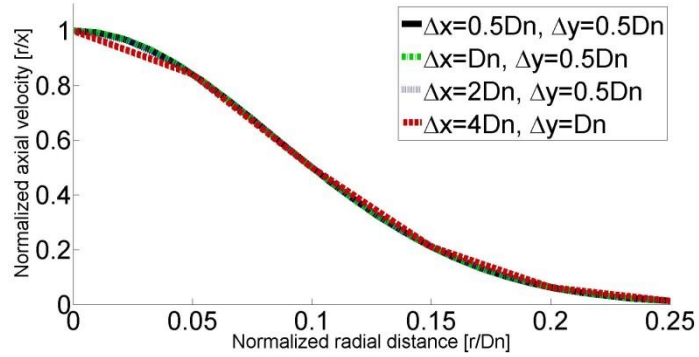


Figure B-1: mesh study in radial and axial directions

The effect of mesh size on the AHRR is shown in Figure B-2. In AHRR graphs, the shape of the AHRR from different mesh sizes are almost the same; however, the fluctuations in the results increase as the mesh size increase as well. It is because more fuel is suddenly converting from non-reacting to reacting in each cell, if the cell is located inside the reacting zone.

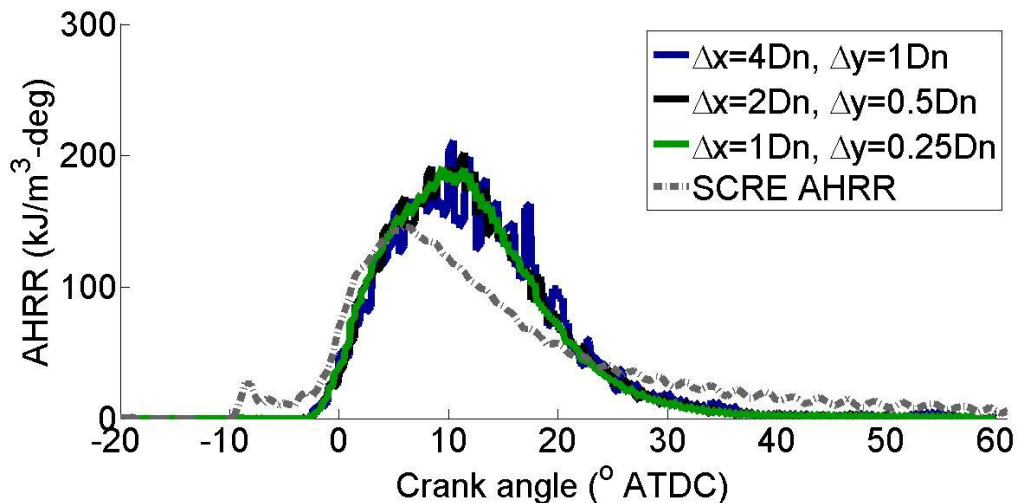


Figure B-2: mesh study for AHRR graph for different mesh size

Table B-1 shows the engine-out PM for different mesh size. The difference between fine and medium mesh is less than 10%. This difference is large enough to warrant further

study, but much smaller than the order of magnitude PM emission changes that are the focus of this work.

Table B-1 engine-out PM for different mesh size

Mesh size	$\Delta x=4D_n, \Delta y=1D_n$	$\Delta x=2D_n, \Delta y=0.5D_n$	$\Delta x=1D_n, \Delta y=0.25D_n$
PM (g)	1.3×10^{-5}	0.95×10^{-5}	0.87×10^{-5}

TSM Computational Time

Since the TSM solves the flow only in the axial direction, the computational time is significantly lower than any CFD simulation of the same case. Compared to the CFD package for engine simulation, the TSM is on the order of 1000 times faster. Moreover, the following methods have been used to keep computational time low: only solve slices between nozzle and tip of the jet (saving major computational time at the start of injection) and the time steps are adjusted according to: $\Delta t = \min(\Delta x_i / u_i)$. Since velocity decreases sharply after the end of injection, computational time is reduced significantly for after EOI.

The computational time will differ depending on the injection velocity and duration. Total computational time for high load modes (highest computational time) are about 15-30 minutes and an additional 10 minutes for soot simulation on a normal desktop computer (Intel® Core™ i5 3.2 GHz, 8GB Memory). For high load modes, about 70% of the time (10-15min) will be spent on fluid mechanics calculations (velocity, mixture fraction and integrals) and about 30% of the time on updating the mixture fraction maps using the equilibrium solver.

TSM Soot tuning

Different tuning methods for soot model have been used in the current study. The tuning methods, constants and the logic behind the tuning method are listed in Table B2. Each method requires 3 points to complete the tuning process. The first tuning method uses the

CFD in-cylinder soot simulation for tuning (maximum total in-cylinder soot and soot at 60° ATDC). The second model uses three experimental points to tune the model, B75, B75-0EGR and repeat mode (A35). The last model adjusted to have PM-CAD graph close to CFD while having much higher oxygen dependency.

Table B-2 Different methods of tuning of the soot model¹⁷

Method #	Af	Aox	C ₃	Note
Tuning 1	75	1.7×10^{-6}	5	Adjusted to match the CFD PM-CAD graph of B75 and the B75-0EGR
Tuning 2*	100	4×10^{-6}	5	Adjusted to fit experimental points B75, B75-0EGR and Repeat Mode (A35)
Tuning 3	100	60×10^{-5}	20	Adjusted to match the CFD PM-CAD graph of B75 and C ₃ fixed to 20.

* This tuning method has been used for simulations and discussions in Chapter 6.

The PM-CAD graph of different tuning methods is presented in Figure B-3. The “tuning 1” has the PM-CAD graph almost identical to the CFD simulation of the baseline point. If we tune the model by three experimental points, the formation of soot is much more than the “tuning 1”. While “tuning 1” oxidizes about 80% of the maximum soot in cylinder, “tuning 2” oxidizes about 90% of the maximum soot in the cylinder. By setting much higher oxidation rate, “tuning 3” have lower maximum in-cylinder soot compared to “tuning 2”.

¹⁷ The soot oxidation rate should be always less than the collision rate defined by the molecular theory [36]. We compared the oxidation rate defined by the collision with the model oxidation rate. The collisions considered between oxygen molecules and the soot particles. The results show that the model oxidation rate is many order of magnitudes less than the maximum oxidation defined by the collision theory.

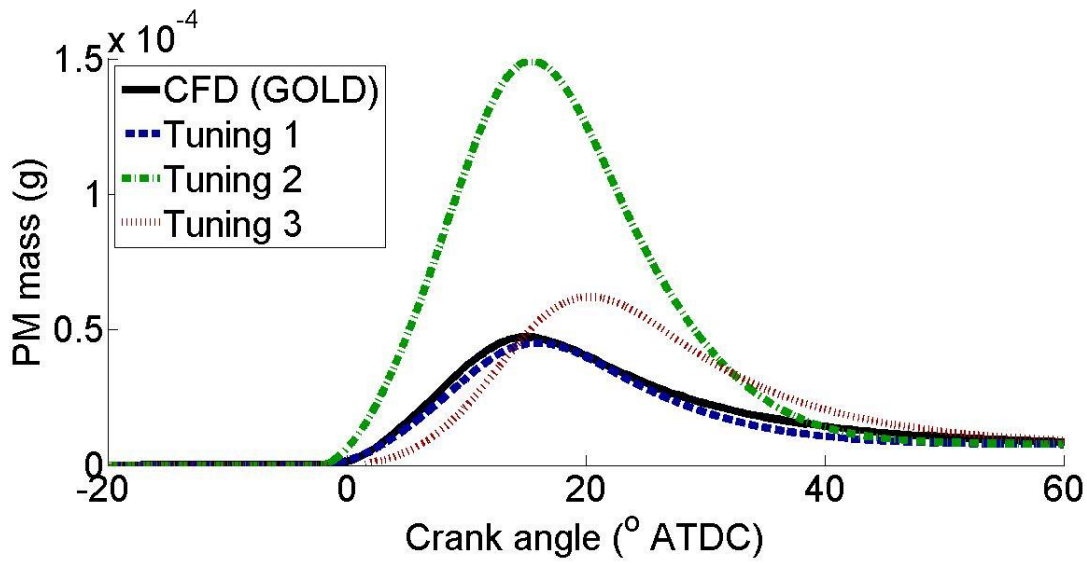
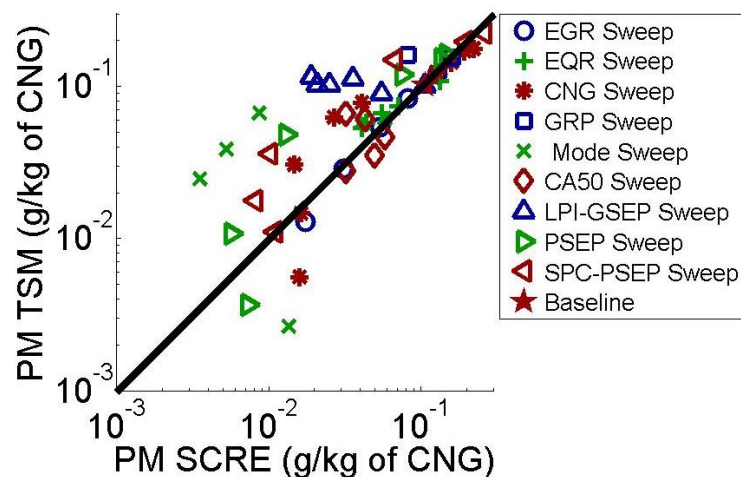
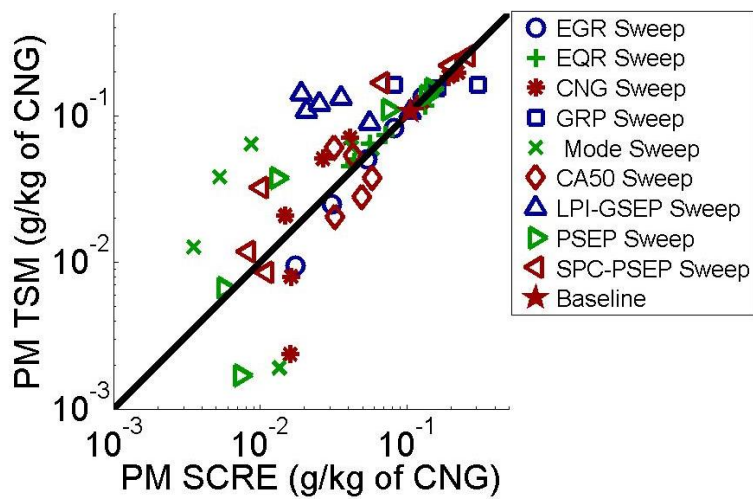


Figure B-3 PM-CAD graphs for different tuning methods

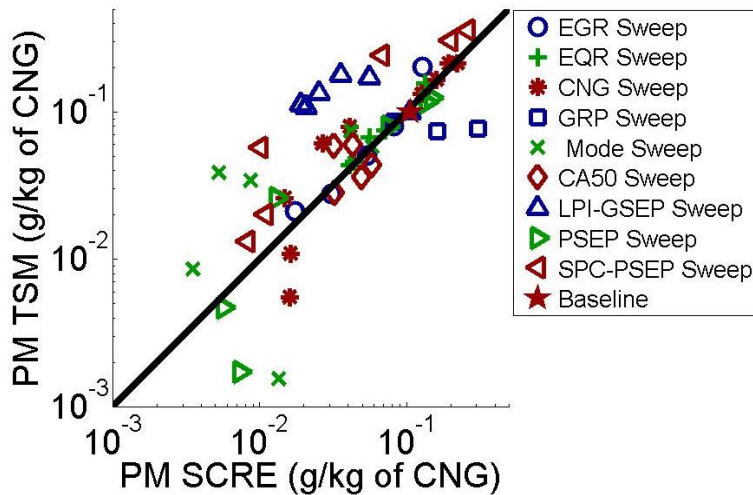
The results of all the tuning methods are shown in F. Although the tuning processes of all three models are significantly different, the changing of engine-out soot with an engine parameter is almost identical for the different methods. The magnitude of the engine-out PM might not be the same; however, the trends in changing the engine parameters remain almost identical. The “tuning 2” method has been used for simulation of the HPDI points in the current study, since for tuning of this method just experimental points have been used.



(a) Tuning 1 (matching GOLD)



(b) Tuning 2 (matching 3 SCRE points)



(c) Tuning 3(matching GOLD with constrained C₃ parameter)

Figure B-4 PM simulated by the TSM versus the experimental results for all tuning methods

Appendix C: A Physical Ignition Model (for future TSM development)

Pilot Ignition Delay (PID)

The diesel ignition delay defined as the delay time of ignition after diesel injection. Diesel ignition delay is a complicated chemical phenomenon. The diesel ignition delay and ignition propagation is a function of the history of pressure and temperature of each cell. However to find the start of the diesel ignition, we assume the pressure and temperature is uniform in the cylinder. While there is no combustion in the cylinder prior to the diesel ignition, the temperature of the cylinder is a function of the pressure of the cylinder. Therefore, the diesel ignition model is a function of cylinder pressure. One more simplification step is taken and diesel ignition delay is assumed to be only the function of cylinder pressure at the diesel injection time.

$$PID_{sim} = \frac{C_1}{P_{PSOI}} \quad (\text{C-1})$$

This simple physical model is compared with over 700 points of the experiments in very different conditions and different injectors. For all the points the diesel injection delay (command to actual injection) is assumed to be 0.7 ms (same as all the other parts of TSM). The constant C_1 is set to 330 for a maximum R^2 of the correlation. We also tried to use available diesel ignition correlations in literature [166] developed for diesel engines, however, the results show poor correlation with the current experimental data. The correlations in the literature were developed specifically for diesel engine conditions and present the local ignition delay, while here the global in-cylinder start of ignition is important.

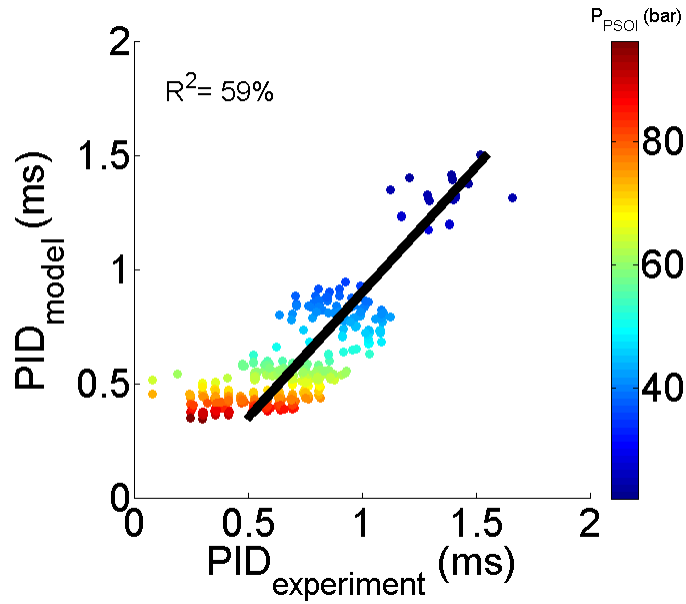


Figure C-1: Diesel ignition delay correlation compared with the experimental points

The R^2 of the correlation is 59%; it seems there is a bound of ± 0.3 ms of the experimental points around the prediction line. There are different aspects might affect the prediction accuracy:

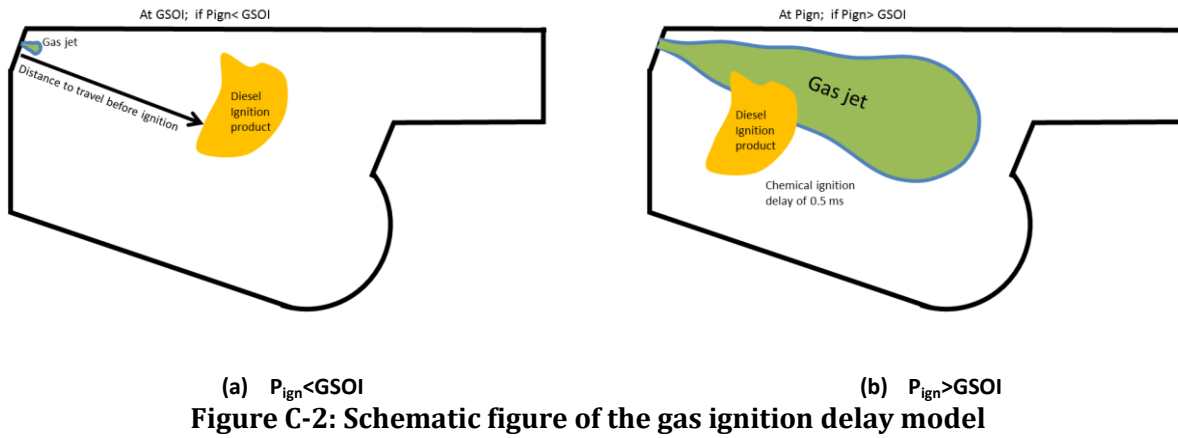
- Finding the PID_{exp} based on the AHRR contain some error in selecting the point due to the noisy AHRR graph.
- There are variations even in the repeat of one single point e.g. mode B74 variations for 8 months, for PID it is ± 0.1 ms.
- Not constant injection delay for all the cases
- Other parameters also affecting the pilot ignition delay which has not been considered here

We do not use pilot ignition delay directly in the model, however, we use this to predict the gas ignition delay as an input of the model.

Gas Ignition Delay (GID)

For the gas ignition prediction two cases have been considered. A schematic of this model is shown in Figure C-2. The model divides the cases based on relative timing of diesel ignition (P_{ign}) to GSOI. If the diesel ignition is before gas injection then the ignition of gas occurs

when the gas riches the diesel products. On the other hand, if the gas is already injected before the diesel ignition the gas ignition is happening after a constant chemical delay after the pilot ignition.



The penetration time of the gas is assumed to be a scale of the penetration time of the diesel; also it is assumed that the ignited pilot location does not move after ignition due to low momentum of diesel. In this equation PID_{model} is calculated from equation (C-1).

$$GID_{model} = C_2 PID_{model} \quad \text{if } P_{ign} \leq GSOI \quad (\text{C-2})$$

When both gas and diesel are available, the gas ignition happens with a chemical delay (constant C_3) after the pilot ignition. In this equation P_{ign} is calculated from equation (C-1) using PID_{model} and PSOI.

$$GID_{sim} = C_3 + \frac{(P_{ign} - GSOI)}{N \times 0.06} \quad \text{if } P_{ign} > GSOI \quad (\text{C-3})$$

This simple physical model is compared with over 700 points of the experiments in very different conditions and different injectors. For all the points the gas injection delay (command to actual injection) is assumed to be 0.7 ms. The constants C_2 and C_3 are set to 0.8 and 0.85 for a maximum R^2 of the correlation.

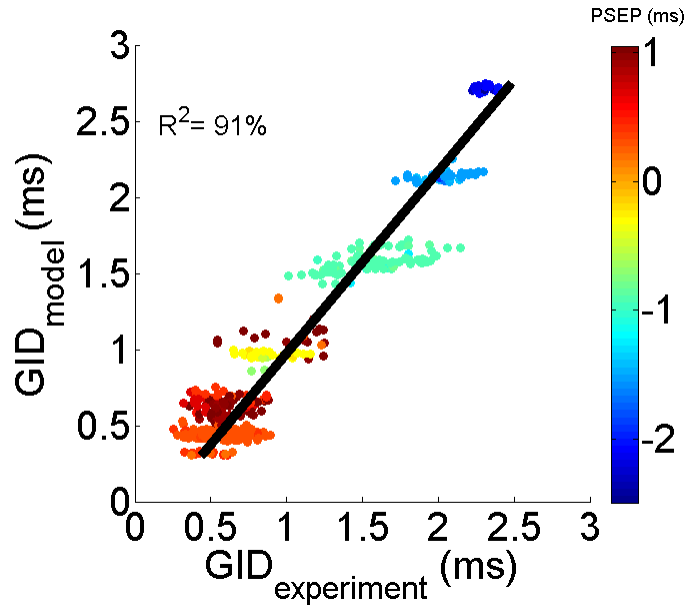


Figure C-3: Gas ignition delay correlation compared with the experimental points

The correlation for gas ignition delay shows R^2 of 91%. There is, however, a bound of ± 0.3 ms of the experimental points around the prediction line. There are different aspects that might affect the prediction accuracy: noisy AHRR graph, variability of one point in each repeat and also other factors that have not been considered here for simplicity.

Appendix D: Sample Calculation for In-Cylinder Integrals

The mass fraction of oxygen in a non-reacting jet will be calculated based on equation (3-12) in this part.

$$O2_{cyl} = \frac{\int_0^{tip} \int_{r=0}^{\infty} \rho(x, r, t) [O2(x, r, t) - O2_a] 2\pi r dr}{m_{cyl}} + O2_a \quad (\text{D-1})$$

For a non-reacting jet the Oxygen mass fraction can be written based on mixture fraction as:

$$O2 = (O2_n - O2_a)Z + O2_a \quad (\text{D-2})$$

Substituting equation (D-2) into equation (D-1):

$$O2_{cyl} = \frac{\int_0^{tip} \int_{r=0}^{\infty} \rho [(O2_n - O2_a)Z + O2_a - O2_a] 2\pi r dr}{m_{cyl}} + O2_a \quad (\text{D-3})$$

It can be further simplified as:

$$O2_{cyl} = O2_n \frac{\int_0^{tip} \int_{r=0}^{\infty} \rho Z 2\pi r dr}{m_{cyl}} - O2_a \frac{\int_0^{tip} \int_{r=0}^{\infty} \rho Z 2\pi r dr}{m_{cyl}} + O2_a \quad (\text{D-4})$$

Finally it can be written as:

$$O2_{cyl} = O2_n \frac{m_{inj}}{m_{cyl}} + O2_a \left(1 - \frac{m_{inj}}{m_{cyl}} \right) \quad (\text{D-5})$$

Analytical calculation also shows the same mass fraction results for the non-reacting case.

Appendix E: Different Methods of Setting the Point for PPW Sweep

A preliminary study was performed to find out whether it is better to control the separation between the end of diesel and start of gas injections (PSEP), or the “relative injection timing” (RIT). Figure E-1 shows the AHRR of different methods of setting the point for PPW sweep. The goal is to see the effect of pilot mass but keep the AHRR similar to the baseline point. Three different methods have been selected: constant GSOI-PSEP, constant PSOI-PSEP and constant PSOI-GSOI (RIT constant). It seems that PSOI is a dominant parameter in defining the point of ignition for both diesel and gas, not the PPW, although Gign is advancing by couple of degrees for higher PPW values. By setting PSOI and GSOI we can keep the AHRR almost unchanged while we increase PPW.

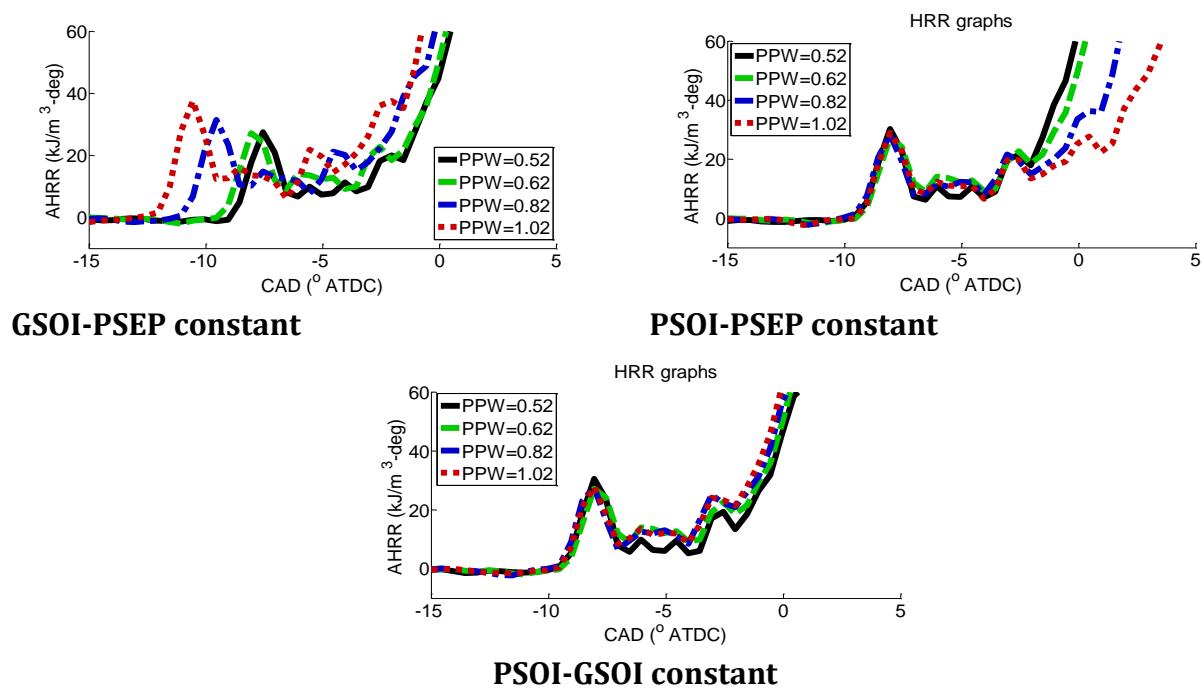


Figure E-1: Apparent heat release rate for different methods of setting the point for variable PPW

Appendix F: AHRR of the Normal PSEP Sweep Cases

Figure F-1 shows the AHRR of the negative PSEP cases. The data here are the same graphs as Figure 5-1. The AHRR graphs are plotted all in one graph here to better show the AHRR phasing differences between the cases.

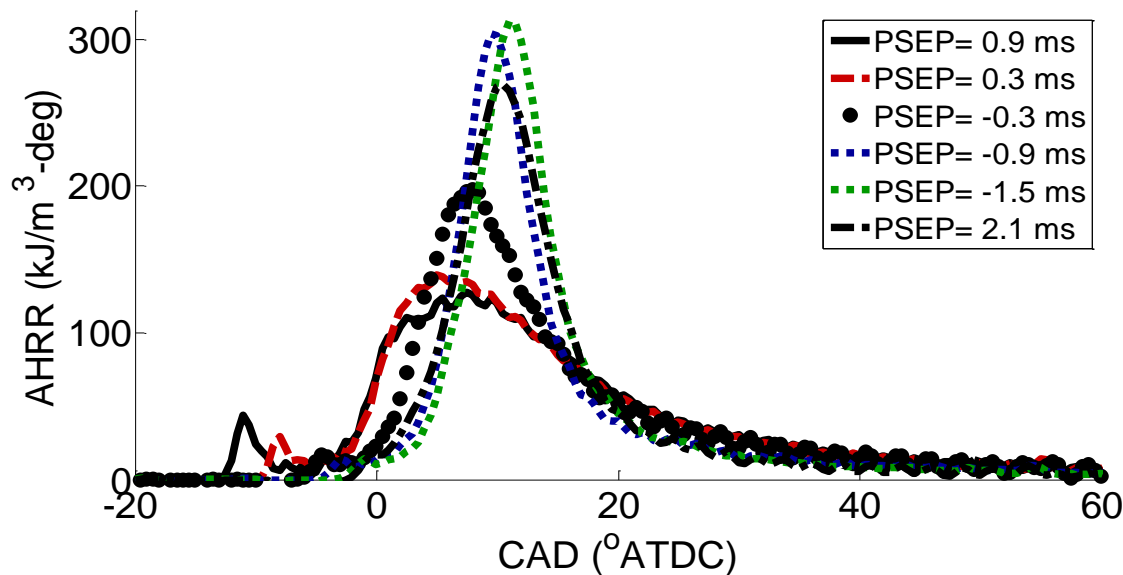


Figure F-1 AHRR of the normal PSEP sweep cases

Appendix G: Electronic Archives and Data Processing

Electronic Archives

There were 2 main computers used for data storage and processing of the data during the course of this work. The SCRE computer was located in CERC; it is the engine operator computer. All the engine data were stored in a hard drive and the data are saved based on the acquisition time (D:\Engine Experiments\Data\2014). All the files were initially stored on this computer. The data were then transferred to my desktop computer in room CERC 278. The data in this computer is stored by data acquisition date and also by the subject of the study. An electronic appendix to this work is provided with a copy of all raw data files to Dr. Steven Rogak.

Data Processing

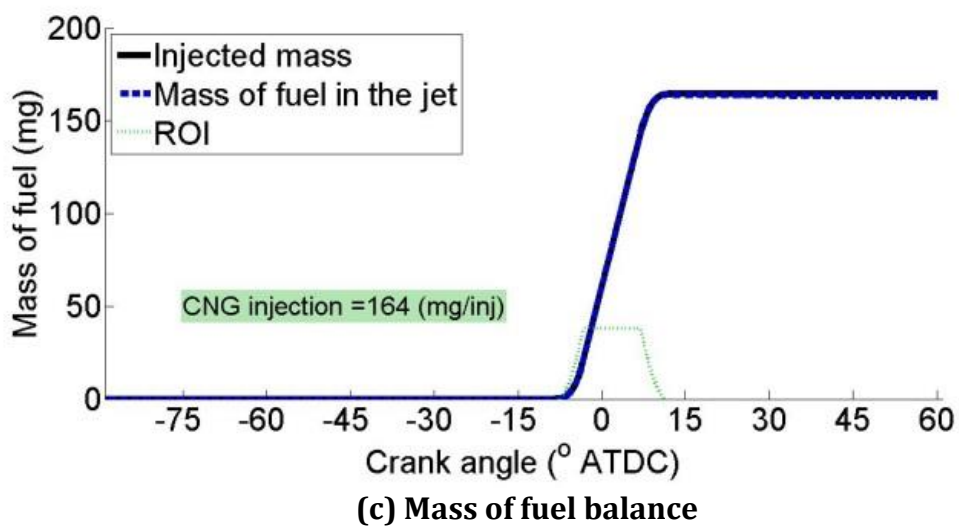
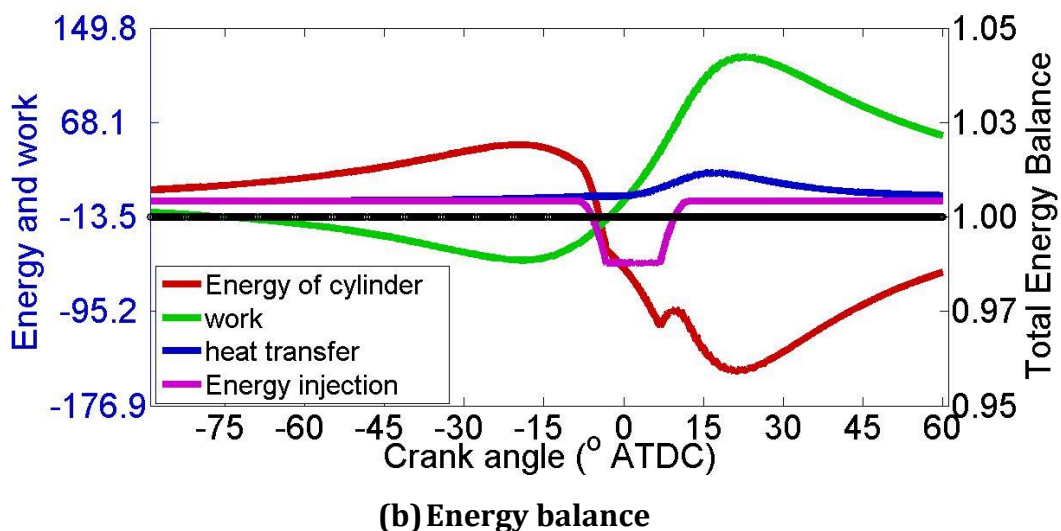
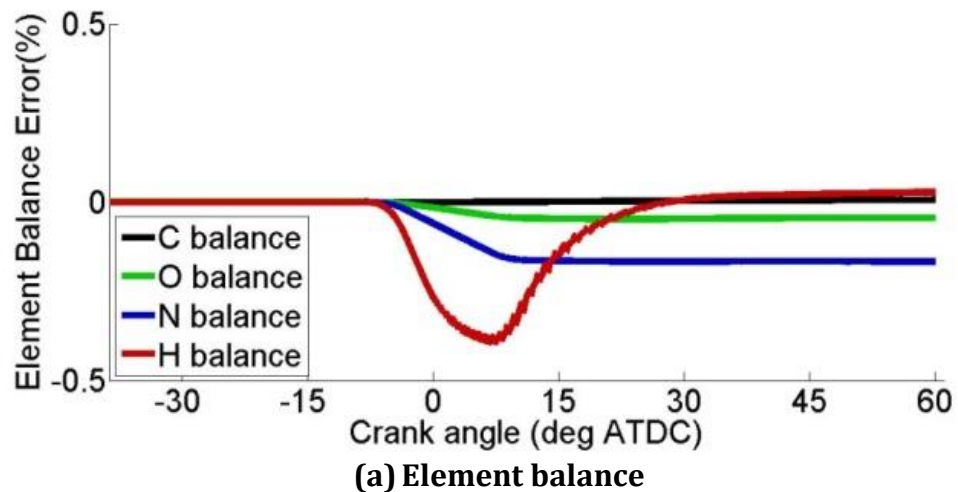
Originally, the data were saved as “fast” collection and “slow” collection in Excel files. Fast data includes in-cylinder pressure, intake manifold pressure, and crank encoder and calculation of AHRR. Slow data includes all the emission and engine power parameters. Each data point includes thousands of measurements and calculations and after years of testing a huge data set will be created. A post processing package has been developed in the current study and has been used in this study and in the other parallel studies [45]. The post processing package includes several scripts. The “DataLoader.m” script loads all the data in the source folder into a Matlab data set. The ignition timing has been calculated using a method described in reference [55], [56]. For the current study, the start of combustion was found as the intercept of the AHRR curve of the combustion event with the zero AHRR axis. This intercept was calculated by finding the slope between 30 kJ/m³/deg and 50 kJ/m³/deg. This script will also pull information from the pressure and AHRR traces from the unprocessed fast files to calculate the ignition timing and save images of that AHRR graphs for the user. The output matrix will be filtered by the criteria set by the user. This will be done in a Matlab file called “PointFinder.m”. A default filter is the permitted range for setting parameter discussed in

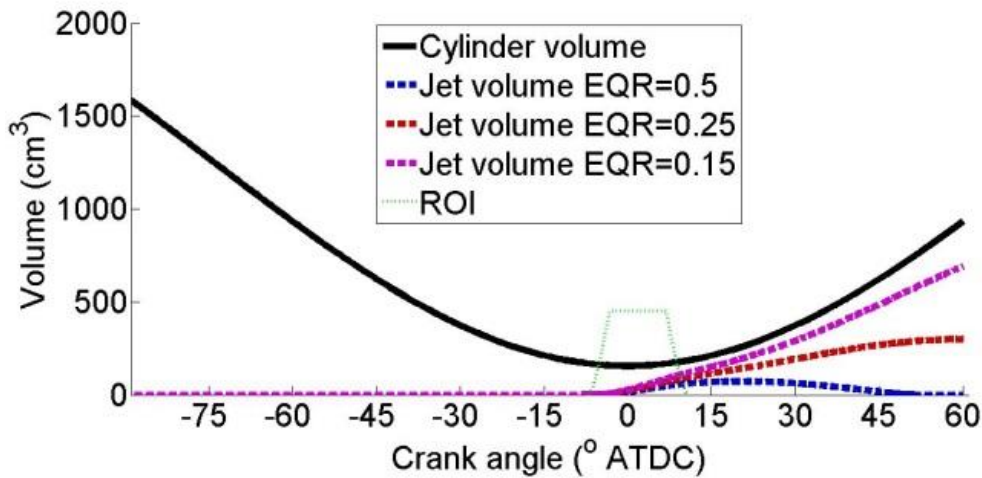
From this point, several other scripts have been used for plotting, variability analysis, cycle-cycle variability, ignition studies, history monitoring etc. Some of these scripts are specifically developed for this study; however, they might be used in future in other studies.

Appendix H: Balances for Engine Simulation

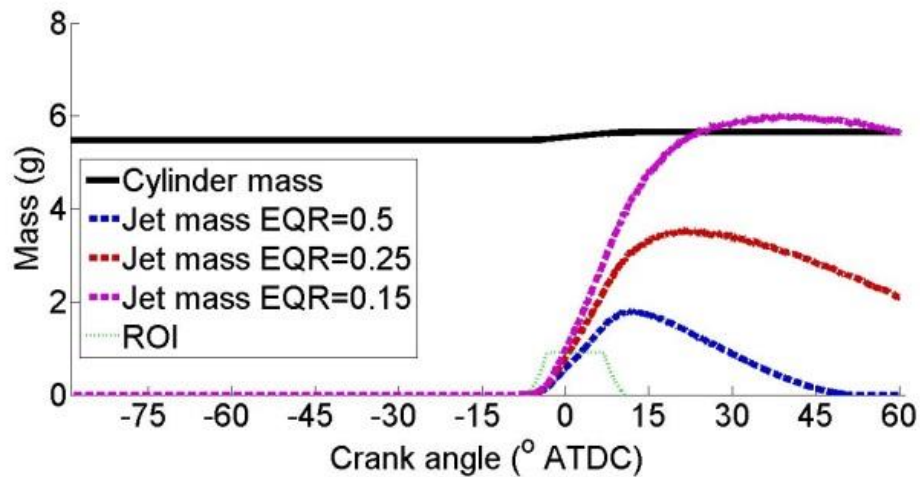
In the current model we solve the jet in the free environment and map it into the cylinder. The balances of elements, species and energy in the cylinder should be satisfied by the model. The results presented here are for mode B75, however, all other cases show the same trend in balances. Figure H-1 (a) shows element balance for simulation of mode B75. Generally the error in the element balance is less than 0.5%; the error in the calculations comes from using the GRI3.0 mechanism with 56 species while in the model we only tracked 7 major species (N_2 , O_2 , CO, CO_2 , H_2O , CH_4 and H_2). While in thermodynamics script we calculated all species mass fractions in the equilibrium calculations, we just counted these 7 major species. The errors in balances are negligible though. The element balances show the same trend for all other cases considered in this paper also.

Energy balance is shown in Figure H-1 (b), while the energies from different sources are shown in the left axis, and the balance is conserved and shown in the right axis. This energy balance is from Equation 3-17 for the cylinder, not the jet. The mass of the fuel in the jet domain compared to the injected fuel mass is shown in Figure H-1 (c). In this graph ROI is the rate of the injection shape; the units are not relevant for ROI. The fuel mass is very close to the injected mass for model B75. Volume and mass of the jet for different boundaries of the jet are compared to the mass or volume of the cylinder. The results are for mode B75 where in this high load the jet has a large volume compared to the other modes. The volume of the jet remains within the volume of the cylinder even for lean mixture boundaries ($EQR=0.15$). The mass of the jet, however, exceeds the mass of the cylinder slightly for lean mixture boundary ($EQR=0.15$). Mass balance of the cylinder is conserved Equation 3-15, and it is independent from the jet mass calculations based on different boundaries. However, this comparison of mass and volume of the jet evaluates the assumptions of the model in using the free jet for cylinder calculations. Although the mass of the jet might exceed the mass of the cylinder, it happens only in very lean mixture values which should not affect the goal of the model in the prediction of AHRR and soot.





(d) Volume of jet vs cylinder



(e) Mass of jet vs cylinder

Figure H-1: Balances for mode B75

Appendix I: Engine-out PM and Peak AHRR Location vs. RIT for all SPC Experiments

The engine-out PM for all the SPC experiments are shown in Figure I-1. For the negative RIT experiments, engine-out PM is not sensitive to engine parameters like EGR, EQR and pilot mass while for positive RIT experiments the engine parameters can change engine-out PM by a factor or eight. All the points in negative RIT cases have peak AHRR after EOI consistent with the conceptual graph of Figure 1-5, despite the differences in combustion and PM formation process of PPCI and SPC.

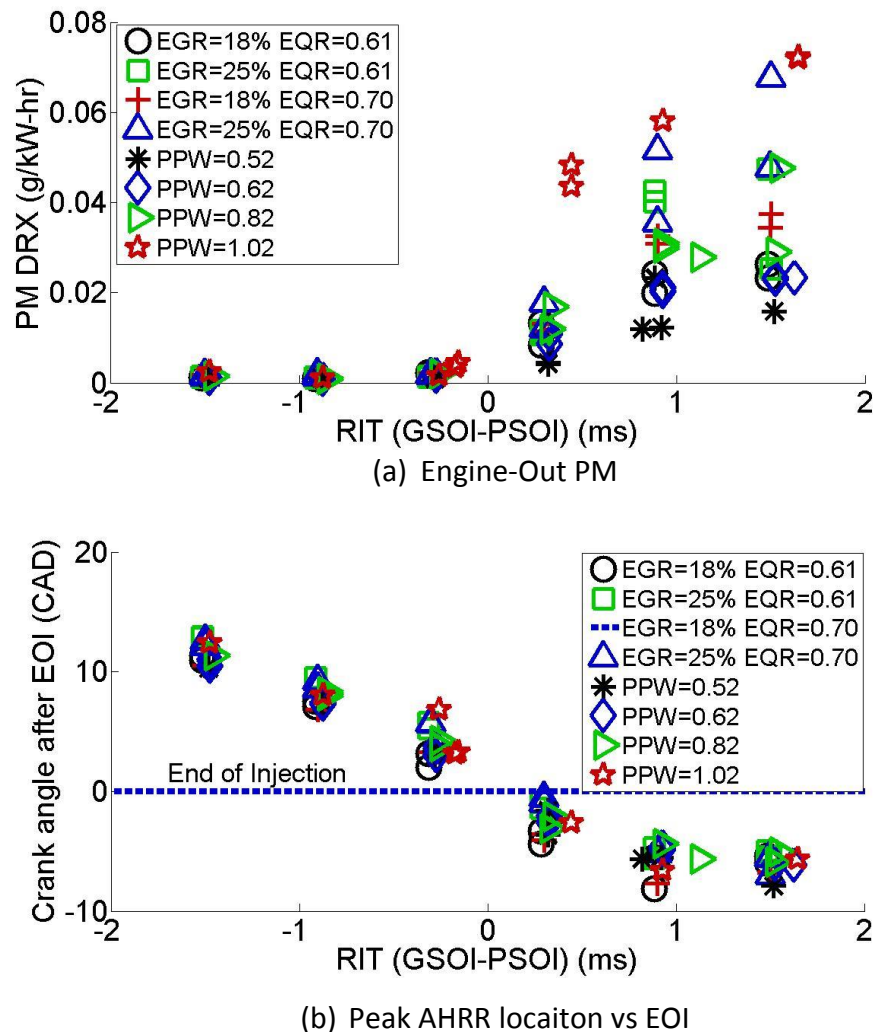


Figure I-1 engine-out PM and peak AHRR location for all the SPC experiments

Appendix J: Particulate Matter Sampling System

In order to measure the particulate (PM) from the exhaust stream, dilution system was used. As illustrated in Figure J-1, a small portion of the raw exhaust from the engine was drawn into the dilution line by a pump and mixed with a clean diluent (compressed air). The dilution ratio was determined by measuring the CO₂ concentration in the exhaust gas, the diluted flow and the compressed air. During the measurement, the dilution ratio varied from 9:1 to 15:1. Furthermore, three-way valve setting was added prior to the Aethalometer measurement to ensure that the particle mass concentration of the sample flow did not surpass the maximum limit of the instrument.

At UBC we have many methods available to measure particulate matter. For measuring total particulate matter mass concentration there are two methods, a tapered element oscillating microbalance (TEOM) and by gravimetric filter analysis. The TEOM collects mass on filter that is mounted on the end of a long tapered cantilever element. The element oscillates at its natural frequency and knowing this frequency and a calibration constant the mass change for a unit time can be calculated. For the gravimetric analysis, filters are pre-weighed before a sample passes through them and post-weighed after collecting the sample. The sample is pulled through the filters with the help of a pump and the flow is measured with a mass flow meter.

For measuring the portion of the particulate that is black carbon (soot) the Aethalometer is used. The Aethalometer uses light to determine the level of black carbon on a filter paper. The light that passes through the dirty filter spot is correlated with the amount of black carbon mass collected on the filter paper.

Particle size distributions can also be determined by using a TSI model 3085 scanning mobility particle sizer (SMPS). This equipment consists of a Differential Mobility Analyzer (DMA) and a condensation particle counter (CPC). The DMA basically sorts particles by size based upon their electrical mobility within an electric field. The DMA scans through different voltages on a center rod to induce an electrical field. Particles with the right electrical mobility pass through a sample slot and are counted in the CPC. After scanning through a number of voltages the result is a size distribution of particles (# of

particles/cm³ versus particle size). The SMPS is capable of measuring particles in the range of approximately 10nm up to 300nm.

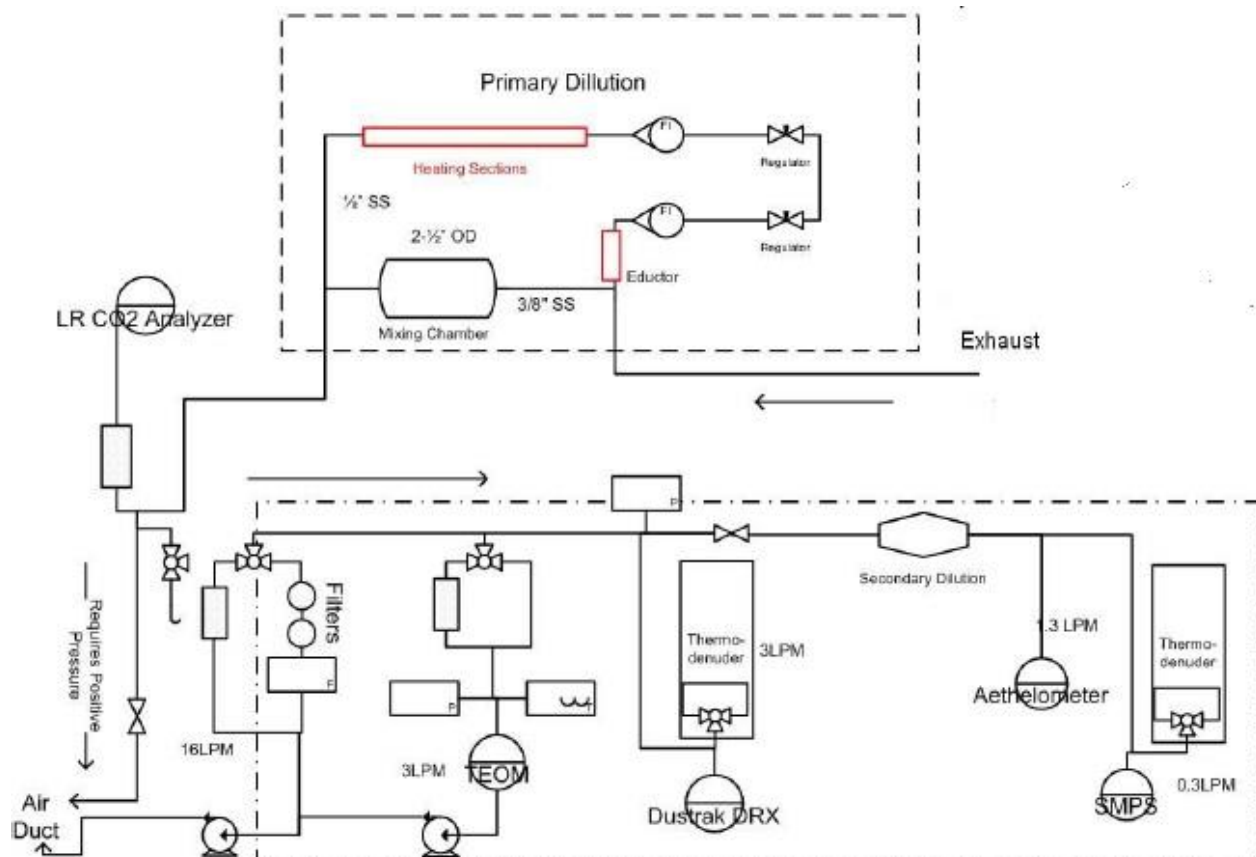
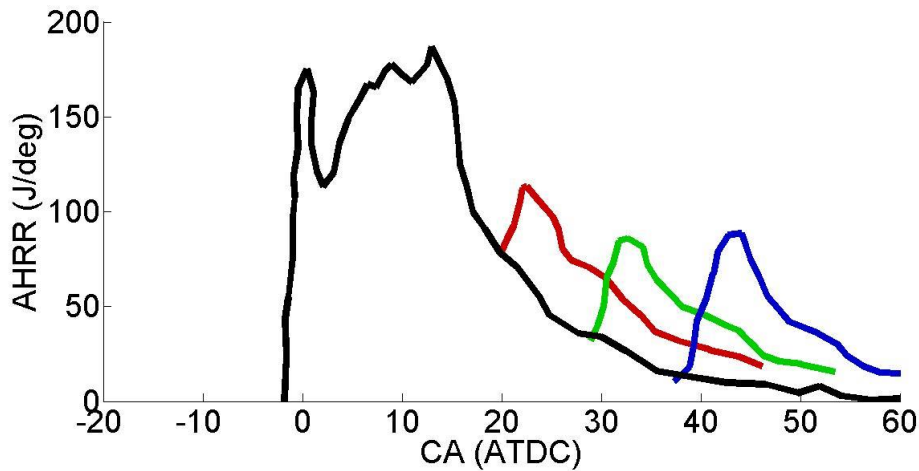


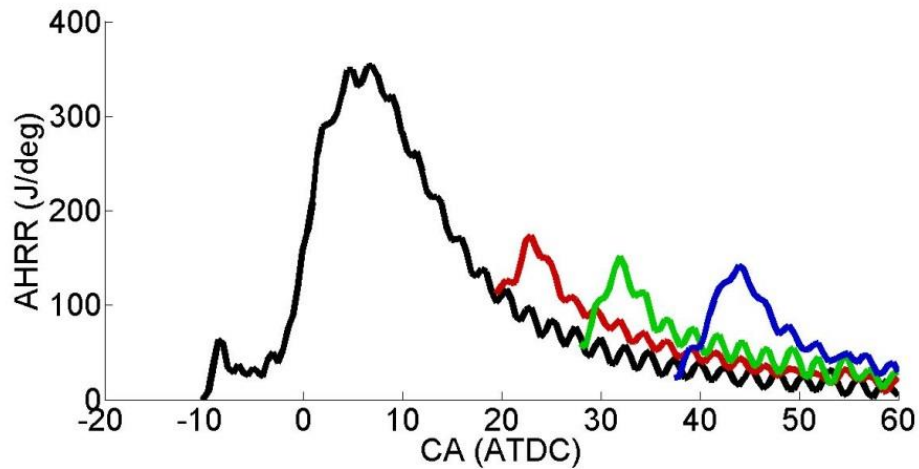
Figure J-1 Particulate sampling system layout

Appendix K: AHRR of Post Injections

Apparent heat release rate (AHRR) of late post injection (LPI) from HPDI is compared to AHRR of diesel engines in Figure K-1. In order to be able to compare the results, start of AHRR of second pulse (SOH2) is defined for both engines by visually inspecting the AHRR graphs. SOH2 of 18, 28 and 38 is shown in Figure K-1 for HPDI and diesel engine. The fraction of fuel in the second pulse (SI) in the diesel engine experiment is 17%, while for HPDI it is 15% of fuel in the second injection. However a 2% difference in mass of fuel injection in the second pulse (SI) should not affect AHRR significantly (see AHRR of LPI in Figure 4-3).



(a) Diesel engine (adapted from [59]) Engine speed=1200 rpm, GIMEP=9-10 bar, GRP=160 Mpa, EGR=55%



(b) HPDI engine, mode B75, Engine speed=1500 rpm, GIMEP=16.6 bar, GRP=25 Mpa, EGR=18%

Figure K-1 Comparison of AHRR between diesel and HPDI engine based on same start of AHRR for second injection

Appendix L: Air Handling Systems of SCRE

Exhaust and EGR System

The exhaust gas recirculation (EGR) system diverts some of the exhaust gas back into the intake air stream. The diverted exhaust gas increases the amount of inert gas in the intake air, which reduces the amount of NO_x produced during combustion. A schematic of the air exchange system is shown in Figure 2-1.

Exhaust gas is routed from the exhaust manifold to a 50-liter surge tank that dampens the pressure fluctuations in the exhaust stream. The surge tank is constructed of 304 stainless steel, hydro-tested to 192 psig, and certified to operate at 45 psig and 1200°F (650°C). Pressure relief is provided by a rupture disk with a 45 psig burst rating at 1000°F. For safety, the rupture discs on both the intake and exhaust surge tanks are plumbed back into the exhaust line in order to contain the rupture disc fragments. Disc check valves are installed after the burst discs to ensure that the large pressure fluctuations from one exploding burst disc will not prematurely trigger the rupture the other disc.

From the surge tank, the exhaust is expelled through three remotely-controlled, high temperature pressure regulators to atmosphere through the muffler on the roof of the building. A wastegate is also installed to provide pressure relief at lower pressures. Currently it is set to open at 28 psig. All samples for emissions and PM testing are taken downstream of the back pressure valves. To withstand high exhaust temperatures, and to ensure accurate engine out emissions measurements the piping from the exhaust port to the surge tank is all 316 stainless steel.

If desired, some of the exhaust can be routed through the EGR loop. The EGR loop is comprised of a water-cooled heat exchanger and a manually-controlled flow control valve. A schematic of the P&ID of the EGR system is shown in Figure L-1.

The piping and components of the EGR system must withstand high temperatures, pressures up to 3 atmospheres, and a corrosive environment. Flexible bellows are installed at some flanged joints to allow for thermal expansion and misalignment of the piping. All

elements must comply with the appropriate pressure vessel and piping code. All the piping was pressure-tested before installation.

Air Intake System

A schematic of the P&ID of the air supply system is shown in Figure L-1. Under naturally aspirated operation, intake air is drawn through a filter. The charge air is routed to a surge tank suspended from the support frame, and then to the engine intake manifold. The charge air surge tank is constructed of carbon steel, hydro-tested to 58 psig, and certified to operate at 45 psig and 250°F (120°C). It also has a rupture disk with a 45 psig burst rating at 250°F. A viewglass and drain are positioned at the bottom of the intake surge tank to drain condensed water from the intake surge tank when EGR is used. At one time over 20L of water needed to be drained from the surge tank in the previous design.

Flexible bellows are installed at some flanged joints to allow for thermal expansion and misalignment of the piping. All elements must comply with the appropriate pressure vessel and piping code. All the pipes were pressure tested before installation. The air system will operate at pressures up to 45 psig (3 bar) and temperatures up to 250°F (121°C).

To provide high boost pressures and air flow rates, an Ingersoll-Rand Rotary Screw Compressor has been installed. The compressor is located the floor above the test cell in the mechanical room 2.79. It is an industrial rotary-screw type compressor capable of delivering the maximum 3 bar boost. The compressor is equipped with filters and a 2.5 kW refrigerated air dryer (dewpoint of -40°C) to deliver clean dry air. Pulsations are damped out by a large upright storage tank located next to the compressor. The air is then filtered (with both standard and coalescing filters) and the pressure is regulated down to the desired line pressure before entering the intake air heater and then the manifold. The air flow-rate is determined by measuring the pressure drop across a custom-designed venturi.

The air is heated with a Wiegand Industrial 6kW, 230VAC - 3 phase immersion heater. The heater power is controlled through a 40hp Baldor inverter drive. The current from the inverter is fed first through a line reactor (with impedance simulating a motor) and then to the heater. The inverter drive is set to quiet constant torque mode and has a maximum current programmed in at 15A. A potentiometer on the top of the main engine control

panel labelled “intake heater control” is used to control the heater current. The air heater was sized to provide a 70 degree increase in temperature of a 200kg/hr air flow. Care must be taken not to turn on the intake air heater unless a sufficient amount of air flow (at least 120kg/hr) is passing through it. The heater inner wall temperature can be read on channel 6 of the temperature monitor on the main engine control panel. This temperature should not exceed 450°C.

After passing through the intake heater the air passes through a three-way valve that passes either naturally aspirated air to the surge tank or boosted air. For EGR testing, exhaust gas is mixed into the charge air upstream of the 3-way valve but after the intake air heater (so that only air passes through the heater and not exhaust gas). The intake air and recirculated exhaust gas then pass through the intake surge tank located on the roof of the test cell before entering the engine through the intake manifold. The P&ID drawings of the air handling system can be seen in Figure L-1.

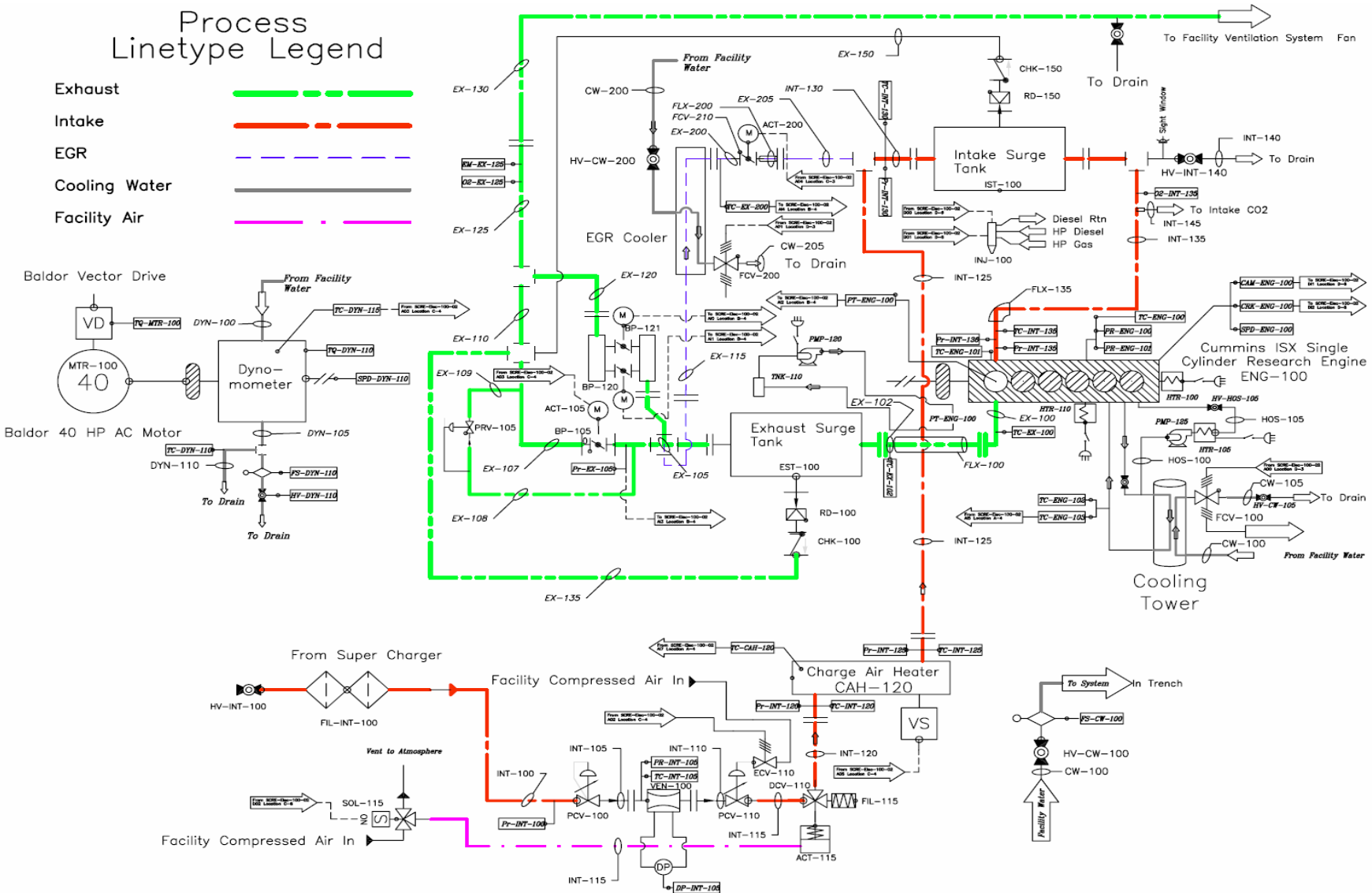


Figure L-1 Air handling, EGR and intake air P&ID drawing of SCRE

Appendix M: HPDI-Fuel Conditioning

The fuel conditioning module (FCM) regulates and monitors the pressure and temperature of the high-pressure diesel and natural gas supplied to the engine. The gas supply pressure is maintained slightly below the diesel supply pressure, preventing natural gas from leaking into the diesel lines via the interstices of the HPDI injector. The HPDI fuel conditioning system design was based on existing systems at Westport. A schematic of the fuel conditioning system is shown in figure M-1. Diesel is drawn from the day-tank through a water-cooled heat exchanger and a mixing valve to control the supply temperature of the fuel. The diesel fuel is first circulated by a Holley diesel priming pump providing approximately 10psi delivery to the inlet of the high pressure pump. The diesel fuel is then pressurized to high pressure by a Bosch diesel pump (Westport part number 10000541), with the pressure being controlled by a manual backpressure regulator. A pressurized accumulator dampens fluctuations in the diesel supply line. A three-way solenoid is installed on the high-pressure diesel supply line. Under normal running operation, the three-way valve is powered and a small amount of high-pressure diesel continually drains. The purpose of this is to relieve some of the flow from going through the back-pressure regulator. When either the "HPDI Operation" switch on the front of the control panel is turned-off or an E-Stop is triggered, power to the three way solenoid is cut and diesel quickly drains out of the system. In the past, the rate at which the diesel drained out of the system was much faster than the rate of gas venting so the problem was that the gas needle of the injector was not held closed by the diesel control pressure and consequently gas entered the engine. To remedy this problem, a needle valve was added to the diesel drain line to reduce the rate of diesel drain and allow the natural gas to drain down before losing diesel control pressure.

The natural gas is supplied at high pressure from a multistage gas screw-type compressor. The natural gas pressure being supplied to the engine is regulated by the diesel fuel pressure through a dome loaded regulator. This compressor can operate continuously for a maximum of 5 hours at which time the mode selection switch needs to be toggled from "auto" to "off" and back to "auto". The maximum supply pressure from the compressor is 5000 psi. The cut-in and cut-out set points are usually set to 4200 and 4800 psi.

A three-way solenoid opens during normal operation to allow gas through to the engine fuelling rail. During shutdown, power to this solenoid is cut and gas is sent directly to vent. The supply line to the engine rail has a check valve so as not to allow back-flow from the engine to the FCM. This was added because of an instance where diesel fuel was leaking past the dummy injector o-ring seals into the gas rail and flooding back into the gas piping lines. This check valve will ensure that diesel does not flow back and enter the gas supply lines.

The high-pressure piping for this system is 316L stainless steel 3/8"x0.049" (ASTM A2131, A269, and ASME SA213) with a working pressure of 4800 psi. All fittings are stainless steel Swagelok and all high-pressure components are rated above 4800 psi. A description of the system components is given on page 20 including some previous experience with each component.

Heat exchanger (HEX-100): Low-pressure (250 psi) one pass shell-in-tube water-cooled heat exchanger to cool the warm diesel line.

Intelli-Faucet mixing valve: Intelli-Faucet for mixing warm and cool diesel lines to maintain diesel inlet temperature, powered by a 12 V supply. This device has modified seals (Viton) to handle diesel.

Fuel filter: A standard Cummins remote dual filter head.

Priming pump: Holley pump providing approximately 10psig delivery to the high pressure pump.

High pressure diesel pump: A Bosch CP3.3 5000 psi diesel pump coupled with a 600V, 1800 rpm, 5hp Hyundai motor. The pump has a direct line to drain for excess flow.

Pressure relief valves: Westport has reported problems with Whitey (Swagelok) valves leaking over time. A Parker valve is used, although Westport reports that the preset is not repeatable after depressurization.

Accumulator: A Hydac 0.6L nitrogen charged bladder accumulator which is sized as the "smallest possible". It is attached to the fuel line with a custom made adapter. The accumulator was charged to 2000 psi for a working pressure of 3600 psi.

Inline diesel filter: For the high-pressure diesel line. It is a 3 micron Hydac inline filter (5000 psi rating). This filter is for high flow and low-pressure drop, and is a large filter so it does not clog quickly.

Inline gas filter: A 2-micron Nu-Pro (Swagelok) inline filter.

Back pressure regulator: Rated for 5000 psi.

Check valves: These are Swagelok and rated at 1/3, 1, and 10 psi. The purpose behind the 10 psi check valve on the diesel drain line is to prevent or reduce cavitation in the injector, which causes "foamy" diesel in the return line. The 1/3 psi check valve on the gas vent is to ensure that there is no gas back flow from the vent line. The 1 psi check on the gas line is to ensure that fuel in the fuel rails does not back flow into the supply. Finally the 1 psi check on the diesel drain line from the back pressure regulator is to allow some of the excess diesel flow to pass through the metering valve rather than all through the back pressure regulator.

Manual 1/4 turn valves: These are Swagelok ball valves and are rated for 5000 psi.

Dial pressure gauge: For both gas and diesel lines. Installed for operator to see the pressure of both fuel lines and to allow manual setting of the regulator.

Pressure transducer: Energy Kinetics Setra 209 type transducers, both gas and diesel lines. 0 - 5000 psi.

Temperature sensor: K-type thermocouple probes in Swagelok fittings.

3-Way solenoid valves: For remote shutdown and venting of the high-pressure diesel and gas. The gas valve is a Circle Seal solenoid due to its superior seals. The diesel valve is Hydac cartridge type valve. Both are "normally open" and rated for 5000 psi.

Metering valves: This a variable orifice valve to slow the diesel line depressurization rate during shut-down so that the gas pressure does not exceed the diesel pressure within the injectors and result in gas leaking into the diesel line. It is made by Hoke and has a 5000 psi pressure rating.

Dome-loaded self-venting regulator: Custom regulator from Go. Original unit replaced/modified after a failure in which one of the diaphragms stuck. Another failure of the regulator occurred in April 2005 and the regulator was once again replaced.

2 Swagelock needle valves: Two needle valves used to control the diesel/gas bias for co-injector operation.

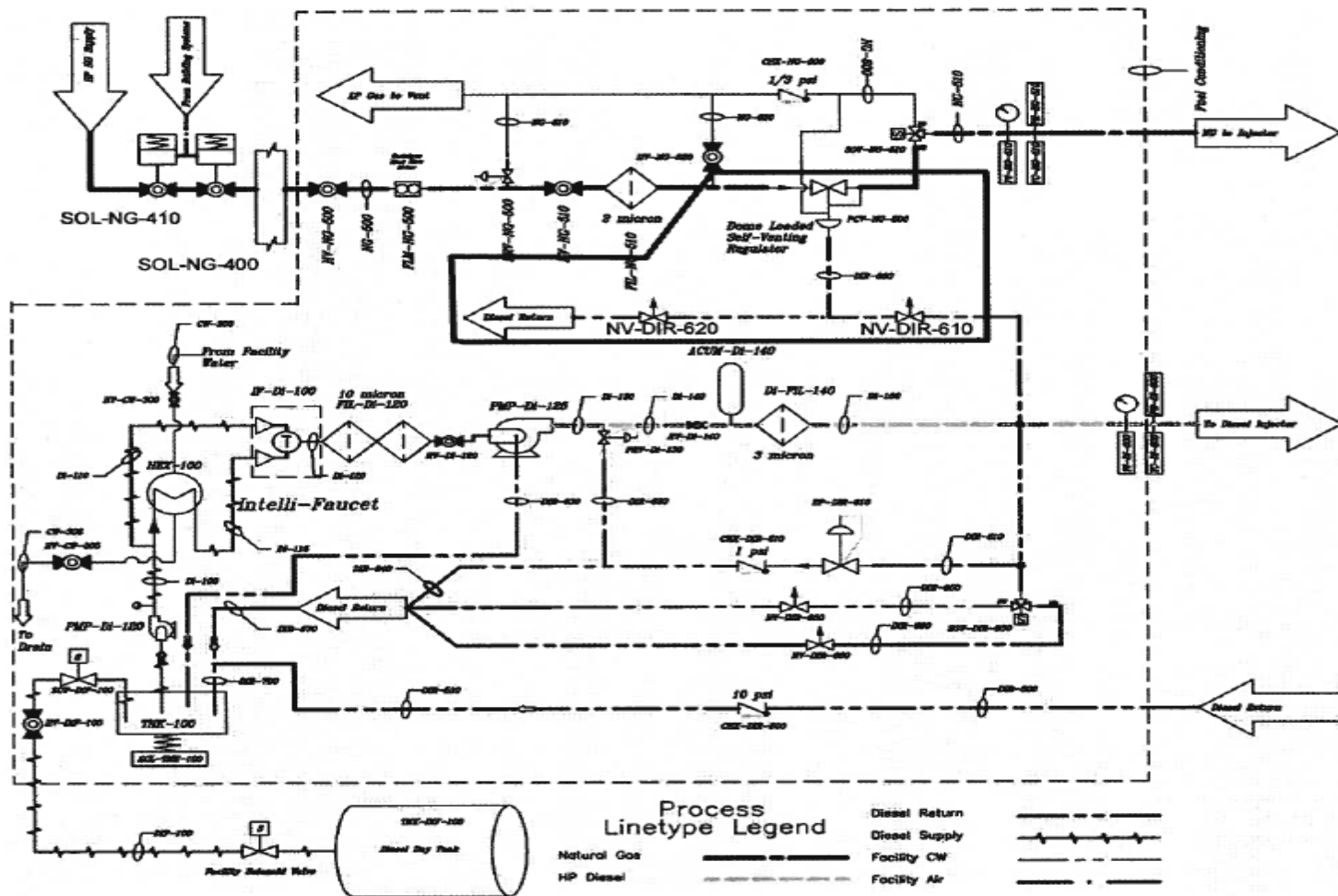


Figure M-1 SCRE fuel conditioning module (FCM)

Appendix N: Emissions Bench

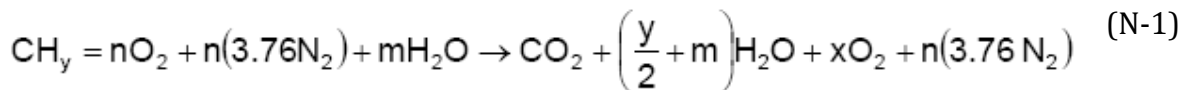
The gaseous emissions (O_2 , CO_2 , CO, CH_4 , uHC, and NOx) measurements are taken downstream of the exhaust surge tank in order to ensure homogeneity in the exhaust stream. The exhaust passes through a heated line and filter to arrive at the AVL Emissions Bench, CEB II, which has limit monitoring and automatic calibration. Inside the emissions bench the exhaust is split into two branches: the wet measurements and the dry measurements. On the wet side (water not removed) the CH_4 , uHC, and NOx concentrations are measured. All other gases are measured as on the dry side. All emissions are measured according to SAE vehicle exhaust measurement standards (SAE 1993, 1995). Table N-1 lists the span gas concentrations used for calibration of each analyzer each day.

Table N-1 Span gas concentrations used for calibration of the AVL bench

	Low	High		Low	High
THC (ppm)	269	1288	COM (%)	2109	
CH4 (ppm)	498	3900	COH (%)	8.01	
NOx (ppm)	501	2400	CO2 (%)	4.5	13
NO (ppm)	483	2572	O2 (%)	20.91	
			INTCO2 (%)	4.5	

The uHC and CH_4 are measured using a Flame Ionizing Detector (FID). In the emissions bench used in 2006, only the uHC was measured in this fashion. A hydrogen flame inside a constant electric field ionizes organic carbon to produce a current proportional to the amount of carbon present. A portion of the sample is passed through a thermochemical converter which converts all non-methane hydrocarbons to CO_2 and water. The CH_4

concentration is measured through a second FID. The resulting currents are compared against the reference span gases of methane, and propane. During postprocessing, the propane-equivalent measurement of the uHC is converted to a methane equivalent measurement by dividing by 3 (the carbon number ratio for propane to methane). The NOx is measured using a chemiluminescent detector (CLD) which measures the light intensity of NO burning with ozone. To measure the NOx concentration, NO₂ is first reduced NO using a thermo-catalytic converter. During the oxidation process, light is generated between 600 and 1200 nm. Low absolute pressures are used to increase the probability of producing light and reduce the cross sensitivity from other components. The NOx is multiplied by the K-NOx correction factor which is used since the amount of NO formed in combustion is dependent on the humidity of the inlet air (SAE International 1995). The remaining constituents need to be measured with the water removed. The amount of water in the exhaust (used for calculating the “wet” concentrations of O₂, CO₂, CO) is calculated assuming complete combustion of the fuel in air, minus the uHC, which is usually negligible. The following approach can then be used in converting the dry measurements to wet measurements (SAE 1995), starting with the stoichiometry,



In this equation, the variables y, n, and m, and x represent the atomic hydrogen-to-carbon ratio of the gas/diesel injection, the moles of oxygen in air to the engine, the moles of water in the combustion air, and the moles of excess oxygen (SAE 1995).

$$W = \frac{0.5y + (7.63 \times 10^3 h)n - 2tHC_{C1}}{(4.76 + 7.63 \times 10^3 h)n + 0.25y} \quad (N-2)$$

In this equation, h is the specific humidity expressed in terms of gH₂O/kg dry air. The conversion factor (CF) to convert the dry values is therefore CF = 1-W.

Oxygen concentrations are measured using the paramagnetic properties of the gas (O₂ becomes magnetized when under an external magnetic field). The instrument consists of an oxygen free gas enclosed in a dumbbell shaped body under a non-uniform magnetic

field. The oxygen will migrate towards the magnetic field at one side of the dumbbell and the resulting higher pressure will cause the dumbbell to rotate. The voltage needed to keep the dumbbell horizontal is proportional to the oxygen concentration (ABB Automation 2001). The interference factor can be calculated by Equation 3.4 (SAE 1993).

$$\text{Interference} = 28.8 \times \% \text{NO} \times 0.01 + 0.623 \times \% \text{CO} \times 0.01 \quad (\text{N-3})$$

Although other gases such as CO₂ and CO are weakly paramagnetic, and NOx are diamagnetic (repelled by a magnetic field), the interference for the worst case (high CO₂ low NOx) for this study was less than 0.03% (SAE 1993). CO and CO₂ are measured with Non-Dispersive Infrared absorption (NDIR) instrumentation. Non-elemental gases will absorb discrete bands of infrared energy. The frequency of light absorbed depends directly on the type of gas. A light emitter of known frequencies and amplitudes goes through the sample gas and light is absorbed. Constant pressure columns of the reference gases are located at the other end which converts light absorption into volume change of a diaphragm (ABB Automation 2000).

Appendix O: Injector-Injector Variations

Injectors in direct-injection engines are a key part of the fuelling system. The current report is the first report on injector-injector variability. Five injectors (same model) have been tested on SCRE for difference load, speed and EGR level in the first block of testing, among these five injectors four of them were selected for the second block of testing. The full result of these two test blocks were reported to Westport Innovations Inc. in October 2014. The new injection strategies, Late Post Injection (LPI) and Slightly Premixed Combustion (SPC), were a focus of this study as well. The results show that the injector to injector variation contributes to emission and engine performance. Here we focus on the output of the results and the effect on injector-injector variability on injection strategies identified in the current study.

Injectors

Five injectors from same model have been used in this study listed in the following table.

The injectors are named by baseline injector, Inj-1, Inj-2, Inj-3 and Inj-4. Among the injectors, Inj-3 has higher gas mass flow rate compared to the other injectors.

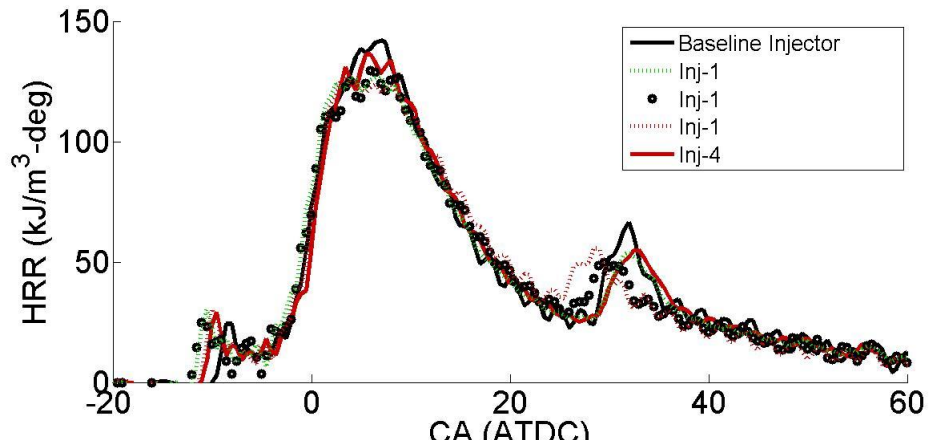
After some preliminary studies internally submitted to Westport Innovations Inc., four injectors were selected for the second block of testing. The injector Inj-4 was removed from the second block since it had similar characteristics as injector Inj-1.

Heat Release rate comparison of LPI points (from first test block)

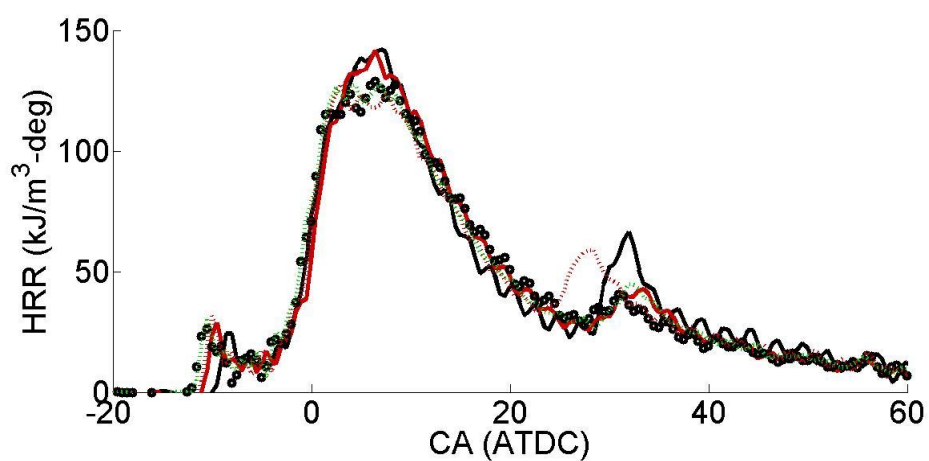
When you set LPI based on mass, the magnitude of the second peaks are very close, although the timing of second pulse is different since GPW for each injector is different too (especially for Inj-3). The high mass flow injector (Inj-3) second pulse is closer to TDC because the first pulse is shorter.

When we set LPI based on 2GPW (here all the HRR are chosen based on closest 2GPW to 0.6ms), the magnitude of second peak is different for each injector. Most of the injectors

have lower second peak which means less effective post injection compared to baseline injector.



LPI mass based



LPI 2GPW based (closest to 0.6ms chosen)

Figure 0-1: HRR comparison for five injectors

Test Matrix of the second test block

The test matrix of the second block is included here; it has been repeated for four injectors. The test matrix and the results of first block of testing was reported to Westport on October 2014.

In this test matrix:

Method A (traditional method): This method was set the point by traditional method of setting the points in SCRE experiments (RPM, GIMEP, 50% IHR, PSEP, GSEP, EQR, EGR, GRP and PPW). For the second pulses GPW2 and GSOI2 are kept constant for all the injectors; 0.6 ms and 20° ATDC respectively. This will lead to different mass of fuel in the second pulse and GSEP, since GPW-mass flow rate characteristic graph of the injectors are slightly different. Method A was designed to show the performance of each injector separately if the best point of one injector, here baseline injector, was used for all the injectors.

Method B (match timing and airflow): This method was set the points with matching timings (PSOI, GSOL, PPW, GPW, 2GSOI, 2GPW) and intake airflow (by adjusting MAP and constant EGR) with baseline injector.

For LPI points we set 2GPW and 2GSOI constant for all the injectors.

Diesel PPW was set to 0.55 ms; it is the minimum PPW could be set in SCRE. Lower PPW resulted in higher combustion instabilities. Engine speed was set to RPM=1493 RPM.

Some of the values in the test matrix depend on the values of the Baseline-A for baseline injector. The air flow of the baseline-A for baseline injector was 205 kg/hr, gas pulse width (GPW) of 1.75 ms and CA50 of 11° ATDC.

The baseline EGR is set to 20% to match the preliminary LPI/SPC tests are multi-cylinder engine (MCE) at Westport. Therefore the best points have slightly different performance especially for SPC points.

Table O-2 Test matrix of the experiments

SCRE-MCE Matching Method			Experiment Code	Injectors	GIMEP	GRP	EQR	Airflow rate (kg/hr)	EGR	CA50	PSEP	GPW2 (or F1)	GSEP
Traditional		Baseline	Baseline-A	Baseline Injector, Inj-1, Inj-2, Inj-3, Inj-4	16.6	25.4	0.61	Not set	18	11.0	0.3	single injection	0
Match timing and air flow with Baseline Injector		Baseline	Baseline-B	Inj-1, Inj-2, Inj-3	Not set, GPW= Baseline-A for Baseline Injector	25.4	No set	Airflow= Baseline-A for Baseline Injector	18	Not set, GSOI= Baseline-A for Baseline Injector, PSOI= Baseline-A for Baseline Injector	No set	single injection	0
Traditional but 2GPW is same for all injectors	LPI	LPI-AA	Baseline	Baseline Injector, Inj-1, Inj-2, Inj-3	16.6	25.4	0.61	Not set	18	Not set, GSOI= Baseline-A for Baseline Injector, PSOI= Baseline-A for Baseline Injector	No set	2GPW=0.60	2GSOI =20
Match timing and air flow with Baseline Injector, keep 2GPW same for all injectors	LPI	LPI-B	LPI-AA	Inj-1, Inj-2, Inj-3	Not set, GPW= LPI-AA for Baseline Injector	25.4	No set	Airflow= LPI-AA for Baseline Injector	18	Not set, GSOI= Baseline-A for Baseline Injector, PSOI= Baseline-A for Baseline Injector	No set	2GPW=0.60	2GSOI =20
Traditional	SPC	SPC-A	Baseline	Baseline Injector, Inj-1, Inj-2, Inj-3	16.6	25.4	0.70	Not set	25	11.0	-0.9	single injection	0
Match timing and air flow with Baseline Injector	SPC	SPC-B	SPC-A	Inj-1, Inj-2, Inj-3	Not set, GPW= SPC-A for Baseline Injector	25.4	No set	Airflow= SPC-A for Baseline Injector	25	Not set, GSOI= SPC-A for Baseline Injector, PSOI= SPC-A for Baseline Injector	No set	single injection	0

Apparent Heat Release graphs

Figure 0-2 shows the AHRR of baseline, LPI and SPC points of the different injectors set by method A and method B.

Heat release rate shape of all the injectors are close together for baseline mode, however the shape of HRR at top is noticeably different. This difference in heat release rate shape implies difference in burning rate, since for both methods of setting the points similar trend was noticed, therefore it is less likely to be the effect of setting the point. This difference in burning rate is likely related to fuel rate shape of each injectors and difference in opening and closing of the needle.

For the LPI points, the heat release of the second pulse is not significant for Inj-2 and Inj-1 compared to the Baseline Injector.

The peak AHRR of SPC-A is lower for Inj-2 compared to the other injectors. When the timing is modified in SPC-B points, all the injectors have similar peak AHRR; however, the timing of the combustion is different between the injectors.

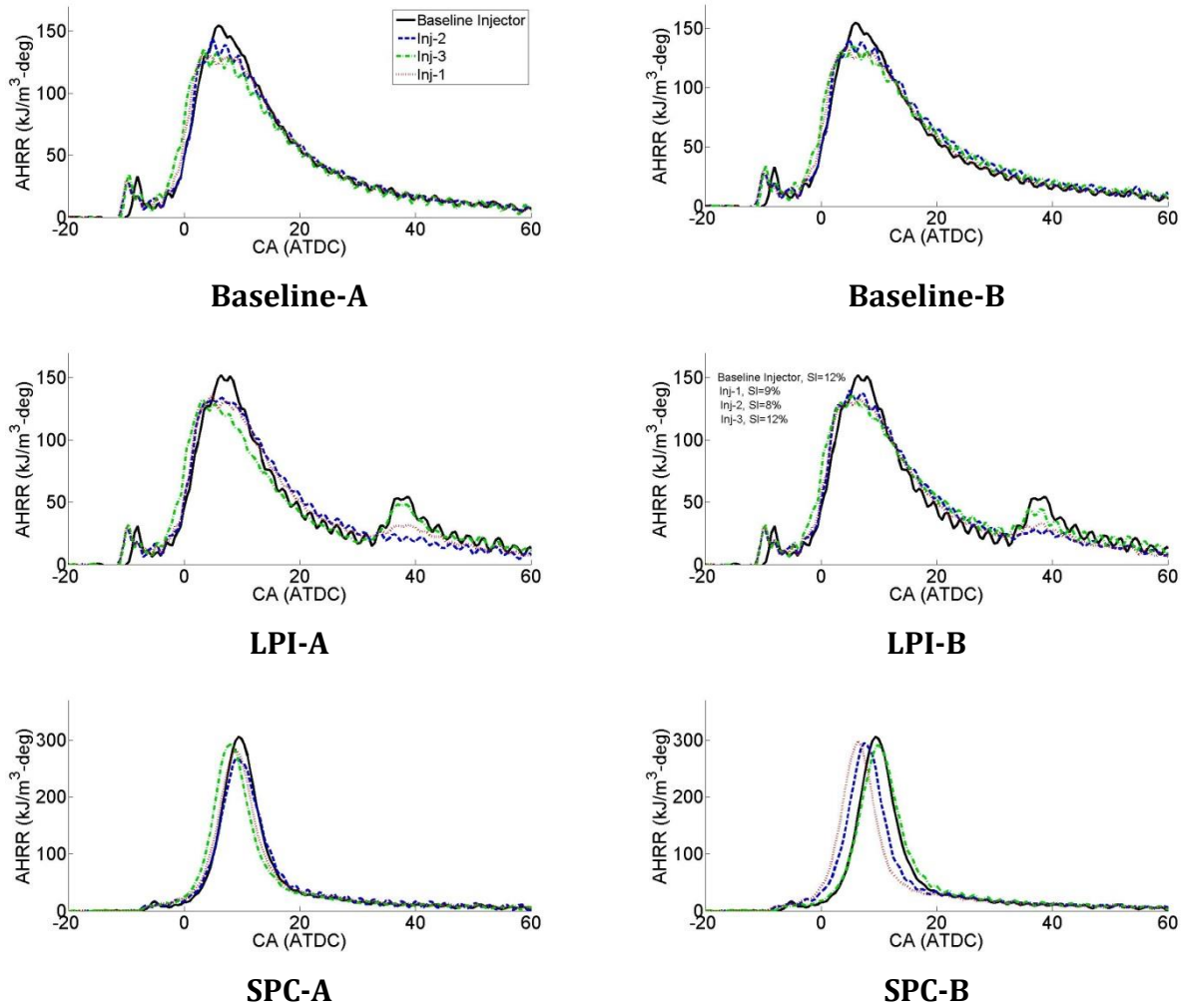


Figure O-2: AHRR of four injectors for baseline, LPI and SPC

LPI Multi-injector tests

When setting with method A, PM level of two injectors (Inj-2 and Inj-3) are about three times higher than the Baseline Injector. The average PM measurement of DRX is 28 mg/kW-hr; with high injector-injector variability of 15 mg/kW-hr. Other emissions and engine performances show much lower variability between the injectors. The study of why these injectors have different PM mass is outside the scope of this thesis.

If the baseline is set by method B, some of the injectors which have higher GPW compared to method A, e.g. Inj-3, will generate much higher PM when all the injectors are commanded with the same GPW. The engine-out PM of Inj-3 is about seven times higher

than the default injector, which part of that is due to higher PM of the injector at mode B75, and part of that is due to higher EQR and GIMEP of this injector compared to the other injectors. The EQR of Inj-3 for baseline-B point is 0.11 higher and GIMEP is about 1.0 bar higher than the default injector.

For the LPI-A points, the PM reduction is 20-75% variable between the injectors compared to their baseline-A values. Lowest PM reduction belongs to Inj-2 injector where the heat release of the second pulse is not evident in AHRR graph, plotted in figure 0-2, Appendix 0. The SI is estimated to be less than 8% for Inj-2 injector (based on removing the second pulse and measuring the NG flow in the first pulse).

The average PM reduction of LPI points for all the injectors are 50% compared to their average baseline value (LPI-A compared to baseline-A and LPI-B compared to baseline-B). Methane emission is about 30% lower based on both methods of setting the points. GISFC is about 1% higher on average, based on both methods. NOx, COV of maximum in-cylinder pressure and maximum cylinder pressure gradient will remain almost unchanged based on the average of the four injectors.

The results suggest that LPI might be slightly less effective in term of PM reduction in a production engine due to injector-injector variability (average of 50% PM reduction compared to 75% for the best injector). Rest of the emissions and engine performance are consistent with the UBC default injector.

Table 0-3 Emission and injector performance of baseline B75 and LPI point for different injector¹⁸.

Point	Injector	PM DRX (mg/kW-hr)	NOx (g/kW-hr)	CH ₄ (g/kW-hr)	GISFC (g/kW-hr)	COV of P _{max} (-)	dP/dθ _{max} (bar/deg)
Baseline-A	Baseline Injector	13±2	1.20±0.04	0.48±0.02	175.2±0.1	1.0±0.2	4.4±0.1
	Inj-2	41±13	1.12±0.04	0.41±0.03	177.6±1.9	0.8±0.0	4.6±0.1
	Inj-3	42±18	1.40±0.17	0.47±0.09	178.7±2.1	0.7±0.0	4.8±0.1
	Inj-1	17±0.6	1.27±0.04	0.41±0.01	174.5±0.1	0.7±0.1	4.6±0.1
Average Baseline-A	All	28±15	1.25±0.14	0.44±0.04	176.5±2.1	0.8±0.2	4.6±0.2
Baseline-B	Baseline Injector	13±2	1.21±0.04	0.48±0.02	175.2±0.1	1.0±0.2	4.4±0.1
	Inj-2	61±20	0.94±0.07	0.43±0.08	180.9±0.6	0.7±0.1	4.5±0.1
	Inj-3	93±14	0.97±0.01	0.52±0.05	187.1±0.3	0.7±0.0	4.7±0.2
	Inj-1	17±0.6	1.35±0.04	0.41±0.01	174.5±0.1	0.6±0.1	4.6±0.1
Average Baseline-B	All	46±40	1.12±0.21	0.46±0.06	179.4±6.3	0.8±0.2	4.4±0.2
LPI-A	Baseline Injector	3±0.5	1.11±0.01	0.38±0.01	178.9±1.5	1.0±0.0	4.2±0.1
	Inj-2	32±2	1.17±0.07	0.31±0.02	178.1±1.1	0.8±0.2	4.3±0.2
	Inj-3	9±2	1.40±0.09	0.24±0.01	180.8±1.1	0.6±0.0	4.7±0.1
	Inj-1	12±0.5	1.17±0.04	0.35±0.03	177.0±2.2	0.7±0.1	4.4±0.1
Average LPI-A	All	14±15	1.21±0.15	0.32±0.07	178.7±1.9	0.8±0.2	4.4±0.3
LPI-B	Baseline Injector	3±0.5	1.11±0.01	0.38±0.01	178.9±1.4	1.0±0.2	4.2±0.1
	Inj-2	28±4	1.13±0.07	0.28±0.01	178.4±1.4	0.6±0.1	4.6±0.2
	Inj-3	49±3	0.85±0.04	0.20±0.02	190.1±0.7	0.7±0.0	4.7±0.1
	Inj-1	9±0.6	1.34±0.04	0.36±0.01	174.4±0.1	0.7±0.0	4.5±0.1
Average LPI-B	All	22±23	1.11±0.25	0.31±0.09	180.5±7.8	0.8±0.2	4.5±0.3

¹⁸ The measurements in this table are reported as Average of two repeats± (maximum-minimum)/2 for each injector based on two measurements. The average of all injectors are reported as Average of all injectors± (maximum-minimum)/2

SPC Multi-injector tests

Similar to the multi-injector results in chapter 4, four injectors (Baseline Injector, Inj-1, Inj-2 and Inj-3) were selected for multi-injector tests. Baseline Injector is the default UBC-SCRE injector; all the graphs in the current thesis are based on this injector's results except multi-injector tests. One of the injectors Inj-3 has higher mass flow rate.

The variability of the injectors in baseline-A and baseline-B points are discussed in chapter 4.

For the SPC-A and SPC-B points, the PM reduction is 75-88% variable between the injectors compared to their baseline values. Lowest PM reduction belongs to Inj-2 injector where the maximum heat release rate is lower in AHRR graph, plotted in figure 0-2. This injector might have different injection timing compared to Baseline Injector, so the PSEP values selected for SPC of Baseline Injector might not mean same premixing level for Inj-2 too.

The average PM reduction of SPC points for all the injectors are about 75% compared to their average baseline value (SPC-A compared to baseline-A and SPC-B compared to baseline-B). Methane emission is about the same on both methods of setting the points and compared to their baseline values. Fuel economy is 2-3% better on average, based on both methods compared to their baseline values. NOx is slightly lower when method B is used, since the EQR and GIMEP of Inj-3 is higher than other injectors. COV of maximum in-cylinder pressure and maximum cylinder pressure gradient for SPC points compared to the baseline B75 point will remain similar to the baseline injector.

The results suggest that SPC strategy is less depend on injector-injector variability compared to LPI strategy. It might be because SPC is based on more premixing so mixing-controlled combustion is less effective for SPC strategy. On the other hand engine air handling differences among the cylinders might be more effective here.

Table 0-4 Emission and injector performance of baseline B75 and SPC point for different injector¹⁹.

Point	Injector	PM (mg/kW-hr)	NOx (g/kW-hr)	CH ₄ (g/kW-hr)	GISFC (g/kW-hr)	COV of P _{max} (-)	dP/dθ _{max} (bar/deg)
Baseline-A	Baseline Injector	13±2	1.20±0.04	0.48±0.02	175.2±0.1	1.0±0.2	4.4±0.1
	Inj-2	41±13	1.12±0.04	0.41±0.03	177.6±1.9	0.8±0.0	4.6±0.1
	Inj-3	42±18	1.40±0.17	0.47±0.09	178.7±2.1	0.7±0.0	4.8±0.1
	Inj-1	17±0.6	1.27±0.04	0.41±0.01	174.5±0.1	0.7±0.1	4.6±0.1
Average Baseline-A	All	28±15	1.25±0.14	0.44±0.04	176.5±2.1	0.8±0.2	4.6±0.2
Baseline-B	Baseline Injector	13±2	1.21±0.04	0.48±0.02	175.2±0.1	1.0±0.2	4.4±0.1
	Inj-2	61±20	0.94±0.07	0.43±0.08	180.9±0.6	0.7±0.1	4.5±0.1
	Inj-3	93±14	0.97±0.01	0.52±0.05	187.1±0.3	0.7±0.0	4.7±0.2
	Inj-1	17±0.6	1.35±0.04	0.41±0.01	174.5±0.1	0.6±0.1	4.6±0.1
Average Baseline-B	All	46±40	1.12±0.21	0.46±0.06	179.4±6.3	0.8±0.2	4.4±0.2
SPC-A	Baseline Injector	2±0.1	1.25±0.05	0.56±0.01	168.6±0.6	3.0±0.0	8.4±0.6
	Inj-2	10±0.8	1.16±0.03	0.41±0.02	174.1±0.5	3.8±1.2	7.7±0.5
	Inj-3	5±0.4	1.39±0.05	0.53±0.04	172.9±1.3	3.1±0.4	8.8±0.6
	Inj-1	9±2	1.11±0.10	0.42±0.01	172.5±0.9	2.7±0.1	8.1±0.1
Average SPC-A	All	7±4	1.22±0.14	0.48±0.06	172.0±2.3	3.2±0.6	8.3±0.6
SPC-B	Baseline Injector	2±0.1	1.25±0.05	0.51±0.01	168.6±0.6	3.0±0.0	8.4±0.6
	Inj-2	10±0.4	1.29±0.13	0.40±0.01	172.6±0.5	2.7±0.1	9.3±0.1
	Inj-3	15±3	0.73±0.01	0.54±0.01	184.1±0.8	4.9±0.4	7.6±0.1
	Inj-1	3±0.3	1.72±0.07	0.40±0.01	168.1±0.6	2.3±0.4	10±0.1
Average SPC-B	All	10±4	0.99±0.54	0.46±0.07	173.4±8.0	3.2±1.3	8.3±1.2

¹⁹ The measurements in this table are reported as Average of two repeats± (maximum-minimum)/2 for each injector based on two measurements. The average of all injectors are reported as Average of all injectors± (maximum-minimum)/2

Appendix P: TSM Simulation of the Effect of Ramp-up/down of the Injection on Engine-out PM

The effect of ramp-up/down of the injection on engine-out PM was studied. The baseline B75 was simulated with assumed same ignition timing for all the cases. Three cases were considered with ramp-up/down (equal ramp-up and ramp-down for each case) of 0.4 ms, 0.6 ms and 0.8 ms. The results showed that engine-out PM is decreasing by faster opening/closing of the injector; however this effect is not significant. The results shows 15% reduction in engine-out PM for reducing ramp-up/down from 0.8 ms to 0.4 ms.

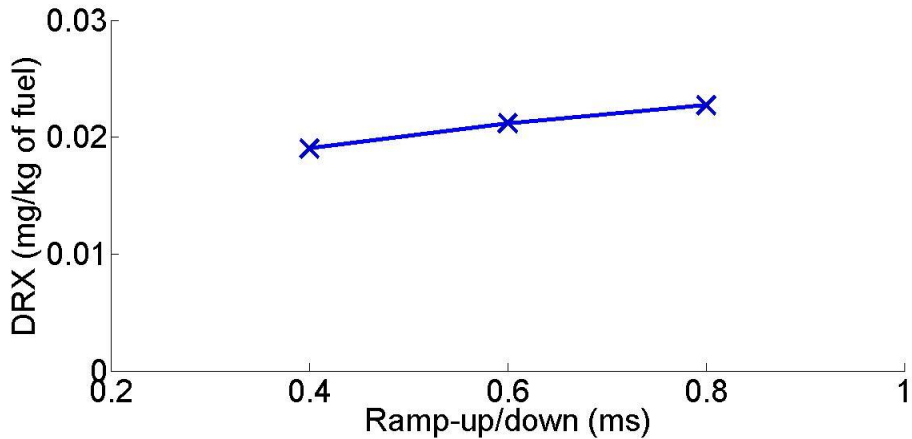


Figure P-1 Effect of ramp-up/down of the injection on engine-out PM

Appendix Q: Injection Timings for LPI Experiments

The injection timings of single injection and LPI (GSEP=2.0 ms, SI=15%) are shown in the Table Q-1. The experimental design parameters are listed in the Table 4-2.

Table Q-1 Summary of the multi-mode injection timings²⁰

Mode	Inj. Type	PSOI (°ATDC)	PPW (ms)	GSOI (°ATDC)	GPW (ms)	GSOI2 (°ATDC)	GPW2 (ms)
A75	S	-13±0.0	0.565±0.02	-5.5±0.0	1.90±0.01	-	-
	LPI	-13±0.0	0.565±0.02	-5.5±0.0	1.60±0.02	22.7±2.0	0.66±0.06
B75	S	-23±0.0	0.62±0.00	-15±0.0	1.81±0.01	-	-
	LPI	-23±0.0	0.62±0.00	-15±0.0	1.50±0.02	16.5±0.0	0.55±0.00
C75	S	-30±0.0	0.53±0.02	-19.5±0.0	1.54±0.02	-	-
	LPI	-30±0.0	0.53±0.02	-19.5±0.0	1.25±0.01	13.2±1.8	0.47±0.03
B87	S	-18.5±0.0	0.62±0.00	-11±0.0	1.95±0.05	-	-
	LPI	-18.5±0.0	0.62±0.00	-11±0.0	1.62±0.04	21.3±1.0	0.59±0.02

The injection timings of LPI points (SI=15%) are shown in the table Q-2. The experimental design parameters are listed in the Table 4-1.

²⁰ The measurements in this table are reported as Average ± (maximum-minimum)/2

Table Q-2 Summary of the GSEP sweep changes²¹

Mode	PSOI (^°ATDC)	PPW (ms)	GSOI (^°ATDC)	GPW (ms)	GSOI2 (^°ATDC)	GPW2 (ms)
Basleine	-22.5±0.5	0.62±0.0	-14.5±0.5	1.72±0.02	-	-
GSEP=1.0 ms	-23±0.0	0.62±0.0	-15±0.0	1.46±0.0	7.0±0.0	0.76±0.06
GSEP=1.5 ms	-23±0.0	0.62±0.0	-15±0.0	1.46±0.0	11.5±0.0	0.81±0.01
GSEP=2.0 ms	-23±0.0	0.62±0.0	-15±0.0	1.46±0.0	15.9±0.1	0.68±0.02
GSEP=2.5 ms	-23±0.0	0.62±0.0	-15±0.0	1.46±0.0	20.4±0.1	0.57±0.01
GSEP=3.0 ms	-23±0.0	0.62±0.0	-15±0.0	1.46±0.0	24.8±0.1	0.60±0.00
GSEP=3.5 ms	-23±0.0	0.62±0.0	-15±0.0	1.46±0.0	29.3±0.1	0.68±0.01

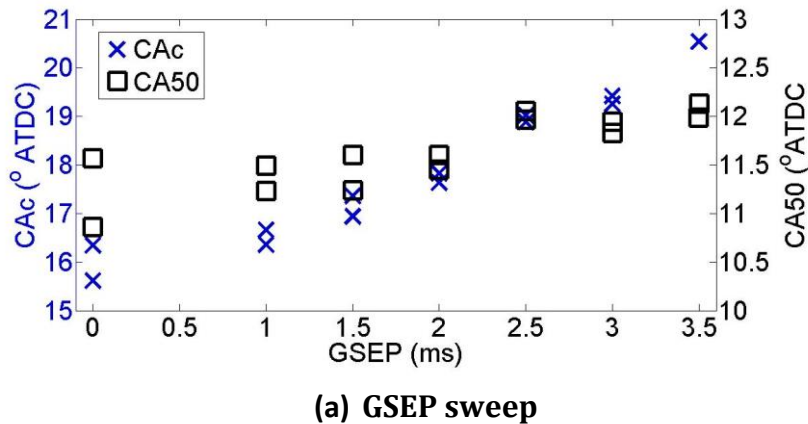
The injection timings of LPI points (GSEP=2.0 ms) are shown in the table Q-3. The experimental design parameters are listed in the table 4-1.

²¹ The measurements in this table are reported as Average ± (maximum-minimum)/2

Table Q-3 Summary of the GSEP sweep changes²²

Mode	PSOI (°ATDC)	PPW (ms)	GSOI (°ATDC)	GPW (ms)	GSOI2 (°ATDC)	GPW2 (ms)
Basleine	-23.0±0.0	0.62±0.0	-14.8±0.2	1.80±0.01	-	-
SI=10%	-23±0.0	0.62±0.0	-15±0.0	1.61±0.0	17.5±0.1	0.44±0.00
SI=15%	-23±0.0	0.62±0.0	-15±0.0	1.50±0.01	16.5±0.1	0.55±0.00
SI=20%	-23±0.0	0.62±0.0	-15±0.0	1.42±0.02	15.9±0.2	0.68±0.02
SI=25%	-23±0.0	0.62±0.0	-15±0.0	1.30±0.0	14.8±0.1	0.75±0.00

Centroid of AHRR (CA_c) and CA50 are shown in the figure Q-1. The CA50 changes about 1° from baseline to GSEP=3.5 ms while the CA_c changes by 6° . For SI sweep also the changes in CA_c is more significant, however, both CA50 and CA_c show the same trend in SI sweep.



(a) GSEP sweep

²² The measurements in this table are reported as Average ± (maximum-minimum)/2

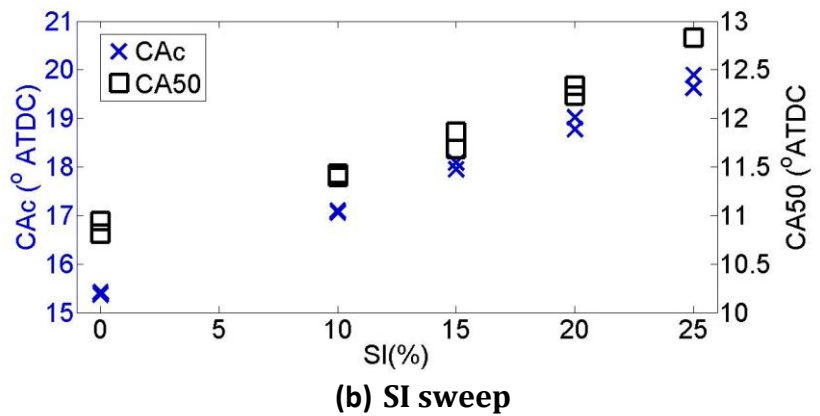
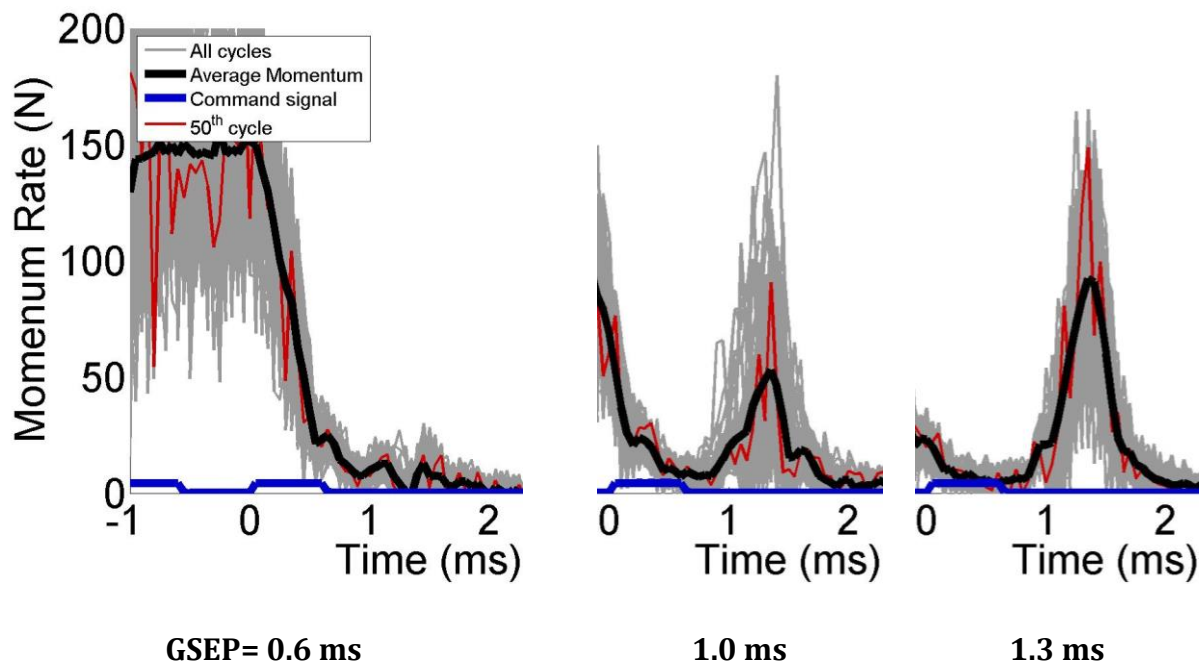


Figure Q-3 CA_c and CA50 for the SI and GSEP sweep experiments.

Appendix R: Injection-Injection Variability of LPI Momentum Measurement Tests

The momentum rate of all injections (100 injections) for post injection tests are shown in figure R-1. The results are the same as Figure 4-1; however, in addition of average momentum rate, all the cycles are shown. The data are not smoothed. The injection-injection variability range is close for all the GSEPs; however, since for $GSEP \leq 1.3$ ms the magnitude of average momentum rate is lower it results in higher COV for smaller GSEPs.



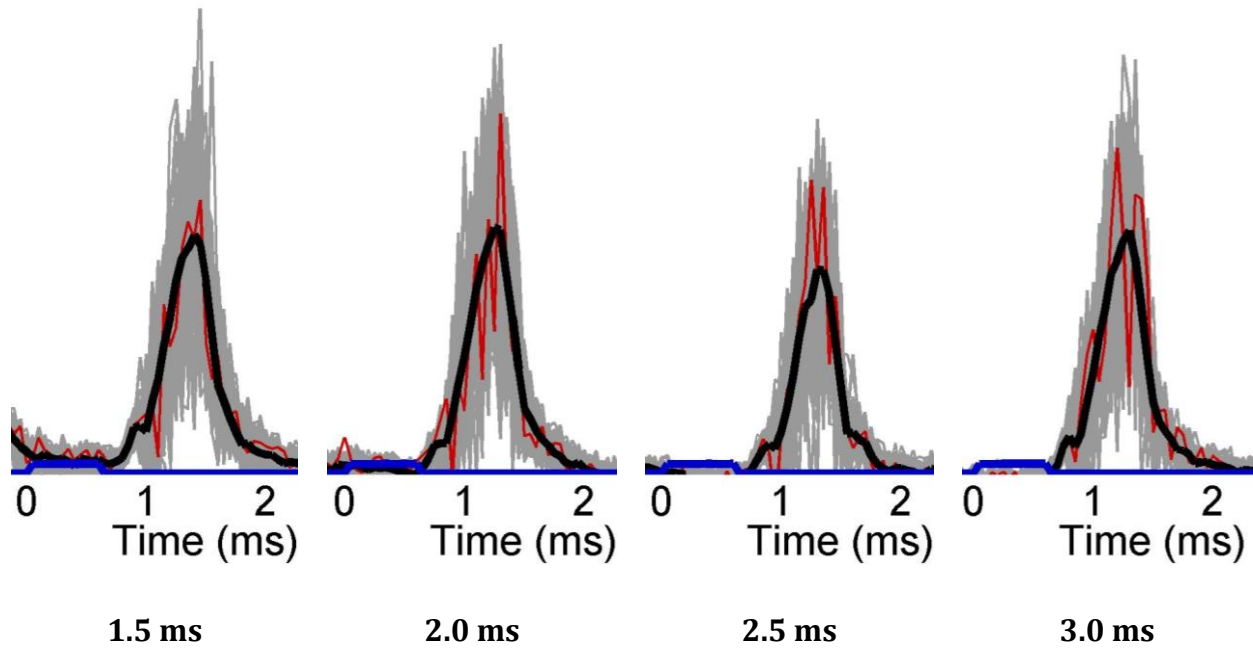


Figure R-1. Momentum rate of split injection tests, GRP=26.2MPa, back pressure of 10MPa and GPW1=1.8 ms and GPW2=0.6ms (the average data are shown in Figure 4 1).